COTUTELLE THESIS

SUBMITTED IN PARTIAL FULFILMENT OF THE REQUIREMENTS FOR THE DEGREE OF

DOCTOR OF PHILOSOPHY IN PLASMA PHYSICS

University of Bordeaux
And University of the Basque Country

Doctoral School **n°209** SCIENCES PHYSIQUES ET DE L'INGÉNIEUR (SPI)
SECTION : DCT ASTROPHYSIQUE, PLASMAS, NUCLÉAIRE

Presented by: **DONALDI MANCELLI**

GENERATION OF LASER-DRIVEN SHOCKS AND THEIR USE TO STUDY SIMPLE COMPOUNDS AT HIGH PRESSURE

Defended on: 15 December 2021

Composition of the committee

M. Ph. GUIONNEAU	Professor, University of Bordeaux	Head of the Jury
M. M. Tatarakis	Professor, Hellenic Mediterranean University	Examiner
M. L. Gizzi	Head, INO CNR Pisa	Reviewer
M. L. Volpe	Professor, University of Salamanca	Reviewer
Mm. K. Batani	Dr., IPPLM Warsaw	Examiner
M. M. Martinez-Canales	Dr., University of Edimburgh	Examiner
Mm. M. Blanco-Rey	Dr., University of Basque Country	Examiner
M. Ph. Nicolai	Dr., University of Bordeaux	Invited
M. D. Batani	Professor, University of Bordeaux	Thesis Director
M. I. Errea	Dr., University of Basque Country	Thesis Director

Titre : Génération de chocs par laser et leur utilisation pour étudier des composés simple a haute pression

Ressumé : La connaissance et la compréhension approfondies de l'équation d'état de matériaux simples tels que le carbone et l'eau dans le régime de la matière dense chaude (WDM) sont essentielles pour la modélisation de la structure interne de nombreux objets astrophysiques, en particulier les planètes joviennes, ainsi que pour la recherche sur la fusion par confinement inertiel (ICF). Une équation précise des données d'état peut être utilisée pour comparer les codes hydrodynamiques et valider des modèles théoriques tels que SESAME, MPQEOS, FEOS et l'équation d'état ab-initio calculée avec les codes de la théorie fonctionnelle de la densité (DFT). Les installations laser PHELIX au GSI en Allemagne et GEKKO-XII à l'Institute of Laser Engineering (ILE) au Japon ont été utilisées pour générer des ondes de choc plaines dans des cibles de diamant et d'eau résultant en conditions WDM. Nous avons utilisé un ensemble de diagnostics indépendants pour mesurer les conditions thermodynamiques du diamant et de l'eau comprimés, y compris l'interférométrie de vitesse pour tout réflecteur (VISAR) et la pyrométrie optique résolue en temps (SOP). En plus du travail sur la compression laser, on present aussi les résultats d'une campagne expérimentale utilisant la compression laser dynamique sur des échantillons d'eau précomprimés de façon statique en utilisant des cellules à enclume de diamant. La dernière partie de la thèse est consacrée à un travail théorique Ab-initio sur LiH utilisant les codes Quantum Espresso et CALYPSO, 'a la recherche de candidats intermédiaires pour expliquer la transition de phase métal-isolant $B1 - B2$**. Enfin, nous présentons les résultats préliminaires de la campagne expérimentale préparatoire sur l'expérience à haute puissance et taux de répétition élevé pour la plate-forme L4n sur P3 à ELI-Beamlines en soulignant les défis auxquels nous devons faire face et les avancées qui résulteront d'une telle installation laser.**

Mots clés :Shock waves, EOS, Ab-initio, Carbon, Water, LiH, Quartz, VISAR, SOP, DAC

Titulo : Generación de choques impulsados por láser y su utilización para el estudio de compuestos simples a altas presiones

Extracto/Resumen : El conocimiento profundo y la comprensión de la ecuación de estado de materiales simples como el carbono y el agua en el régimen de materia densa cálida (WDM) es esencial para el modelado de la estructura interna de muchos objetos astrofísicos, en particular los planetas jovianos, asıcomo para los planetas inerciales. investigación de fusión de contención (ICF). Se pueden utilizar datos precisos de ecuaciones de estado para comparar códigos hidroeléctricos y validar modelos teóricos como SESAME, MPQEOS, FEOS y ecuaciones de estado ab-initio calculadas con códigos de teoría de función de densidad (DFT). Las instalaciones de láser PHELIX en GSI Alemania y GEKKO-XII en el Instituto de Ingeniería Láser ILE en Japón se utilizaron para impulsar ondas de choque planas en objetivos estructurados de múltiples capas de diamante y agua, lo que resultó en condiciones de WDM. Usamos un conjunto de diagnósticos independientes para medir las condiciones termodinámicas de WDM, incluida la interferometría de velocidad para cualquier reflector (VISAR) y pirometría óptica rayada (SOP), diamante denso y agua. Además del trabajo de compresión láser, también se presentan los resultados de la campaña experimental que utilizó compresión estática en muestras de agua precomprimidas con el uso de celdas de yunque de diamante. La última parte de la tesis la dedicaremos al trabajo teórico ab-initio sobre LiH utilizando el código Quantum Espresso y CALYPSO para la predicción de la estructura cristalina (CSP) a presiones elevadas y el sistema de tres unidades de fórmula diferente, buscando un candidato intermedio para explicar la fase del aislante metálico. transición B1 - B2. Finalmente, presentamos los resultados preliminares de la campaña experimental preparatoria sobre el experimento de alta potencia y alta tasa de repetición para el L4n en la plataforma P3 en ELI-Beamlines, señalando los desafíos que tenemos que enfrentar y los avances que resultará de dicha instalación láser.

Palabras-clave :Ondas de choque, EOS, Ab-initio, Carbono, Agua, LiH, Cuarzo, VISAR, SOP, DAC

Title : Generation of laser driven shocks and their use to study simple compounds at high pressure

Abstract : Deep knowledge and understanding of the equation of state of simple materials such as the carbon and water in the warm dense matter (WDM) regime is essential for the modelling of the inner structure of many astrophysical objects, in particular Jovian planets as well as for inertial confinement fusion (ICF) research. Accurate equation of state data can be used to benchmark hydro codes and validate theoretical models such as SESAME, MPQEOS, FEOS and ab-initio equation of state calculated with density function theory (DFT) codes. The PHELiX at GSI Germany and GEKKO-XII at Institute of Laser Engineering ILE in Japan, laser facilities were used to drive planar shock waves in multi layered structured targets of diamond and water resulting in WDM conditions. We utilised a set of independent diagnostics to measure the thermodynamic conditions of WDM including velocity interferometry for any reflector (VISAR) and streaked optical pyrometry (SOP).This work presents a full set of measurements of the thermodynamic properties for different laser intensity drivers creating warm dense diamond and water. In addition to the laser compression work, results from experimental campaign using static compression on precompressed water samples with the use of diamond anvil cells are also being presented. The last part of thesis we will dedicate on theoretical ab-initio work on LiH utilising Quantum Espresso code and CALYPSO for crystal structure prediction (CSP) at elevated pressures and three different formula units system, searching for intermediate candidate to explain the metal-insulator phase transition $\mathrm{B1-B2}$. Finally we present preliminary results from preparatory experimental campaign on high power and high repetition rate experiment for the L4n on P3 platform at ELI-Beamlines pointing out the challenges we have to face and the advances that will results from such laser facility.

Keywords : Shock waves, EOS, Ab-initio, Carbon, Water, LiH, Quartz, VISAR, SOP, DAC

UMR 5251 −Université de Bordeaux. 351, cours de la Libération − F 33 405 TALENCE.
&
Donostia International Physics Centre, University of the Basque Country
Manuel de Lardizabal 5, 20018 Donostia

Acknowledgments

I have conducted this Cotuttele PhD under a financial support from the DIPC - University of the Basque Country and CELIA - CEA University of Bordeaux . I acknowledge financial support to the research presented in this Thesis from the Donostia International's Physics Centre and French Alternative Energies and Atomic Energy Commission. Complementary training's necessary for the validation of this PhD have been funded by the University of Bordeaux and by the Erasmus+ program.

I start the professional part of these Acknowledgments by thanking my supervisors, Dimitri Batani and Ion Errea, for their guidance throughout the ups and the downs of this long and challenging journey, who taught me a lot about the different aspects of this work, from the use of data analysis and simulation codes to the preparation and conduction of the experimental campaigns. I thank Porf. Luca Volpe and Dr. Leonida Gizzi for their useful corrections and suggestions for this Thesis for their interesting inputs during the discussion. I also want to thank my colleagues Francesco Barbato and Luca Antonelli, Alessandro Tentori, not only for their support but also for the many good moments we shared, and Jocelain Trela for his good advices and the always useful discussions. At this point I would like to thank Arnaud Colaitis, Thibault Goudal, Victorien Bouffitier, Eduardo Rovere, Christos Vlachos,Olena Turianska, Diego Viala for the fun and nice time and discussions we had through out this big journey. I thank the many colleagues I have had the pleasure to work with in the context of our national and international collaborations. Between them, Luca Antonelli (York University), Matthew Khan (University of York, United Kingdom), Guillaume Boutoux (CELIA-CEA), Dimitri Khagani (GSI - CELIA), and Michael Ehret (CELIA),Gabriele Christoforeti (CNR, italy), Prof. Stefano Atzeni (Sapienza, Italy), Paul Neumayer (GSI, Germany), Norimasa Ozaki, Keisuke Shigemori, Koki Kawasaki, Yohei Fujimoto, Yuhei Umeda (Osaka University, Japan), Noemi Jourdain and Prof. Vladimir Tikhonchuk for his valuable discussions throughout those years.

Many thanks go to the members of the CELIA and DIPC support teams and to the CELIA and DIPC facility staff members, whose contribution to the preparation of the experiments and to their success has been critical. I would like to thank also the staff of the other facilities I used during my work, GEKKO XII (Osaka, Japan) and Rutherford Appleton Laboratory, Harwell Campus,(United Kingdom), PHELIX GSI (Darmstadt, Germany) and Prague Asterix Laser System(Prague, Czech Republic).

I warmly thank my whole family, and especially my parents, and Georgia for their continuous support and advice. To all my friends, currently scattered around the world.

Dédication

The necessary in nature, then, is plainly what we call by the name of matter, and the changes in it. Both causes must be stated by the physicist, but especially the end, for that is the cause of the matter, not vice versa and the end is 'that for the sake of which', and the beginning starts from the definition or essence...
Aristotle, Physics II 9

"Empty your mind, be formless, shapeless, like water. Be water, my friend." – Bruce Lee

0.1 Thesis plan

This thesis is divided in three parts: **Part I** includes chapter (1 - 3) treats the necessity of EOS study and the application in planetary science and inertial confinement fusion studies. **Part II** including chapter 4 and 5 describes experimental results on three different high power laser facilities on diamond and water samples at Mbar pressures. **Part III** including chapter 6 and 7 shows results from ab-initio coupled with crystal structure prediction on LiH searching possible candidate for the metal insulator transition and the last chapter on preliminary experiment on High power high repetition rate and the challenges that we need to surpass.

- **Part I: Equation of state of simple compounds from ab-initio to laboratory**
  - **Chapter 1** presents the domain of the EOS and its applicability in ICF and planetary science. Our current knowledge about EOS and the limits and questions that are still open.
  - **Chapter 2** is describing shock chronometry and the theoretical background of the shock formation and propagation in media. Also we describe the Impedance Mismatch method which will be used to analyse experimental data.
  - **Chapter 3** is devoted to the description of the physics of shock waves and the experimental and theoretical tool that we used for EOS studies.With main focus on optical velocimetry and pyrometry (VISAR and SOP) as main experimental platforms. And radiative hydrodynamic codes and DFT methods applied for EOS studies.

- **Part II: Experimental Results (Diamond & Water)**
  - **Chapter 4** presents experimental data on diamond samples relevant for planetary science and ICF research. It shows results on metallic diamond targets in the Mbar regime held at PHELIX GSI laser facility.
  - **Chapter 5** treats experimental results on dynamic compression of water samples from two experimental campaign's (GEKK) XII and PHELIX laser facilities): We present the target design used for EOS study of water and its interplay in planetary astrophysics. Results are compared with theoretical models of SESMAE database.

- **Part III: Ab-initio calculations and high power and high repetition rate laser facilities**
  - **Chapter 6** treats ab-initio DFT calculation and crystal structure prediction if LiH systems.

- **Chapter 7** is devoted on preliminary experimental results held at PALS laser facility in the context of the preparation of and experimental campaign on the new laser facility at ELI-Prague. On the challenges we will face on the preparation and running of a high power and high repetition rate laser facility. Some of the challenges are (targetry, data collection, diagnostics optimisation etc.).

In the **Conclusions and Perspectives** we summarise the main technical and scientific advancements of the work described in this Thesis. A complete Bibliography is listed and the Annexes list of publication is presented and technical information about the hydro code used in this work. As well additional results that are supporting this work.

Abbreviations

ICF Inertial Confinement Fusion
DAC Diamond Anvil Cell
WDM Warm Dense Matter
HEDP High Energy Density Physics
EOS Equation of State
SOP Streak Optical Pyrometer
VISAR Velocity Interferometer for Any Reflector
IM Impedance Mismatch
DFT Density Function Theory
MD Molecular Dynamics
FPMD First-Principles Molecular Dynamics
CSP Crystal Structure Predictions
PSO Particle Swarm Optimisation
HRR High Repetition Rate

Contents

List of Figures

List of Tables

Part I

Equation of State of simple compounds from ab-initio to laboratory

Chapter 1

Introduction

Contents

In this Chapter we will motivate the scientific goals of the experimental and theoretical work presented in this manuscript. First, we will introduce the context of Equation of State and the study of dynamic behaviour of simple compounds. We will then present the foundations of the models describing the interior structure of planets, the generation of planetary magnetic fields, and the evolution of planets and the significance of their study on inertial confinement fusion and hydrodynamic phenomena. We will highlight the necessity of characterising the behaviour

of the components and the thermodynamic conditions, which is the subject of this Thesis. Then we will overview four experimental campaigns, one at PHELIX (GSI, GERMANY) on Diamond samples, and the second on Water samples at GEKKO-XII (OSAKA, JAPAN) irradiating pre-comppressed samples utilising DAC (Diamond Anvil Cell) and un-compressed multilayered samples as well. The third experimental study on un-compressed multilayered Water cell samples at PHELIX December 2021 this will be addressed in Chapter 6. Finally, we present ab-initio calculations for LiH sinlge crystals performed using the PW and PHonon packages of Quantum-Espresso [Giannozzi et al., 2009, Giannozzi et al., 2017, Giannozzi et al., 2020] resulting in an accepted experimental proposal at PHELIX laser facility.

1.1 Outstanding question on Equation of State of simple compounds

Material equation of state (EOS) models, relating the thermo-dynamic state variables of a material, are essential to materials science, high energy density physics, and warm dense matter studies since they are required to close the equations for hydrodynamic simulations [J Castor 2004]. In high energy density physics applications, the EOS must describe the material response over large ranges of conditions covering a variety of phases from crystalline or amorphous solid to ionized plasma. The large range of conditions and their extreme nature make it impossible to completely explore the EOS experimentally and so researchers must rely on theoretical calculations [Militzer et al., 2021], bench-marked against experiments at a few (T, ρ) points. Where data do not exist, confidence in EOS models can be built by comparing calculations from fundamentally different approaches. This process is essential to the development of reliable EOS models. In inertial confinement fusion (ICF) [Betti and Hurricane, 2016] experiments, the EOS plays an essential role in determining the overall implosion performance (measured by the total fusion yield). The

EOS determines the overall drive efficiency through the ablation pressure and hydrodynamic coupling efficiency to the deuterium-tritium fuel [Robey et al., 2012], the timing of shock waves [Robey et al., 2012, Robey et al., 2016, Goncharov et al., 2006, Boehly et al., 2009, Boehly et al., 2011] driven through the target, the growth rates of hydrodynamic instabilities [Clark et al., 2010, Hammel et al., 2010, Hu et al., 2015, Hu et al., 2018], and the compressibility of both the fuel and ablator [Hu et al., 2008]. As a result, the EOS is an essential piece of ICF design calculations; in turn, ongoing ICF experiments have stimulated very rapid developments in state-of-the-art EOS simulations and experiments. The recent interest on developing more accurate equation of state models calibrating EOS data with ab-initio calculation, and experimental points will also result in a better understanding of the material behaviour in extreme thermodynamic conditions.

1.2 Warm dance matter and high energy density physics

Within this context, computer simulations provide a crucial contribution, as they can be used to predict the behavior of matter at extreme conditions. However, this approach is quite challenging, due to the elusive theoretical description of the WDM regime as shown in Figure 1.1. Indeed, WDM is partially or highly coupled (the electrical potential between charged particles is of the same magnitude or dominates over thermal energy) and partially degenerate (the quantum wave-functions of atoms partially overlap). It also displays a complex physical-chemical behavior as distinct states of ions, atoms, molecules, clusters, and lattices often coexist. In absence of a complete theory describing the WDM, it is possible to use a numerical approach based only on the first principles of quantum mechanics: ab-initio calculations. Within this framework, a quantum treatment of electrons is done using the density functional theory, while the motion of ions is simulated via classical molecular dynamics [Bonitz et al., 2020, Behunin et al., 2014, French et al., 2012]. Unfortunately, this kind of simulations long computation times even when using state of the art super-computers

and their results need an experimental validation. The basic challenges of any experimental approach are the generation of WDM states in the laboratory and their characterization [Falk, 2018]. The extreme conditions of interest can be achieved via static and dynamic methods. Figure 1.2 shows three of such methods. Static methods, typically using Diamond Anvil Cells (DAC) allow precise measurements but are limited in pressure and temperature. Dynamic methods are based on the propagation of compression waves (which can be generated with different methods: explosion, magnetic pinch, gas-gun, high-power laser ablation) and allow to explore higher pressures and temperatures compared to static methods. Dynamic methods allow the generation of the desired states for very short times (from the microsecond to the nanosecond scale), which may complicate their characterization and require in any case ultra fast diagnostics. In the context of dynamic methods, the simplest possible approach is single-shock compression of a material starting from ambient conditions. This method allows to explore a locus of thermodynamic states called principal Hugoniot curve [Pierre-Henri Hugoniot, 1889]. The loading of a shock wave is a highly entropic phenomenon: this means that a huge fraction of the shock wave energy is employed in heating, instead than in compressing the sample. For this reason, single-shock loading permits to study high temperature conditions. Such temperatures are much higher than those generally encountered in planetary interiors, but anyway interesting for the study of early planetary histories, the interiors of giant and hot exo-planets, and planetary impacts with giant astronomical objects. Those high-pressure / high-temperature conditions are also of primary interest for the characterization of the WDM regime and as a benchmark of ab-initio simulations [Militzer et al., 2020]. However, the generation and characterization of moderate-temperature states remains essential to directly probe planetary interiors conditions and to extend the frontiers of the charted region of the phase diagram of WDM. To achieve lower temperature conditions, the main strategy consists in increasing the density of the sample prior to shock loading, in order to decrease the entropy jump associated to the propagation of the shock wave. This can be done statically (using a DAC) or dynamically (e.g. with the propagation a weak shock wave prior to the main

shock). On the one hand, coupling DAC and shock compression is challenging, mainly because of the difficult optical access to the target and of the important thickness of the anvil, which complicates the propagation of the shock wave; On the other hand, also the propagation of two shocks is challenging as it requires considerable simulation efforts to carefully shape the laser pulse profiles and a complicated analysis to determine the double-shocked state from the observable. The combination of the described static and dynamic methods, including pre-compression strategies, allows to span a wide region of the phase diagram encompassing diverse phases and conditions.

1.3 Thermonuclear Fusion

Our society is putting a great effort in reducing its energy supply needs and looking for alternative ways for reducing its waste products. Photovoltaic and thermal solar energy sources do not means to be able to cover future humanity its energy needs. A big international effort has gone into alternative sources such as solar panels and thermal conversion. An alternative to capturing the energy using the same mechanism of the Sun is to produce fusion power directly by means of controlled thermonuclear fusion reactions. Thermonuclear fusion occurs when the short-range attraction of the strong nuclear force overcomes the electrostatic repulsion of two nuclei. Overcoming this repulsion, known as the Coulomb barrier, requires the plasma to be extremely hot. The deuterium-tritium (DT) fusion cycle has the lowest energy threshold and thus it is the focus of nearly all major experimental fusion efforts. The cross section of fusion reaction for various nuclei are are shown in Figure 1.3. The most probable fusion reaction at low temperature is that of $D-T$, whose cross-section at $10\ keV$ is up to two orders of magnitude higher then for other reactants.The three relevant fusion reactions in a DT cycle are

$$ {}^{2}_{1}D + {}^{3}_{1}T \rightarrow {}^{4}_{2}He + n + 17.6MeV $$

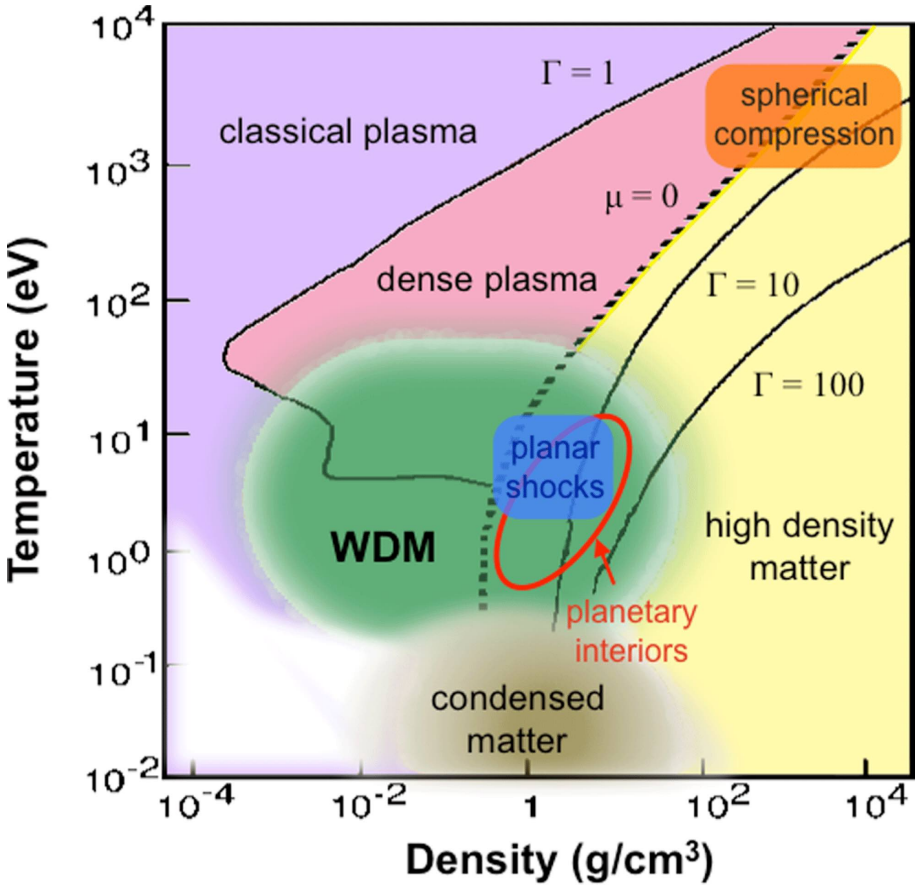

Figure 1.1: Phase diagram for the WDM regime. WDM lies between condensed matter, hot dense matter and ideal plasma (low densities), and overlaps the planar laser-generated shocks in matter as well as the astrophysical conditions.Γ is the coupling parameter (ratio of Coulomb and thermal energy) so the $\Gamma = 1$ line separates the strongly and weakly coupled regimes. μ is the chemical potential and the $\mu = 0$ line signifies the regime where the Fermi energy equals $\kappa_B T$, below this line we get Fermi degenerate matter, adapted from [Falk, 2018].

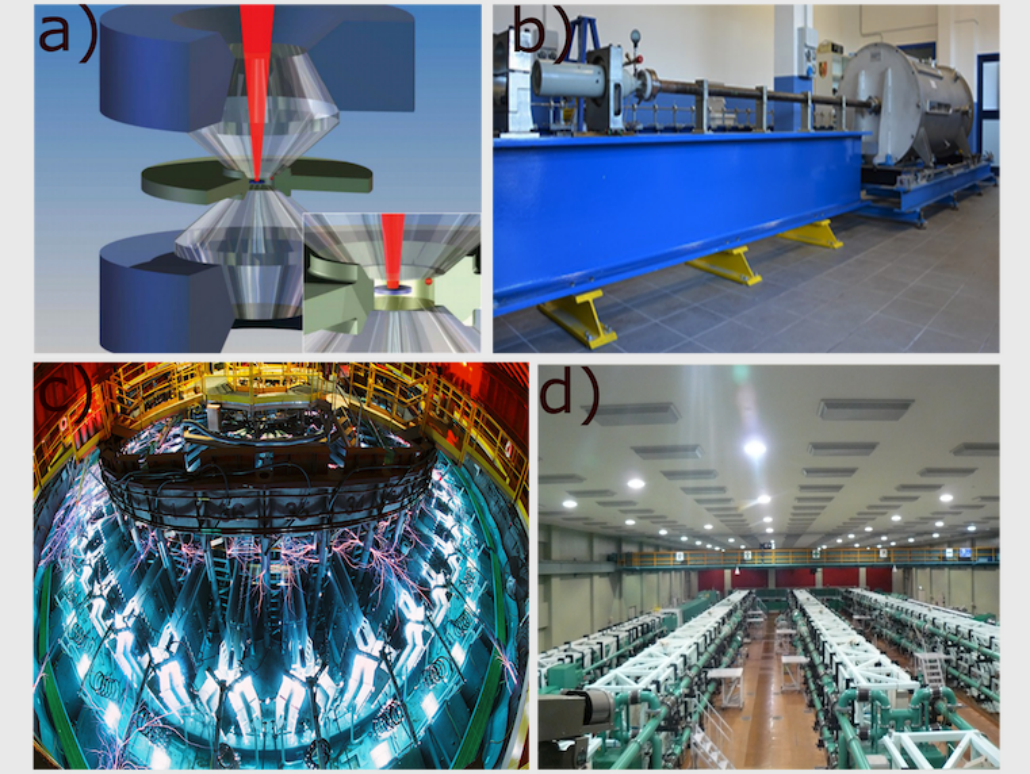

Figure 1.2: Different compression methods to achieve Warm Dense Matter conditions. (a). Detail of a Diamond Anvil Cell [Boehler, 2005]. (b). Gas gun. TECHDYN (Rome Italy. (c). Magnetic pinch: the Sandia Z machine (Albuquerque, New Mexico, USA). (d) GEKKO XII laser facility hall (ILE Osaka)

$$D + D \rightarrow^{3} He + n + 3.3MeV$$

$$T + T \rightarrow \alpha + 2n + 11.3MeV$$

where $17.6MeV$ is the kinetic energy released in the fusion process and it is shared between α particle $3.56MeV$ and the neutron $14.03MeV$

The majority of the energy released in the DT fusion cycle is in the form of energetic neutrons. Because neutrons do not have electric charge, extracting this energy requires a method to convert their kinetic energy to heat, which can be used to generate power with a steam turbine. The majority of experimental efforts to achieve controlled ther-

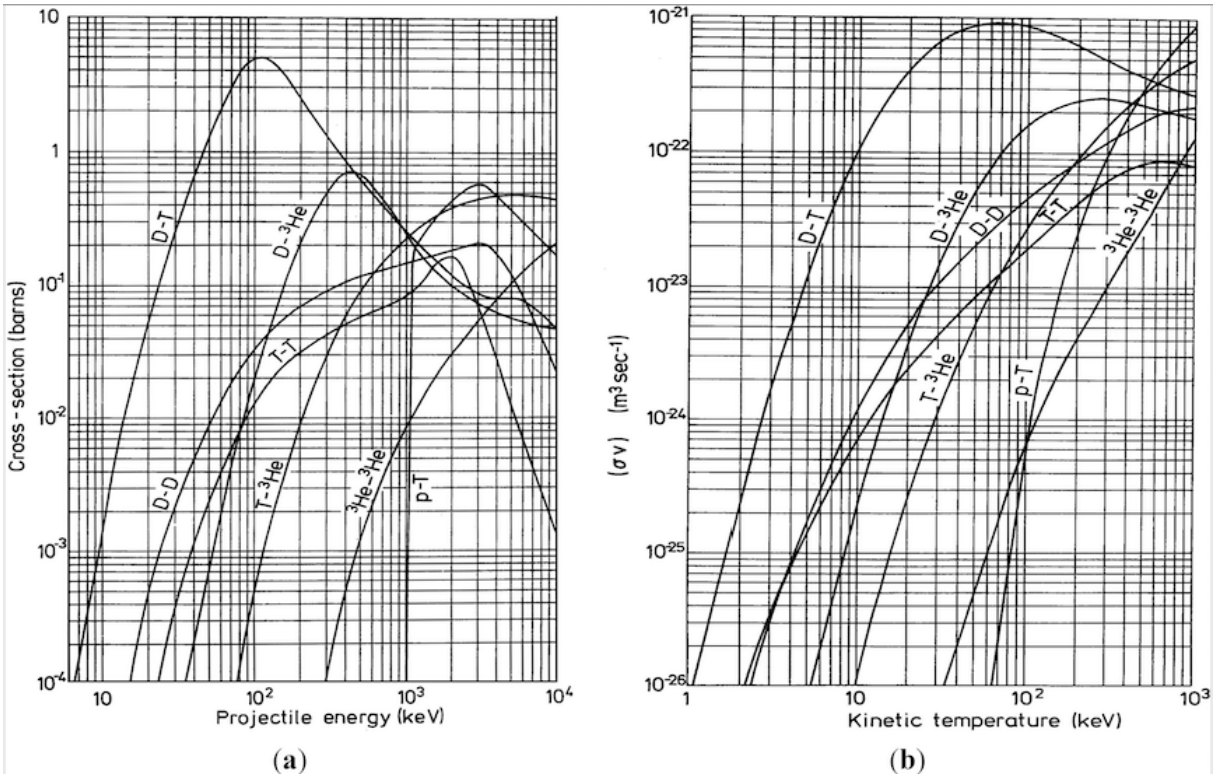

Figure 1.3: ($left$) fusion reaction cross sections (in barns , i.e. $10^{-28}\ m^2$) as a function of the relative kinetic energy between nucleus in keV, and ($right$) thermal reactivity for the fusion reactions (in m^3/s) as a function of the kinetic temperature in keV Figures from $http://www.kayelbau.npl.co.uk$.

monuclear fusion fall into one of two categories: inertial confinement fusion (ICF) or magnetic confinement fusion (MCF). ICF uses a spherical implosion to rapidly compress the fuel, initiating a fusion reaction in the central hot-spot when the material converges at the center of the sphere. MCF experiments create a steady-state plasma confined using powerful magnetic fields, where the rate of fusion is controlled by adjusting the inputs of the reaction. There are several active experimental campaigns to achieve fusion power. The National Ignition Facility (NIF) [Lindl, 1995] at Lawrence Livermore National Lab (LLNL) is the largest facility for ICF, with 192 laser beams producing a total of 1.8 MJ to drive fusion implosions. NIF has been in operation since 2009 (with all 192 beams) and continues to conduct experiments in an attempt to reach ignition. ITER, the International Thermonuclear Experimental Reactor, currently under construction will be the largest MCF facility. Although ITER does not aim to be an operational power plant, the goal is to produce 500 MW of power for hundreds of seconds while only needing 50 MW to heat the plasma. At the time of this writing, the first plasma at ITER is scheduled for December 2025

1.4 Inertial Confinement Fusion

The aim of ICF [Betti and Hurricane, 2016] is to produce the conditions required for thermonuclear fusion by compressing the fuel using converging shock waves. Figure 1.4 shows the basic principle of ICF, where a) the outer layer of a spherical shell of fuel is heated by an intense external radiation source and b) material near the outer surface rapidly expands, acting as a rocket to force the remaining material inwards. Next, the converging material c) stagnates near the center, producing a dense core which d) ignites the fusion reaction, releasing a vast quantity of energy. The external radiation source can be in the form of direct laser irradiation (direct drive) [NUCKOLLS et al., 1972, Basov et al., 1985, Basov et al., 1992, Lindl, 1995, Lindl and Moses, 2011] or from thermal x-rays from a surrounding surface (indirect drive) [NUCKOLLS et al., 1972, Lindl, 1995]. The current design at NIF uses an indirect

drive geometry, with a spherical fuel capsule placed inside a small gold cylinder, known as a hohlraum. Early predictions for the requirements suggested that as little as $1\ kJ$ of laser energy may be sufficient to achieve breakeven, defined by when the input energy and fusion energy output are equal, and $> 100\ kJ$ for electrical gain in a functioning power plant [NUCKOLLS et al., 1972, Lindl, 1995, Lindl and Moses, 2011]. Following these predictions, several large laser facilities were built to explore the physics of ICF and attempt to achieve ignition. LLNL, in particular, has built several Nd:glass laser systems since the early 70s, starting with the Long path laser, followed by the Argus, Shiva, Novette, and Nova lasers, OMEGA at Rochester University. The lessons learned from these systems ultimately led to the development of NIF [Lindl and Moses, 2011]. ICF experiments at NIF have encountered several difficulties preventing ignition. Four primary areas of concerns include implosion symmetry, implosion velocity, the implosion adiabat, and fuel and hot-spot mix. Achieving sufficient implosion symmetry requires careful control of the drive beam temporal and spatial profiles, both of which are complicated in the indirect drive geometry. Drive asymmetries, created by the tent holding the spherical capsule in place, have been especially difficult to overcome. Implosion velocity and adiabat are closely related, as operating at a higher adiabat generates higher implosion velocities at the expense of creating more entropy in the compressed fuel. The high foot campaign at NIF [Hurricane et al., 2014, Edwards et al., 2013] used this approach, reaching higher and neutron yields [Landen et al., 2020], but the additional entropy created by the higher adiabat ultimately prevents ignition. Nevertheless, probing the conditions created using this technique may prove to be useful in understanding fusion-relevant WDM physics. Finally, hydrodynamic instabilities result mixing of the layers of the target in the fuel and hot-spot. This deviation from the ideal case of spherical symmetry reduces compression of the fuel and prevents ignition.

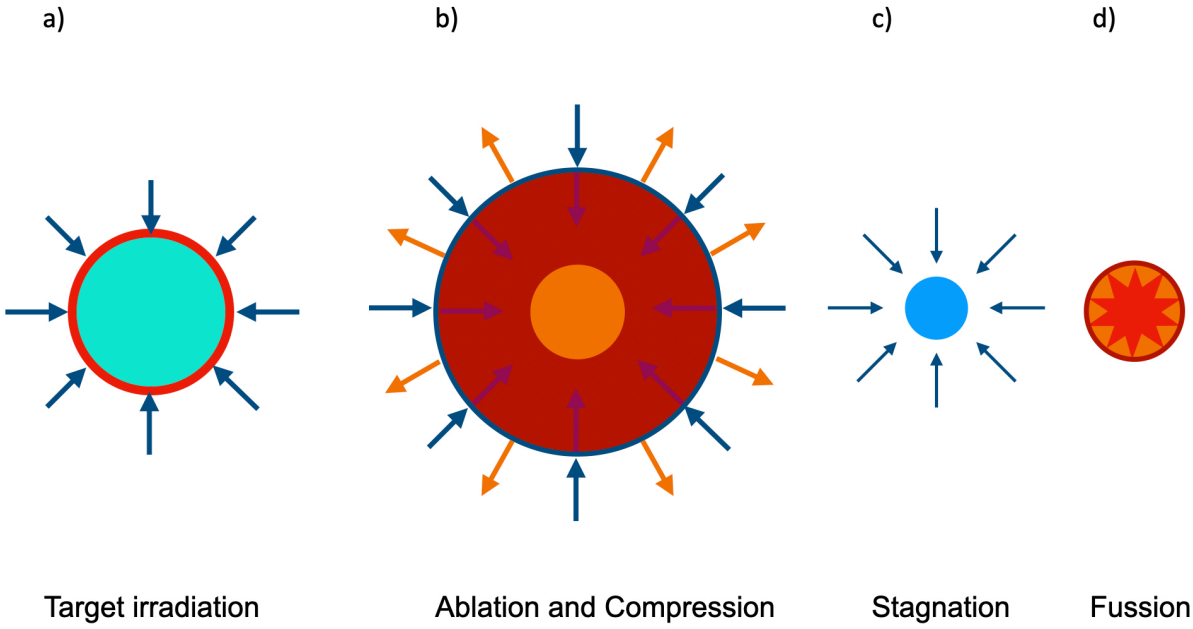

Figure 1.4: Schematic showing the basic principle of ICF. A spherical shell of fuel is a) heated by external radiation b) causing the outer material to rapidly expand, launching the remaining material inwards, resulting in c) stagnation at the center of the sphere and d) thermonuclear fusion of the remaining fuel. Adapted from wikipedia.org

1.5 Laser matter interaction

In the direct drive approach to inertial confinement fusion, the shell of fusion fuel is illuminated by laser radiation. In the classical scheme, the laser intensity is moderate (10^{12} to a few $10^{14} W/cm^2$) and collisional absorption is the main mechanism of absorption of the laser energy into plasma temperature. In this chapter, the quasi-stationary ablation profile created by collisional absorption is presented.

1.5.1 Ablation and Critical density

When a solid target is illuminated by an intense laser radiation, matter is first vaporized and ionized though multi-photon absorption [Mora, 1982a], creating a plasma which expands in the vacuum toward the laser radiation. The laser then propagates in an increasing profile of electron density, where it has to satisfy the plasma dispersion relation for electromagnetic waves

$$k^2 c^2 = \omega^2 - \omega_p^2 \tag{1.1}$$

where k and ω are the wave number and frequency of the electromagnetic wave, respectively, c is the speed of light in vacuum and ω_p is the electronic plasma frequency. This frequency is characteristic of the electron plasma wave in the plasma, and depends on their density

$$\omega_p = \sqrt{\frac{n_e e^2}{\epsilon_0 m_e}} \tag{1.2}$$

where n_e is the number electron density, e the elementary charge, ϵ_0 the permittivity of free space and $\mathrm{m_e}$ the electron mass. Along the propagation of the laser radiation in the plasma, the electron density increases and, following the dispersion relation, the wave number of the electromagnetic wave decreases. When it reaches $k = 0$, for $\omega = \omega_p$, the electromagnetic wave cannot propagate any further in the plasma and it is then reflected or absorbed. The electron density corresponding to this condition is called the

critical density

$$n_c[cm^{-3}] = \frac{\epsilon_0 m_e \omega^2}{e^2} \simeq \frac{1.1 \quad 10^{21}}{\lambda^2[\mu m^2]} \tag{1.3}$$

where λ is the laser wavelength. For shorter wavelengths, the critical density is higher, meaning that the laser radiation penetrates deeper in the plasma. The wavelength considered for direct drive ICF is $\lambda = 0.351\ \mu m$, such that the critical density is $n_c \simeq 9 \times 10^{21}$ cm^{-3}. This density is much lower that the electron density of the solid target, which for the case of a fully ionised CH is $\simeq 3.4 \times 10^{23}\ cm^{-3}$, showing that the laser radiation does not propagate up to the solid target.

1.5.2 Collisional absorption

The electrons of the plasma oscillate in the electric field of the laser. This motion is coherent and after one optical period, the electrons are back to their original position and velocity, so that no energy has been transferred from the laser to the plasma. But, if during this coherent motion an electron collides with an ion, resulting in a change of its momentum, its motion is no longer coherent. The energy gained by this electron is then transferred to the plasma though electron-electron collisions, rising its temperature. A more detailed description of the electron-ion collision shows that the conservation of momentum imposes the absorption of a photon during the collision. This three body collision is called inverse Bremsstrahlung and it is the main mechanism of absorption of laser radiation at intensities relevant for the classical scheme for ICF (of the order of $10^{14}\ W/cm^2$).

The evolution of the intensity of the laser radiation along its propagation axis x can be expressed as

$$\frac{\partial I_L(x)}{\partial x} = -\kappa I_L \tag{1.4}$$

where κ is the is the collisional absorption coefficient and is given by

$$\kappa = \frac{v_{ei}}{c} \left(\frac{n_e}{n_c}\right)^2 \frac{1}{\sqrt{1 - n_e/n_c}} \tag{1.5}$$

The electron-ion collision rate v_{ei} is the characteristic frequency of this absorption and, within the Spitzer's model, is given by

$$v_{ei} = \frac{4\sqrt{2\pi}}{3} \frac{n_e Z e^4 ln\Lambda_{ei}}{m_e^{1/3} T_e^{3/2}} \tag{1.6}$$

where Z is the plasma charge state, Λei the electron-ion Coulomb logarithm and T_e the plasma temperature in energy unit.

The absorption coefficient is strongly dependent on the electron density and it becomes very large when n_e tends toward n_c. This shows that, in the regime where the laser radiation is not fully absorbed before it reaches the critical density, most of the intensity is absorbed close to n_c.

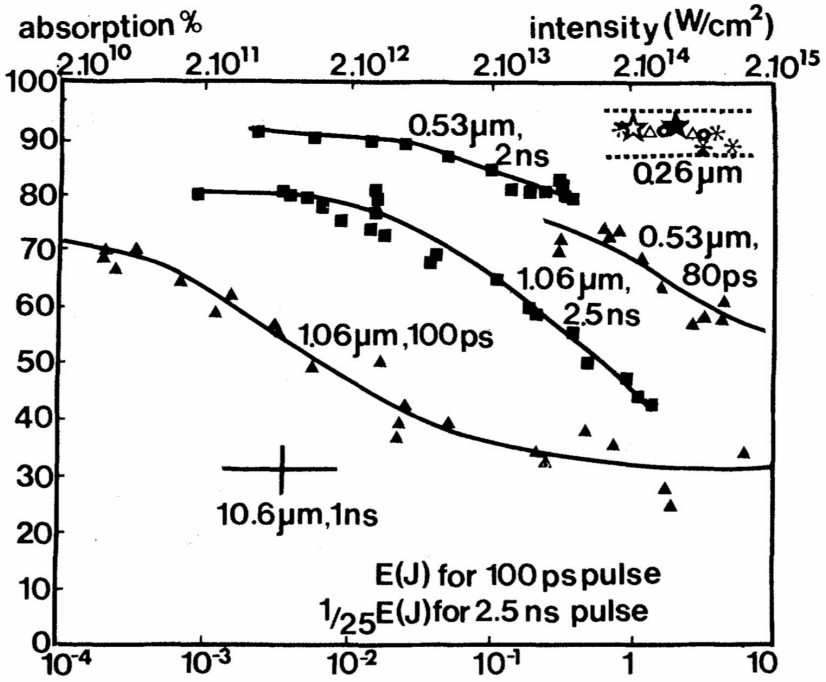

Figure 1.5: The fraction of absorbed laser light versus incident flux for various experimental conditions, figure adapted from[Garban-Labaune et al., 1982].

Figure 1.5 [Garban-Labaune et al., 1982] presents the fraction of absorbed laser light as a function of the laser intensity for several wavelengths and pulse duration's. It

shows that the absorbed fraction decreases when the laser intensity increases. This is due to the increase of electron temperature and the density gradient steepening. Another important results is the increase of absorbed fraction when the laser wavelength is reduced. Indeed, lasers with shorter wavelength penetrate to higher densities, leading to a more efficient absorption.

1.5.3 Stationary laser-driven ablation

Few hundreds of pico-seconds after the beginning of the laser matter interaction, the plasma reaches a quasi-stationary state. Figure 1.6 presents the temperature and density profiles corresponding to this state, in which four zones can be identified:

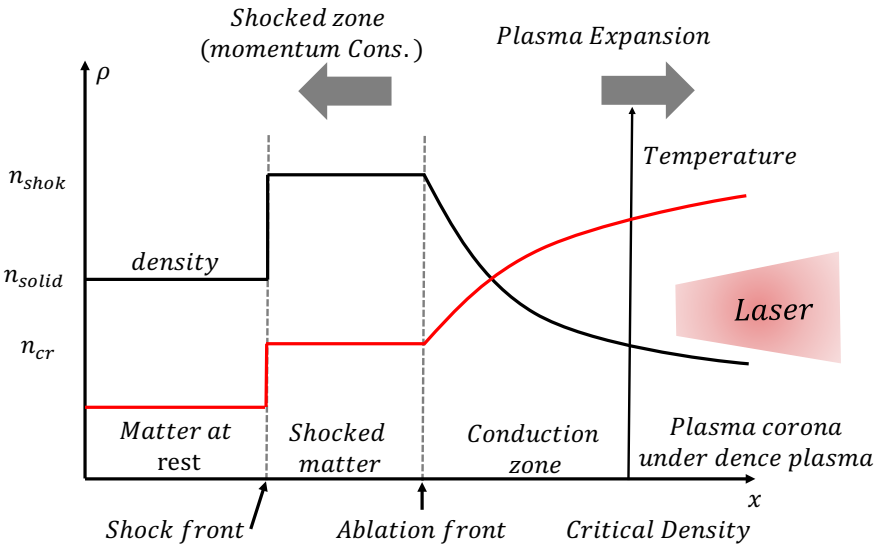

Figure 1.6: Profiles of density (in black) and temperature (in red) in stationary laser-driven ablation. Four zones are visible: the unperturbed target, the shocked target, the conduction zone and the plasma corona. These zones are separated by the shock front, the ablation front and the position of the critical density, respectively.

- The plasma corona: It corresponds to under-critical plasma. It is the only region in which the laser radiation propagates and therefore it is absorbed. In this region

the plasma has a low density and a high temperature. Due to its high electronic conduction, the plasma corona is approximately isothermal.

- The conduction zone: It corresponds to the over critical plasma. In this zone the thermal energy is transported from the hot corona to the colder dense part of the target, mostly though electronic conduction. In this region the density and temperature change a lot, but the pressure is rather constant.

- The shocked target: The pressure created by the ablation process leads to the creation of a shock wave that propagates in the solid target. The density, temperature and pressure in this region are higher than in the unperturbed target due to the non-isotropic compression induced by the shock wave.

- The unperturbed target: This is the zone not reached yet by the shock wave. Its density is the initial solid density of the target and its temperature is the ambient temperature.

The stationary ablation does not refer to a situation where all of these zones are at equilibrium. It only refers to the equilibrium of energy flux at the critical density, separating the corona from the conduction zone, which writes

$$I_{abs} = u\Delta E + Q \tag{1.7}$$

where $I_{abs} = A\ I_L$ is the absorbed laser intensity, $u\Delta E$ the flux of energy per unit surface associated with the flux of mass passing though the critical density and Q the heat required in order to maintain the corona at a constant temperature, compensating its cooling down due to its expansion. Assuming that the laser energy is locally deposited at the critical density, the ablation process can be described by a Chapman-Jouguet deflagration [Atzeni and Meyer-ter Vehn, 2004]. In these conditions, the plasma corona at the critical density has a velocity u equal to its isothermal sound velocity $c_T = \sqrt{(P_c/\rho_c)}$, where P_c and ρc are the pressure and density of the corona at the critical density. The

pressure is discontinuous at the critical density so that the pressure in the conduction zone P_{cond} is twice the pressure in the plasma corona P_c. Because the P_{cond} is equal to the ablation pressure P_a, it writes $P_a = P_{cond} = 2\ P_c$. Applying these assumption to formula 1.7 we have:

$$I_{abs} = 4\rho_c c_T^3 \tag{1.8}$$

From this relation, the temperature at the critical density, the ablation pressure and the mass ablation rate can be expressed as functions of the laser parameters only. Indeed, the mass density is related to the electron number density and therefore to the laser wavelength by formula. The definition of the isothermal sound velocity allows determining the temperature at the critical density

$$\frac{1+Z}{Am_p}T_c = c_T^2 = \left(\frac{I_{abs}}{4\rho_c}\right)^{2/3} \tag{1.9}$$

The ablation pressure is twice the pressure of the corona at the critical density $P_a = 2P_{corona}$:

$$P_a = 2\rho_c c_T^2 = (\rho_c/2)^{1/3}\, I_L^{2/3} \tag{1.10}$$

The mass ablation rate is the flux of mass passing though the ablation front. Since the conduction zone is stationary, the same mass flux go through the critical density. Also, at the critical density, $u = c_T$ so that the mass ablation rate writes

$$\dot{m}_a = \rho_c c_T = \left(\frac{\rho_c}{2}\right)^{(2/3)} I_L^{1/3} \tag{1.11}$$

In many design for ICF, the DT shell is coated with CH ablator in order to increase laser absorption. Using CH average mass number $A = 13/2$ and atomic number $Z = 7/2$, explicit expressions for these relations are obtained, we can estimate the ablation pressure using empirical formula [Lindl, 1995, Dahmani, 1993, Mora, 1982a]

$$P(Mbar) = 8.6 \left(\frac{I \frac{W}{cm^2}}{10^{14}} \right)^{2/3} (\lambda(\mu m))^{-2/3} (A/2Z)^{1/2} \tag{1.12}$$

where I_{14} is the laser intensity in units of $10^{14} W/cm^2$ and laser wavelength in units of micrometers. Figure 1.7 shows ablation pressures calculated using above mentioned empirical scaling law for a range of irradiance for the 1st, 2nd, and 3rd harmonic of Nd:glass laser systems.

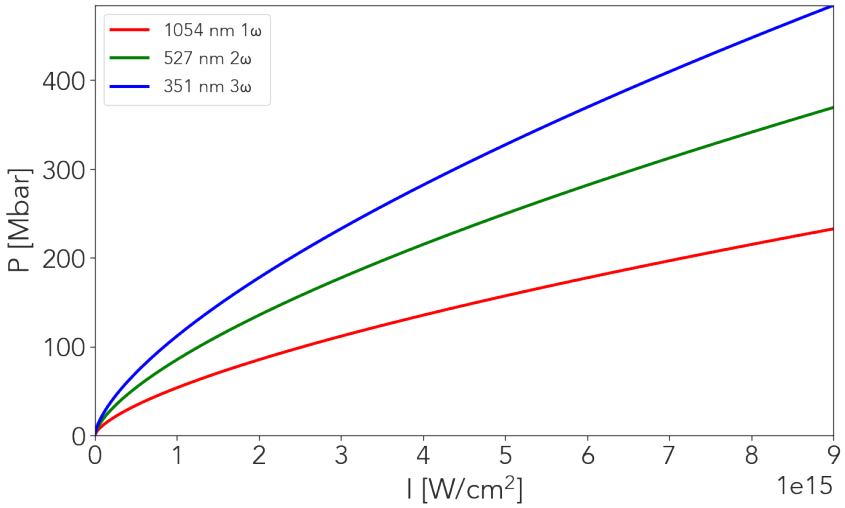

Figure 1.7: Ablation pressure for 1st, 2nd, and 3rd harmonic of Nd:glass laser systems with a fundamental wavelength of $1054\ nm$. Doubling or tripling the laser frequency (2ω and 3ω) can significantly increase the ablation pressure for a given driving intensity.

1.6 Conclusion and perspectives

In this chapter we described the main motivation that drive the study of the equation of state and the key factors that are keeping this domain ongoing for decades. Then we pinpoint the importance of the EOS and the warn dense matter which can be created in laboratory conditions. The key role of EOS in ICF and WDM research. Then we do a brief introduction to Laser matter interaction mechanism followed by ablation when laser beam heats a solid target. Finally we described the basic scaling laws with respect

to laser intensity. Therefore in the next Chapter we will treat the basic Physics of shock waves and the laws that govern them, these laws will be used to treat the experimental data analysis in the following Chapters.

Chapter 2

Shock chronometry

Contents

2.1 Physics of Shock Waves

A shock wave is the propagation of a discontinuity of pressure and density in a material. Shocks play a key role in the ICF, they allow fuel compression, thus accessing thermonuclear ignition. We first consider the shock wave in general, then we will introduce Rankine-Hugoniot relations, as well as the dynamics of a shock associated with the entropy it creates. Let us first consider a sound wave, propagating in a material medium an infinitesimal perturbation of the state (pressure, volume ...) and of movement (material speed) of the medium.

2.2 Fluid Equations

The wave propagation equations are established from the fluid equations. We describe each element of the fluid by its speed $\vec{u}$, its density ρ and its pressure P,as a functions of position and time. In fluid mechanics there are two types of equivalent representations of a flow. Euler representation uses the partial derivative operator $\frac{\partial}{\partial t}$ and describes the temporal evolution of a quantity at a fixed point in space. Lagrange representation describes the variation of this quantity by following a moving particle, it uses total derivative operator defined as:

$$\frac{D}{Dt} = \frac{\partial}{\partial t} + \vec{u} \cdot \vec{\nabla} \tag{2.1}$$

Three conservation equations can be derived from the two representations.

- Mass Conservation:

$$\frac{\partial \rho}{\partial t} + \vec{\nabla} \cdot \rho \vec{u} = 0 \tag{2.2}$$

$$\frac{D\rho}{Dt} + \vec{\nabla}\rho \cdot \vec{u} = 0 \tag{2.3}$$

- Momentum Conservation:

$$\frac{\partial \vec{u}}{\partial t} + \vec{u}\vec{\nabla} \cdot \vec{u} = -\frac{1}{\rho}\vec{\nabla}P \tag{2.4}$$

$$\frac{D\vec{u}}{Dt} = -\frac{1}{\rho}\vec{\nabla}P \tag{2.5}$$

Here we only considered the force applied by pressure, while viscosity terms are neglected.

- Energy Conservation:

$$\frac{\partial}{\partial t}\left(\rho E + \frac{\rho u^2}{2}\right) = -\vec{\nabla} \cdot \left[\rho\vec{u}\left(E + \frac{u^2}{2}\right) + P\vec{u}\right] \tag{2.6}$$

$$\rho\frac{D}{Dt}\left(E + \frac{u^2}{2}\right) = -\vec{\nabla} \cdot (P\vec{u}) \tag{2.7}$$

We consider adiabatic flow, in that case there is no thermal conduction and that no other force than pressure is applied (neglecting shear and viscosity). We introduce the specific internal energy of the fluid *E*, as well as the specific volume $V = 1/\rho$.

2.3 Perturbation theory of fluid motion

For simplicity, we are now working only in one dimension with plane waves. We can therefore write: $u(x,t)$, $\rho(x,t)$ and $P(x,t)$. A sound wave represents the propagation of a small variation of pressure which involves a variation of density and a variation of speed. ΔP and ρ are considered to be very small compared to the initial pressure P_0 and the initial density ρ_0. With $\frac{\Delta\rho}{\rho} \ll 1$and

$$\rho = \rho_0 + \Delta\rho \tag{2.8}$$

$$P = P_0 + \Delta P \tag{2.9}$$

$$u = u_0 + \Delta u \tag{2.10}$$

with $\Delta u/c << 1$

$$\partial(\rho_0 + \Delta\rho)_t + \partial((\rho_0 + \Delta\rho)u)_x = 0 \tag{2.11}$$

$$(\rho_0 + \Delta\rho)\partial u_t + (\rho_0 + \Delta\rho)u\partial(u)_x = -\partial\Delta P_x \tag{2.12}$$

Simplifying the above equations we get:

$$\partial\Delta P_t = -\rho_0\partial u_x \tag{2.13}$$

$$\rho_0\partial u_t = -\partial\Delta P_x \tag{2.14}$$

In the case of a sound wave, as heat exchanges do not take place and the variations are reversible, the motion of a particle is considered to be isentropic.

$$\Delta P = \left(\frac{\partial P}{\partial \rho}\right)_S \Delta\rho \equiv c_s^2\Delta\rho \tag{2.15}$$

We differentiate 2.13 with respect to time and 2.14 with respect to x and using the definition of c, equation 2.15 the cross derivative $\partial^2 u/\partial t\partial x$ appears in both equations. Subtracting these equations so that the cross derivative simplifies, leads to the wave equation for density

$$\partial^2(\Delta\rho)_{t^2} = c_s^2\partial^2(\Delta\rho)_{x^2} \tag{2.16}$$

The pressure change $\Delta P = c_s^2 \Delta\rho$ and the fluid velocity change u also satisfy wave equation2.15.Here c_s is the sound velocity and is given by the following formula

$$c_s = \sqrt{\left(\frac{\partial P}{\partial \rho}\right)_S} = \sqrt{\frac{dP_s}{d\rho}} = \sqrt{-V^2 \frac{dP_s}{dV}} \tag{2.17}$$

These equations have two families of solutions

$$\Delta\rho = \Delta\rho(x \pm c_s t), \quad \Delta P = \Delta P(x \pm c_s t), \quad u = u(x \pm c_s t) \tag{2.18}$$

The solutions with the negative /positive sign correspond to the propagation of the perturbation at sound velocity towards the positive and negative x, respectively.

2.4 Formation of shock wave

A shock is a disturbance in a material that moves faster than the sound speed (c_s) in the unperturbed material. This results in a rapid change in the state of the medium, compressing and heating material as it propagates. The sound speed in the shocked material is higher due to the increased pressure, making the motion of the shocked material subsonic relative to the shock front. For most materials and pressure ranges, c_s increases with increasing pressure, causing an initial pressure gradient to steepen into a shock as shown in Figure 2.1 In this example, we consider three points on the initial pressure gradient, each with a local sound speed and particle velocity. Due to the fact that c_s increases with pressure, the material at higher pressure moves faster than the leading edge of the disturbance. This results in the steepening of the shock and the creation of a sharp interface traveling at a single shock velocity, *D*. In this work the shock velocities are denoted by*D* and particle velocities by *u* for clarification.

2.5 Rankine-Hugoniot Relations

The most fundamental information about the propagation of shock waves through any material are provided by Rankine-Hugoniot (R-H) equations, which are derived

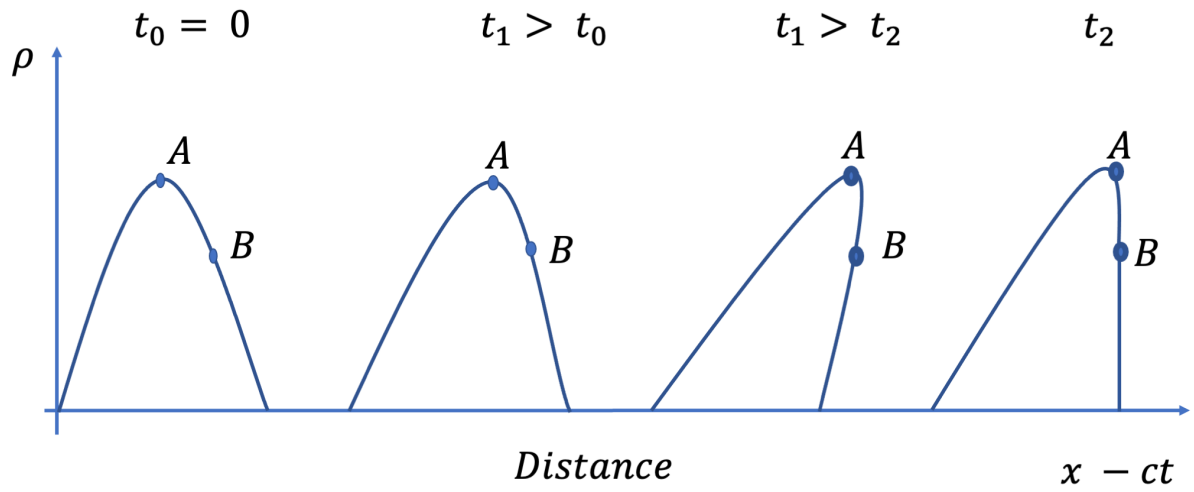

Figure 2.1: Diagram showing the steepening of a strong amplitude wave forming a strong shock. At t_0 initial amplitude wave profile. At $t_1 > t_0$ the distance between the A point and B decreases deforming the wave profile. In the case of $t_1 > t_2$ correspond to physically unrealistic case where point A passes point B. And at time t_2 stiffens to form a vertical profile forming with discontinuity at t_2.

from the conservation laws of mass, momentum, and energy. These equations include terms containing the velocities of the material on both sides of the shock wave. If the equations are manipulated to eliminate these terms, then a single equation containing only thermodynamic variables of state is obtained. This is the Hugoniot equation, and it is the starting point for many investigations. If two other equations, called the Raleigh equations, both of which are also obtained by manipulation, are appended to the Hugoniot equation, then they comprise an equivalent set to the R-H equations[Zel'dovich and Raizer, 2002].

The shock induces an increase of the pressure, the density and the velocity downstream its front. We write D the shock velocity in the laboratory frame. The link between the upstream quantities (subscript 0) and the downstream quantities (subscript 1) are obtained with the conservation laws for the mass, the momentum and the energy. In the Figure 2.2 we represent the compression of matter by a piston which moves with velocity D.

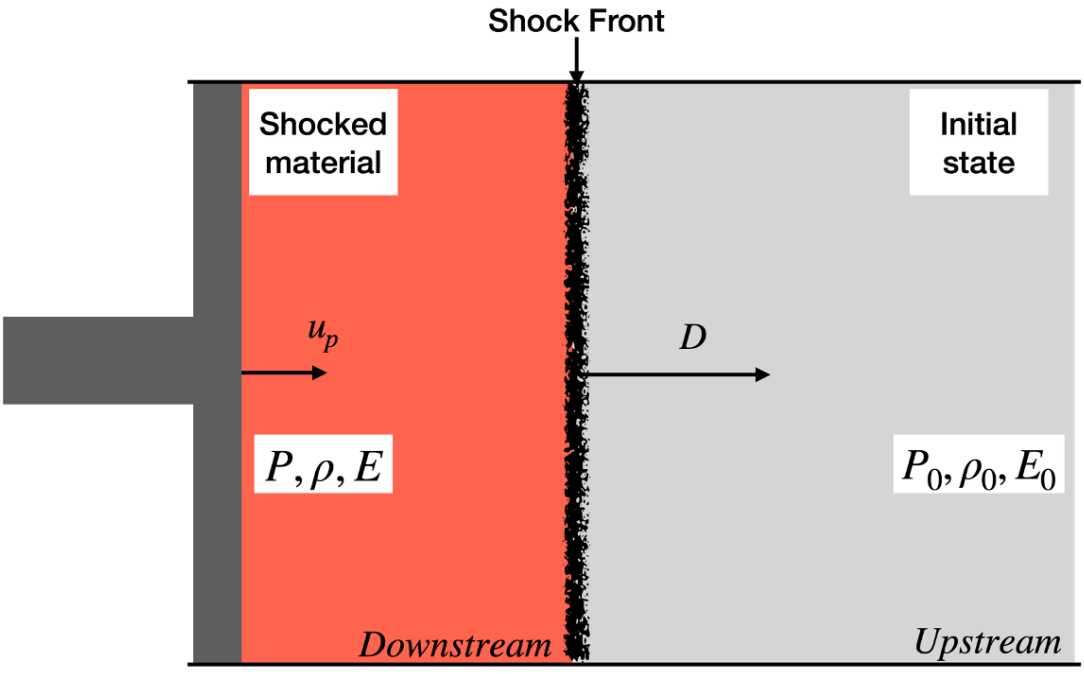

Figure 2.2: Propagation of shock generated by piston

Then we will describe a medium in which the shock wave propagates its pressure to density and energy. The shock wave which is formed travels with a velocity D. The initial state of the medium is ρ_0, P_0, E_0 and $\mathrm{u_0}= 0$. After the shock pass through the medium its characteristic state of the medium are ρ_1, $\mathrm{P_1}$, $\mathrm{E_1}$ and $\mathrm{u_1}$. Differentiating this thermodynamic discontinuity, the transition of the shock wave can be expressed by the three Rankine-Hugoniot conservation relations (mass, momentum and Energy conservation laws). Therefore we have:

- Mass Conservation:

$$\rho_0 DtS = \rho_1 \left(D - u_1\right) tS \tag{2.19}$$

then by eliminating t and S we obtain the following:

$$\rho_0 D = \rho_1 \left(D - u_1\right) \tag{2.20}$$

- Momentum Conservation:

$$\rho_0 D u_1 tS = \left(P_1 - P_0\right) tS \tag{2.21}$$

similarly eliminating *t* and *S* we have

$$\rho_0 D u_1 = P_1 - P_0 \tag{2.22}$$

- Energy Conservation:

$$\rho_0 SDt \left(E_1 - E_0 + \frac{1}{2} u_1^2\right) = P_1 u_1 St \tag{2.23}$$

by combining the equation 2.22 and equation 2.23 we obtain the following formula

$$E_1 - E_0 = \frac{1}{2} \left(P_1 - P_0\right) \left(\frac{1}{\rho_0} - \frac{1}{\rho_1}\right) \tag{2.24}$$

Concluding the results from the mass, momentum and energy conservation laws set of Rannkine-Hugoniot equations are :

$$\rho_0 D = \rho_1 (D - u_1) . \tag{2.25}$$

$$\rho_0 D u_1 = P_1 - P_0. \tag{2.26}$$

$$E_1 - E_0 = \frac{1}{2} (P_1 - P_0) \left(\frac{1}{\rho_0} - \frac{1}{\rho_1} \right) \tag{2.27}$$

Using the set of Rankine-Hugoniot (RH) equations, which are required for the determination of the two parameters experimentally, against five unknown can determine another quantity of unique states of matter.

2.6 Ideal Gas EOS

The ideal gas EOS is often used for weakly coupled, non Fermi-degenerate systems, or as a first approximation due to its simplicity. In this model, the pressure of an ionised plasma is given by

$$p = N k_B T = \frac{\rho(1 + Z^*) k_B T}{A m_p} \tag{2.28}$$

where $Z^*$is the mean ionization state in the plasma, A is the average atomic mass number of the ions in the plasma, m_p is the proton mass, and $N = 1 + Z^*$ is the number of particles in the system. The specific energy in an ideal gas is given by

$$\rho\epsilon = \frac{p}{\gamma - 1} \tag{2.29}$$

where γ is the polyrtropic parameters if the material, defined as the ration of s specific heats at constant pressure and volume, $\gamma = C_p$ / C_V. The number of degrees of freedom for each element in the system, α is related to the polytropic parameter by

$$\gamma = 2 + 2/\alpha \tag{2.30}$$

For monatomic gas with only 3 degrees of freedom $\gamma = 5/3$. The sound speed in an

System	γ	Compression
Monoatomic	5/3	4
Diatomic	7/5	6
Diatomic vibrational	9/7	8

Table 2.1: Compression limits along Hugoniot considering different systems.

ideal gas is given by

$$c_s = \sqrt{\frac{\gamma p}{\rho}} \tag{2.31}$$

We can obtain an explicit form of the Hugoniot curve given by

$$\frac{p}{p_0} = \frac{(\gamma+1)V_0 - (\gamma-1)V}{(\gamma+1)V - (\gamma-1)V_0} \tag{2.32}$$

rearranging for specific volume the above formula becomes

$$\frac{V}{V_0} = \frac{(\gamma-1)p + (\gamma+1)p_0}{(\gamma+1)p - (\gamma-1)p_0} \tag{2.33}$$

The temperature ratio follows the form

$$\frac{T}{T_0} = \frac{pV}{p_0 V_0} \tag{2.34}$$

In the strong shock limit, where the pressure behind the wave front is much higher than the initial pressure, the density dose does not increase with increasing strength but approaches certain finite value[Zel'dovich and Raizer, 2002]. The limiting density or volume ratio across the shock ave is a function of the specific heat ratio only and is given by

$$\frac{\rho}{\rho_0} = \frac{V_0}{V} = \frac{\gamma+1}{\gamma-1} \tag{2.35}$$

The asymptotic behaviour of the Hugoniot curve of a perfect gas and the maximum compression limit can be seen in Figure 2.3.

Table 2.1 shows comparison of different system and its compression limits:

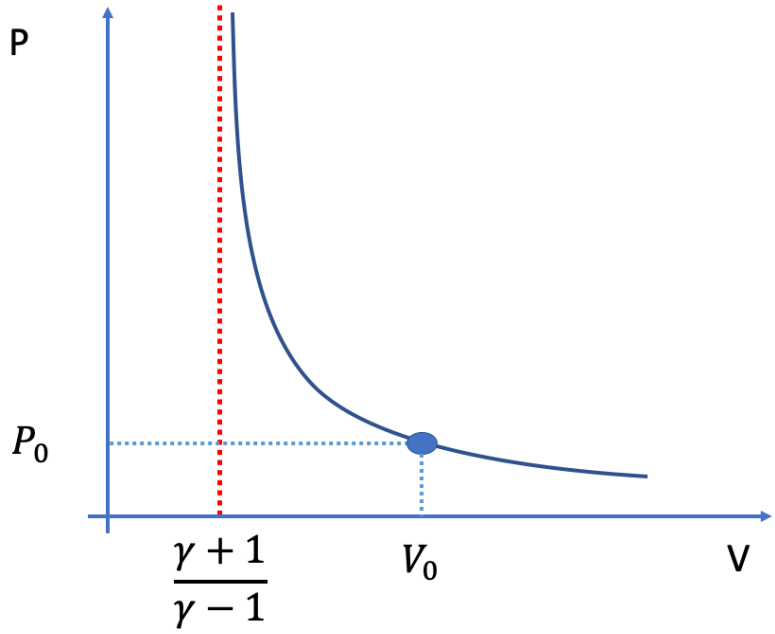

Figure 2.3: Hugoniot curve of a perfect gas.

2.7 Entropy increase along Hugoniot

Now we can describe the dynamics of a shock by defining the Hugoniot curve for a given state initially (ρ_0, v_0).

$$P = H(v, P_0, v_0) \tag{2.36}$$

In the second principle of thermodynamics, the variation of specific entropy, the variation of the internal energy and the work of the pressure forces are related:

$$TdS = dE + Pdv \tag{2.37}$$

where S is the specific entropy and E is the internal energy. This equation is rewritten with the equation (2.24) as follow:

$$TdS = \frac{1}{2}(P - P_0)(v_0 - v)\left(\frac{dP}{P - P_0} + \frac{dv}{v_0 - v}\right) \tag{2.38}$$

using equations (2.20) and equation (2.22) we have:

$$u^2 = (P - P_0)(v_0 - v) \tag{2.39}$$

by setting:

$$X = \frac{P - P_0}{v_0 - v} = \rho_0^2 D^2 \tag{2.40}$$

therefore we obtain:

$$\frac{dX}{X} = \frac{dP}{P - P_0} + \frac{dv}{v_0 - v} = 2\frac{dD}{D} \tag{2.41}$$

The equation of variation of entropy becomes:

$$TdS = \frac{1}{2}u^2\frac{dX}{X} = u^2\frac{dD}{D} \tag{2.42}$$

Simplifying the above equation we have:

$$\left(\frac{dS}{dD}\right)_H = \frac{u^2}{TD} > 0 \tag{2.43}$$

This means that the entropy increases as a shock wave passes along the Hugoniot resulting in irreversible transformation. As a result of the increase in entropy, some of the shock energy is lost as heat.

2.8 Shock propagation at the interface between two different materials

When a shock wave propagates at the interface of two media compression occurs and is fundamental for studying equation of state based on dynamic compression. At the interface between the two materials interesting process happens, such as shock wave reflection. The interface is in equilibrium state where the fluid velocity and pressure of the two material are equal. On the other hand, the density and the temperature of the two materials are determined by the equation of state, meaning that they can be different in the two media. The final state locus of the sample in the (P,U) plane is called shock polar. Figure 2.4 shows the shock polar of Quartz extracted form SESAME tabular data [LANL, 1992]. If (A) is the final state of the shock the slope of (OA) line

is call Rayleigh line or commonly as shock impedance. From momentum conservation Eq.2.20 in the strong shock limit the shock impedance Z is defined as

$$Z = \rho_0 D \tag{2.44}$$

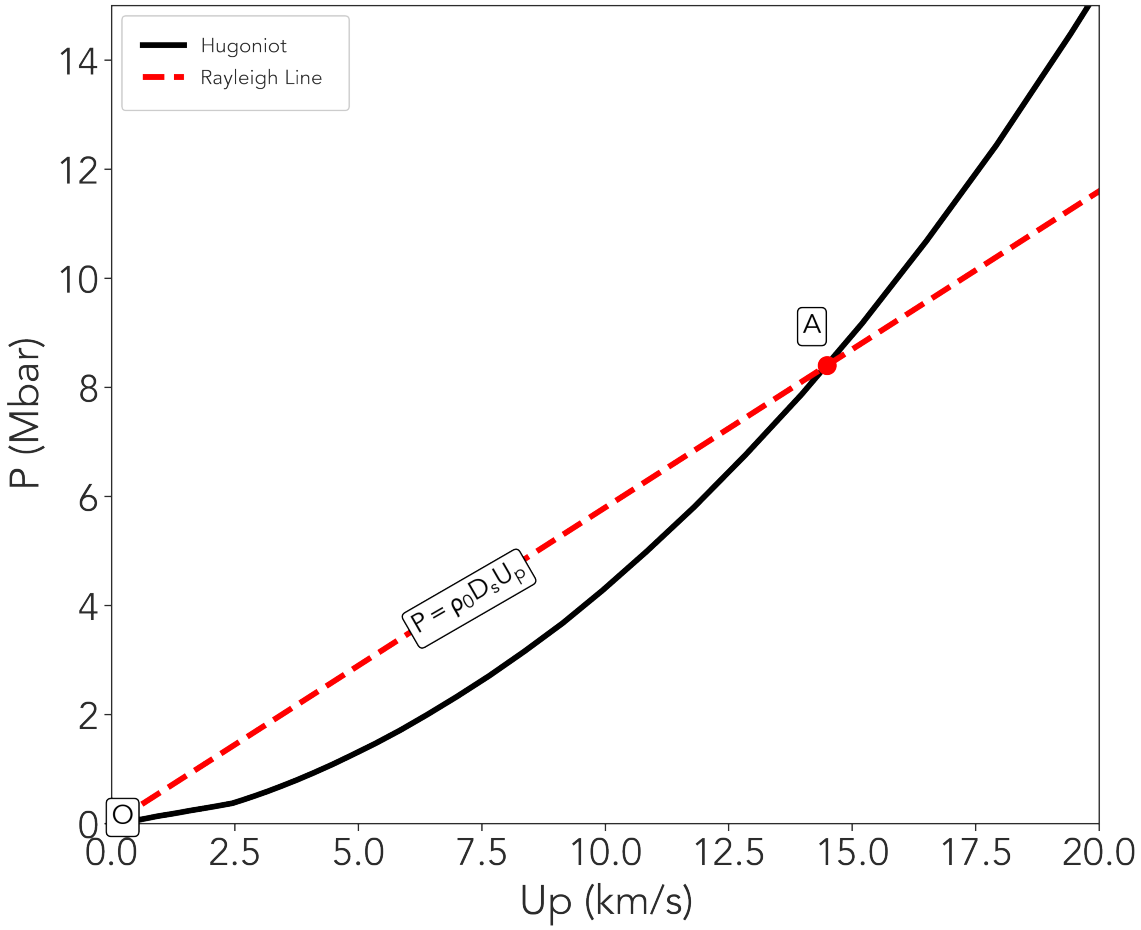

Figure 2.4: Shock polar of Quartz obtained from SESAME tabular data.The slope OA is called Rayleigh line or **shock impedance**.

Due to experimental constrain and the complexity of absolute measurement of the EOS which require two thermodynamic variables to me measured at the same time, a relative measurement approach is commonly employed. When a shock is transmitted from a medium (A) to a medium (B), two possible phenomena are observed.

- Z_A <Z_B: a shock at higher pressure us transmitted to material (B) and a shock is

reflected back to material (A) with the same pressure of the shock in (B).

- Z_A >Z_B: a shock wave at lower pressure is transmitted at to (B) and a rarefaction wave propagates backward into (A). This effect is similar to the shock breakout at a free surface.

2.8.1 Z_A <Z_B

In this case of a standard material (A), whose EOS is well known, can be before the sample to be studied (B). The shock compress the material (A) to the state A in the (P, U) plane as shown in Figure 2.5 along the Hugoniot H_A. From this point a reflected shock wave moves back into (A) along the curve H_{AR} . The pressure of the shock wave transmitted in B can be found by intersecting H'_{AR} with polar curve H_B at point B. From this figure we can note that the reflected wave brings A far from its initial Hugoniot state, to a higher pressure state. This process allows the study of the phase diagram, using multilayered targets with standard material.

2.8.2 Z_A >Z_B

A release wave is reflected in material A. In the (P,U) plane as shown in Figure 2.6, the pressure in the releasing medium A is given by the intersection of the isentrope, calculated from point A on the Hugoniot H_A, with the H_B shock polar curve. The shock release decrease progressively the pressure in medium A. In the case of weak shock limit we can estimate the free surface velocity of the free surface unloading in vacuum.

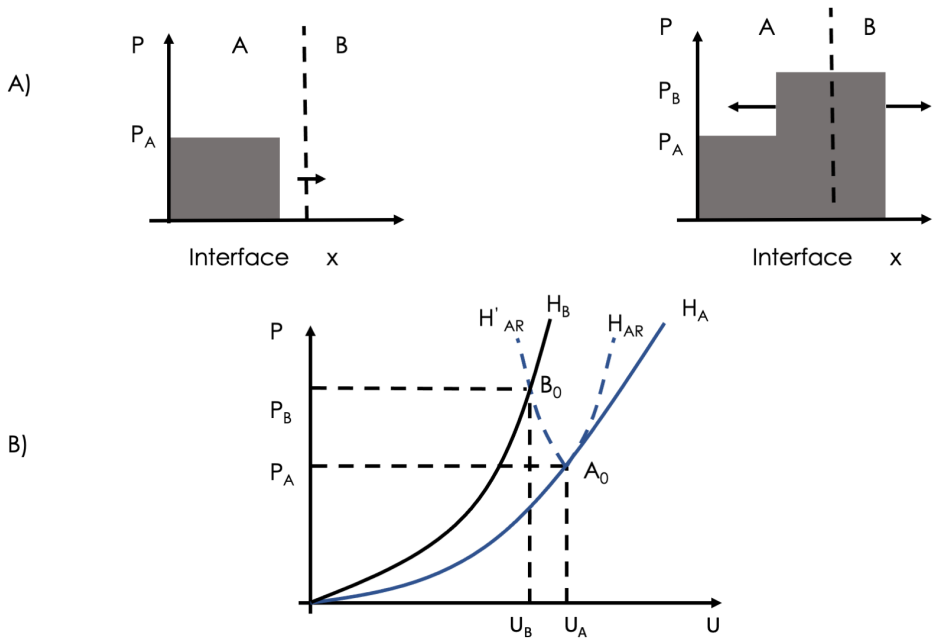

Figure 2.5: Pressure profile produced after the reflection of a shock wave at the surface between a low impedance material (A) and higher impedance medium (B) and graphical construction in the (P,U) plane.

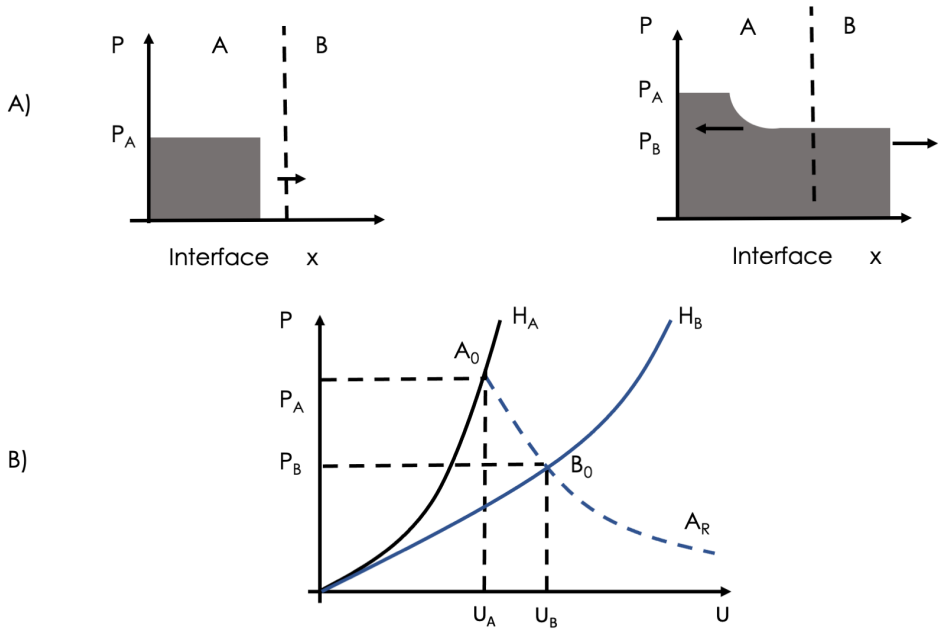

Figure 2.6: Pressure profile produced after the reflection of a shock wave at the surface between a high impedance material (A) and low impedance medium (B) and graphical construction in the (P,U) plane.

2.9 Conclusions and perspectives

In this chapter we describe basic theory of shock waves, and the mechanism that drive them. In the next chapter we will introduce the Optical time resolved methods which can be employed to probe laser driven shock waves and study the dynamic behaviour of the shocked material of interest and those the Equation of State being the main subject of this manuscript. We Introduce three methods such us (Velocity Interferometry System for Any Reflector (VISAR), Streak Optical Pyrometry (SOP) in the next Chapter.

Chapter 3

Physics of Shock Waves

Contents

3.1 VISAR: Velocity Interferometry System for Any Reflector

Line-imaging VISAR (Velocity Interferometer System for Any Reflector) as shown in Figure 3.1 is a useful diagnostic for measuring the shock wave or fluid (particle) velocity on a nanosecond timescale.

Velocity measurements are crucial in dynamic compression research. When combined with mass and momentum conservation, the measurements of the velocity of matter (fluid velocity and the velocity of shocks) yield essential information for materials under extreme conditions [Barker and Schuler, 1974].

Numerous optical techniques exist for measuring velocity under extreme conditions. Active shock breakout [Barker and Hollenbach, 1972, Barker and Schuler, 1974], where changes in the reflected light intensity signal the arrival of shocks, is one example. The most versatile optical velocity measurements are based on changes optical phase, of a reflected laser beam. An interferometer is used to measure the difference between the optical phase at two different times.

VISAR was developed in the late 1960s to early 1970s as a tool for measuring the velocity history in plate-impact experiments and the velocity of projectiles [Barker and Schuler, 1974]. At that time, VISAR analysis used laser interferometry to obtain velocity versus time profiles for any spectrally or diffusely reflecting surface in motion by measuring the resulting shift in fringe pattern produced by Doppler shift of light. However, the only way to actually make a measurement was via photomulti-

plier tubes and oscilloscopes. A decade later, in the early 1980s, an optical version of VISAR was developed [Bloomquist and Sheffield, 1983], which took advantage of high-speed electronic streak cameras to record interferometer fringe motion. This was named ORVIS, for Optically Recording Velocity Interferometer System. This led to the development of line-imaging VISAR [Bolme and Ramos, 2013, Celliers et al., 2004a], which utilises the ability of electronic streak cameras to resolve both the spatial and temporal components of the resulting fringe pattern, thus allowing for spatial information to be recorded as well.

3.2 Doppler velocimetry

Doppler velocimetry is the most routinely used diagnostics in the framework of shock compression. As we have seen in (Chapter 2), the shock and material velocity are fundamental parameters to measure to have an access to the thermodynamic state of the shocked sample. In particular, via the RH relations, one can determine the shocked density and pressure. The principle of Doppler velocimetry diagnostics is to measure the velocity U of a reflecting object by sending a probe laser of wavelength λ_0 onto it and measuring the Doppler shift of the reflected beam wavelength λ_r. This is directly linked to the velocity of the object via

$$\frac{\lambda_r}{\lambda_0} = \frac{1 - U/c}{1 + U/c} \tag{3.1}$$

In the non relativistic case $U << c$, equation 3.1 can be reduced to as

$$\lambda_r \approx \lambda_0 (1 - \frac{2U}{c}) \tag{3.2}$$

The Doppler velocimetry technique is widely used in shock experiments by means of the VISAR.

3.3 Sensitivity-Velocity per Fringe

In order to calculate the free-surface velocity (FSV) of the object in motion one needs to know the sensitivity of the VISAR, i.e. velocity per fringe or VPF. The magnitude of the fringe shift (i.e. the change in phase) is multiplied by the VPF to calculate the FSV. The VPF is given as:

$$S \equiv VPF = \frac{\lambda}{2\tau\left(1+\delta\right)} \tag{3.3}$$

where λ is the wavelength of the Doppler shifted laser light, τ is the temporal delay between the two arms of the interferometer caused by the insertion of an etalon, and δ is the dispersion is a material and wavelength dependent correction term for dispersion in the material that accounts for the chromatic dispersion in the etalon. This equation was first derived by Barker and Hallenbach in 1970 [Barker and Hollenbach, 1972, Barker and Schuler, 1974], and later extended to VISAR analysis in their 1972 paper [Barker and Hollenbach, 1972] and expanded upon by Barker and Shuler in 1974 [Barker and Schuler, 1974]to include the δ term. Also derived in the previous papers is the equation for the temporal τ delay caused by the etalon see Figure 3.2:

$$\tau = \frac{2e}{c}\left(n - \frac{1}{n}\right) \tag{3.4}$$

where e is the thickness and n is the index of refraction of the etalon, and c is the speed of light. If the incident light does not enter the etalon orthogonal to its front edge, a corrective factor can be added to the denominator of the above equation to account for the angle of light path through the etalon [Bolme and Ramos, 2013].

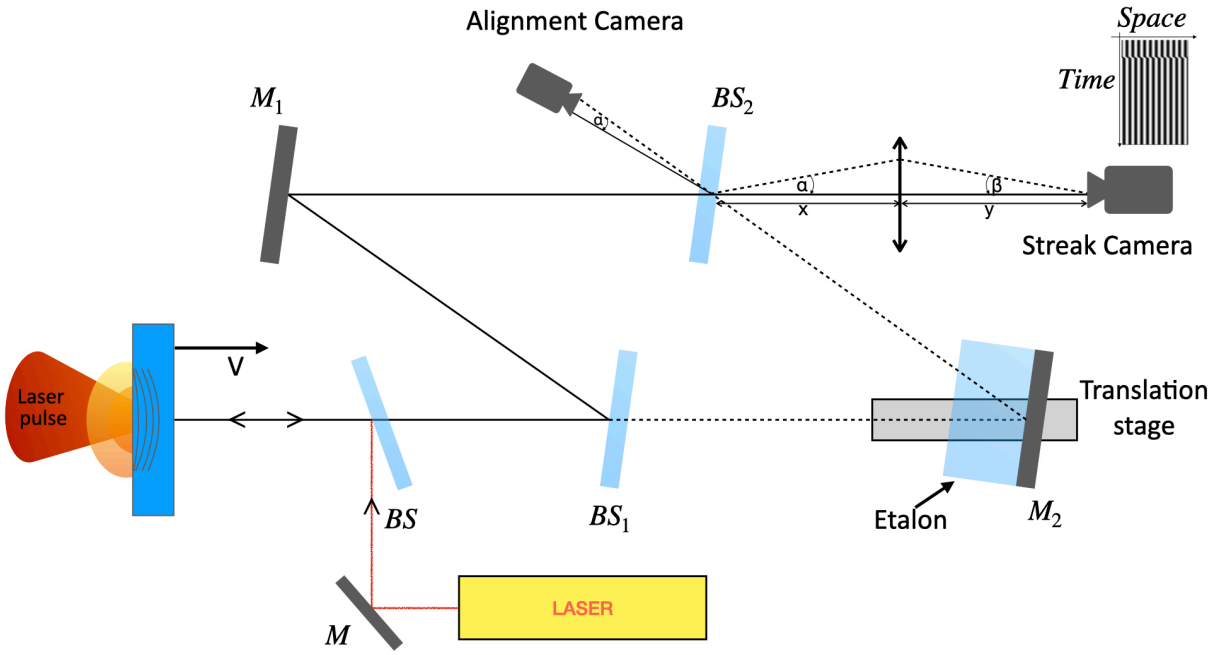

Figure 3.1: Modified Mach-Zehnder interferometer implemented on VISAR diagnostic system: the probe beam is reflected from the target rear side, the tilted M2 mirror results in the formation of fringes on the alignment camera after recombination of the two images from the two arms of the interferometer.

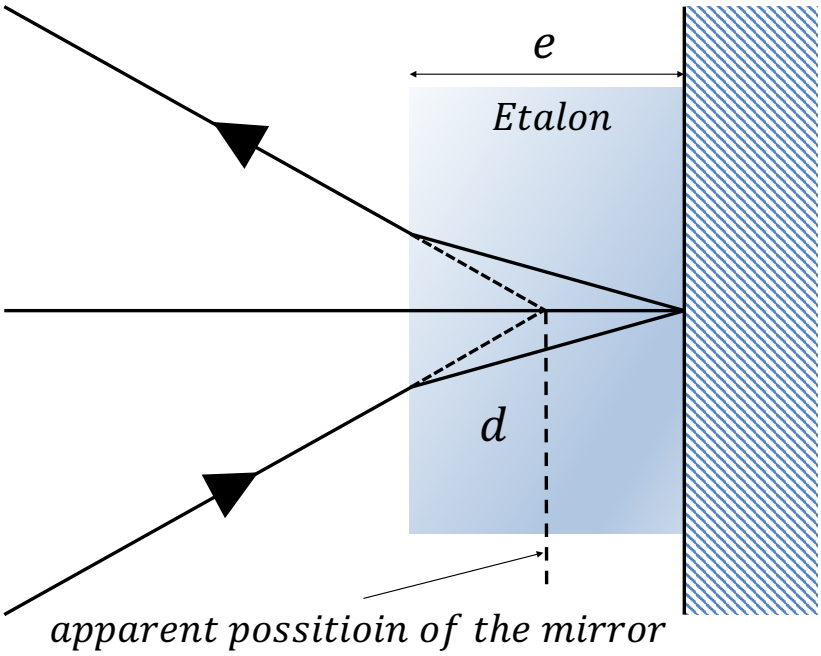

Figure 3.2: Correction of the mirror position after the insertion of the etalon on one arm of the interferometer.

3.4 Etalon

A core piece of the VISAR are the two etalons positioned in the Mach-Zehnder interferometers. However, by Doppler effect, the wavelength of the beam incident on the interferometer is variable and it is necessary to consider the dispersion of the etalon. To first order we can write:

$$n(\lambda) = n_0 + \left(\frac{dn}{d\lambda}\right)_{\lambda_0} (\lambda(t) - \lambda_0) \tag{3.5}$$

where $\lambda(t)$ is given. From the notation proposed by Braker, we can write an expression for the delay introduced by etalon:

$$\tau \simeq \tau_0 + 2\tau_0 \frac{n_r v}{c} \delta \tag{3.6}$$

$$\tau = \frac{2e}{c}\left(n - \frac{1}{n}\right) \quad and \quad \delta = -\frac{\lambda_0 n_0}{n_0^2}\left(\frac{dn}{d\lambda}\right)_{\lambda_0} \tag{3.7}$$

We define the jump fringe F as the difference between the phase shift created by a surface at a velocity v and the initial stage of shift $\phi(v=0)$ divided by 2π.

$$\phi(v=0) = \phi_0 = \frac{2\pi}{\lambda_0} c\tau_0 \tag{3.8}$$

$$F = \frac{\phi(v) - \phi_0}{2\pi} = \frac{1}{\lambda_0}\left[2\tau_0 \delta n_r v + 2\Delta L(\tau = \tau_0 + 2\tau_0 \frac{n_r v}{c}\delta)\right] \tag{3.9}$$

Therefore we can simplify the above equation since $c \gg v$ as $\tau \gg \tau_0 \delta v/c$:

$$F = \frac{2}{\lambda_0}\left[\tau_0 \delta n_r v + \Delta L(\tau_0)\right] \tag{3.10}$$

3.5 Velocity Measurements

A Fast Fourier Transform (FFT) method [Takeda et al., 1982] is used to extract the phase from the raw VISAR images. For example, an integer number of fringes over the region of interest in Figure was selected for the FFT. The fringe intensity as a function of space and time is represented as

$$S(x,t) = B(x,t) + A(x,t)cos\left[\phi(x,t) + 2\pi f_0 x + \delta_0\right] \tag{3.11}$$

where B is the background signal, A is the amplitude of the fringes, f is the phase, f_0 is the spatial frequency of the fringes (carrier wave) and δ_0 is an arbitrary offset, where $2\pi f_0 x + \delta_0$ is the linear phase ramp across the image (spatial direction). The signal can be rewritten in terms of complex exponentials such that

$$S(x,t) = B(x,t) + C(x,t)e^{i(2\pi f_0 x + \delta_0)} + cc.. \tag{3.12}$$

where $C(x,t) = A(x,t)\frac{1}{2}e^{i\phi(x,t)}$ contains the information about the fringe amplitude (reflectivity) and phase (velocity).

$$s(f,t) = b(f,t) + e^{i\delta_0}\int_{-\infty}^{\infty} C(x,t)e^{-i2\pi x(f-f_0)}dx + cc.. \tag{3.13}$$

One-dimensional spacial Fourier transform at given time yields

$$s(f,t)b(f,t) + c(f - f_0, t) + c^*(f + f_0, t) \tag{3.14}$$

where we can easily apply background subtraction which is function $b(f,t)$ and the phase information provided in c. The Fourier transform of Figure 3.3(a) is shown in Figure 3.3(b). The sum of the signal in Figure 3.3(b) over time, shown in Figure 3.3(c), shows the DC component at $f = 0$ and the two fundamental spatial frequencies of the fringe pattern ($\pm f_0$). A filter [dashed vertical lines in Figure 3.3(c)] is applied about the signal at f_0. This carrier wave frequency and higher frequencies within the filter are kept. The higher frequencies correspond to spatially dependent modulations superimposed on the carrier wave. The signal from the spatial frequencies outside the filter, which includes $b(f,t)$ and $c^*(f + f0)$, is set to zero. Inverse Fourier transforming the filtered FFT image gives

$$D(x,t) = \frac{A(x,t)}{2}e^{i[\phi(x,t) + 2\pi x f_0 + \delta_0]} \tag{3.15}$$

which is shown in Figure 3.3(a). The amplitude, or intensity of the reflected signal, is found by $A(x,t) = 2|D(x,t)|$ and is shown in Figure 3.3(b). The "wrapped" phase bounded by $[-\pi, \pi]$ is

$$W[\phi(x,t) + 2\pi x f_0 + \delta_0] = arctan\left[\frac{Re[D(x,t)]}{Im[D(x,t)]}\right] \tag{3.16}$$

The wrapped phase function W is bounded in the interval $[-\pi, \pi]$, resulting in discontinuities when the phase passes through odd multiples of π. The final two steps are to unwrap the phase, remove the $2\ \pi$ discontinuities, and to subtract the background, that is $2xf_0 + \delta_0$ leading to the extracted phase. A graphical illustration of this procedure showing the main steps is shown in Figure 3.3.

3.6 Surface movement in vacuum

The simplest case is that of a surface moving at constant speed in a vacuum. This situation is encountered when a shock reaches the rear face of the target. The target interface / vacuum as shown in Figure 3.4 is then set in motion at velocity $v = 2u$. The variation in optical path length is $\Delta L = v\tau$. Such reflection of the light wave take place in a vacuum, we will use $n_r = 1$.

$$F = \frac{2}{\lambda_0}\left[\tau_0 \delta v + \tau_0 v\right] \tag{3.17}$$

solving for velocity we have:

$$v = FS \tag{3.18}$$

3.7 Surface movement in medium

As seen above, sometimes a strong shock induces a transition to non-metallic / metal phase. In this case the shock front is a reflective surface that with the speed $v = U_s$ in the middle of undisturbed $n_r = n_1$ index as shown in the Figure 3.4. In this case, the variation in optical path length is $\Delta L = n_1 \tau v$.

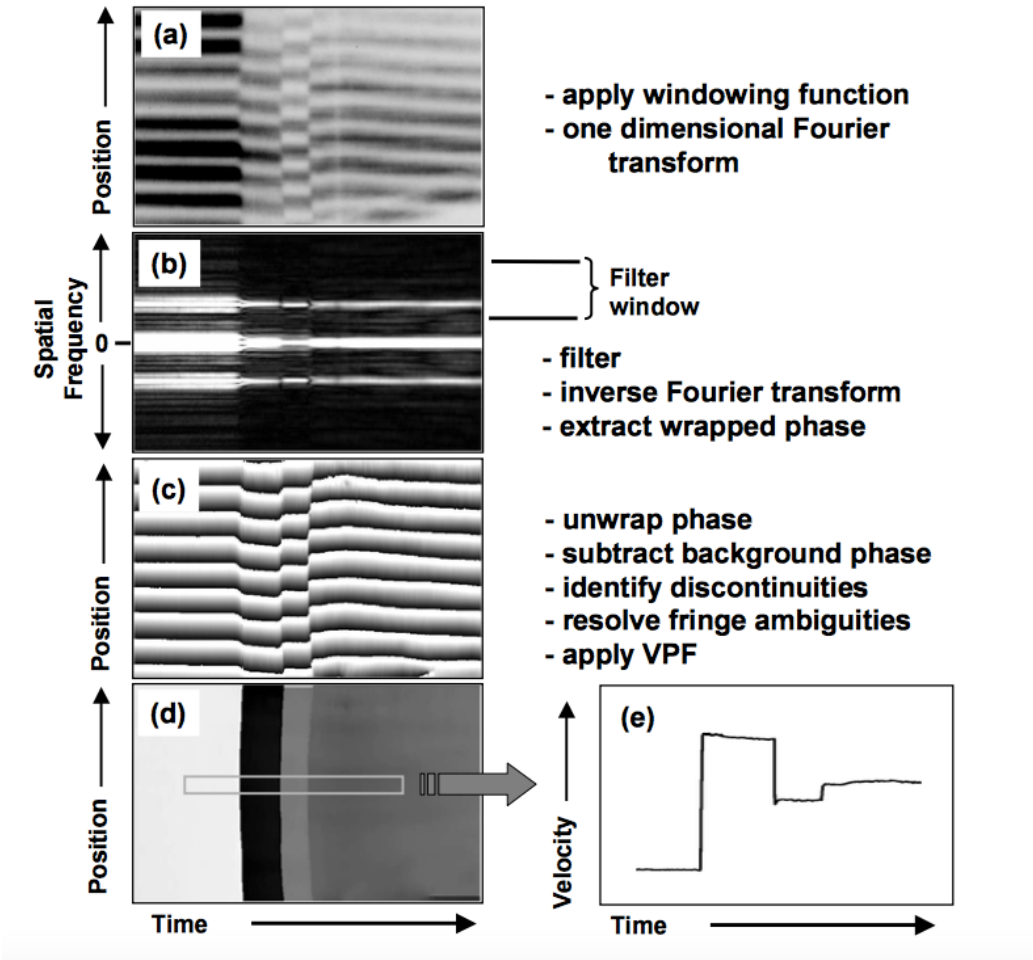

Figure 3.3: VISAR analysis process, main step is the phase extraction procedure using the Fourier Transform Method (FTM) [Takeda et al., 1982]: (a) Raw data loading and selection of area of interest, (b) One dimensional Fourier analysis on the selected region, (c) Extracted the unwrap phase image in order to identify discontinuities and resolve fringe ambiguities, (d) apply VPF to get the velocity map then from the velocity map we extract the velocity profile in time. Figure adapted from [Celliers et al., 2004a]

$$F = \frac{2}{\lambda_0}\left[\tau_0 n_1 \delta v + \tau_0 n_1 v\right] \tag{3.19}$$

we can simplify this by using the sensitivity equation of a VISAR:

$$v = \frac{FS}{n_1} \tag{3.20}$$

3.8 Non metalizing shocks

If the shock is not strong enough, it does not induce a metalization. In this case, the reflective surface is the front face of the transparent medium. This shock, in propagating in the transparent medium, density the material and thereby changes the index of the medium. For the non shocked region the refractive index is n_1 and a middle shocked region with index $n_2(n_2 > n_1)$ see Figure 3.4. The shock propagates at the speed U_s and the fluid velocity of the rear side of the shock (and therefore the speed of the reflective surface) is u_p. The change in the optical path can be written:

$$\Delta L = n_1 \tau U_s + n_2 \tau (u_d - U_S) \tag{3.21}$$

The reflection takes place in the medium of index $n = n_2$. Neglecting terms containing $1/c$, is obtained for the jump fringe:

$$F = \frac{2\tau_0 n_2(\delta + 1)}{\lambda_0} u_d + \frac{2\tau_0(n_1 - n_2)}{\lambda_0} U_s \tag{3.22}$$

if the variation of the refractive index of the material follows Glastone-Dale law

$$n - 1 = \kappa\rho \tag{3.23}$$

where κ is a coefficient dependent on the material.

we finally get:

$$u_p = \frac{FS}{1 + (n_1 - 1)\frac{\rho_2}{\rho_1}\frac{\delta}{\delta+1}} \tag{3.24}$$

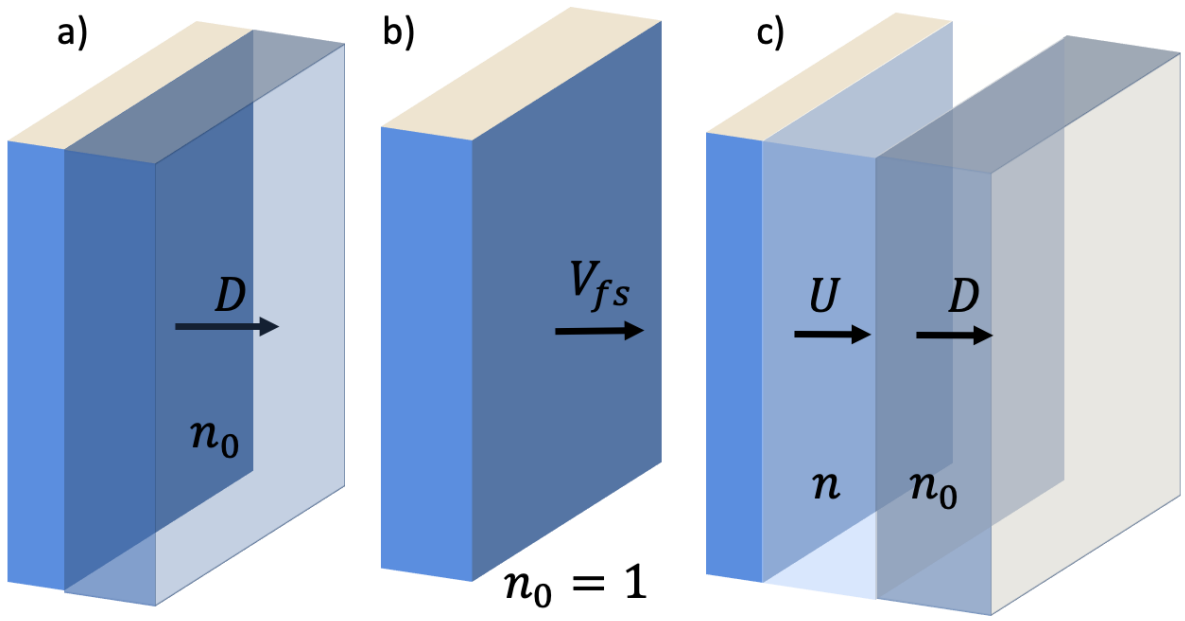

Figure 3.4: Different cases of reflective surfaces: a) Surface movement in vacuum, b) Surface movement in medium and c) Non metalizing shocks

3.9 Fringe shift and jump uncertainty

When the target goes from zero speed to a speed v, the fringes will jump from $F = F_1 + f_1$ where F_1 is the integral part of the shift f_1 and its fractional part. Only the fractions can be measured on the interferogram Figure 3.5. To remove the uncertainty on the total fringe shift, it is necessary to have a second interferometer having a different sensitivity (with a different thickness of etalon). S_1 and S_2 are known and denote the sensitivities of the two VISAR's therefore f_1 and f_2 are measured. Just find what F_1 and F_2 values give the same speed.

$$v = S_1(F_1 + f_1) = S_2(F_2 + f_2) \tag{3.25}$$

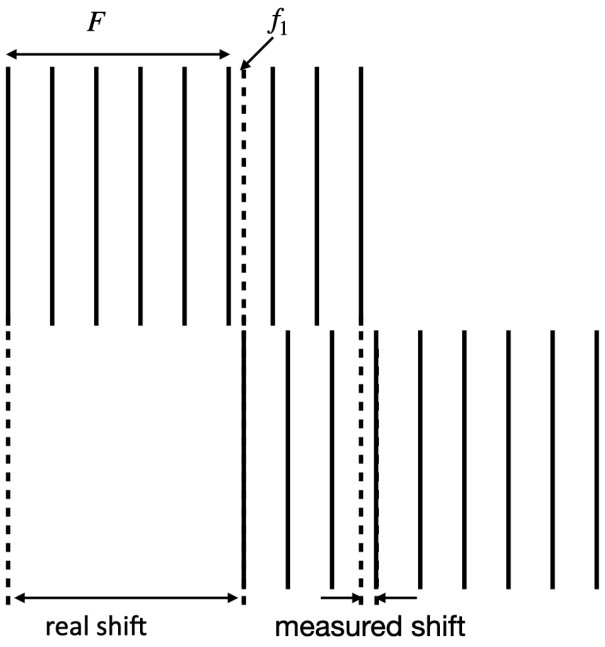

Figure 3.5: Fringe offset, f_1 represents the experimentally measured shift and F the number of fringes allowing to obtain the real shift.

3.10 Optical Pyrometry

We have seen that the use of VISARs allows to determine, via the Rankine-Hugoniot relations, the density and pressure of the shocked sample. Nevertheless, another critical parameter in the equation of state should be measured: the temperature T. The principle of optical pyrometry is to collect the thermal self-emission of the sample heated by the shock loading and estimate its temperature using Planck law. According to this law, the spectral radiance of a black body is

$$B(\lambda, T) = \frac{2hc^2}{\lambda^5} \frac{1}{exp\left(\frac{hc}{k_B \lambda T}\right) - 1} \tag{3.26}$$

where λ is the considered wavelength and T is the black body temperature. A physical body at temperature T exhibits a lower spectral radiance than a black body, that can be expressed as:

$$L(\lambda, T) = \epsilon(\lambda, P, T) B(\lambda, T) \tag{3.27}$$

where $\epsilon(\lambda, P, T)$ is the ratio between the radiance of the physical body and that of a black body, which depends on the thermodynamic state of the body is called emissivity.

In the context of shock experiments, Streaked Optical Pyrometer (SOP) is generally used. Such a diagnostics is able to measure the time-resolved self-emission of the sample by using a streak camera. A bi-dimensional output image is produced by a CCD placed after the streak: one of the two dimensions is the horizontal line out of the sample, the other one represents the temporal evolution of the signal. An example of SOP output is provided in Figure 3.6, which shows the SOP image and the time-dependent number of counts relative to a shot at the GEKKO XII facility on a target composed by an quartz standard for pre-compressed utilising a novel design and uncompressed water targets .

For determining the intensity, the solid angle, magnification, and spectral transmission of the imaging system must be measured. It is also important to filter out possible other light sources such as the drive laser or the probe laser, which is typically done with interference filters. A cross calibration with a known temperature standard is necessary

to verify the performance of the system.

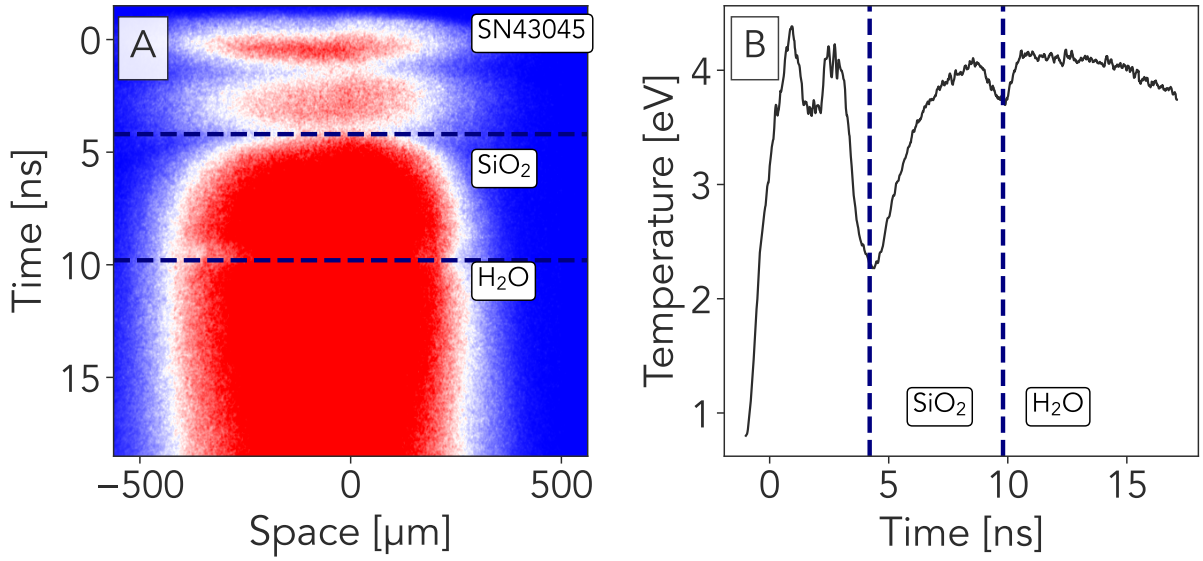

Figure 3.6: (A) SOP result for shot $SN43045$ at laser energy of $1.1\,\mathrm{kJ}$ the highest energy shot obtained at our experiment and (B) temperature estimation taking into account the mean reflectivity of VISAR-1 and VISAR-2. The initial luminosity ($\mathrm{t} \leq 4$ns is due to scattered laser light.

3.11 Streak camera

In shock experiments, a critical aspect to be considered is the time dependence of the properties of the shocked samples, given the fast temporal scales involved when WDM states are produced in the laboratory. The time scale of the studied phenomena is very short, typically of the order of $10\ ns$ if high-power lasers are used to generate the shock, so that a high time resolution, in the picosecond regime, is needed to properly characterize them. A streak camera is a device capable of diagnosing these fast phenomena. It delivers information about the intensity of a collected light signal as a function of time (over a window that can typically range from $0.55\ ns$ to $1\ ms$) and of one spatial dimension (in shock experiments, this is usually the horizontal line-out of the target). A streak tube, sketched in Figure 3.7, works as follows. The light signal passes through

an entrance slit. A photocathode then converts the light signal into a proportional electronic signal. The produced electrons are accelerated along the tube axis. Inside the tube, the electrons pass through a capacitor (also called sweep electrode) whose voltage linearly varies in time over the acquisition time window of the streak. This means that electrons are accelerated (and thus deflected) towards the top depending on the time the pass through the capacitor. The vertical spatial axis is thus used as the arrow of time. After this stage, the electrons hit a micro-channel plate (MCP), which has a multiplying effect, and then impact against a phosphor screen, which has the function to convert the electron signal into a light signal, which is collected by a charge-coupled device (CCD), coupled with the main streak unit figure not shown.

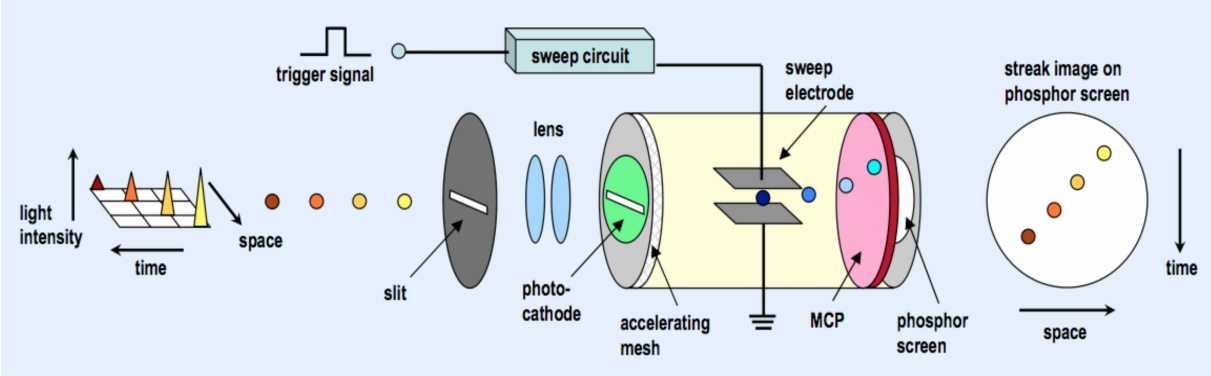

Figure 3.7: Operating principle of a streak tube. Source: www.hamamatsu.com.

A streak camera with a S20 photocathode will be used for each VISAR arm and the SOP. A S20 cathode is preferred due to its high sensitivity for visible light. The best temporal resolution should be 10 ps and the longest time window at least $\sim 20\ ns$. A narrow band pass filter (1 nm width) blocks scattered light from the drive laser for the VISAR. In the case of the SOP, a combination of interference filters and notch filters will remove light from both drive and VISAR laser. The spectral range has to be adapted for the sample type and pressure range.

3.12 Velocity versus Time

The end-goal of VISAR analysis is to measure velocity versus time for the object in motion or the velocity of the shock. The velocity of the object in motion is most commonly referred to as the particle velocity. When the velocity-per-fringe equation is applied to each spatial point on the graph of the unwrapped phase function, a plot is produced which contains information about the particle velocity at each location in space for any given point in time. This is known as the velocity map or final velocity field. By extracting a line out for a single spatial point for a duration of time, the velocity versus time can be plotted. This is what is known as the velocity history. The proposed steps are shown in the following Figure 3.3 .

3.13 Hydrodynamic simulation MULTI 1D

Hydrodynamic simulations allows to study the response of the target to the drive laser pulse and to the subsequent propagation of a shock wave. This is crucial for the design of the drive laser pulse parameters (energy, time shape, duration, and delay) and of the target, in order to avoid shock reverberations or pre-heating of the sample. It also allows to choose good diagnostics parameters (such as time window and delay). In the experimental work presented in this Thesis, we used the MULTI code, developed by Ramis et al. (1988) at the Max-Planck-Institut f$\ddot{u}$r Quantenoptik (Garching, West Germany). The post-processing used in this work has been developed at LULI [Vinci (2006)]. We have performed hydrodynamic simulations to develop an alternative dynamic pre-compression method for the exploration of high-pressure / moderate-temperature states, presented in Chapter 5. Within this context, extensive simulation runs have been useful to understand the hydrodynamic path that a sample undergoes when it is compressed by a double-shock structure. They also allowed to design the laser pulse shapes and the target structures. Moreover, MULTI simulations have been performed in the context of single-shock compression to optimise the target structures,

in particular for the high-energy shots on Diamond samples (see Chapter 4). Using hydrodynamic simulations we could design a target in which the reverberations did not modify the initial thermodynamic state of the water sample. We will now present the theoretical basis of the MULTI code. MULTI is a one-dimensional code. This means that it requires a reasonable computation time (in most cases, from a few tens of seconds to a few minutes on a typical laptop computer), but the cost to pay is the complete loss of information about the spatial profile of the shock inside the target and its evolution over time. In particular, the transverse relaxation taking place at the boundaries of the shocked volume is not considered. This can be problematic especially in the case of a small drive-laser focal spot area and a thick target. In such case, two-dimensional codes may represent a better alternative, though they need a much higher computation time. MULTI is a one-dimensional Lagrangian code, meaning that the target is decomposed in cells of constant mass and that the code follows their trajectories over time. Each cell i is identified by its initial position x_0^i, and each property F_i of the cell is represented as a function of the initial position x_0^i and of time t:

$$F_i = F(x_0^i, t) \tag{3.28}$$

in contrast with an Eulerian approach which uses the current position of the material cell:

$$F_i = F(x_i, t) \tag{3.29}$$

The Lagrangian picture is advantageous since it naturally rules out the flux of matter through two adjacent cells, hence reducing the computation time. Shock compression can be generated by a mechanic force or by a high-power laser. In the first case, MULTI simulates a piston acting on one end of the target, and the piston velocity (which can vary over time) must be fixed by the user. In the second case, several laser pulses can be simulated, with the choice for each pulse of the wavelength, intensity, time shape (rectangular, Gaussian, triangular, with or without rise and fall times), and time delay.

MULTI also allows the possibility of using the actual time profile of the drive laser to reproduce a shot already performed. The drive-laser beam is absorbed by the target via inverse Bremsstrahlung when it enters the corona and propagates up to the critical density (see Section 1.6), where it is reflected. Also the reflected beam loses energy via inverse Bremsstrahlung when it propagates backwards towards the source. The deposited power per length S is defined as the sum of the power per length lost by the incident beam and by the reflected beam (which is equivalent to the difference between the intensity gradients of the incident beam and the reflected beam). Multi-layered targets can be easily treated with MULTI. Each material composing the target is divided in a cell. The cell length Δx_ican be constant or can exponentially vary depending on the cell number:

$$\Delta x_i = k\Delta x_{i-1} \tag{3.30}$$

with the parameter k (the geometrical ratio of the progression in equation) chosen by the user together with the number of cells of each material. As general rules, the target mesh should respect two conditions:

1. the first cells on the drive-laser side must have a thickness which is at least 10 times smaller than the drive-laser wavelength, in order for the code to correctly simulate the laser energy deposition onto the target;

2. at each transition between two layers, the masses of the adjacent cells must not differ of more than 10%, to avoid non physical, mesh-related effects. An example of mesh is provided is shown in Figure 3.8

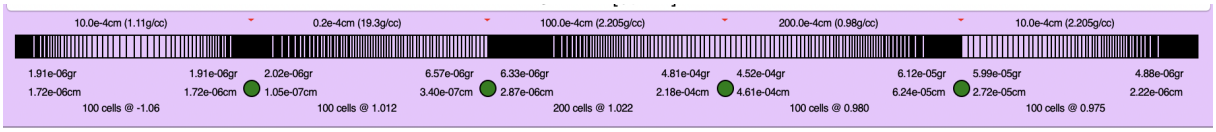

Figure 3.8: Mesh refinement in MULTI 1D for each particular layer of the multilayered target, the masses of the adjacent cells must not differ of more than 10% as indicated in green.

MULTI describes the shocked material as a single fluid with one or two temperatures depending on the user choice. Using two temperatures becomes interesting when the dynamic under study is more rapid than the typical energy exchange time scale between the electronic and ionic populations. The electronic heat flux q is simulated using the harmonic mean between the Spitzer-Harm flux and a free-streaming limit corrected by a limiting factor $f \sim 0.06$. This is done to take into account the effect of strong temperature gradients. The ionic heat flux is neglected. The details are presented in [Ramis et al., 1988].

Radiation transfer effects can be taken into account depending on the user choice. If this is the case, opacity tables must be provided to the code for each target layer. The opacity for each specified frequency interval is modelled using the Planck and Rosseland mean opacities. Including radiation effects considerably increases simulation times (from less than a minute to a few minutes) but is mandatory for an efficient target design in the case of high drive-laser intensities ($\sim 10^{13}\ W/cm^2$), where the risk of unwanted sample pre-heating is high. MULTI solves the three hydrodynamic equations that state the mass, momentum, and internal energy conservation. They are treated in the form:

$$\partial \rho_t = -\rho^2 \partial u_m \tag{3.31}$$

$$\partial u_t = -\partial (P_{real} + P_{artif})_m \tag{3.32}$$

$$\partial \epsilon_t = -(P_{real} + P_{artif}) \partial u_m - \partial q_m - \frac{Q}{\rho} + \frac{S}{\rho} \tag{3.33}$$

where ρ, u, and ϵ are the density, fluid velocity, and internal energy density, m is the Lagrangian coordinate (defined as the total mass at the left of the considered position), P_{real} is the physical pressure, P_{artif} is a viscous-like artificial stabilising term, q is the thermal flux, Q is the radiated energy density, and S the energy density deposited by

the laser. It should be noticed that m is a proper Lagrangian coordinate since the total mass at the left of a given cell position is invariant over time (there is no mass transfer between different cells). It is also worth noticing that temperature does not explicitly appear in the system of equations 3.31-3.33, but is implicitly included in the terms q and Q. In the case of a two-temperatures treatment, equation 3.33 must be separately written for each species (electrons and ions). The system of equations 3.31-3.33 must be closed by providing an equation of state, in the form

$$P = P(\epsilon, T) \tag{3.34}$$

$$\rho = \rho(\epsilon, T) \tag{3.35}$$

The employed EOS must cover a quite wide range of thermodynamic conditions. MULTI simulates the whole process of laser-target interaction, including laser ablation and the generation of a low-density, high-temperature corona and the response of the target to the shock loading and the subsequent release. Even if the EOS are not precise over the whole range of conditions, the output of the MULTI simulations nevertheless gives a rough anticipation of the response of the target to the drive laser and to the shock propagation. The EOS can be provided in an analytical form or as a table. In the last case, equations 3.34 and 3.35 are provided for a given set of ϵ and T. In the case of two-temperatures treatment, separate electronic and ionic equations of state must be used. $SESAME$ EOS tables are commonly used to run hydrodynamic simulations. They are developed and maintained by the Mechanics of Materials and Equation-of-State Group (T-1) of the Theoretical Division at the Los Alamos National Laboratory (New Mexico, USA) [LANL, 1992]. It has to be noticed that $SESAME$ tables are in the form $P(\rho,T)$, $\epsilon(\rho,T)$, so that they have to be inverted to respect the form of equations 3.34 and 3.35. In the case where no $SESAME$ table is available for a given material or for given conditions, one can build a quotidian equation of state (QEOS) [More et al., 1988, Kemp and ter Vehn, 1998], which is less accurate and based on a Thomas-Fermi free

electron gas model. Alternatively one can use the semi-analytical method used in the newly developed Frankfurt equation of state (FEOS) package provides an easy and fast access to the EOS [Faik et al., 2018], based on QEOS model with the possibility of using soft sphere model for more accurate EOS calculation.

3.14 Density functional theory

The development of density functional theory began in 60's by Kohn, Sham and Hoheberg,in parallel with technological advancement resulting strong computational power the theory start to become popular. Since then it became the standard method for studying molecular an solid state systems. In 1998 Kohn and and Sham were awarded the Nobel Price for their contribution to DFT. A simple definition of DFT: is a theory applied for obtaining an approximate solution to the Schrödinger equation of a many-body system. DFT theory can be used to study magnetic, structural, electronic and optical properties of crystals and molecules.

3.14.1 The adiabatic Born-Oppenheimer approximation

The microscopic description of a system requires the description of the interaction between its fundamental units of particles. In classical molecular dynamics, the atoms are represented by empirically fitted interaction potentials. Therefore, we expect a complex bonding behavior between the different atoms, highly dependent on thermodynamic conditions. Additionally, we do not know how the addition of electrolytes will affect the system. Consequently, we need to describe the system at the fundamental level of the interactions between the electrons and the nuclei. This problem is extremely complex: because of their small mass the electrons are subject to quantum effects, implying the resolution of the time-dependent Schrödinger equation for a large number of particles which is impractical. Heavier, the nuclei generally behave as classical particles. In 1927, Born and Oppenheimer [Born and Oppenheimer, 1927] propose that the large mass difference between the nuclei and the electrons lead to a decoupling of their dynamics. At the time-scale of the nuclei motion, the electronic cloud instantaneously adopts the electronic ground-state corresponding to the nuclei positions. Considering the Born-Oppenheimer adiabatic assumption [Born and Oppenheimer, 1927], the electronic problem becomes time-independent and the dynamics of the nuclei is decoupled

from the one of the electrons. The total hamiltonian of the system can be split into a electronic hamiltonian $\mathcal{H}_e$ that depends on the ensemble of the nuclei positions $\{\mathcal{R}_\mathcal{I}\}$ at a given time, and into a nuclear part $\mathcal{H}_\backslash$ that accounts for the electronic screening. The two parts of the total hamiltonian are separated in a kinetic and a potential energy terms. Their respective expressions for an isolated system are detailed in equations 3.38 and 3.39 [Parr and Weitao, 1994].

Ab initio simulations are an essential tool for predicting the structural, transport, and optical-electrical properties of materials on a wide range of thermodynamic conditions, encompassing the Warm Dense Matter regime which is not covered by the well-established theories describing condensed matter or classical plasma's. As their name suggests, such simulations find solutions to the initial problem the quantum many-body problem for a system of nuclei and electrons that are based only upon the first principles of quantum mechanics. This means that no empiric parameter or model derived from experimental data is introduced in the process. Whatever the case, the proper framework to describe a piece of matter is quantum mechanics and, in the absence of external potentials acting on the system under analysis, the problem reduces to solving the time-independent Schrödinger equation

$$\mathcal{H} \mid \Psi_A\rangle = E_A \mid \Psi_A\rangle \tag{3.36}$$

where E_A is an eigenvalue with quantum number A and

$$\langle r|\Psi_A\rangle = \Psi_A\left(r_1, ..., r_N, R_1, ..., R_M\right) = \Psi_A(r, R) \tag{3.37}$$

its corresponding eigenfunction of the quantum mechanical system consisting of N electrons at positions $r \equiv r_1, ..., r_N$ and M nuclei of atomic number Z at

$R \equiv R_1, ..., R_M$. The Hamiltonian that governs this equation is, for the non-relativistic case,

$$\mathcal{H}_e = \underbrace{\sum_{i=1}^{N_e} \frac{P_i^2}{2m_e}}_{\text{kinetic energy } e^-} \overbrace{- \frac{1}{4\pi\varepsilon_0} \sum_{i=1}^{N_e} \sum_{I=1}^{N_n} \frac{Z_I e^2}{\mid R_I - r_i \mid}}^{\text{Coulomb interactions } e^- \text{ / ions}} + \underbrace{\frac{1}{4\pi\varepsilon_0} \frac{1}{2} \sum_{I \neq j} \frac{e^2}{\mid r_i - r_j \mid}}_{\text{Coulomb interactions } e^-/e^-} \tag{3.38}$$

$$\mathcal{H}_n = \underbrace{\sum_{I=1}^{N_n} \frac{P_I^2}{2M_I}}_{\text{kinetic energy nuclei}} + \overbrace{\frac{1}{4\pi\varepsilon_0} \frac{1}{2} \sum_{I \neq J} \frac{Z_I Z_J e^2}{\mid \mathcal{R}_I - \mathcal{R}_J \mid}}^{\text{Coulomb interactions nuclei / nuclei}} + \underbrace{E_{e,0}(\{\mathcal{R}_\jmath\})}_{\text{electronic ground state energy}} \tag{3.39}$$

where N_e (N_n), $p_i(P_I)$, $r_i(R_I)$, $m_e(M_I)$ respectively refer to the number, the momentum, the position and the mass of the electron i (nucleus I). e is the elementary charge, Z_I is the number of protons of the nucleus I and ε_0 is the void permittivity. Now, the two problems can be treated separately at each time step; the positions of the nuclei constitute an external parameter for the electronic problem, and the electronic ground state potential energy surface adds to the total potential energy surface of the nuclei before the integration of the equations of motions. Nevertheless, the determination of the ground state energy of the electrons $E_{e,0}$ ($\{R_I\}$) is a many-body problem impossible to solve directly. The main complexity arises from the electron-electron interactions and the electron quantum properties due to their fermionic nature (exchange). Several formulations allow for tackling the problem using different approximations (Hartree-Fock methods etc.). Hereafter, the resolution of the electronic problem is performed in the framework of the density functional theory (DFT).

We adopt Hartree atomic units: $\hbar = m_e = e = 4\pi/\epsilon_0 = 1$

3.14.2 Hohenberg and Kohn theorem

Hohenberg and Kohn [Hohenberg and Kohn, 1964] demonstrate that the external potential V acting on the electronic sub−system ($i.e.$ interactions electrons / nuclei in equation 3.38) is a unique functional of the electronic density $n(r)$. This implies that the total energy of the electronic sub−system is also a functional of the electronic den-

sity. Moreover, they state that a unique functional for the total electronic energy E_e can be expressed in terms of the electronic density (see equation 3.40). If the electronic density verify the normalisation condition $\int n(r)dr = N_e$, the minimisation of this functional gives the ground state energy of the electronic sub-system.

$$E_e[n(r)] = \underbrace{\int V_e(r)n(r)dr}_{\text{external source}} + \underbrace{F_e[n(r)]}_{\text{electron kinetic and potential contribution}} \tag{3.40}$$

However, the dependence of the electronic kinetic energy, correlations, and exchange in terms of the electronic density is still unknown.

3.14.3 Kohn-Sham formulation

In 1965, Kohn and Sham (Kohn and Sham, 1965) propose to split $F_e\ [n(r)]$ into three different terms:

$$F_e[n(\mathbf{r})] = \frac{1}{2}\int\int \frac{n(\mathbf{r})n(\mathbf{r}')}{\mid \mathbf{r}-\mathbf{r}' \mid} d\mathbf{r}d\mathbf{r}' + \mathcal{T}[n(\mathbf{r})] + E_{xc}[n(\mathbf{r})] \tag{3.41}$$

the functional $E_{xc}[n(\mathbf{r})$ is the **exchange-correlation functional** which it includes also the difference between the kinetic energy of the system of interacting electrons and the kinetic energy of the system of non-interacting electrons at the same density. By applying equation 3.40 in equation 3.41 and the application of a variation principle leads to the introduction of N_e independent orbitals (the Kohn-Sham orbitals) that satisfies the electronic density in each point. The following set of equations is known as the Kohn-Sham equations:

$$\left(\frac{-\hbar}{2m_e}\nabla^2 + V_{eff}(\mathbf{r})\right)\phi_i(\mathbf{r}) = \varepsilon_i\phi_i(\mathbf{r}) \tag{3.42}$$

$$V_{eff}(\mathbf{r}) = V_e(\mathbf{r}) + \frac{1}{2}\int \frac{n(r')}{\mid \mathbf{r}-\mathbf{r}' \mid} d\mathbf{r}' + V_{xc}(\mathbf{r}) \tag{3.43}$$

$$n(\mathbf{r}) = \sum_{i}^{N_e} \mid \phi_i(\mathbf{r}) \mid^2 \tag{3.44}$$

where $V_{xc} = \frac{\delta E_{xc}[n(\mathbf{r})]}{\delta n(\mathbf{r})}$ is the exchange-correlation potential. ϕ_i and ε_i respectively denote a given Kohn-Sham orbital and its energy. The Kohn-Sham equations are solved self-consistently. First, the orbitals are computed from a guess electronic density that fixes the effective potential V_{eff}. The new density is calculated, and then the new orbitals. The procedure continues up to the convergence of the electronic density. The ground state energy of the complete electronic system is obtained by the intermediary of $\mathcal{T}$ that relates equation 3.40 with the Kohn-Sham equations. Indeed, the kinetic energy of the system of N_e independent electrons is the sum of the kinetic energies of the independent electrons. Consequently, the ground-state energy is expressed as:

$$E_{e,0} = \sum_{i=1}^{N_e} \varepsilon_i - \frac{1}{2} \int \frac{n(r^{'})}{\mid \mathbf{r} - \mathbf{r}^{'} \mid} d\mathbf{r}^{'} \tag{3.45}$$

However, the problem of the choice of the exchange-correlation term subsists. We present the generalised gradient approximation (**GGA**) functional that we use in this thesis.

The exchange-correlation energy arises from two phenomena:

- first, the fermionic nature of the electrons requires that two electrons of the same spin must occupy distinct orthogonal orbitals, this reduces the electronic density as it removes the repulsion energy and forms an exchange hole
- two electrons with different spins are allowed to occupy the same orbital but repulse together because of their negative charge, this also reduces the electronic density and forms a correlation hole. Combined together, these two interactions forms the exchange-correlation holes in the electronic density.

The full consideration of this effect requires to account for the Coulomb interactions between the electron with the exchange-correlation holes.

The simplest approximation consists in considering the exchange-correlation as locally dependent of the electronic density. This is reasonable as the long-range effects (at least for the gas of independent electrons) are already accounted in the terms of kinetic energy $\mathcal{T}$ and of the average electrostatic interactions. The exchange-correlation functional was approximated by generalised gradient approximation (GGA) of the Perdew-Burke-Ernzerhof form to evaluate the exchange and correlation contributions to the energy. A part of the exchange-correlation functional $E_{xc}^{GGA}[n(r)]$ contains the exact formulation of the exchange and correlation for a homogeneous electron xc gas while the other part needs to be parameterised. The exchange-correlation potential v_{xc} is then obtained by derivation of $E_{xc}^{GGA}[n(r)]$ and the Kohn-Sham equations can be solved.

3.14.4 Basis set wave-functions

Although the DFT simplifies considerably the many-body problem, the Kohn-Sham equations cannot be solved for the number of particles characteristic of a macroscopic system. To limit the number of particles, the resolution is performed at the microscopic scale in a periodic supercell.

According to the Bloch theorem (Bloch, 1928), in a periodic system the electronic wave-function differs from a plane wave only by a proper periodic modulation of wave-vector $\mathbf{k}$. This implies that the wave-function may be expressed as the product of two plane-waves: a first one $u_i^k(r)$ that has the same periodicity as the primitive volume, and a second one $exp(i\mathbf{k}\cdot\mathbf{r})$ with its own period corresponding to a k-point of the reciprocal space associated to the primitive cell. The wave-function associated to the modulation of wave-vector $\mathbf{k}$ is:

$$\psi_i^{\mathbf{k}}(\mathbf{r}) = u_i^{\mathbf{k}}(\mathbf{r})exp(i\mathbf{k}\cdot\mathbf{r}) \tag{3.46}$$

The expansion of $u_i^k(r)$ in a Fourier series leads to the following expression for $\psi_i^{\mathbf{k}}(\mathbf{r})$:

$$\psi_i^{\mathbf{k}}(\mathbf{r}) = \sum_{\mathbf{G}} c_{i,\mathbf{G}}^{\mathbf{k}} exp(i\mathbf{G}\cdot\mathbf{r})exp(i\mathbf{k}\cdot\mathbf{r}) = \sum_{\mathbf{G}} c_{i,\mathbf{G}}^{\mathbf{k}} exp(i(\mathbf{G}+\mathbf{k})\cdot\mathbf{r}) \tag{3.47}$$

where **G** are vectors of the reciprocal lattice associated to the primitive cell that impose the plane-wave to respect the primitive cell periodicity. $c^{\mathbf{k}}_{i,\mathbf{G}}$ are the Fourier coefficients of the plane-waves of wave-vectors **G**. Moreover, the choice of the **k**-points can be limited to the first Brillouin zone. This leads to:

$$\psi^{\mathbf{k}}_i(\mathbf{r}) = \sum_{\mathbf{G}} c^{\mathbf{k}}_{i,\mathbf{G}} exp(i(\mathbf{G}+\mathbf{k})\cdot\mathbf{r}) \tag{3.48}$$

The expansion of the orbitals in a plane-wave basis leads to the reformulation of the Kohn-Sham equations in the reciprocal space. In the reciprocal space, their resolution corresponds to the diagonalization of a hamiltonian matrix whose size in not infinite and depends on the truncation at the cutoff kinetic energy of the plane-wave basis set. The diagonalization is performed iteratively with respect to the plane wave coefficients. The truncation occurs at a value $\mathbf{G}_{cut}$ indirectly choosen in term of cutoff kinetic energy minored by the highest kinetic energy accessible to the electron, the one of the free electron: $E_{cut} \geq \frac{\hbar}{2m_e} \mid \mathbf{k}+\mathbf{G} \mid^2$

Ideally, the electronic eigenstates should be evaluated for all k-points of the first Brillouin zone.

3.15 Conclusion and perspectives

In this Chapter We have introduced the optical diagnostics we have used in our work and that are common in the WDM domain: Doppler velocimetry and pyrometry. Finally, we have presented the simulation tools that have been essential for the interpretation of our experimental results: hydrodynamic simulations and Ab-initio simulations and their applicability on equation of state study (material science etc.) at extreme pressures.Therefore, in the next Chapter we will show results and data analysis of a quasi-stationary laser driven shock on Diamond multilayered target. The experiment was preformed at PHELIX GSI laser facility.

Part II

Experimental Results (Diamond and Water)

Chapter 4

Experimental Results of Diamond samples

Contents

4.1 PHELIX laser facility

The Petawatt High-Energy Laser for Heavy Ion Experiments (PHELIX) [NEUMAYER et al., 2005] is a laser facility, at GSI Darmstadt (Germany), delivering intense laser beams with energies up to 1 kilojoule. Figure 4.1 shows a sketch

of PHELIX, which employs two frontends (nanosecond and femtosecond frontend), a pre-amplifier and a main amplifier. The nanosecond frontend is used generating high energy beams, which deliver arbitrary pulse shapes and pulse durations between 1 and $10\,\mathrm{ns}$. The femtosecond frontend is coupled to a chirped pulse amplification scheme (CPA) [Strickland and Mourou, 1985],where a femtosecond laser pulse is stretched in time, amplified and recompressed generating pulse laser with intensities $> 1\times10^{20}\,\mathrm{W/cm^2}$. The first element of a CPA scheme is the stretcher where a laser pulse is stretched in time. Increasing the time duration of the laser pulse, the intensity peak powers is kept below the laser damage threshold of the optical components in the following amplification chain. The stretched pulse is then amplified up to $30\ mJ$, by two Titanium doped sapphire regenerative amplifiers with a repetition rate of $10\ Hz$.

After the regenerative amplifier, the pulse is injected into a pre-amplifier, which is based on two Nd:Glass flash-lamp pumped amplifiers working in double pass configuration. After the pre-amplifier, the nanosecond and femtosecond pulses are magnified by a Keppler telescope, the exit beam diameter is $28\ cm$, and injected in the main amplifier. The main amplifier is based on 5 Nd:Glass disks units flash-lamp pumped, which works in double pass configuration. The main amplifier can deliver a maximum pulse energy up to $1\ kJ$, using only the nanosecond frontend, or $250\ J$ using only the femtosecond frontend, the repetition rate is one shot every 1 hour and half.

The last element of the CPA scheme is the compressor, which uses two $48\ cm$ wide gratings, working in single-pass configuration. The compressor configuration is kept fixed, while varying the stretcher it is possible to adjust the pulse duration. Table 4.1 shows the main parameters of the laser. The laser pulses after the compressor are injected inside a vacuum chamber (length $2040\ mm$, width $1290\ mm$ and height $830\ mm$). For the experiment described in this work (chapter 4), we used only the long pulse laser beam since we used the seeded laser for the VISAR probe beam.

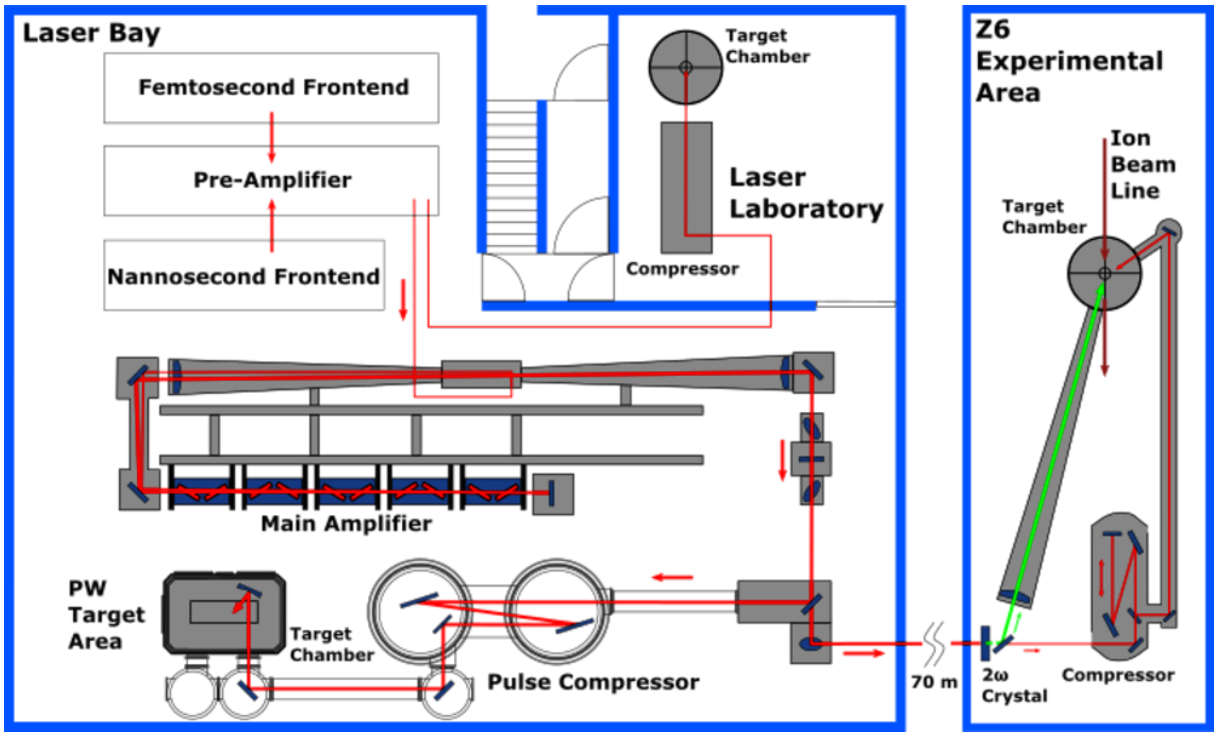

Figure 4.1: Sketch drawing of the PHELIX laser facility at GSI in Germany.

4.2 Context

The equation of state (EOS) of carbon at high pressures (megabar or multimegabar regime) is of interest for several branches of physics. In material science, carbon is a unique element due to its polymorphism and the complexity and variety of its state phases, including graphite, graphene, diamond, etc. Diamond is one of the known hardest materials with a bulk modulus of 4.42 Mbar. The EOS of carbon has

	long pulse	short pulse
Pulse duration:	1-10 ns	0.5 - $20\,\mathrm{ps}$
Energy:	0.3 - 1 kJ	up to 200 J
Max. Intensity:	$10^{16} W/cm^2$	$2 \times 10^{21} W/cm^2$
Contrast:	50dB	down to 120 dB

Table 4.1: Parameters of PHELIX laser for long pulse and short pulse beam in terms of pulse duration, energy, maximum achievable intensity and contrast.

been the subject of several recent important experimental and theoretical scientific works [Van Vechten, 1973, Shaner et al., 1984, Grover, 1979, Yin and Cohen, 1983, Biswas et al., 1984, Fahy and Louie, 1987, Ruoff and Luo, 1991, MAO, 1978, Bundy, 1989, Grumbach and Martin, 1996, Sekine, 1999, Benedetti et al., 1999, Scandolo et al., 1996, Cavalleri et al., 2002, Batani et al., 2004, Paleari et al., 2013, MacKinnon et al., 2014, Gregor et al., 2017, Millot et al., 2018a]. The important phenomenon of carbon metallisation [Bundy, 1989] at high pressure (Mott transition) has long been predicted theoretically but until now never clearly experimentally proved. In astrophysics the description of high-pressure phases is essential for developing realistic models of planets and stars [D. Saumon, 1995, Guillot, 1999, Fox, 2007]. Carbon is a major constituent (through methane and carbon dioxide) of giant planets such as Uranus and Neptune but also of and extrasolar planets (e.g. Gliese 436 b [Ross, 1981]) and white dwarf stars. High pressures are thought to produce methane pyrolysis with a separation of the carbon phase and the possible formation of a diamond or metallic layer [Ross, 1981, Nellis et al., 1997, NELLIS et al., 1988, Ancilotto et al., 1997]. Metallization of the carbon layer in the mantle of these planets (the "ice layers") could give a high electrical conductivity and, by the dynamo effect, be the source of the observed large magnetic fields [Ness et al., 1989, NESS et al., 1986, Connerney et al., 1987]. The impact of carbon structure in astrophysics was first pointed out by M.Ross in a now-famous article on "diamonds in the sky" in 1981 [Ross, 1981] . As shown in [Eggert et al., 2010b], the issue is still open, and "even if it is now accepted that the high-pressure, high-temperature behaviour of carbon is essential to predicting the evolution and structure of such planets, still, one of the most defining of thermal properties for diamond, the melting temperature, has never been directly measured" [Eggert et al., 2010b].

In this context, we performed an experiment to study the behaviour of carbon at pressures up to $9\ Mbar$. We used the PHELIX laser facility at GSI Darmstadt to irradiate multilayered diamond targets to induce laser-driven shock compression producing high-pressure and high-temperature states. Our measurements show that for the pres-

sures obtained in diamond, the propagation of the shock induces a reflecting state of the material. Shock dynamics was modelled using the Lagrangian-hydrodynamic, 1-dimensional code $MULTI$ [Ramis et al., 1988] accounting for radiation transfer. We used different equation of states for carbon, showing that our results are compatible with the Sesame tables developed for diamond (and not with others EOS of carbon).

4.3 Experimental Setup

The experiment was performed at GSI facility using the Phelix laser, a flash lamp-pumped Nd:glass laser frequency doubled to a wavelength $\lambda = 532\ nm$. The temporal profile was gaussian with a duration of $1\ ns$ FWHM as shown in Figure 4.4 and the spatial profile was flat-top with spot $\sim 500\ \mu m$ FWHM obtained by an appropriate phase plate [Koenig et al., 1994] for a typical result see Figure 4.2. Thanks to the large spot, 2D effects were negligible in our experiment (the total target thickness being of $\sim 300\ \mu m$). The laser was focused on multilayered targets (plastic/nickel/diamond/nickel) producing a maximum on-target intensity $I \sim 8 - 9 \times 10^{13}\ W/cm^2$. This intensity allows to generate shock pressures of the order of $10\ Mbar$ in the ablator, as can be estimated for instance using well-known scaling-laws given by Eq. 1.12 [Lindl, 1995, Mora, 1982b, Dahmani, 1993, Mora, 1982a]

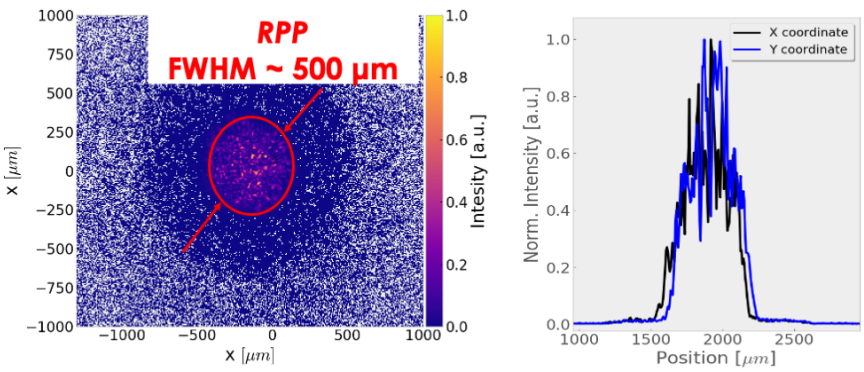

Figure 4.2: Experimental optimisation of the intensity profile of the PHELiX GSI laser facility using Random Phase Plate to produce $\sim 500\ \mu m$ Gaussian spot. $[left]$ Effect of the RPP normalised and background removal, $[right]$ line out along x and y axis after fitting a gaussian function we get a $FWHM \sim 500\ \mu m$.

The laser intensity is given by

$$I_L = \frac{nE_L}{\tau_L \pi R^2} \tag{4.1}$$

where E_L is the Laser Energy, τ_L lasers pulse duration, n absorption factor in $\%$ and R the radius of the laser beam. The typical ablation pressure in plastics is $\sim 12\ Mbar$, in agreement with the previous scaling law, and then increases in nickel due to impedance mismatch [Batani et al., 2001], to decrease again when the shock is transmitted to diamond. This is shown in details by hydrodynamics simulations (described in section 4.6).

A schematic and an optical photo of diamond target used in this experiment is shown in Figure 4.3 Polished synthetic single crystal (SC) type-IIa chemical vapor deposition (CVD) (100)-oriented diamond substrates ($3 \times 3\ mm^2$ in size) were used as target. These substrates were produced by SONI TOOLS & SONI CVD DIAMONDS, INC., Mumbai, India (www.sonitools.com). Nickel layers of about $20\ \mu m$ in thickness were deposited both on front side and on half rear side (see Figure 4.3) by means of a metallic stencil at the Institute for Microelectronics and Microsystems (IMM) of CNR. In particular, $1\ \mu m$ thick Ni films were first deposited on diamond surfaces by RF sputtering technique in diode configuration, using a commercial MRC 8620 system equipped with a cryogenic vacuum pump. The background pressure of the system is lower than 10^{-7} $Torr$. The sputtering conditions were as follows: RF power $350\ W$, target 6" Ni (purity 99.999%), substrates to target distance $5\ cm$, Ar flow rate $90\ sccm$, total pressure 3 $mTorr$ and substrate temperature $260\ ^\circ C$.

It is worth to point out that although Nickel is not a standard EOS reference (e.g. like Al) in high-pressure physics, it was chosen in this experiment because of its better adhesion performance on diamond surface. After that, the pure Ni thick layer (about $19\ \mu m$ in thickness) was made by electroplating deposition by using a standard manual galvanic growth system (nickel plating solution at $55\ ^\circ C$, current density $1\ A/dm^2$).

Finally, on some targets, $5\ \mu m$ of plastics (parylene C_8H_8 with density $\rho = 1.1\ g/cm^3$) were deposited on target front side to act as a low-Z ablator. The detailed character-

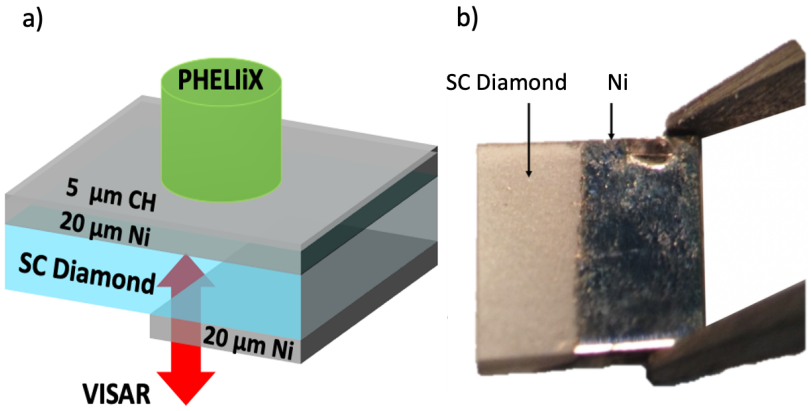

Figure 4.3: a) scheme of the target used in the experiment, b) image of Ni layer deposited on target rear side (taken before deposition of Ni layer on target front side).

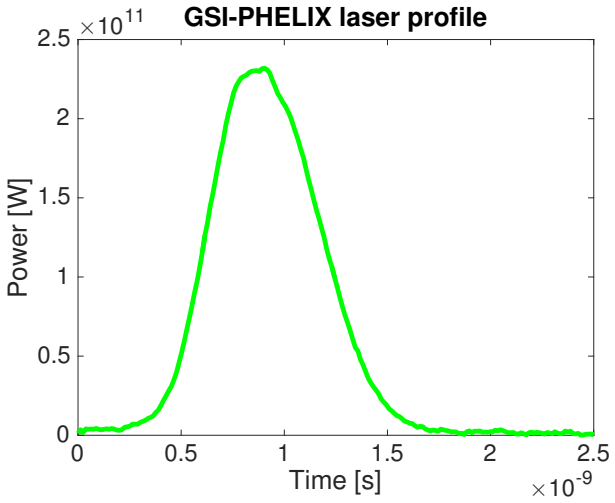

Figure 4.4: Experimentaly retrieved laser pulse for the PHELiX laser during our experimental campaign.

istics of the targets can be found in Table 4.2 for the 4 useful laser shots obtained in the experiment (over a total of 10 laser shots). Due to the low-Z of the ablator, X-ray emission is low and characterized by low photon energy. Such X-rays are completely stopped in the Ni layer, so that preheating of diamond is negligible in our experiment. The Ni layer also acts as reflecting surface for the laser probe beam, used for the VISAR diagnostics. This target design allows to detect the shock breakout at the Ni/diamond, Diamond/vacuum, and Ni/Vacuum interfaces, thereby allowing to determine average shock velocities in diamond and nickel. In addition, the evolution of shock dynamics can be continuously followed in diamond by looking at the VISAR fringe shift. Finally, after shock breakout, we can measure the Ni and diamond free surface velocities by looking again at the VISAR fringe shift. As diagnostics we used a VISAR system a typical setup can be showing in Figure 4.5. This is a standard diagnostic allowing to measure the velocity of a reflecting surface through Doppler effect [Barker and Hollenbach, 1972, Barker and Schuler, 1974, Celliers et al., 2004a, Bloomquist and Sheffield, 1983, Bolme and Ramos, 2013]. The main component of the VISAR diagnostic are a seeded probe laser with a $\lambda_0 = 660\ nm$ and two Mach-Zehnder interferometers. The probe beam reflects back from the target, and an imaging system creates an image of the target rear side on the output beam splitter in the interferometer. Finally, this is imaged on the slit of a streak camera to provide temporal resolution. A linear fringe pattern is formed due to the interference of the two beams going through the two interferometer arms with a different delay. The streak camera provides a continuous measurement of the shock evolution for several nanoseconds with spatial resolution and temporal resolution of the order of $\pm 300\ ps$. An optical delay element (etalon) is added to one of the arms of the interferometer to provide the optical delay while maintaining the spatial coherence between the two arms. The thickness of the etalon fixes the sensitivity of the VISAR system. The velocity is measured from the fringe shift. The sensitivity S of the VISAR is measured in $km/(s.fringe)$ and given by Eq. 3.3 where τ_0 is determined by the etalon thickness and $d \sim 0.03$ is determined by the optical dispersion of the etalon glass.

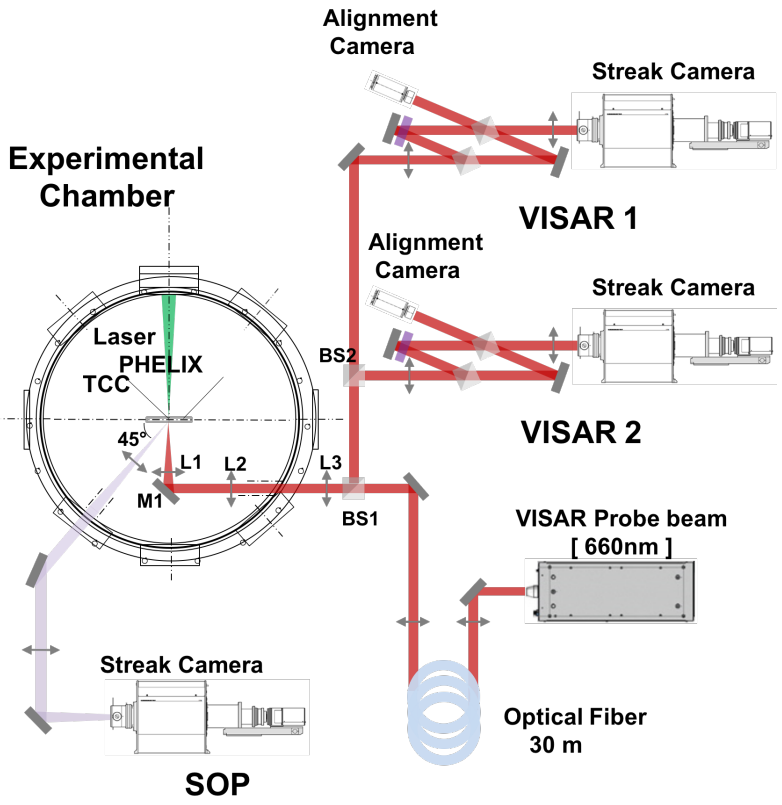

Figure 4.5: Diagram of the SOP and VISAR optical setup used at GSI PHELiX facility.

The relation between fringe shift, the sensitivity, and the velocity depends on the environment around the reflecting surface. Basically there are two cases.

The first case is when the pressure is strong enough to induce a phase transition to a reflecting state, it is directly the shock front travelling in the material which reflects the probe beam. In this case, the velocity of the shock front is measured as

$$D = SF/n_0 \tag{4.2}$$

Here $F = \Delta\Phi/2\pi$ is the fringe shift, and n_0 is the refraction index of the crossed material (in our case diamond and $n_0 = 2.417$). This formula also applies to the case of the reflection from a free surface moving in vacuum and in this case of course $n_0 = 1$. This is indeed what happens after shock breakout at the rear side when the whole target begin to move. The second case corresponds to weaker shocks which compresses the material but does not induce a reflecting phase, so that it remains transparent. In this case, the probe beam can be reflected from another material behind the transparent one. In this case, the interface moves at a velocity U which corresponds to the fluid velocity of the transparent material behind the shock front. The different cases were shown in Chapter 3 Figure 3.4.

In the second case, the beam is reflected from the interface but the velocity U is not directly measured because the fringe shift also depends on the thickness of the compressed material between the interface and the shock front. The relation is in this case given by

$$Dn_0 - n(D - U) = SF \tag{4.3}$$

where n is the refraction index of the compressed material. We see that U cannot be directly extracted. However if both D and U are known, or measured, this formula allows measuring the refraction index of the compressed material. This approach has been used in [Batani et al., 2015b, Jakubowska et al., 2019] to measure the refraction index of water in the Megabar pressure range. However, if we use Gladstone-Dale's law to describe the refraction index

$$n - 1 = \kappa\rho \tag{4.4}$$

where ρ is the density of the compressed material and where κ is a coefficient dependent on the material, after some algebra we can arrive to the formula

$$U = SF/\left[1 + (n-1)\frac{\rho}{\rho_0}\frac{\delta}{\delta+1}\right] \tag{4.5}$$

Again, this is not an explicit formula because the measurement of U depends on the degree of compression, i.e. on the ratio of the density of the compressed material to its initial density ρ_0. In practical cases, however, physical insight or results from numerical simulations can suggest an appropriate value for ρ/ρ_0 so that formula 4.5 can be used to get a "reasonable" value of U. Finally, the standard approach used in laser-driven shock experiments is to use two VISAR systems, i.e. two interferometer's with different sensitivity S (given by different etalons). This is related to the intrinsic ambiguity in the VISAR measurements as a result of the 2π periodicity in the fringe interference: using two VISARs allows to reduce the ambiguity in fringe jumps. From the VISAR raw data we can extract the phase shift using a Fourier transform algorithm [Takeda et al., 1982, Celliers et al., 2004a].

4.4 Experimental Results: Shock chronometry

In this section, we start the presentation of the shots obtained in our experiments and listed in Table 4.2. Figure 4.6 shows typical experimental results. These refer to shot $\#15$ as reported in Table 4.2.

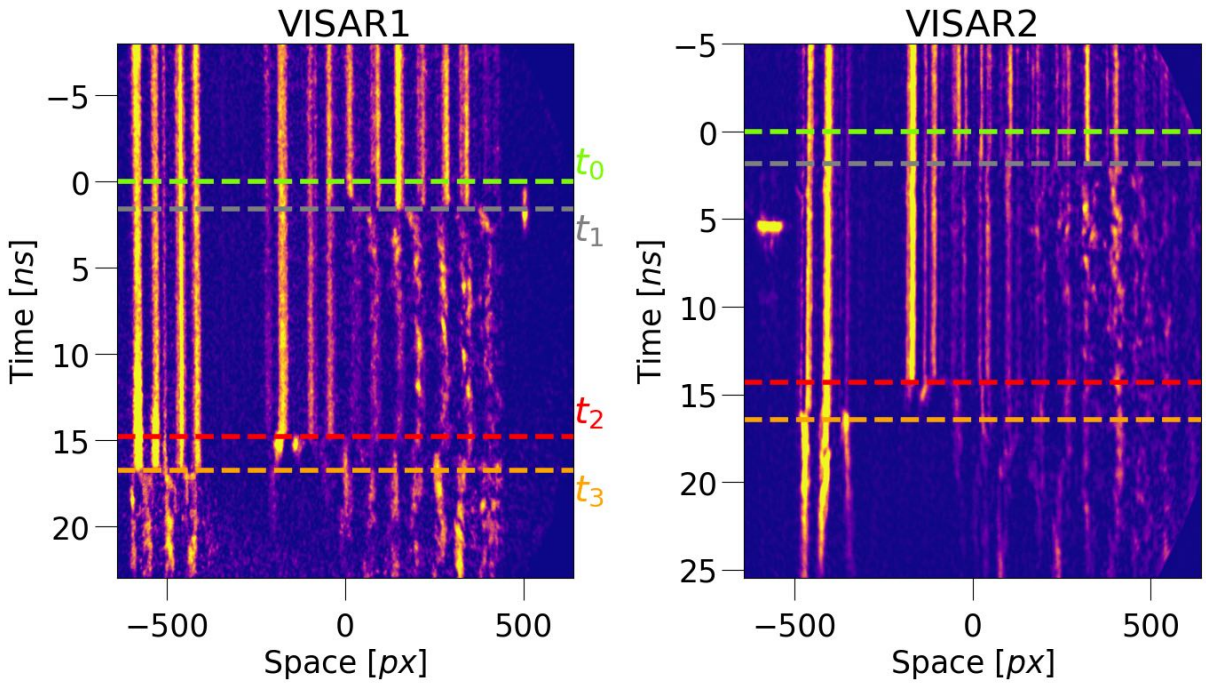

Figure 4.6: VISAR streak camera images from shot $\#15$. Left) VISAR with sensitivity $S = 11.3\ km/(s.fringe)$, Right) VISAR with sensitivity $S = 4.62\ km/(s.fringe)$. The total time windows are $32.98\ ns$ for VISAR1 and $30.47\ ns$ for VISAR2. Images were recorded on a $16-$bit CCD with $1280 \times 1024\ pixels$ giving a conversion of $\sim 30\ ps/pixel$.

In the images, we can clearly identify the passage of the shock from one material and the other by the changes in reflectivity and the fringe jumps. This allows performing shock chronometry and, since the thickness of the various layers is known, to infer the average shock velocity in each material. For instance, in 4.6 the gray dashed line corresponds to the shock breakout at the nickel/diamond interface (t_1), the red dashed line to the shock breakout at the diamond/vacuum interface (t_2), the bottom orange dashed line to the shock breakout at the nickel/vacuum interface (t_3). Finally, the

upper green dashed line corresponds to the arrival of the (maximum) of the main laser pulse on target front side (t_0). This is obtained from the time fiducial: the short signal on the right of the left image and on the left of the second image. Such a time fiducial is obtained by sending a small part of the laser pulse onto the streak camera slit by using an optical fiber. The time interval between such time fiducial and the arrival of the maximum of the main laser pulse on target front side is obtained thanks to a calibration shot which is performed without target (i.e. the main laser pulse is directly sent to the streak, after attenuation, together with the time fiducial). From this we can directly obtain the shock transit times in the plastic/nickel, diamond, and rear-side nickel layers, and then we can get the average shock velocity in each layer, as reported in Table 4.2. The times (and the velocities) obtained from the two VISARs are in fair agreement once the experimental error bars are taken into account. The time resolution of $\pm 300\ ps$ for the shock breakout at two interfaces, together with a maximum (estimated) error in measurement of the thickness of less than $\pm 0.5\ \mu m$, gives a typical error on shock velocity measured in diamond of

$$\frac{\Delta D}{D} \approx \sqrt{2\left(\frac{0.3ns}{14ns}\right)^2 + \left(\frac{0.5\mu m}{250\mu m}\right)^2} \approx 0.03 \tag{4.6}$$

The images also show that the shock breakout is quite flat both at the nickel/diamond interface and at the target rear side. This shows indeed that $2D$ effects in hydrodynamics are negligible in our experiment. Also, from the measured average shock velocities, we can obtain an evaluation of the pressure reached in diamond by considering the Hugoniot curve of this material, according to which a shock velocity of $\sim 20\ km/s$ corresponds to a shock pressure $\sim 5.5\ Mbar$ [LANL, 1992].

Our experimental data reflect the expected trends, that is the shock breakout time decreases when the laser energy increases or when the target thickness decreases. For instance by comparing shots 18 and 21 (which have almost the same thickness) we see that increasing the energy the shock breakout at the diamond vacuum interface (t_2) decreases. Similarly, by comparing shots 15 and 21 which have almost the same energy, we see that decreasing the target thickness implies a decrease of shock breakout time.

4.5 Experimental Results: Fringe shifts

Unfortunately, in our experiment the fringe quality is poor, which makes difficult to use the fringe shift for a very precise determination of velocities. In our images, we can confidently evaluate a fringe shift of $1/3$ of the wavelength only which, with a sensitivity of $4.62\ km/(s.fringe)$ gives an incertitude in shock velocity of $\Delta D \sim 1.5\ km/s$. Nevertheless, the images are usable and we can retrieve the velocities of reflecting surfaces. In order to extract velocities from the fringe shift recorded on using streak cameras, we used the software NEUTRINO developed by T. Vinci and A. Flacco [Flacco A., 2011]. This software also allows to remove the so-called ghost fringes, i.e. the fringes which arise because of spurious reflections (e.g. from the rear side window of the target or from optics in the pathway). The basic question to be asked is what we are seeing in VISAR images, i.e. is the probe beam reflected from a reflecting shock front or rather

Shot #		Time $\Delta t[ns]$		Velocity $[km/s]$		Thickness d$[\mu m]$	E_L [J]
		VISAR 1 $S = 11.3$	VISAR 2 $S = 4.63$	D1	D2		
15	$t_1 - t_0$	1.59	1.83	15.72	13.66	270	149
	$t_2 - t_0$	14.79	15.449	20.46	19.77		
	$t_3 - t_0$	16.75	17.45	10.20	10.20		
18	$t_1 - t_0$	2.20	2.58	11.36	9.69	260	128
	$t_2 - t_0$	16.22	15.34	18.54	20.37		
	$t_3 - t_0$	19.46	17.42	6.17	9.62		
19	$t_1 - t_0$	2.00	2.51	12.50	9.96	230	126
	$t_2 - t_0$	15.24	15.24	17.37	18.07		
	$t_3 - t_0$	18.12	17.52	6.94	8.77		
21	$t_1 - t_0$	0.79	2.51	13.64	9.96	250	142
	$t_2 - t_0$	14.07	15.75	18.82	18.88		
	$t_3 - t_0$	15.61	17.38	12.99	12.27		

Table 4.2: Obtained experimental results using shock chronometry. We report the thickness of the diamond layer, the laser energy, the shock breakout times from VISAR data, and the corresponding shock velocities. For the first layer, the shock velocity is just an average value obtained by dividing the total $25\ \mu m$ thickness (plastic ablator + first nickel layer) by the shock breakout time.

diamond remains transparent and it is reflected by the nickel layer behind the shock; In the first case, we should use formula (4.2) with the value of the refraction index of diamond ($n_0 = 2.417$). In the second case we should use formula (4.5), which allows retrieving the fluid velocity of the nickel interface U only if the value of ρ/ρ_0 is known. The hydrodynamics simulations presented in Section 4.6 shows that the shock is not completely stationary and that the compression degree changes from an initial $\rho/\rho_0 \sim 1.7$ when the shock enters in diamond, to a final $\rho/\rho_0 \sim 1.3$ when the shock breaks out at diamond rear side. This would correspond, using Gladstone Dale law, to refraction indexes of compressed diamond respectively of 2.84 and 3.41. Such values seem to be a bit larger than what can be extrapolated form the recent experimental measurements by Ozaki et al. [Katagiri et al., 2020] who reported $n \sim 2.55$ at $\rho \sim 4.4 g/cm^3$ (i.e. a compression $\rho/\rho_0 \sim 1.25$) but the change is not too important for the discussion which follows. Calculating the denominator in formula 4.8 we see that the initial value is ~ 1.248 and the final value 1.206. We see that the variation is not large, hence we can use an average value of the denominator ~ 1.23 in formula 4.8 to deduce U from fringe shift F with a reasonable accuracy.

So, first we tested the possibility that the probe beam is reflected from the nickel interface by using formula 4.8 as just described before. In this case, we cannot retrieve an initial value of the fluid velocity which is in agreement with the available Hugoniot curves for diamond (this would give $U \sim 8 - 10\ km/s$, for a shock velocity $D \sim 20\ km/s$). In addition, at later time, as it will be clearly shown by the simulations in the next section, the interface velocity U strongly decreases, while the VISARs provide an almost constant velocity (as implied by the almost straight vertical fringes in Figure 4.6). Therefore, we can conclude that the observed fringes are almost certainly produced by a reflection of the probe beam on the shock front. In this case, Figure 4.7 shows the variation of shock velocity in time obtained from simultaneously analysing the fringe shifts from the two VISARs. As we see, the value of shock velocity is in fair agreement with what we have found from shock chronometry (see Table 4.2) and the measured velocity is almost constant, again as implied by the almost straight vertical fringes in

Figure 4.6. Actually, Figure 4.6 shows a small decay of velocity in time, i.e. the shock wave as it travels in diamond, in agreement with our expectations (see next section). However, such reduction is not easily measurable due to the low fringe quality in our experiment

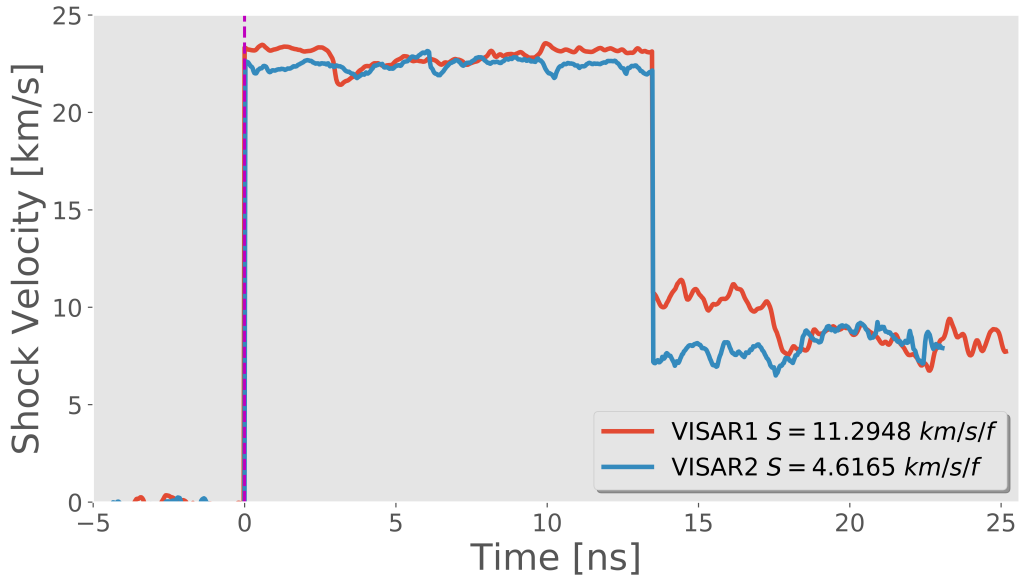

Figure 4.7: Time history of the shock velocity in diamond obtained by analysing the fringe shift of the two VISARs from shot # 15 (Figure 4.6). Here $t = 0$ is the time of shock breakout at the inner nickel/diamond interface and the shock breakout at diamond rear side takes place $13.48\ ns$ afterwards. The first part of the graph represents the shock velocity in diamond. The second part the free surface velocity of diamond after shock breakout at target rear side.

Finally, after the shock breakout at the rear of the target, we still observe a fringe shift. From this, we can calculate the velocity at which the rear-side surface is moving. This is called "free surface velocity" V_{FS} and can be obtained by extrapolating the impedance mismatch conditions to zero pressure and density [in this case we used $n_0 = 1$, the refraction index of vacuum, to calculate the speed]. In the case of weak shocks, such free surface is related to the fluid velocity U (the velocity of matter behind the shock front) by the relation $V_{FS} \sim 2U$ [Zel'dovich and Raizer, 2002]. From the analysis of the fringe shifts from the two VISARs, we got the free surface velocities of diamond

and nickel which are reported in Table 4.3.

4.6 Hydro Simulations and data interpretation

In order to interpret our experimental results, we performed 1D radiative hydrodynamic simulations with the code MULTI [Ramis et al., 1988]. The $1D$ approximation is justified because of the large focal spot ($\sim 500\ \mu m$) as compared to the total target thickness ($\sim 300\ \mu m$). The laser pulse was flat top in time with a plateau duration of $1\ ns$ and rise and fall times of $0.1\ ns$. In the simulations, we used the SESAME Table 3100 for nickel and the SESAME table 7770 for Parylene [LANL, 1992]. As for diamond, we tested different EOS tables coming from the SESAME data base [LANL, 1992], from QEOS [More et al., 1988] and FEOS [Faik et al., 2018], in all cases setting the initial density at $\rho_0 = 3.515\ g/cm^3$. Figure 4.8 shows the density map and the pressure map from MULTI $1D$ simulation reproducing shot $\#15$. Here we used the table SESAME 7830 for Diamond. Table 4.3 reports the detailed numerical comparison between experimental and numerical results for the shot $\#15$, while Table 4.4 summarises the main results for all our 4 useful shots. As said before, the typical ablation pressure in plastics is ~ 12 $Mbar$ for this shot (for which $I = 9 \times 10^{13}\ W/cm^2$), in agreement with the previous scaling law, and the increases in nickel due to the impedance mismatch up to a maximum pressure if $\sim 26\ Mbar$ as can also be seen using the analytical formulas reported in [Batani et al., 2001] for the shock passage between two materials (labelled 1 and 2).

$$\frac{P_2}{P_1} = \frac{4\rho_2}{(\sqrt{\rho_1} + \sqrt{\rho_2})^2} \tag{4.7}$$

Before reaching the nickel/diamond interface the pressure in nickel decreases down to $\sim 15\ Mbar$. Indeed as the shock is transmitted from plastic to nickel, a reflected shock with the same pressure ($\sim 26\ Mbar$) is reflected back into plastics. As soon as this shock reaches the ablation surface (where the pressure applied by the laser is still $\sim 12\ Mbar$), a rarefaction wave is generated and quickly reaches the shock front decreasing its pressure.

At this point, the pressure generated in diamond is $\sim 9\ Mbar$, again in agreement with formula 4.7. Later the shock in diamond decreases down to $\leq 4\ Mbar$ at the time

of shock breakout at the diamond rear side. Although the pressure is non constant, the shock is quasi stationary (as shown by both experimental results and simulations) i.e. the variation in shock velocity are smaller. This is due to the square root dependence of shock velocity on pressure which implies that the ratio of final shock velocity to initial shock velocity is at most $\sim (4/9)^{1/2} = 0.67$. Indeed the simulation shows a decrease of instantaneous shock velocity in diamond from the initial value $\sim 24\ km/s$ to a final value of at shock breakout $\sim 18\ km/s$ (i.e. a ratio of ~ 0.75). By comparison, the graph in Figure 4.7 only shows a decrease of shock velocity from $\sim 24\ km/s$ down to $\sim 22\ km/s$.

We performed two sets of simulations, with and without the final Ni layer, corresponding to what takes place in the two halves of the target. The importance of performing such separate simulations is that when a very refined mesh is used, they allow evaluating the free surface velocity of Ni and diamond, and these results can also be compared to experimental values obtained from VISAR fringe shifts.

Shot # 15	$t_1 - t_0$	$t_2 - t_0$	$t_3 - t_0$	$D_{Diam.}$ $[km/s]$	D_{Ni} $[km/s]$	$U_{fs}Diam.$ $[km/s]$[1]	$U_{fs}Ni$ $[km/s]$
Experiment[2]	1.66	15.14	17.10	20.11	10.20	$\sim$ 8.70	$\sim$ 8.00
Simulation 9×10^{13}	1.30	15.10	16.65	19.56	12.90	9.80	8.77

[1] Average of two VISARs.
[2] Just after shock breakout.

Table 4.3: Comparison of experimental and numerical results for the shot #15. Simulations performed using the SESAME table 7830

Again, the fact that the experimental evidence of a quasi-stationary shock dynamics are confirmed by the results of hydrodynamics simulations performed with MULTI gives evidence that the VISAR probe laser is really reflected by the shock front traveling in the transparent diamond, proving that shock compression brings diamond to a reflecting state.

Concerning the comparison of experimental and numerical fluid velocities, we see that the agreement is mainly qualitative. Again this is due to the poor fringe quality

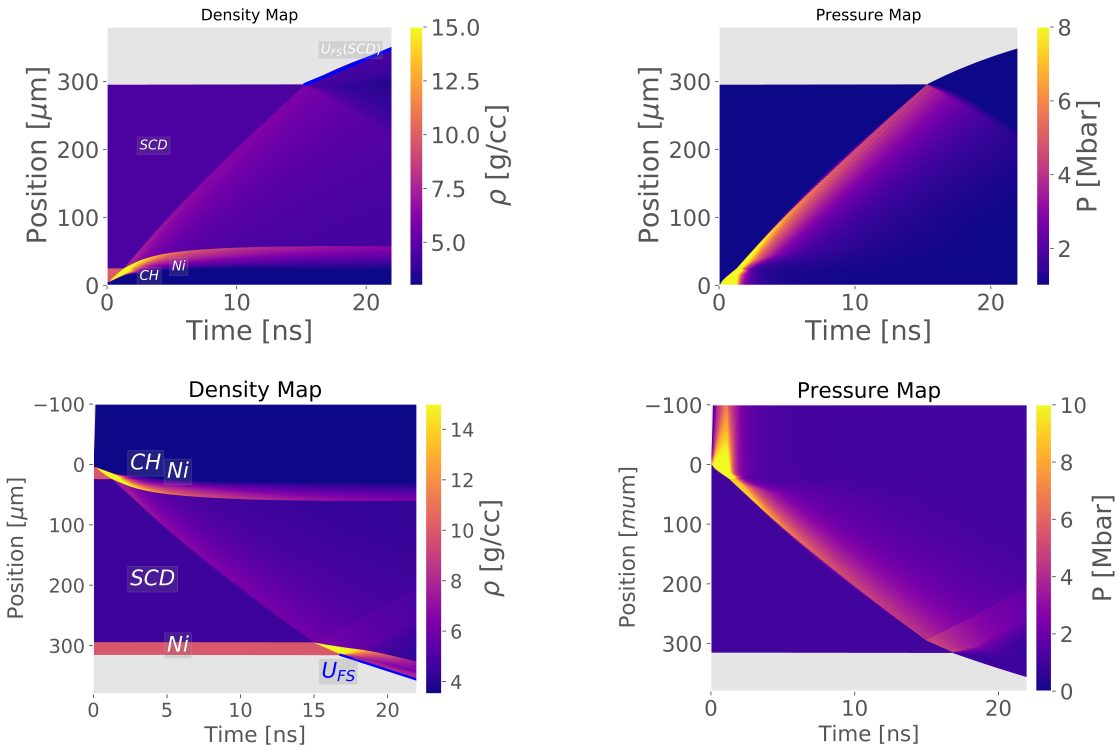

Figure 4.8: Hydrodynamic simulations reproducing shot #15, top) Density and pressure map of the same shot without Ni layer. Bottom) figures left and right represent hydrodynamic simulations with the Ni step. Such plots allow estimating the Free Surface velocity for the Ni step and the Diamond layer respectively.

in our experiment. We also see that in our case the free surface velocity in diamond is larger than twice the fluid velocity (by about $\geq 10\%$ in all cases), which shows that indeed the weak shock approximation does not hold here.

Shot #	d Diamond [μm]	I [W/cm^2]	E_L [J]	D_{tt} [km/s] [a]	D_{FS} [km/s] [b]	$D_{sim.}$ [km/s]	$U_{fs(Diam.)_{(Exp.)}}$ [km/s]	$U_{fs(Diam.)_{(Sim.)}}$ [km/s]
15	270	9×10^{13}	149	20.11	24.00	19.56	$\sim$ 8.70	9.80
18	260	7.6×10^{13}	128	19.46	19.08	18.91	$\sim$ 6.00	6.44
19	230	3×10^{13}	126	17.72	19.23	18.07	$\sim$ 7.00	6.41
21	250	6×10^{13}	142	18.85	19.02	18.68	$\sim$ 7.00	7.81

[a] Average of two VISARs.
[b] At the time of shock breakout at the first nickel/diamond interface.

Table 4.4: Comparison of experimental and numerical results for all shots

4.7 Discussion

In our experiment we have tested a multi-layered target design which allows simultaneously measuring the shock velocity in the various layer by using shock chronometry and/or fringe shift (VISAR). Using the laser PHELIX, we have then been able to produce pressures up to $9\ Mbar$ in diamond and we obtained the evidence that the generated shock is a quasi-stationary reflecting shock, inducing a transition in diamond from transparent/insulator to reflecting. In principle, the target design allows to measure the reflectivity of shocked diamond but, due to the absence of an absolute calibration of reflectivity, this was not performed in our experiment. We can only see that the target reflectivity decreases when the shock crosses the nickel /diamond interface, implying that the reflectivity of shocked diamond is smaller than that of nickel. In following experiments using the same experimental set-up, instead of nickel one can use aluminium or quartz which are a standard reference material commonly used for EOS experiment, including the possibility of performing an absolute measurement of reflectivity. Experimental results are well reproduced by hydrodynamics radiative simulations performed with the code $MULTI\ 1D$. The large focal spot used in our experiment (as compared to target total thickness) justifies the absence of $2D$ effects in hydrodynamics, as observed in experimental images showing a flat shock breakout. Of course, the choice of the EOS for carbon is essential in order to allow reproducing experimental results. Indeed we have seen that these are reproduced if we use the $SESAME$ table 7830 and 7834 but are not reproduced if we use 7831, 7832 or 7833. A-priori this is not a surprise (the first two tables were developed for diamond while the last two for graphite from compressed powder and 7831 for liquid carbon) but it nevertheless shows the sensitivity of our measurements to the change of EOS. To check the hydrodynamic behaviour of of the shock on diamond, we built an EOS table using the software $MPQEOS$ [Kemp and ter Vehn, 1998] (which implements the $QEOS$ model [More et al., 1988]) using the correct value of density and bulk modulus of diamond, and we found that simulations using such a table do not reproduce our experimental

results (for instance, for shot # 15 the breakout time at the rear side of diamond would be 20 ns instead of $\sim$ 15 as measured in experiment and provided by simulations using the $SESAME$ table 7830 with the same laser intensity on target, i.e. 9×10^{13} W/cm^2). Such comparison is shown in Figure 4.9.

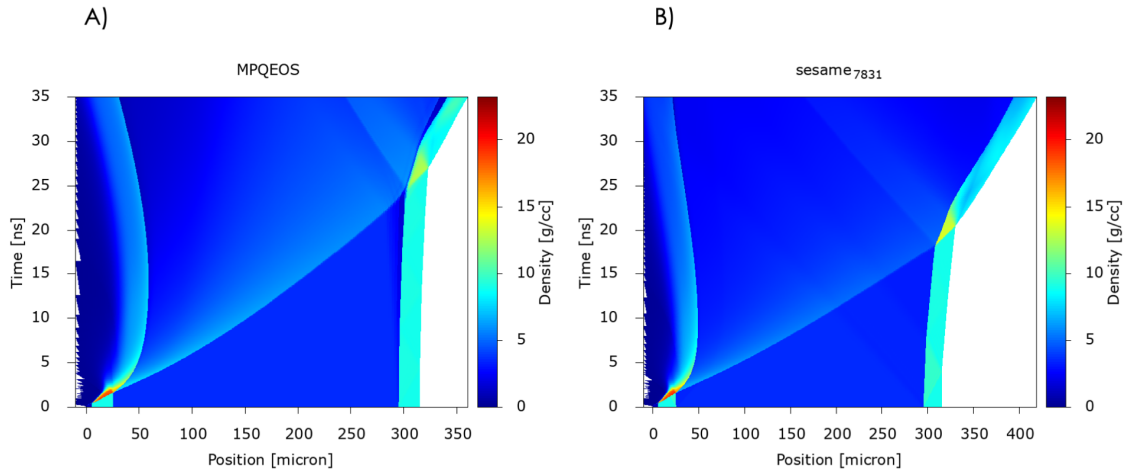

Figure 4.9: Comparison of SESAME 7831 and MPQOES tabulated EOS data for Diamond used with MULTI 1D code. (A) MQEOS model dose not reproduce the shock breakout time at the rear side of the Diamond and (B) SESAME 7831 gives higher value for the shock breakout in Diamond, we also observe expansion of the target.

Finally, our target design allows measuring the free velocity of the target surface after shock breakout, a result which again is fairly well reproduced by hydro simulations. The persistence of the fringes after shock breakout could at first seems strange since very often VISAR fringes are seen to disappear after breakout. This is due to the vaporisation of the material on target rear side and the creation of an absorbing plasma which implies a very strong decrease in reflectivity [Benuzzi et al., 1998] and the disappearing of fringes. On the contrary, in some experiments with double shocks, fringes have been observed after shock breakout [Benuzzi-Mounaix et al., 2004]. This

has been interpreted as the results of the fact that the final state of the material was still solid/liquid, implying the presence of a sharp matter/vacuum interface implying high reflectivity. So the presence of the fringes after shock breakout implies that:

a) the material is not vaporised and changed to plasma state, i.e. in solid or liquid state, which depends on whether the final state is above or below the melting curve of the material

b) the material is reflecting, with the possible implication that it is conducting. Let's first analyse the first point, i.e. discuss whether the material is solid, liquid, or plasma.

In our experiment, considering again for instance shot $\#\ 15$, the pressure at shock breakout is of the order of $\leq\ 4\ Mbar$, which could be considered as "high" pressure. However, indeed, this is not the case since such a pressure must be compared to the bulk modulus of the material, which is $4.42\ Mbar$ for diamond. Shock velocities in diamond in our experiment are of the order of 18-20 km/s, which are not so large when compared to the sound velocity in diamond ($12\ km/s$). One can also consider that the latent heat of vaporisation in diamond is $\sim 356\ kJ/mole$ or $\sim 30\ MJ/kg$. The increase in internal energy per unit mass $\Delta\epsilon$ produced by the shock is given by Zeldovich and Raizer [Zel'dovich and Raizer, 2002] as

$$\Delta\epsilon = \frac{1}{2}\left(P + P_0\right)\left(\frac{1}{\rho_0} - \frac{1}{\rho}\right) \tag{4.8}$$

In our case, at shock breakout we have $P \leq 4\ Mbar$ and density is $\rho \sim 5.5\ g/cm^3$. This implies $\Delta\epsilon \sim 20\ MJ/kg$ which is indeed below the vaporisation limit. This is of course even more true for the other shots corresponding to lower laser intensities and shock pressures. Finally, the graph in Figure 4.10 is a phase diagram for carbon (taken from Ref. [Grumbach and Martin, 1996]) to which we have superimposed the Shock Hugoniot from SESAME 7834. We see that for the pressures reached at shock breakout for our shot $\#15$ ($P \leq 4\ Mbar$), diamond is still in a solid phase. For the higher pressure

($\sim 9\ Mbar$) reached when the shock enters into diamond, we may get a liquid phase. According to Grumbach and Martin [Grumbach and Martin, 1996], but also other Ab-initio models, diamond is predicted to melt on its Hugoniot in the range of $7 - 7.45$ $Mbar$. Therefore we can conclude that in our experiment, diamond is generally still in a solid phase (except, possibly, for the higher pressure shots but only for initial times after the shock enters into diamond). In any case, we are far enough from getting a plasma state.

Let's now consider the second point, i.e. the fact that the material is reflecting, with the possible implication that it is conducting. The melted state could either be a semi-metallic fluid or a metallic fluid. According to Martin and Grumbach, the transition is at $\sim 5\ Mbar$ which implies that the melted fluid in our case is metallic and could explain the presence of a reflecting shock front. However, again this boundary is subject to the usual uncertainties of EoS models. Also, according to Grumbach and Martin, the insulator/metallic transition is exactly coincident with the melting. Other EOS models differ on this point. For instance, several authors [Fahy and Louie, 1987, Grover, 1979, Gerald I. Kerley, 2001] predict that diamond will transform to a metallic BC8 phase before melting, i.e. an insulating-solid to metallic-solid transition followed by melting into a metallic liquid. This transition, along the Hugoniot, would take place at $4.3 - 5\ Mbar$. The situation is different according to Romero and Mattson [Romero and Mattson, 2007]. Their calculations show that the band gap of solid phase of diamond E_g, which is initially $E_{g0} \sim 5.5\ eV$, reduces along the principal Hugoniot but closure before the onset of melt is not observed and $\Delta\epsilon$ does never decreases below $2.0\ eV$ before melting. All phase transitions produce a change in slope along the Hugoniot. For instance, the insulating-solid to metallic-solid transition predicted in [Fahy and Louie, 1987, Grover, 1979, Gerald I. Kerley, 2001] is incorporated into the phase diagram proposed by Kerley and Chhabildas [Gerald I. Kerley, 2001] and produces a change in slope along the Hugoniot at $4.3 - 5\ Mbar$. Similarly, but in opposite direction, the Hugoniot calculated from SESAME 7834 (Figure 4.10) shows a small kink in the Hugoniot curve at $\sim 9\ Mbar$ which is not present in the table 7830. From the

experimental point of view, Nagao et al. performed measurements of the Hugoniot of diamond in the pressure range 5 to 20 $Mbar$ and they did not observe any "kink" [Nagao et al., 2006]. This however may be due to the relative large error bars in the experiments. More recent measurements of diamond Hugoniot up to 26 $Mbar$ were performed in [Eggert et al., 2010a] and [Gregor et al., 2017]. As for optical properties, Bradley et al. [Bradley et al., 2004] performed an experiment at the Omega laser facility and their results seem to show that diamond is solid for $P < 5.50$ $Mbar$ and fluid for $P > 10$ $Mbar$ (however, they did not determine shock pressure independently but used a theoretical EOS model [van Thiel and Ree, 1995]). They conclude that melting takes place in the range $8 - 10$ $Mbar$.

They have measured the reflectivity of shocked diamond (which is not possible in our case due to the low quality of our VISAR images), and modelled reflectivity data using a density dependent mobility gap. They concluded that the energy gap reduces with density along the Hugoniot and that finally diamond undergoes band overlap metallization at $P \sim 10$ $Mbar$. In this sense, their experimental measurements do not show the presence of the insulating to metallic-solid transition at $4.3 - 5$ $Mbar$, and seems to support the models which predict that metallization takes place at higher pressures. Interestingly, Glenzer et al. [Glenzer et al., 2016, Gamboa et al., 2015] found that the band gap in diamond increases with pressure. However, they were working at lower pressures (up to 3.7 $Mbar$) and their measurements refer to the Penn gap, i.e. the average separation between the valence and conduction bands. Their data show that diamond remains an insulator to densities of at least 5.3 g/cm^3 and pressures of 3.7 $Mbar$. We notice that Romero and Mattson [Romero and Mattson, 2007] show that ΔE increases along the Hugoniot until approximately 1.65 $Mbar$.

Finally, we constate with large evidence that most of our shots induce a state of diamond which is solid and non-metallic. This conclusion is however puzzling because solid non-conducting diamond is expected to be transparent while we have concluded that we see reflection from the travelling shock. One possibility to explain this contradiction is that the high temperature reached in diamond (of the order of $2500 - 10000$

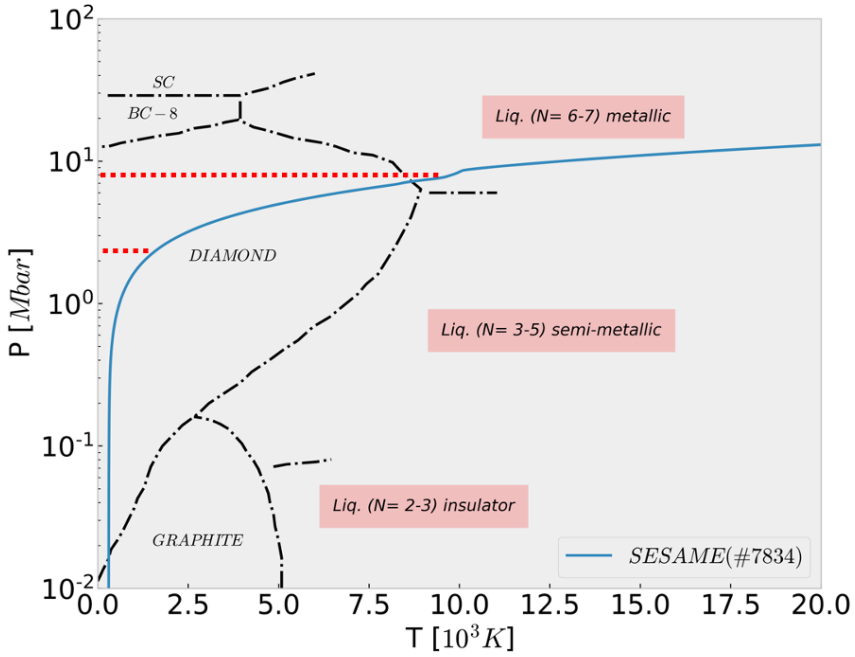

Figure 4.10: Phase diagram of Carbon according to Grumbach and Martin [Grumbach and Martin, 1996] and shock Hugoniot from the SESAME table 7834. The two dashed horizontal red lines show the range of pressures reached in diamond in our shot #15

.

K) induce a significant number of electrons to move from the full valence band to the (initially empty) conduction band. These quasi-free electrons behave like a plasma and can therefore reflect the probe beam provided their density is larger than the critical density corresponding to the wavelength of the VISAR laser. The refraction index of diamond n^* in presence if a large density of electrons in the conduction band n_{ncond} can be written as

$$n^* = \sqrt{n^2 - \frac{n_{cond}}{n_{cr}}} \tag{4.9}$$

where $n_{cr} = 2.5 \times 10^{21}\ cm^{-3}$ is the critical density corresponding to the wavelength of the VISAR probe laser ($660\ nm$) and n is the refraction idea of compressed diamond (given by Glastone Dale law). The initial band gap of diamond is quite large ($\sim 5.5\ eV$), to prevent a significant number of electrons to reach the conduction band in usual conditions. However shock compression reduces the width of the gap and at the same time increases the temperature, thereby strongly affecting the density of electrons in the conduction band.

In order to test this idea, we have performed a simple qualitative calculation using Fermi-Dirac statistics. We calculated the density of free electrons in the conduction band as in the activated gap model of Celliers et al.[Celliers et al., 2004b], i.e., by interpreting the Fermi-Dirac distribution function $f(E)$ over the density of states $g(E)$ between $E_F + \frac{E_g}{2}$ and ∞, where E_F is the Fermi energy of the system located in the middle of the band gap.

$$n_{cond} = \int_{E_F + \frac{E_g}{2}}^{\infty} g(E) f(E) dE \tag{4.10}$$

$$f(E) = \frac{1}{exp(\frac{e - E_F}{T}) + 1} \tag{4.11}$$

here we used the simple approximation that the density of states follows a square root behaviour $g(E) = g_0 E^{1/2}$. As for free electrons in a flat potential well. We have taken into account the reduction of band gap energy with temperature using Varshni's formula [Varshni, 1967] which describe the reduction of the band gap due to temperature

effects.

$$E_g = E_{g0} - A\frac{T^2}{(T+\theta_D)} \tag{4.12}$$

Where $A = 5\times10^{-4}\ eV/K$ and θ_D is the Debye temperature of diamond. Let's notice that available data on the band gap energy of diamond [Logothetidis et al., 1992], obtained in static experiments using diamond anvil cells are better interpolated using the modified Varshni's formula proposed in [Li et al., 2017, Karsai et al., 2018]. However this dose not seem adapted to high temperature since it produces an unrealistic band gap closure at $T = 4000\ K$. Also the original Varshni's formula gives, as expected, a linear behaviour of the band gap energy vs temperature, while the modified Varshni's formula gives quadratic dependence. The results of the calculations, band gap and density of electrons in the conduction band, are shown in the graph of Figure 4.11. Of course this model dose not take into account that shock compression induces a change in density of matter (and hence of electrons) and that the gap shrinks not only due to temperature but also due to the increase in density. To consider these effects, we repeated the calculations using the formula by Bradley et al [van Thiel and Ree, 1995] according to which, along the principal Hugoniot of diamond

$$E_g = E_{g0} - A\,(\rho/\rho_0 - 1) \tag{4.13}$$

where $A = 6.01\ eV$. Here, being along the Hugoniot, the gap reduction is due to both increase in temperature and in density. The results of this alternative model are also shown in Figure 4.11. As expected, in this case the density of electron in the conduction band is larger because density effects add to changes in temperature. Of course both models are only qualitative and certainly more detailed models should be used to calculate the internal ionisation in diamond. Indeed we did not consider the real shape of the density of states g(E) in diamond nor as it changes with compression. Also it is clear how these results depend critically on the details of the model describing the reduction of band energy gap. Finally, since the electron density in the conduction band is a direct result of temperature increase, any preheating source preset in the experiment is likely to strongly affect it. Although in our experiment we did not see

any clear signature of preheating, this is also a possibility which could be taken into account.

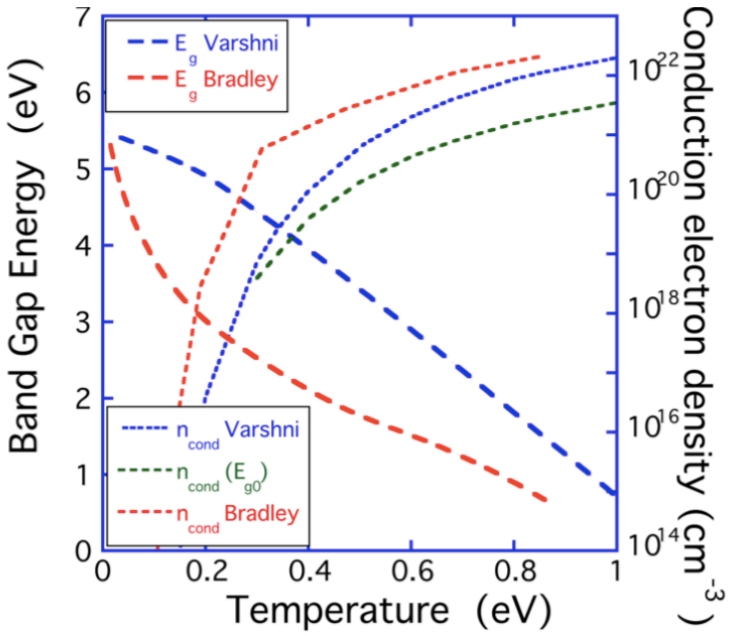

Figure 4.11: Energy gap vs. temperature and electron density in the conduction band calculated using the formula from Varshni (constant density, effect of temperature only) and the one Bradley (along the Hugoniot). In this last case, the temperature has been related to compression through the Sesame Table 7834. For comparison we also show the case in which there is no variation of density and of energy gap (i.e. the increase in temperature only affect the Fermi-Dirac distribution of electrons).

4.8 Conclusions and perspectives

In this Chapter we have reported on the study of behaviour of Diamond at Mbar pressures using laser based dynamic compression techniques. In our experiment we used a multi-layered target design which allows simultaneously measuring the shock velocity by shock chronometry and by fringe shift . The results are explained by assuming that the VISAR probe beam is reflected from the shock front travelling in diamond. Experimental results are well reproduced by $1D$ radiative hydrodynamic simulations using the code MULTI and the Sesame table 7830 or 7834 for diamond. Due to the large focal spot, as compared to target thickness, the $1D$ code proves to be able to well reproduce the data. The shock pressure is not maintained in time due to the duration of the laser pulse which is relatively short. However the changes in velocity of the shock are small, so we can speak of a quasi-stationary shock. The reflectivity of the shock front is explained as likely being due to the increase of electron density in the conduction band. Such quasi free electrons behave like a plasma and can reflect the probe beam when the density is larger than the critical density corresponding to the wavelength of the VISAR laser. The next we will report on study of two different compression techniques, using combined DAC and Laser heating with novel DAC design, to study Water samples at GEKKO XII laser facility at ILE Osaka.

Chapter 5

Water cells at Mbar pressures on high power laser facility

Contents

5.1 GEKKO XII Laser

The Gekko XII Laser is a high-power [Fujioka et al., 2012], 12-beam, Nd:glass laser at the Osaka University's Institute for Laser Engineering constructed in 1983, which is used for high energy density physics and inertial confinement fusion research. The system consist of twelve individual beam lines shown in Figure 5.1, used to amplify the laser energy and this can deliver up to $24\,\mathrm{kJ}$ and power of $50\,\mathrm{TW}$. Fundamental wavelength of the laser facility is $1.053\,\mu\mathrm{m}$, and the laser wavelength can be converted to 0.53 or $0.35\,\mu\mathrm{m}$ with a large nonlinear crystal. Compared to most Nd:glass laser ICF experiments, *GEKKO* is also quite small, with beam lines about 10 m long. The 12 beams of the *GEKKO* laser are capable of delivering about $10\,\mathrm{kJ}$ per 1 to 2ns pulse (10-20 terawatts).

Figure 5.1: The GEKKO XII (right) and LFEX (left) lasers at ILE, Osaka University, Japan (picture courtesy of Osaka University)

5.2 Vacuum Chamber

There are two vacuum chambers, in which high-energy-density plasma's are generated. In the chamber-I, a target can be irradiated uniformly by 12 *GEKKO* laser beams arranged in spherically symmetric geometry. 4 *LFEX* laser beams are also available in the chamber I. In the chamber II, the 12 *GEKKO* beams are bundled. A planar target is irradiated uniformly by the bundled 12 beams from the one-side also used in this work Figure 5.2 shows the configuration of the focusing lenses array.

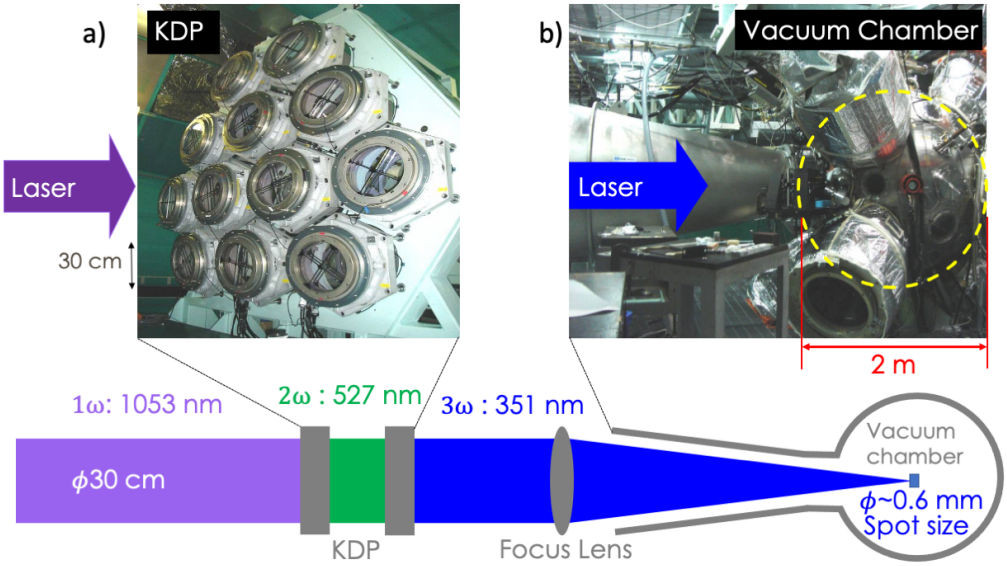

Figure 5.2: a) GEKKO XII laser laser system focusing array of the 12 beams for planar geometry one side irradiation, b) the interaction chamber-II used in this work.

5.3 Introduction Scientific Interest

Equation-of-State (EOS) of matter at extreme thermodynamic states is of relevance for several fields in physics especially in inertial confinement fusion (ICF) where precise knowledge of EOS is required. Water is predicted to be abundant in the outer planets of the Solar System, as well in many of the re-

cently discovered exoplanets. In particular, it is one of the principal ingredients of the mantles of giant planets such as Uranus, Neptune, and Jupiter [Mazevet et al., 2019]. The observation of large and asymmetric magnetic fields in those planets [NESS et al., 1986, Connerney et al., 1992, Chen et al., 2021] indicated that the mantle is the origin of the field. As the dynamo theory requires the presence of a conductive material, it was suggested that one or all of the main ingredients of the mantle (carbon, methane, ammonia, and water [Wang et al., 2021, Jakubowska et al., 2021]) experience a phase transition to a conducting state. Pioneering theoretical work has been done calculating the properties of the super-ionic phase of water at planetary conditions [Cavazzoni et al., 1999, Mattsson and Desjarlais, 2006, French et al., 2009]. Therefore, water at very high pressures has been extensively studied in recent works [Kimura et al., 2015, Mattsson and Desjarlais, 2006, Goldman et al., 2009, Pan et al., 2014, Dolan et al., 2007, Nagayama et al., 2002]. Recently [Millot et al., 2018b, Millot et al., 2019], the super-ionic phase of water was detected experimentally along the Uranus and Neptune isentropes at about $1.5\,\mathrm{Mbar}$, by laser shocking water samples pre-compressed up to $28\,\mathrm{kbar}$. The new super-ionic phase is predicted to span the pressure range of 1.5 to $6\,\mathrm{Mbars}$.

Super-ionic water is a solid system that has high ionic conductivity well below the melting temperature. Whether H_2O in planetary interiors is in the super-ionic or metallic state, is of great importance for understanding the source of the planetary magnetic field.

Laser-driven shock compression is a useful technique for generating high pressure and temperature conditions similar to the inner part of Neptune and Uranus. However, measuring simultaneously P-ρ-T is challenging, particularly temperature, as this requires absolute intensity measurements which are not necessary for the determination of the pressure or the density. In this work, we conducted laser-driven shock experiments on H_2O samples up to $4.6\,\mathrm{Mbar}$ along with pressure and density we evaluated the temperature from measured reflectivity and thermal emission of the shocked sample.

The impedance mismatch (IM) method is widely used for the determination of the Hugoniot of sample material. Given that one knows the Hugoniot of a "standard" material that is used as a reference, the Rankine-Hugoniot (RH) [Zel'dovich and Raizer, 2002] set of equations, expressing the conservation laws, can be used to relate the experimentally measured shock velocity ($\mathrm{D_s}$) in the standard material before the shock reaches the standard-sample interface in the sample after it passes through the interface. In this work, we used z-cut α-Quartz ($\mathrm{SiO_2}$) as a reference material [Knudson and Desjarlais, 2013, Brygoo et al., 2015] which at ambient pressure is transparent to visible light and becomes reflective at pressures above $1\,\mathrm{Mbar}$ [Laudernet et al., 2004]. As diagnostic tools, we used the velocity interferometer system for any reflector (VISAR) [Celliers et al., 2004a, Bloomquist and Sheffield, 1983, Bolme and Ramos, 2013, Barker and Hollenbach, 1972, Barker and Schuler, 1974] which allowed us to make a precise measurement of shock wave parameters and characterize the EOS of water. The RH set provides information of P and ρ, but not of T, whereas T is also an important thermodynamic parameter. Indeed in this work, we also measured the temperature using streaked optical pyrometry (SOP) diagnostic data.

5.4 Experimental setup

5.4.1 GEKKO XII at ILE laser facility

The first experiment was carried out on the HiPER (High-Intensity Plasma Experimental Research) laser facility, a uni-axial irradiation chamber of the GEKKO XII (GXII) laser at the Institute of Laser Engineering (ILE), of Osaka University. Up to 12 beams of neodymium-doped yttrium aluminum garnet Nd: yttrium aluminum garnet(YAG) laser, frequency tripled ($351\,\mathrm{nm}$) were used in the experiment. The laser pulse temporal profile was approximately square shape in time with full width at half maximum (FWHM) $2.5\,\mathrm{ns}$ with typical rise and fall time of $100\,\mathrm{ps}$ each. The focal spot diameter was $600\,\mu\mathrm{m}$

flat-top. SSD (Smoothing by Spectral Dispersion Technique) was applied to smooth out the beams. Kinoform phase plates were also used to achieve uniform irradiation, resulting in good shock front planarity.

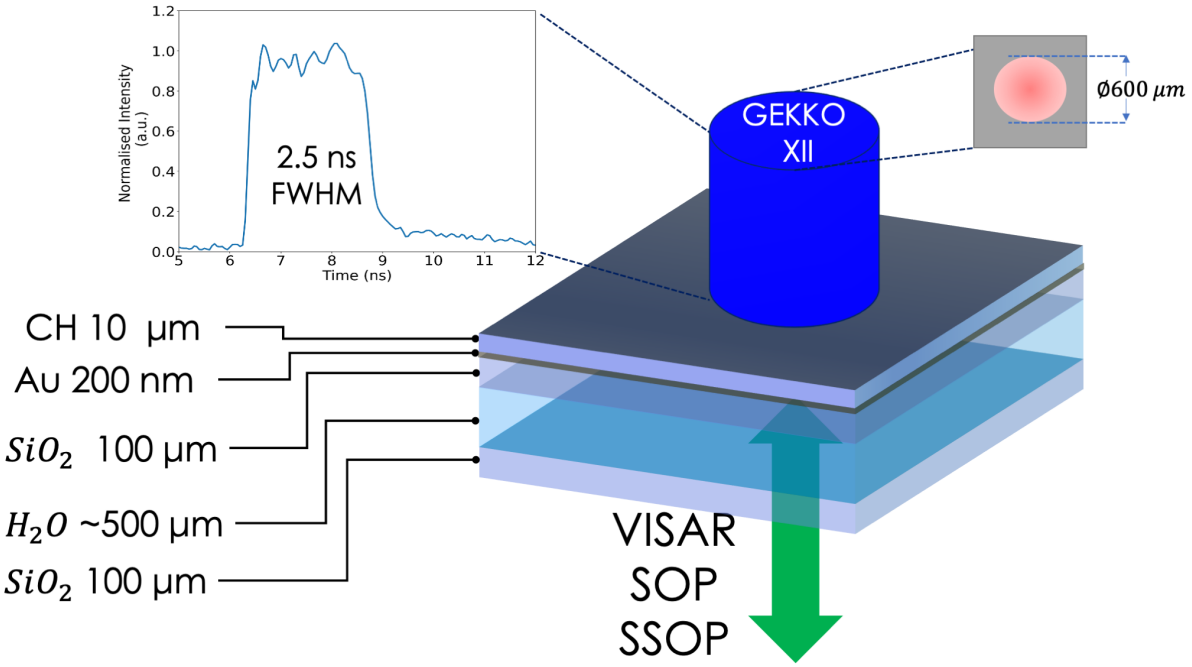

Figure 5.3: Experimental setup: sketch of the multilayered target design in planar geometry with-its associated thicknesses used in our experiment. Drive laser from top. From bottom the VISAR and SOP measure the shock velocity and the self-emission on the rear side.

Figure 5.3 shows the experimental setup and target configuration. A typical target assembly consist of $10\,\mu\mathrm{m}$ parylene (C_8H_8) will be referred as CH / $200\,\mathrm{nm}$ Au / $100\,\mu\mathrm{m}$ Quartz (with $\mathrm{AR@1054\&532}$ both sides) nominally $\sim 500\,\mu\mathrm{m}$ water / $100\,\mu\mathrm{m}$ Quartz (with $\mathrm{AR@1054\&532}$ both sides). The laser initially hits the $0.1\,\mu\mathrm{m}$ thick Al layer, coated over the CH layer to avoid laser shine through. The CH layer is the actual ablator and the Quartz is the pusher layer. The $200\,\mathrm{nm}$ gold layer was placed to stop any X-rays from the plasma corona and avoid preheating of water. Water cells were produced at the Technical University Darmstadt (Germany) target fabrication department. Due to the low Z ablator and the low laser intensity, X-ray radiation is low and characterized by low photon energy. The Au layer is capable to stop the X-ray radiation

thus preheating of water is negligible.

The primary diagnostics were the VISAR and SOP. Two line-imaging interferometers VISAR's allows to record time resolved Doppler shift of the velocity of the fast moving reflector also the optical properties such as (reflectivity)[Celliers et al., 2004a, Bloomquist and Sheffield, 1983, Bolme and Ramos, 2013, Barker and Hollenbach, 1972, Barker and Schuler, 1974, Yan et al., 2021]. These two VISAR's had different velocity per fringe (VPF) sensitivity to resolve the 2π phase jump ambiguities due to the shock velocity jump at material interfaces. The sensitivity of the two VISAR's were $7.523\,\mathrm{km/s}$ and $4.476\,\mathrm{km/s}$ taking into account the refractive index of SiO_2. The VISAR probe beam was an injection-seeded Q-switched YAG laser. The pulse duration of the probe was $\sim 10\,\mathrm{ns}$ at the FWHM and its wavelength of$532\,\mathrm{nm}$. The post-processing of the VISAR raw data obtained in the experiment allows determining [Flacco A., 2011] the fringe position to $10\,\%$ of a fringe, while the multiple fringe shifts allows the precision of the shock velocity measurements to be a few percent. Our VISAR analysis showed uncertainties in the measured D_s of the order of $3\,\%$.

To measure the shock temperature we used SOP as a main diagnostic platform [Miller et al., 2007, Gregor et al., 2016, He et al., 2019]. The self emission of the shocked sample at wavelength $450\,\mathrm{nm}$ with $38\,\mathrm{nm}$ bandwidth, was recorded spatially and temporally resolved, using an absolutely calibrated SOP.

5.4.2 PHELIX GSI laser facility

The second experiment was conducted at the GSI facility using the PHELIX laser, a flash-lamp-pumped Nd: glass laser utilizing the second harmonic at wavelength $527\,\mathrm{nm}$. The spatial profile was flat-top with spot $350\,\mu\mathrm{m}$ FWHM obtained by an appropriate phase plate [Koenig et al., 1994] and the temporal profile was top-hat with a duration of $3.5\,\mathrm{ns}$ (FWHM). The laser was focused onto a multilayered target with intensity I varying from $5.49\times10^{12}\,\mathrm{W/cm^2}$ to $2.52\times10^{13}\,\mathrm{W/cm^2}$. The ablation pressure was approximately

$12\,\mathrm{Mbar}$ and was generated in our plastic ablator (parylene with gross chemical formula C_8H_8), was estimated from the well-known scaling-laws using Eq. 1.12 [Mora, 1982b, Lindl, 1995, Chen et al., 2020], for given intensities.

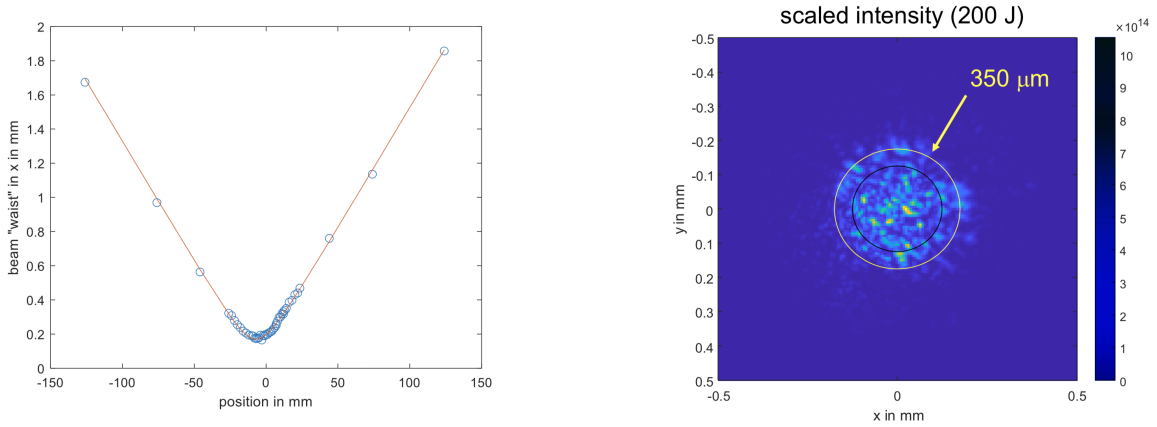

Figure 5.4: Phase plate optimisation for the requested $350\,\mu\mathrm{m}$ focal spot.

A schematic of the PHELIX experimental setup is shown in Figure 5.5. Targets were also produced at (GSI) target department.

Figure 5.5 shows the experimental setup and target configuration. The target consist of $15\,\mu\mathrm{m}$ CH / $5\,\mu\mathrm{m}$ Epoxy / $10\,\mu\mathrm{m}$ Al / $7\,\mu\mathrm{m}$ Epoxy / $100\,\mu\mathrm{m}$ Quartz (with $\mathrm{AR@1054\&527}$ both sides) nominally $500\,\mu\mathrm{m}$ water / $100\,\mu\mathrm{m}$ Quartz (with $\mathrm{AR@1054\&527}$ both sides). The laser first hits the $0.1\,\mu\mathrm{m}$ thick Al layer, which is coated over the CH layer to avoid direct laser shine through. Epoxy was used to glue CH/Al and Al/Quartz interfaces. The CH layer is the actual ablator and the Quartz the pusher layer. The $10\,\mu\mathrm{m}$ Al layer was placed to stop any X-rays from the plasma corona and avoid preheating of the Quartz/Water layers. The VISAR laser had a wavelength of $660\,\mathrm{nm}$ and the associated sensitivities were 1.285 and $4.7\,(\mathrm{km/s/f})$ respectively. Also SOP was looking at the self emission of the shocked target, however here we report only VISAR results and compare with findings on water samples from the GEKKO XII laser facility.

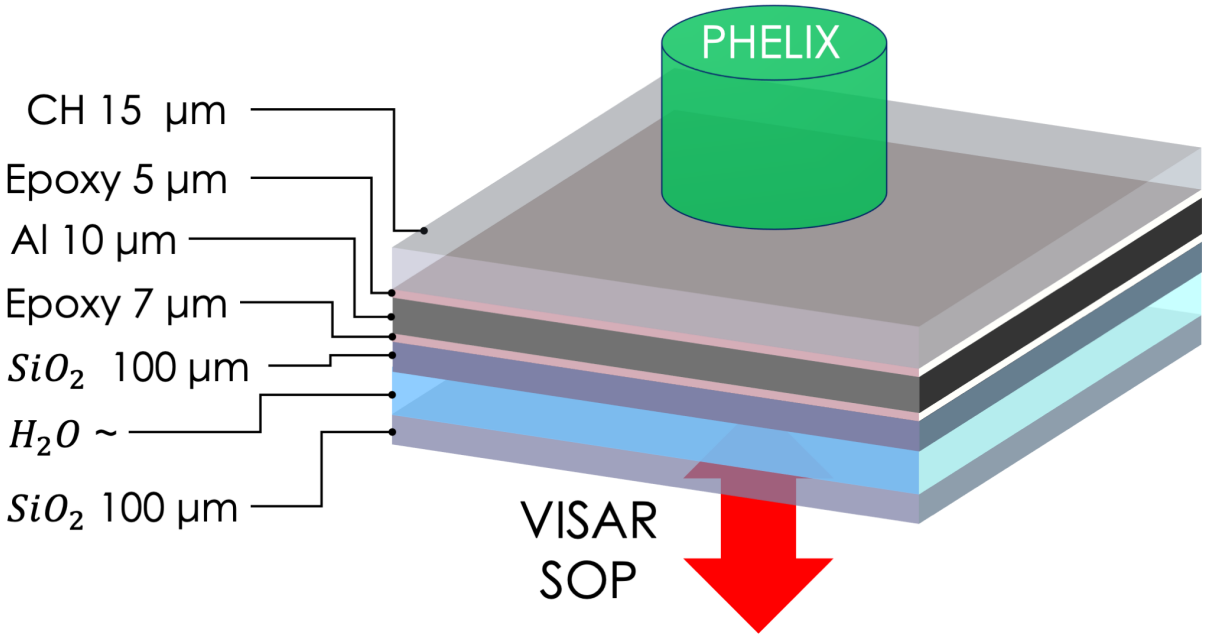

Figure 5.5: Experimental setup: sketch of the multilayered target design at PHELIX laser facility in planar geometry with-its associated thicknesses used in our experiment. Drive laser from top and bottom the VISAR and SOP measure the shock velocity and the self-emission on the rear side.

5.5 Impedance mismatch Method: Single shock data

The impedance-matching method [Zel'dovich and Raizer, 2002, Knudson and Desjarlais, 2013, Brygoo et al., 2015, Marshall et al., 2019] was used to determine the shock state in the water after passing the quartz/water interface, illustrative method is shown in Figure 5.6. Because of the impedance mismatch at the SiO_2/H_2O interface, the shock wave produced a transmitted shock into H_2O and a reflected rarefaction wave propagating back into Quartz. In the rarefaction wave, the shock compressed Quartz undergoes isentropic release until its pressure and particle velocity match those of the shocked water. The IM method requires precise knowledge of the Hugoniot and release behaviour of the standard reference material (Quartz in our case) and the Rankine-Hugoniot (RH) jump relations, which are derived from the

conservation laws, mass, momentum and energy, in order to close the system and derive all the remaining thermodynamic parameters:

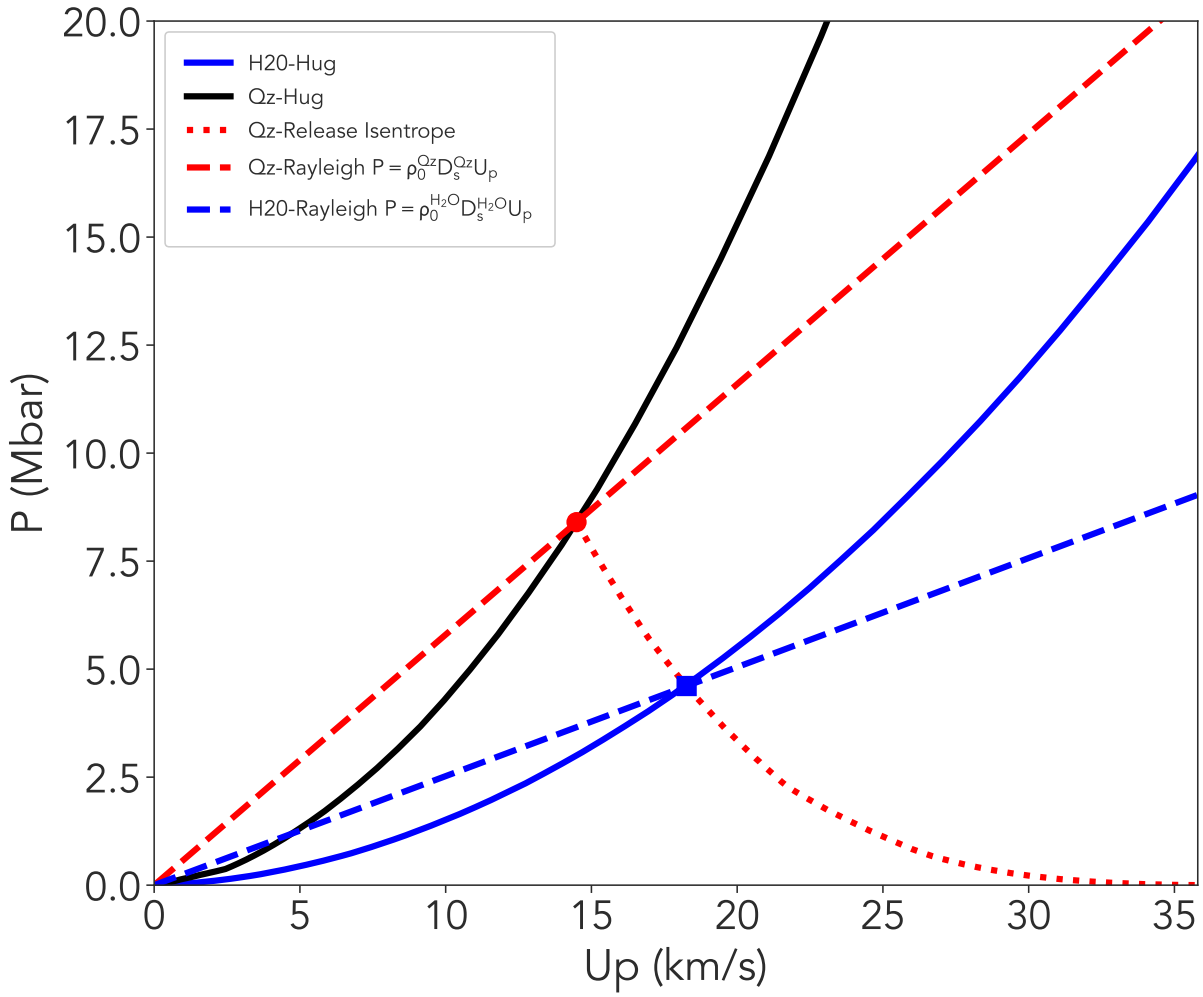

Figure 5.6: $\mathrm{P}-\mathrm{U_p}$ graphical construction of the impedance mismatch procedure for the highest pressure shot of Quartz standard.The shocked state of $\mathrm{H_2O}$ is constrained to lie on the incident Rayleigh line(blue dashed line) defined for $\mathrm{D_s^{Qz}} = 21.8\,\mathrm{km/s}$ for this case. The solid red and dashed lines are the Hugoniot and the Rayleigh line of ($\mathrm{SiO_2}$) respectively, associated with the release curve calculated for the $\mathrm{D_s^{Qz}} = 21.8\,\mathrm{km/s}$. The intersection of the Rayleigh line with the release path blue square determines the IM point and provides (P^{H_2O}, $\mathrm{U_p}^{H_2O}$).

$$\frac{\rho}{\rho_0} = \frac{D_s}{(D_s - U_p)} \tag{5.1}$$

$$P - P_0 = \rho_0 D_s U_p \tag{5.2}$$

$$\varepsilon - \varepsilon_0 = \frac{1}{2}(P + P_0)(\frac{1}{\rho_0} - \frac{1}{\rho}) \tag{5.3}$$

where the ρ, $\mathrm{D_s}$, $\mathrm{U_p}$, P, ε, denote the density, shock velocity, particle velocity, pressure and the internal energy behind the shock. The initial states are denoted with subscript 0. The third equation 5.2 plotted in (P-U) plane gives the so-called Rayleigh line of the material. Figure 5.9 illustrates such method, deriving the shock pressure in water and the particle velocity. The measurement of $\mathrm{D_s^{Qz}}$ determines the shock state ($\mathrm{P^{Qz}}$, $\mathrm{U_p^{Qz}}$). The intersection of the isentropic release of quartz standard with the Rayleigh line of the water sample determines the shock state in water ($\mathrm{P^{H_2O}}$, $\mathrm{U_p^{H_2O}}$).

5.6 Results and Discussion

Figure 5.7 shows a VISAR record where the time zero ($\mathrm{t_0}= 0$) is set to the arrival time of the shock at the $\mathrm{Au/SiO_2}$ interface front side. When the shock front enters into $\mathrm{SiO_2}$ it becomes strongly reflective and its velocity gradually decays. It is indicated in the raw image as $\mathrm{t_0}$. At $\mathrm{t_1}= 7\,21$ ns the shock front strikes the $\mathrm{H_2O}$ layer as shown in Figure 5.7. The transmitted shock in $\mathrm{H_2O}$ becomes also reflective. The shock velocity in $\mathrm{SiO_2}$, used in the impedance mismatch analysis, was obtained by analysing VISAR images first by using shock chronometry i.e the average shock velocity in $\mathrm{SiO_2}$ was given by $\mathrm{D_s^{Qz}}= 100\mu\mathrm{m}/(\mathrm{t_1}-\mathrm{t_0})$. Then the analysis is refined by looking at the displacement of fringe shift and averaging the shock velocities from the two VISAR records taking into account the temporal resolution of the streak camera and the sensitivities of each VISAR. The IM method is applied using the instantaneous value of the shock velocity just before the $\mathrm{t_1}$.

In order to determine $\mathrm{D_s^{H_2O}}$ we instead could rely only on the VISAR images. The

experimental results were compared to a numerical simulation using a one-dimensional radiation hydrodynamics code MULTI [Ramis et al., 1988]. The simulations show that in the present experiment the D_s^{Qz} decays. We observe a decay in the case of $D_s^{H_2O}$. Detailed interpretation of simulations will be shown in section 5.8. Getting Hugoniot points for H_2O requires knowledge of the release isentrope (RI) of SiO_2 from its shocked state. In this work we used a EOS model to calculate the release insentrope for each shock state in SiO_2 utilising an in-house python code coupled with Fortran routines. The IM method provides the Hugoniot state of H_2O as the point where the release isentrope of SiO_2 intersects the Rayleigh line ($P = \rho_0^{H_2O} D_s^{H_2O} U_p$) of water. Such results are shown in the Figure 5.9, with the Hugoniot and the RI of SiO_2 black curve and dotted curves respectively. Solid line denote the Rayleigh lines of SiO_2 and the dashed lines the Rayleigh lines of Water as well with its associated Hugoniot. The Hugoniot curve are derived from SESAME data base [LANL, 1992] and the QEOS [More et al., 1988, Kemp and ter Vehn, 1998], tabulated data 7385 for quartz and 7154 for water. The obtained shocked states of water are compared with other available works and are shown Figure 5.10 in the P-ρ plane and in Figure 5.11 in the P-U_p plane.

Figure 5.9 shows the results of IM analysis in the $P - U_p$ plane.

Facility	Shot ID	D^{Qz} (km/s)	D^{H_2O} (km/s)	$U_p^{H_2O}$ (km/s)	P^{H_2O} (GPa)	ε - ε_0 (kJ/g)	ρ^{H_2O} (gcm^{-3})	$\frac{\rho}{\rho_0}$
GEKKO XII ILE	43045	21.8 ± 0.30	25.78 ± 0.35	18.24 ± 0.25	460.34 ± 21.53	164.44 ± 10.69	3.36 ± 0.16	3.42
	43051	16.13 ± 0.22	18.65 ± 0.25	12.56 ± 0.17	229.83 ± 9.12	78.89 ± 5.13	3.00 ± 0.12	3.06
	43058	14.04 ± 0.19	16.00 ± 0.22	10.46 ± 0.14	164.06 ± 5.96	54.73 ± 3.39	2.83 ± 0.10	2.88
	43063	10.07 ± 0.13	11.61 ± 0.16	7.09 ± 0.09	80.78 ± 2.44	20.98 ± 1.36	2.52 ± 0.07	2.57
PHELIX GSI	S20	8.9 ± 0.12	9.83 ± 0.14	5.43 ± 0.08	52.31 ± 1.28	14.74± 0.96	2.19 ± 0.05	2.23
	S21	18.96 ± 0.26	22.11± 0.31	15.55 ± 0.22	336.93± 15.82	120.9 ± 7.86	3.3 ± 0.16	3.37
	S27	12.91 ± 0.18	14.49 ± 0.20	9.31 ± 0.13	132.20± 4.71	43.34 ± 2.82	2.74 ± 0.1	2.8
	S32	10.87 ± 0.15	12.07 ± 0.17	7.25 ± 0.1	87.76 ± 2.55	26.28± 1.71	2.45 ± 0.07	2.5

Table 5.1: Hugoniot data from impedance mismatch technique with $\alpha - \mathrm{Quartz}$ as a standard. The shock velocity of quartz D^{Qz} and water D^{H_2O} where used in the IM analysis to determine the particle velocity $U_p^{H_2O}$, pressure P_{H_2O} and ρ_{H_2O} on the water Hugoniot. The compressibility $\frac{\rho}{\rho_0}^{H_2O}$was calculated by dividing the ρ^{H_2O} by the initial density. Water target studied at two different high power laser facilities.

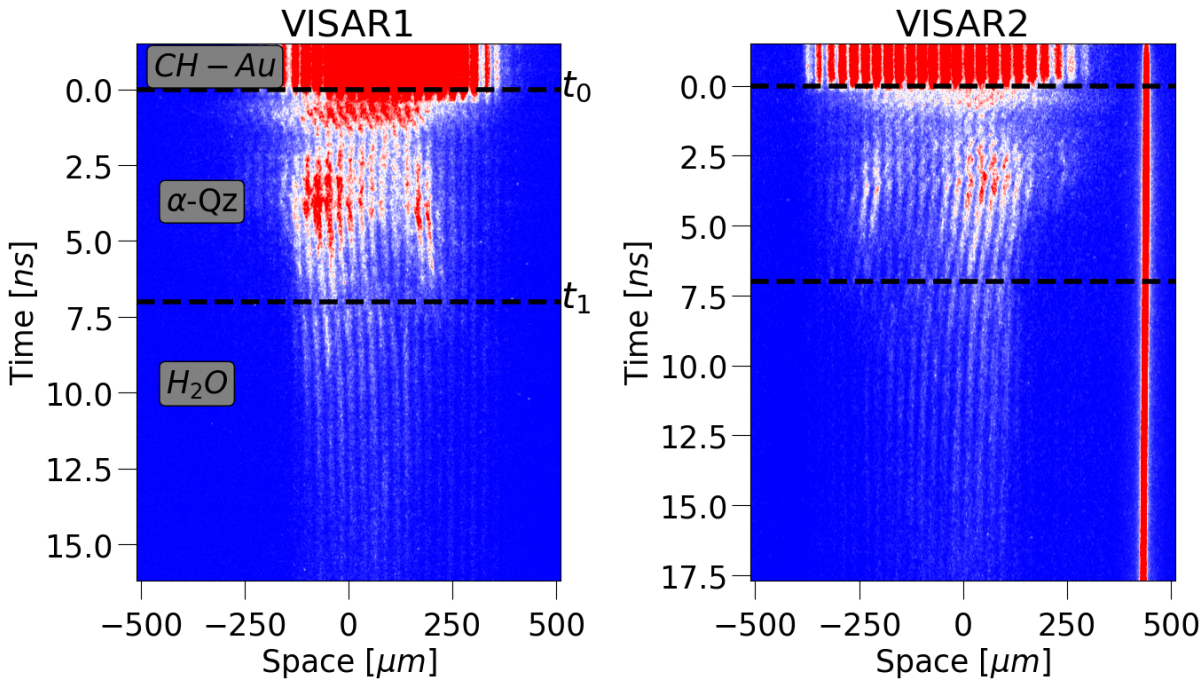

Figure 5.7: Experimentally obtained VISAR images for the shot $\mathrm{SID} - 43058$.

5.7 Temperature Measurement

The shock front emits thermal radiation and in our experiment was collected the SOP [Bossi et al., 1997, Miller et al., 2007]. The absolute spectral radiance of the shock front was measured at a wavelength of $450\,\mathrm{nm}$ with bandwidth $38\,\mathrm{nm}$. Assuming a grey body spectrum, this is given by Planck's black body emissivity ($\epsilon = 1 - R$) corrected for the opacity of the material, which can be calculated using the reflectivity R of the shock front measured by VISARs since the light is either absorbed or reflected. Then

$$I(\lambda, T) = A(\lambda)\frac{2hc^2}{\lambda^5}\frac{1}{e^{hc/\lambda k_B T} - 1} \tag{5.4}$$

The temperate was determined using this formula (where h, c and k_B are Planck's constant, speed of light, and Boltzmann's constants respectively). A(λ) is a parameter taking into account the sensitivity of the streak, the geometry and the collection optics path.

Solving Equation 5.4 with respect to temperature we get:

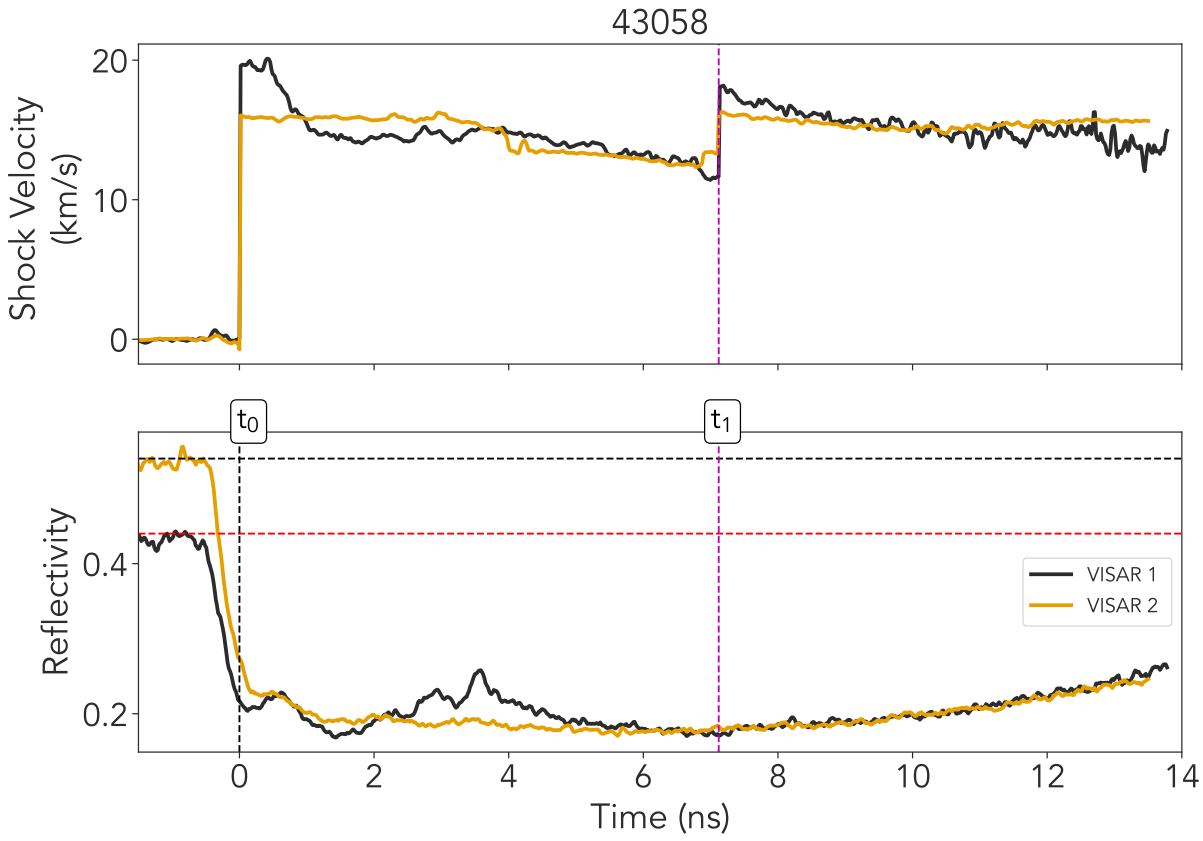

Figure 5.8: (Top) is time history of the shock velocity in both SiO_2 and H_2O extracted from Figure 5.7: (blue) VISAR1, (orange) VISAR2. ($Bottom$) is the reflectivity vs time. This shows a rise after the shock enters the SiO_2 layer due to reverberating wave in SiO_2 (at about $t \approx 3-4$ ns and a second increase at the time were the shock passes the SiO_2 - H_2O interface. Shock velocities are listed in Table 5.1 $SID-43058$.

$$T = \frac{hc}{\lambda k_B \ln\left(\frac{2hc^2 A(\lambda)}{I(\lambda)\lambda^5} + 1\right)} \tag{5.5}$$

SOP calibration has been made in situ using quartz standard (GEKKO XII) [Sano et al., 2011, Guarguaglini et al., 2019]. For the temperature estimation, we used the mean reflectivity of the two VISAR records which were taken simultaneously for each shot. The results of SOP temperature estimation are shown in Figure 5.12 where we report two shots at different laser energy with associated temperature profile in time (Figure 5.12 (A).

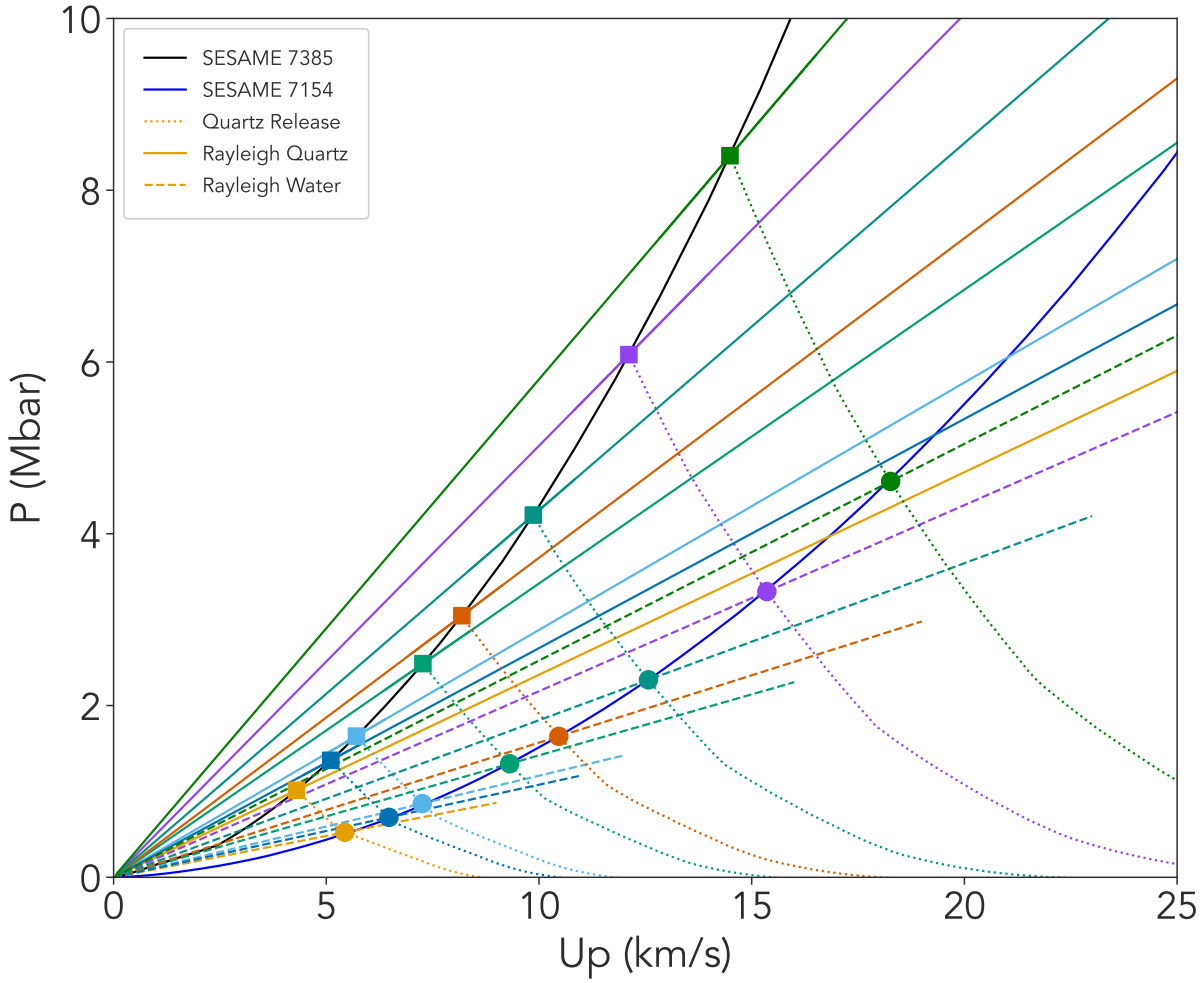

Figure 5.9: Graphical construction of the impedance matching procedure for our 8 shots (4 GEKKO XII at ILE and 4 PHELIX at GSI). Calculated Hugoniot curves are shown in $\mathrm{P}-\mathrm{U_p}$ plane (solid lines) with associated Rayleigh lines, together with calculated isentropic release curves doted (dotted lines), and Rayleigh lines respectively. For a given incident shock velocity $\mathrm{D_s^{Qz}}$, one can determine the incident particle velocity $\mathrm{U_p^{Qz}}$ using a graphic solving method, then for the given $\mathrm{U_p^{Qz}}$ we determine the incident pressure $\mathrm{P^{Qz}}$. In same manner following the release curve until it crosses the water Rayleigh line, one determines the transmitted shock pressure $\mathrm{P(D_{H_2O})}$ and particle velocity $\mathrm{U_p^{H2O}}$.

The pressure as a function of temperature reached at the water layer are shown in Figure 5.13 together with results from Lyzenga et al[Lyzenga et al., 1982] , Kimura et al.[Kimura et al., 2015] and Guarguaglini et al [Guarguaglini et al., 2019] and Hugoniot tabulated curves based on SESAME models (SESAME 7150, 7153, 7154 and P_0 =10 kbar) and Ab-initio Hugoniot from French et al [French et al., 2016].

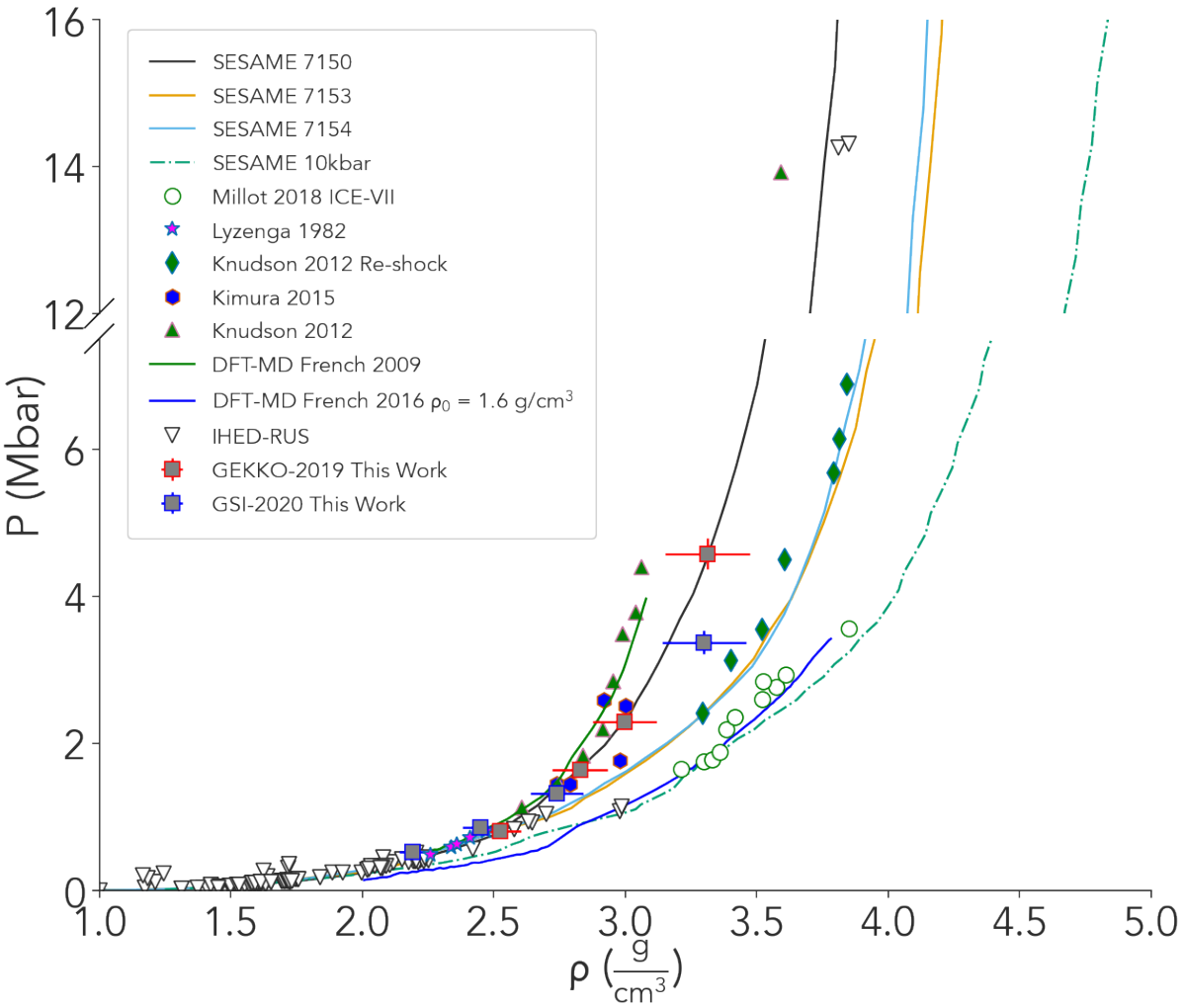

Figure 5.10: Water Hugoniot data in the $P-\rho$ plane. Squared data points: our experimental points. The lines correspond to SESAME (SESAME 7150, 7153, 7154 and P_0 =10 kbar) tabular data are shown Ref. [LANL, 1992]. DFT-MD Hugoniot form French et al [French et al., 2009, French et al., 2016], (diamond) Double shock experiment from Knudson et al. [Knudson et al., 2012], Millot et al. [Millot et al., 2018b, Millot et al., 2019], Lyzenga et al. [Lyzenga et al., 1982] and Kimura et al. [Kimura et al., 2015] and Guarguaglini et al. [Guarguaglini et al., 2019] and Batani et al. [Batani et al., 2015a].

5.8 Hydro Simulations

To interpret our experimental results, we performed 1D radiative hydrodynamic simulations with the code MULTI[Ramis et al., 1988]. The laser pulse was flat top in time

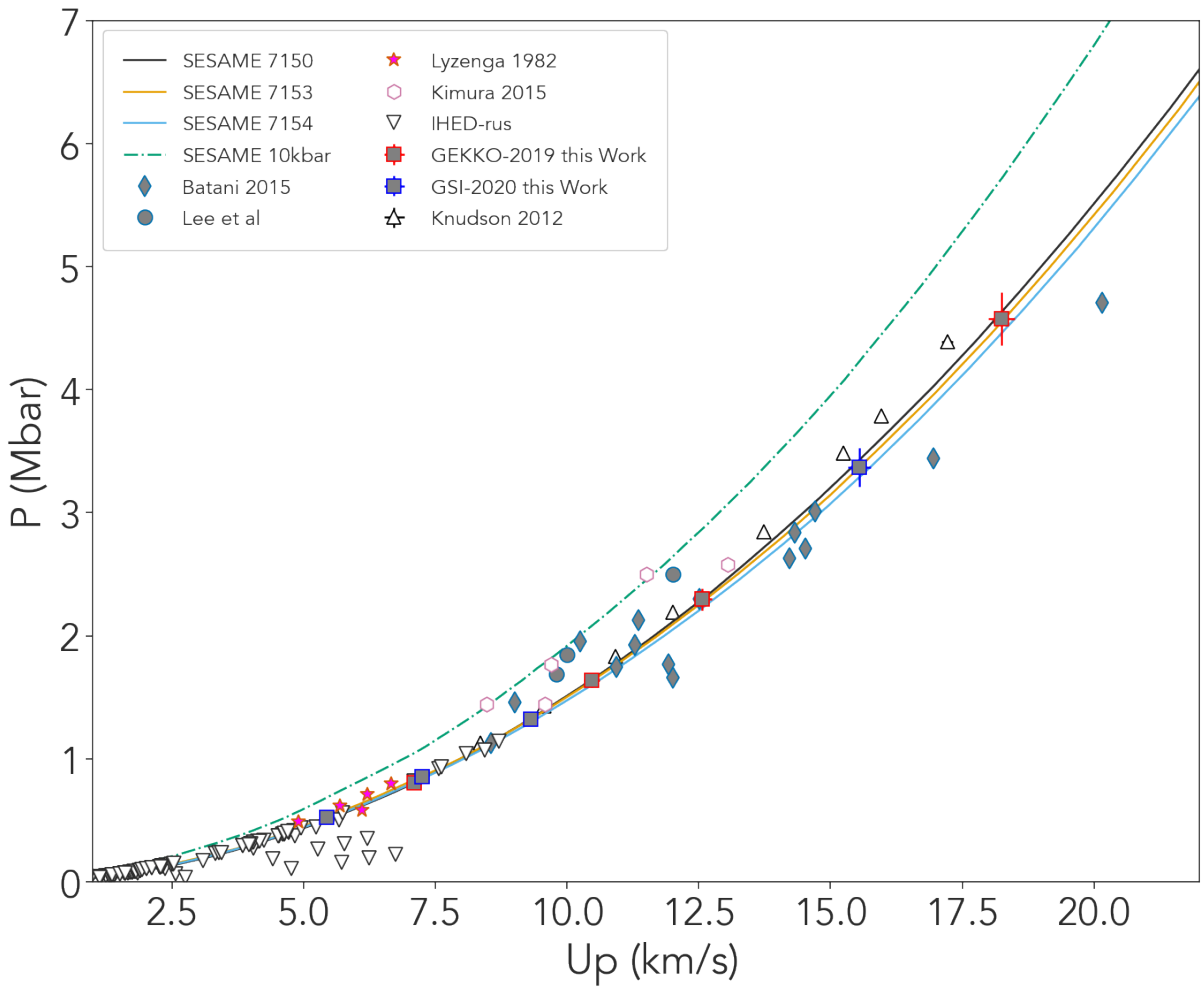

Figure 5.11: Water Hugoniot data in the $\mathrm{P} - \mathrm{Up}$ plane. Our data shown good agreement with the SESAME models available for Water.

with a plateau duration of $2.5\,\mathrm{ns}$ at FWHM and rise and fall times of $0.1\,\mathrm{ns}$. In the simulation we utilised the SESAME tables of the following materials which consist our target SESAME table 7770 for parylene [LANL, 1992], SESAME table 2700 for gold [LANL, 1992], SESAME 7385 for quartz [LANL, 1992] and SESAME table 7150, 7153 and 7154 for water[LANL, 1992]. As for water, we tested different EOS tables coming from the SESAME database[LANL, 1992], from QEOS [More et al., 1988] and FEOS [Faik et al., 2018], in all cases setting the initial density at $\rho_0 = 0.98\ g/cm^3$. Figure 5.14 (A) shows the density map and the pressure map reproducing the shot $\mathrm{SID} : 43058$. Figure 5.14 (B) shows the evolution of the maximum pressure and density, Figure 5.14 (D)

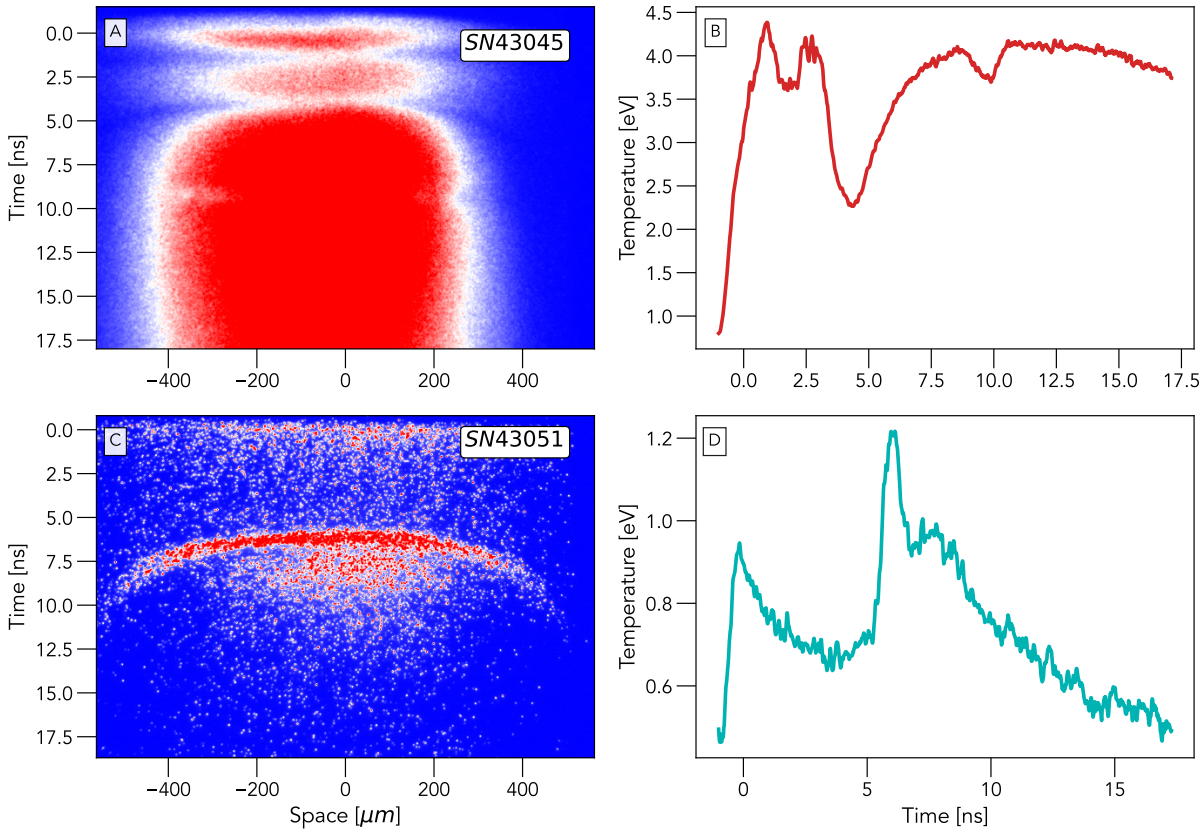

Figure 5.12: (A) SOP result for shot $SN43045$ at laser energy of $1.1\,\mathrm{kJ}$ the highest energy shot obtained at our experiment and (B) temperature estimation taking into account the mean reflectivity of VISAR-1 and VISAR-2. The initial luminosity ($\mathrm{t} \leq 4\mathrm{ns}$ is due to scattered laser light.

the total evolution of pressure along the shock front of the simulated target top figure and the time evolution of the density along the shock front respectively.

The use of 1D simulations in order to interpret our experimental results is justified because the large focal spot ($600\,\mu\mathrm{m}$). In addition, the justification of the 1D approximation comes from two experimental results.

- The VISAR images (see Figure 5.7) show that the shock breakout is quite flat both at metal/SiO_2 and at the SiO_2/H_2O interfaces. Now it is well known that 2D effects will produce a curvature at the shock front, initially affecting the edges of the shock front, but gradually progressing to the centre. The absence of observable curvature in our images suggests indeed that 2D effects in hydrodynamics are

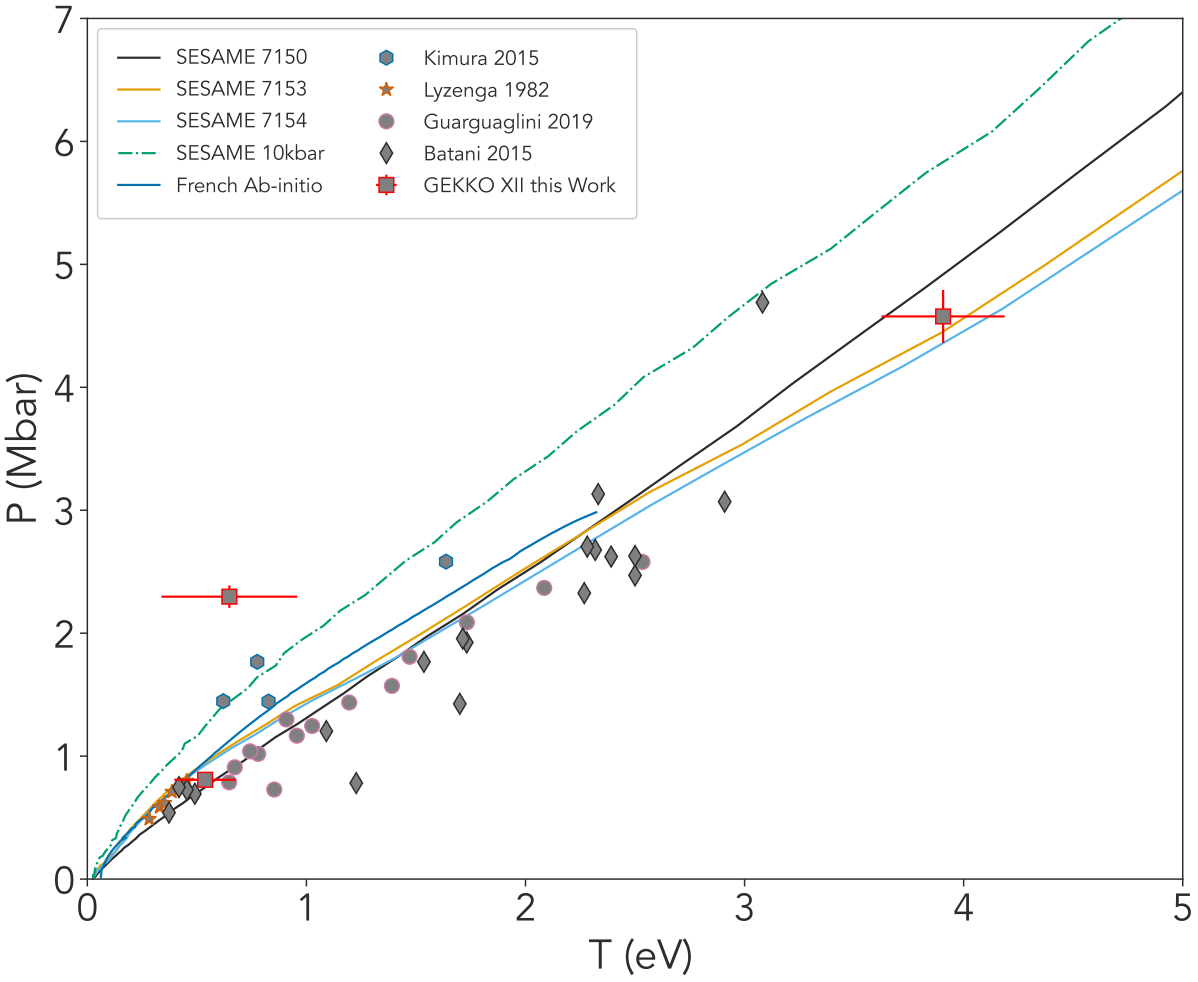

Figure 5.13: Principal Hugoniot data in the P − T plane obtained in this study from the GEKKO XII − ILE laser facility, compared with Lyzenga et al. [Lyzenga et al., 1982] and Kimura et al.[Kimura et al., 2015] and Guarguaglini et al [Guarguaglini et al., 2019] and Batani et al [Batani et al., 2015a]. Also shown SESAME models for for three different tabulated EOS data at slight different initial density.

negligible.

- The velocity of the shock in our case is decaying quite slowly and actually (within error bars) the decay obtained by analysing the VISAR images is compatible with results of 1D simulations. Now the decrease of shock pressure and shock velocity during propagation is due to two phenomena: (a) the relaxation wave from target front side catching up the travelling shock and (b) bi-dimensional effects in

shock front propagation. The fact that the simulations are in fair agreement with experiment considering only the phenomenon (a) is indeed a proof that (b) is not important. If this was the case, we would expect a much faster decay of shock pressure and velocity.

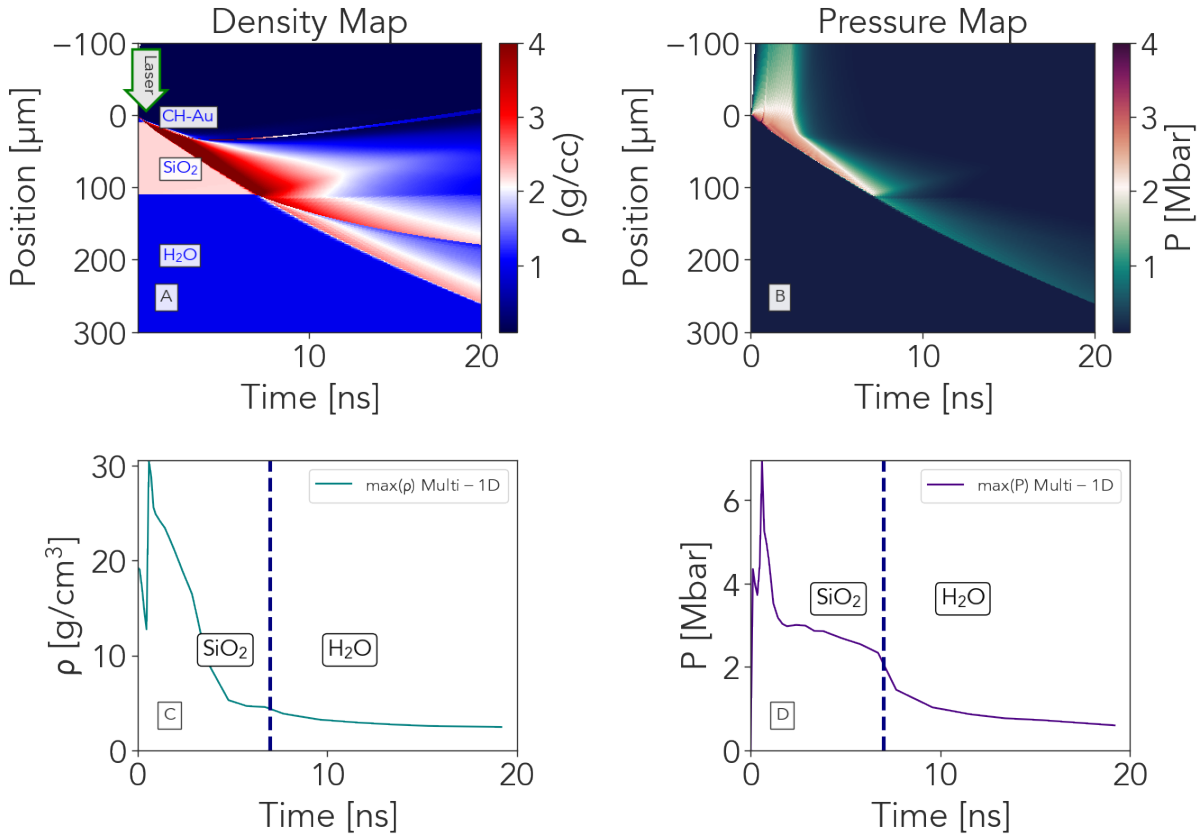

Figure 5.14: (A) Density map of hydrodynamic simulations from MULTI1D reproducing the shot SID : 43058 with nominal laser intensity $1.4\times10^{13}\,\mathrm{W/cm^2}$ for this particular shot 3 beams/12 were used for the main drive delivering a total of 252 J on target. With the above laser parameter the simulation it reproduce well the shock breakout time in SiO_2-H_2O inner interface.(B) Pressure map of the same shot. (C) Time evolution of pressure and density form MULTI simulation for shot SID : 43058. (D) evolution of pressure at shock front (D) evolution of density at the shock front respectively, up to the maximum simulation time.

5.9 Conclusions and perspectives

In summary, we obtained EOS data of Water along the principal Hugoniot up to $5\,\mathrm{Mbar}$. Water samples, contained within a multilayered water cell, were dynamically compressed in planar geometry using the high power laser facilities GEKKO XII (ILE) and PHELIX (GSI). Utilizing quartz as a standard material in both experimental campaigns and the main diagnostics such as VISAR/SOP, substantially reduced experimental errors in optimized experimental conditions. The impedance mismatching analysis allowed to verify that the $P, \rho, (\varepsilon - \varepsilon_0)$ the Hugoniot data are in fair agreement with those predicted by the SESAME table 7150 and on the contrary show a significant difference concerning the Hugoniot curve calculated using DFT-MD simulations. Also, our experimental outcome showed good agreement with simulations performed with the radiation hydrodynamic code MULTI 1D using the SESAME tabulated EOS, the QEOS model, and the FEOS [Faik et al., 2018] model, a modified version of QEOS [Kemp and ter Vehn, 1998]. The agreement with 1D simulations shows indeed that, in our experimental set-up, 2D effects in hydrodynamics are negligible, a result which mainly depends on the use of laser focal spots. For a few shots, we could also measure the temperature of shocked material using calibrated SOP diagnostics. Our data confirm previous experimental results and show that in the pressure range up to $4.6\,\mathrm{Mbar}$ water is in a reflective state.

Part III

Ab-initio calculation and HRR laser facilities

Chapter 6

Ab-initio calculation on LiH single crystal system

Contents

6.1 Introduction

Among the alkali metal hydrides, LiH [Montgomery, 1973, Kundrata et al., 2019] has the highest hydrogen mass content and has, therefore, been widely studied

as a potential hydrogen storage material [Li et al., 2011, Napán and y Blancá, 2012, Reshak, 2013, Banger et al., 2018], particularly in the aviation field and nuclear industry [George and Saxena, 2010]. Also, LiH is a potential candidate for space shielding applications. LiH remains theoretically the most efficient neutron shield material per unit mass, and, with sufficient testing and development, could be an optimal material choice for future flights.

The recent report of metallization in solid hydrogen at 495 GPa [Mao and Hemley, 1994, Dias and Silvera, 2017, Dalladay-Simpson P., 2016, McMahon et al., 2012, Wigner and Huntington, 1935, Gregoryanz et al., 2020, Lei et al., 2021] has renewed interest in the high-pressure physics of hydrides. In addition, LiH offers a perfect system to study the crossover between quantum and classical effects using available Density Functional Theory (DFT) codes and variational Monte Carlo simulations [Boronat et al., 2004]. LiH is expected to metallize at lower pressures than hydrogen, and is therefore a potential candidate for high-temperature superconductivity. Its large zero-point energy (ZPE), the vibrational contribution to the energy at zero temperature, indicates that quantum effects play an important role in determining its properties [Roma et al., 1996].

At ambient conditions, LiH crystallises in the so called B1 phase, with a (NaCl crystal structure Fm-3m(225)), like all other alkali hydrides, and it is a large-gap insulator, with a gap of $4.9\,\mathrm{eV}$ [Kondo and Asaumi, 1988, van Setten et al., 2007]. Under pressure, other alkali hydrides undergo a structural phase transition from B1 to B2 (CsCl structure Pm-3m(221)), with transition pressures decreasing with increasing mass of the alkali atom. The transition pressure varies from $29.3\,\mathrm{GPa}$ in NaH, to $0.83\,\mathrm{GPa}$ in CsH [Sun et al., 2012, Zhang et al., 2007, Jaradat et al., 2017]. However, in the case of LiH the B2 phase has not yet been found experimentally at room temperature. The B1 phase of LiH has been reported to be stable up to a pressure of $252\,\mathrm{GPa}$, at $300\,\mathrm{K}$, in the diamond-anvil cell (DAC) experiment of Lazicki et al. [Lazicki et al., 2012]. First-principles calculations at zero-temperature predict a B1-B2 transition at pressures between 313 and 340 GPa [Biswas et al., 2019], depending on the approximations. The-

ory also predicts that LiH-B1 is an insulator up to the transition pressure, and becomes a metal upon transforming into B2. Using Møller-Plesset perturbation and coupled cluster theories [Møller and Plesset, 1934], Andreas Grüneis predicted transition pressure to be between $330\,\mathrm{GPa}$ and $350\,\mathrm{GPa}$ using quantum chemical wave function based methods and the frozen core approximation [Grüneis, 2015].

Experimental evidence on the other hand for a B1-B2 phase transition at high temperature has been reported recently by Molodets et al., [Molodets et al., 2014] based on multiple shock compression experiments as can be shown from the phase diagram in Figure 6.1. They observed the appearance of finite electrical conductivity above $120\,\mathrm{GPa}$ and $1800\,\mathrm{K}$, and showed, based on a semi-empirical theoretical model for the free energy of the two phases, that the experimental finding is consistent with the occurrence of a transition from B1 to B2 at $120\,\mathrm{GPa}$ and $1800\,\mathrm{K}$. The temperature effects do ot seed to alter significantly the transition pressures, so that the experimental claim obtained with shock waves remains mysterious [Biswas et al., 2019].

To address this puzzling problem in addition to static DFT calculations of B1-B2 phases we have done extensive random crystal structure prediction of LiH system using CALYPSO code based on Particle Swarm Optimisation algorithms [Wang et al., 2010, Wang et al., 2012, Shi et al., 2001, Lu, 2002, Parsopoulos and Vrahatis, 2002], at 100, 250, 300 and 350 GPa pressures and search for potential metallic structures better than the B2. Details are given in Section 6.3.

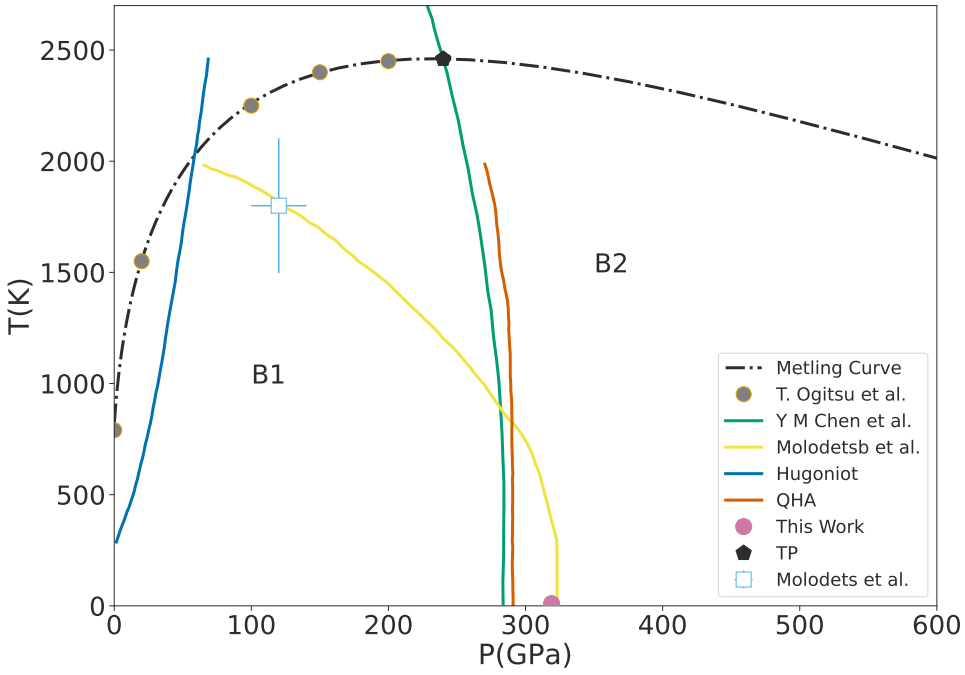

Figure 6.1: B1 - B2 phase diagram. doted line is fit on T. Ogitsu two-phase co-existent study, T.Ogitsu et al[Ogitsu et al., 2003] two phase coexistence, Y M Chen et al[Chen et al., 2016] phase boundary B1-B2, star symbol experimental point from Molodets et al.[Molodets et al., 2014] and the suggested boundary line (yellow curve), blue line is Hugoniot curve[Chen et al., 2016], orange line suggested boundary line from QHA calculations [Biswas et al., 2019], and the pink point is obtained from the B1-B2 phase calculation this work.

6.2 Computational Details

The electronic structure calculations are performed using *ab initio* DFT plane-wave pseudo-potential code ESPRESSO package[Giannozzi et al., 2009, Giannozzi et al., 2017, Giannozzi et al., 2020]. We used the projector augmented wave method in order to treat the electron−ion interactions[Blöchl, 1994]. The exchange−correlation functional was approximated by generalized gradient approximation (GGA) of the Perdew−Burke−Ernzerhof form [Perdew et al., 1996]. A plane−wave basis set was used to expand the electronic wave functions. The cutoff for the basis set and the cutoff for the corresponding charge densities were set at 70 and 700 Ry for the plane wave expansion, respectively. Note that both the core

and the valence electrons of Li are taken into consideration. For both primitive cells, Monkhorst−Pack [Monkhorst and Pack, 1976] grids of size $17 \times 17 \times 17$ were used to generate the k mesh (zone centered) for the corresponding Brillouin−zone sampling. The Methfessel−Paxton smearing technique [Methfessel and Paxton, 1989] was used with a smearing width equal to $0.05\,\mathrm{Ry}$ for metallic systems.

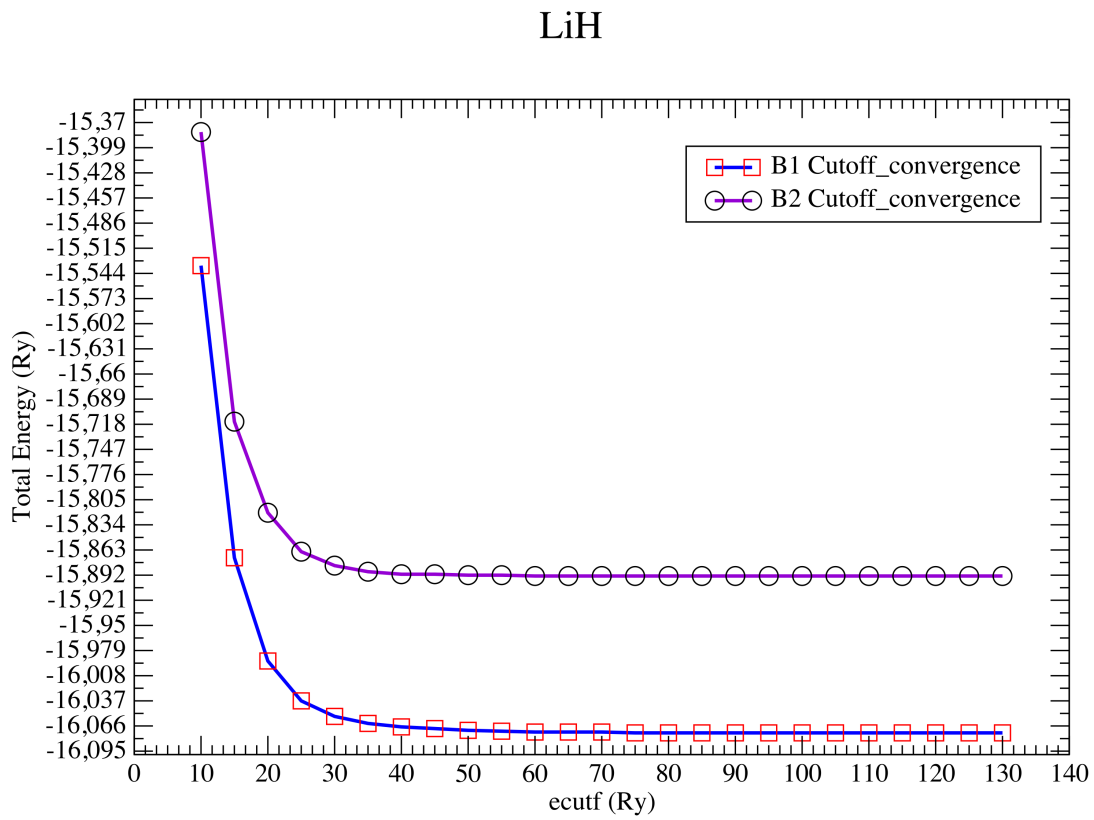

Figure 6.2: Cutoff energy convergence calculation for the B1 and B2 phases of LiH as a function of total energy.

All subsequent calculations were performed using pseudo-potential *Li.pbe-s-rrkjus_psl.0.2.1.UPF* for Li and *H.pbe-rrkjus.UPF* for H. obtained from the QE website *https://www.quantum-espresso.org/pseudopotentials*. To calculate the phase transition is necessary to evaluate the enthalpy as a function of pressure. Therefore it is necessary

to evaluate the total energy for different unit cell volume for both phases B1 and B2. For both crystal structures the total energy was evaluated for a range of different volumes by repeatedly calling the *pw.x* with different lattice constants, such results are shown in Figure 6.3. Then the enthalpy was calculated for the range of pressure 0-1000 GPa, and plotted in Figure 6.4.

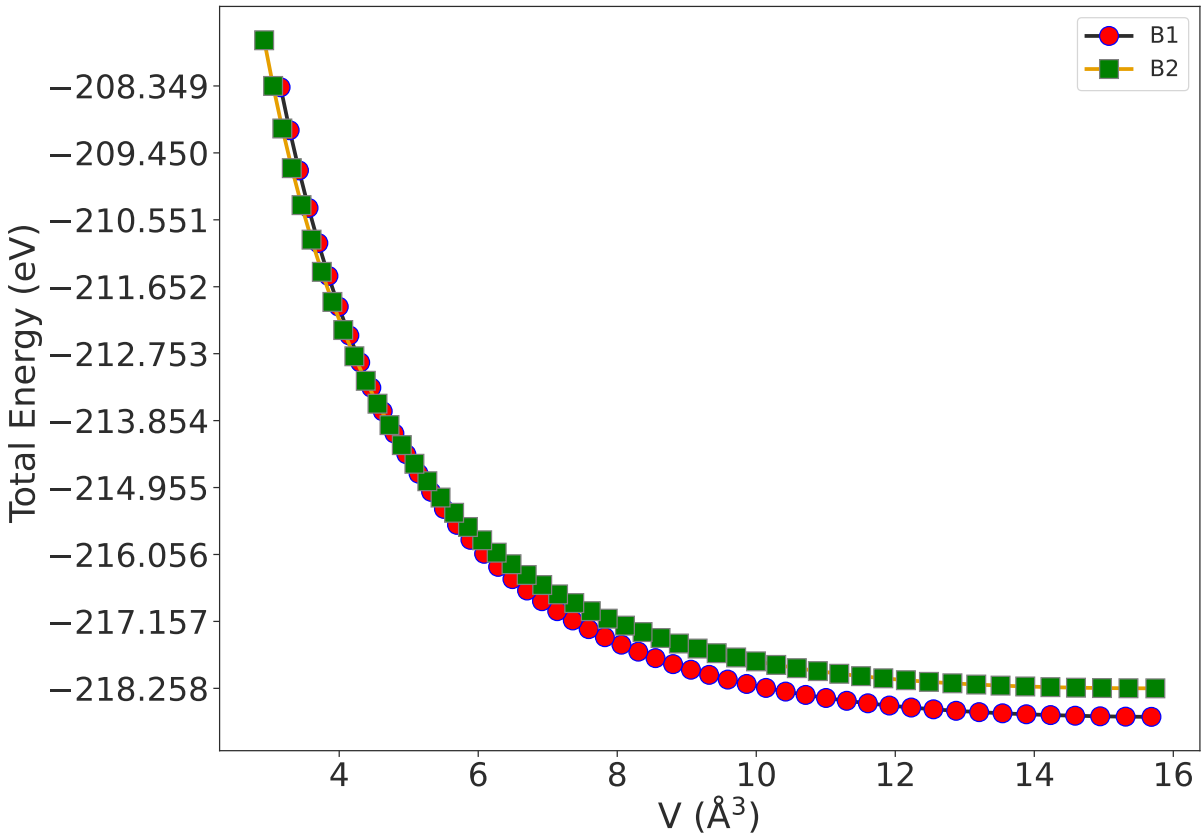

Figure 6.3: Total energy calculation of the B1 and B2 phase of LiH.

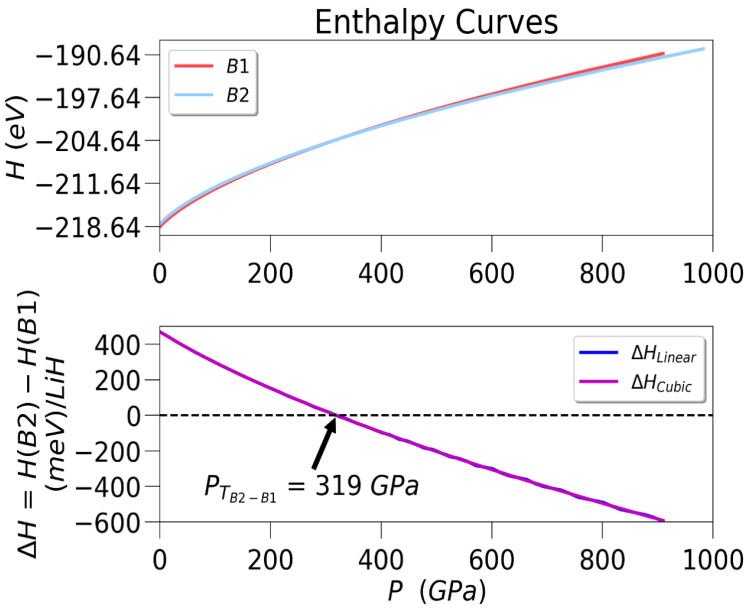

Figure 6.4: (*Top*) Enthalpy curves for the B1 and B2 phases (NaCl(Fm-3m space group number 225) and CsCl(Pm-3m, space group number 221)) and (*Bottom*) the enthalpy difference of the B1 and B2, where we can find the transition pressure at $319\,\mathrm{GPa}$. The enthalpies are fitted with linear and cubic splines, yielding the same result.

6.2.1 Metal-Insulator Transition and experimental challenges

The structural properties of LiH in the *B1* and the *B2* phases have been determined by fitting the calculated total energies as a function of volume to different EOS models: Murnaghan equation of state[Murnaghan, 1944], Birch-Murnaghan[Birch, 1947] and the Vinet[Vinet et al., 1987].

Bulk modulus B_0 is key mechanical parameter for selection and design of materials. This property is frequently used to benchmark DFT electronic structure methods. Bulk modulus provides info about the microscopic features of the material, also is a measure of the ability of material in resisting changes in volume under uniform compression or expansion. Using the equilibrium volume V_0 the bulk modulus B_0 of a crystal can be

defined as follows:

$$B_0 = -V\left(\frac{\partial P}{\partial V}\right)_P \tag{6.1}$$

A dimensionless parameter $B_0^{'}$ can then be defined as its first derivative with respect to the pressure, at constant temperature T:

$$B_0' = -V\left(\frac{\partial B_0}{\partial P}\right)_T \tag{6.2}$$

Let us recall that the pressure P may be written as a function of volume V as:

$$P(V) = -\left(\frac{\partial E}{\partial V}\right)_S \tag{6.3}$$

We can redefine the bulk modulus in equation 6.1 as the second energy derivative with respect to the volume:

$$B(V) = \frac{1}{V}\left(\frac{\partial^2 E}{\partial V^2}\right)_{T,S} \tag{6.4}$$

The enthalpy H (coinciding with Gibbs' free energy G at T=0 K, the standard temperature of ab initio calculations) as a function of volume V simply as:

$$H(V) = E(V) + P(V) \times V \tag{6.5}$$

The Equation of State is a pressure-volume or energy-volume relation describing the behavior of a solid under compression or expansion. In 1944, Murnaghan [Murnaghan, 1944] proposed his famous equation of state which is based on the assumption that the bulk modulus varies linearly with pressure:

$$E(V) = E_0 + \frac{B_0 V}{B_0'}\left[\left(\frac{V_0}{V}\right)^{B_0'}\frac{1}{B_0'-1} + 1\right] - \frac{B_0 V_0}{B_0'-1} \tag{6.6}$$

where V_0 and E_0 are the equilibrium volume and energy, at zero pressure. In the P(V) form Murnaghan's EOS becomes:

$$P(V) = \frac{B_0}{B_0'}\left[\left(\frac{V_0}{V}\right)^{B_0'} - 1\right] \tag{6.7}$$

The third-order Birch-Murnaghan [Birch, 1947] isothermal equation of state (based on the Eulerian strain), published in 1947, reads like:

$$E(V) = E_0 + \frac{9V_0B_0}{16}\{\left[\left(\frac{V_0}{V}\right)^{2/3} - 1\right]^3 B_0' + \left[\left(\frac{V_0}{V}\right)^{2/3} - 1\right]^2\left[6 - 4\left(\frac{V_0}{V}\right)^{2/3}\right]\} \tag{6.8}$$

and the $P(V)$ function becomes if we differentiate the previous formula:

$$P(V) = \frac{3B_0}{2}\left[\left(\frac{V_0}{V}\right)^{7/3} - \left(\frac{V_0}{V}\right)^{5/3}\right]\left(1 + \frac{3}{4}(B_0' - 4)\left[\left(\frac{V_0}{V}\right)^{2/3} - 1\right]\right) \tag{6.9}$$

The Vinet equation was shown by Stacey to be equivalent in formulation to the Rydberg potential:

$$E = D(\alpha r + 1)e^{-\alpha r} \tag{6.10}$$

Which therefore can be written in the energy-volume form as follows:

$$E(V) = E_0 + \frac{2B_0V_0}{(B_0' - 1)^2}\left(2 - (5 + 3B_0'(\eta - 1) - 3\eta\right)e^{-3(B_0'-1)(\eta-1)/2)} \tag{6.11}$$

In the P(V) form:

$$P(V) = 3B_0\left(\frac{V}{V_0}\right)^{-2/3}\left[1 - \left(\frac{V}{V_0}\right)^{1/3}\right] exp\left[\frac{3}{2}(B_0' - 1)\left(1 - \left(\frac{V}{V_0}\right)^{1/3}\right)\right] \tag{6.12}$$

Python tools can be used to fit the $\mathrm{E(V)}$ curve and determine the equilibrium properties and the pressure dependence of the mechanical properties of the crystal. These calculations are typically based on the *static model*, in which the entropy terms and the vibrational zero-point energy are ignored results are shown in Figure 6.5 for the B1 and B2 structures. Also Figure 6.6 we compare the B1 and B2 pressure volume calculation with available experimental data from static compression DAC from Loubeyre et al. [Loubeyre et al., 1998], A. Lazicki et al.[Lazicki et al., 2012]. It is worth mentioning that for given pressure we are overestimating the volume at high pressures. The reason arises from the exchange-correlation functional and in our case we are using *PBE* functional which tends to overestimate volume. We note that the static transition that we evaluated for the B1 and B2 phase was calculated over the pressure range of $0\text{-}900\,\mathrm{GPa}$.

Comparison of the equilibrium parameters fitted with three different EOS models for the B1 and B2 phases are summarised in Table 6.1, and compared with experimental results.

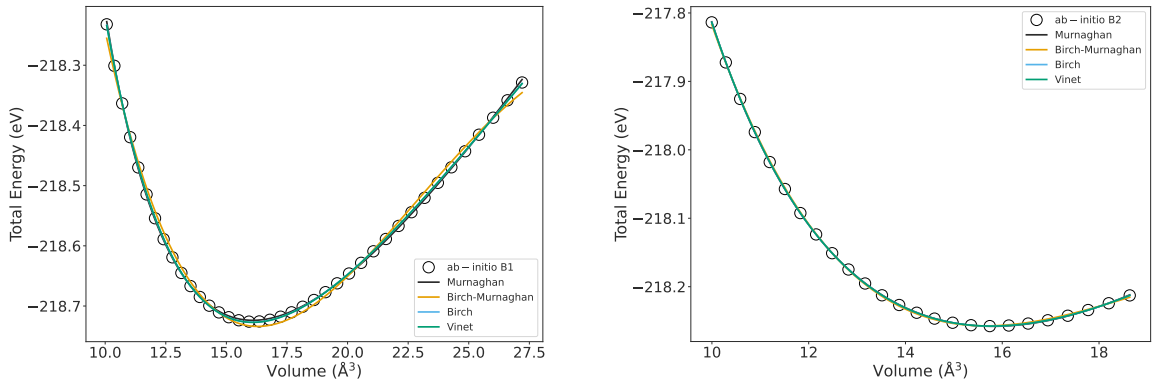

a B1 b B2

Figure 6.5: Total energy versus volume: (a) determination of the equilibrium parameters for the B1 phase fitted with different models [Latimer et al., 2018], (b) similarly for the B2 phase.

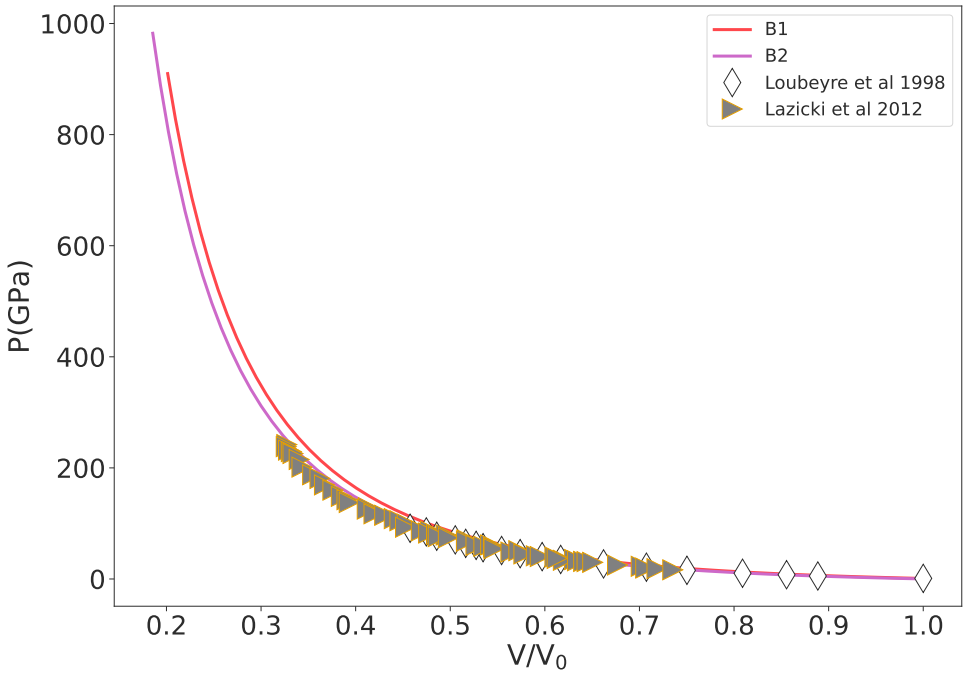

Figure 6.6: DFT calculations of the B1 and B2 phases of LiH P-V curves compared with experimental results from Loubeyre et al. [Loubeyre et al., 1998], A. Lazicki et al.[Lazicki et al., 2012].

	Murnaghan				Birch-Murnagan				Vinet			
	E_0 (eV)	V (Å^3)	B_0 (GPa)	$B_0^{'}$	E_0 (eV)	V (Å^3)	B_0 (GPa)	$B_0^{'}$	E_0 (eV)	V (Å^3)	B_0 (GPa)	$B_0^{'}$
B1	-218.723787	16.092241	34.3	3.34	-218.733896	16.287809	41.4	1.51	-218.727170	16.090000	36.9	3.32
B2	-218.257894	15.805450	35.9	2.91	-218.257257	15.661049	36.3	1	-218.257580	15.776821	35.5	3.41
Expt. [a,b,c]	-	-	36.5	3.63	-	-	-	-	-	-	34.24,36.3	3.80±0.15, 3.32

[a] Reference [Vidal and Vidal-Valat, 1986]
[b] Reference [Gerlich and Smith, 1974]
[c] Reference [Yu et al., 2007, Dammak et al., 2012]

Table 6.1: Results of static calculations without taking into account the zero point motion for LiH: E_0, V_0, bulk modulus B_0 and pressure derivative $B_0^{'}$ of bulk modulus. We also specify the type of equation of state (EOS) used for fitting the numerical data and compared with available experimental results.

6.3 Crystal structure prediction using DFT codes

We searched for high-pressure structures of lithium hydrides using the particle swarm optimization methodology as implemented in the CALYPSO code[Wang et al., 2010, Wang et al., 2012]. In CALYPSO code the methodology for crystal structure prediction is based on particle-swarm optimisation (PSO) method within the evolutionary scheme[Wang et al., 2012] as proposed by Kennedy and Eberhart in mid 1990[Kennedy and Eberhart, 1995, Eberhart and Kennedy, 1995]. The global minimization method in CALYPSO code for predicting crystal structures is implemented in four steps

1. generation of random structures with the constraint of symmetry
2. locally structural optimization
3. post-processing for the identification of unique local minima by geometrical structure parameter
4. generation of new structures by PSO for iteration

The crystal structure with unit cell having N atoms, can be modelled by $3N + 3$(3 unit cell vectors' length, 3 unit cell angles and $3N - 3$ atomic coordinates) variables. Due to the fact that the potential energy surface is not known, the goal of the algorithm is to find a global minimum by comparing the free energies of

the local minima. Nevertheless, due to exponential increase of minima with N, force approach is applied for simple systems. This approach is unbiased to any prior known structure information and has shown good efficiency in predicting high-pressure structures of hydrogen-rich compounds [Zurek et al., 2009] and other novel materials[Oganov et al., 2019]. The size of the system in our structure searches contains 1, 4 and 8 formula units per simulation cell. Each search generation contains 30 structures and the structure searching simulation is usually stopped after generating 300-900 structures. The underlying ab-initio total energy calculations and structural relaxations are carried out using the plane-wave basis and projector-augmented-wave (PAW) method as implemented in the Quantum ESPRESSO ab-initio simulation package [Giannozzi et al., 2009, Giannozzi et al., 2017, Giannozzi et al., 2020]. The use of cutoff energy of 70 Ry and the cutoff for the density was set at $700\,\mathrm{Ry}$ for the plane wave expansion as shown in Figure 6.2 and dense enough k-point sampling grids give good convergence of the calculated enthalpy. We perform structure searches for LiH at pressures of 100, 200, 300 and $350\,\mathrm{GPa}$ for each formula unit. Thermodynamic stability of the LiH compounds under various pressures are then studied by calculating the formation enthalpy (Δ H) and compared with the static calculation of the B1 phase $Fm\bar{3}m$.

6.3.1 100 GPa all f.u. optimisations

Table 6.2 we summarize high pressure crystal structure prediction of LiH ranked with respect to the lowest enthalpy structure analysed with four different tolerance threshold for symmetry analyses of given structure. We have excluded structures labeled with the same space group, we keep always the one with the lowest enthalpy. In Table 6.2 we have combined the structures that are found at the same target pressure from higher formula units (4 and 8) system. One can observe the evolution of the structures that are found with the best being the insulating structure B1 with space group $\mathrm{Fm}-3\mathrm{m}(225)$ in all space group tolerance analysis which is in agreement with theoretical calculations. Although three more insulating structures are followed to have the same trend, with the latest insulating structure transitioning from $\mathrm{P}-1(2)$ with $\mathrm{SG}-0\,05$ to $\mathrm{C}2/\mathrm{m}(12)$ for higher tolerance analysis. Concluding in Figure 6.7 we present the six best ranked optimised structures with the lowest enthalpy difference and the type of the structure which is either metallic or insulating by looking at the DOS calculation and the crystal structure file of the optimised structure. The best structures exhibit insulating features as shown from the DOS calculation. Figure 6.8 shows the two next metallic structures the first being recognised as the $\mathrm{Pm}-3\mathrm{m}$ in agreement with the DFT calculations and $\mathrm{P}-6\mathrm{m}2$ respectively with SG-0.3. Finally Figure 6.9 shows the ranking of the optimised structures with respect to the highest space group tolerance (SG-0.3) for symmetry analyses for given structures. The reduced table after filtering resulted in 10 insulating structures and 8 metallic. For simplicity we show the first six high pressure structures 4 insulating and 2 metallic the rest of the Figures will be shown in the Annexe section always the ones that are ranked as best ones with the lowest enthalpy.

f.u.	Gen.	Con.	E (eV/f.u.)	V (Å^3/f.u.)	P (GPa)	H (eV/f.u.)	ΔH (meV/f.u.)	SG-0.05 (Å)	SG-0.10(Å)	SG-0.20(Å)	SG-0.30(Å)	DOS	H_{B1} (eV/f.u.)
1	32	4	-217.200661	7.457754	99.93769	-212.548797	1.097334	$Fm-3m(225)$	$Fm-3m(225)$	$Fm-3m(225)$	$Fm-3m(225)$	Insulator	-212.549894
8	12	6	-217.123677	7.459411	100.091562	-212.463616	86.278334	$P6_3/mmc(194)$	$P6_3/mmc(194)$	$P6_3/mmc(194)$	$P6_3/mmc(194)$	Insulator	
8	4	3	-217.120377	7.453211	100.322566	-212.453443	96.451334	$R-3m(166)$	$R-3m(166)$	$R-3m(166)$	$R-3m(166)$	Insulator	
8	12	1	-217.005696	7.476224	100.238128	-212.328293	221.601334	$P-1(2)$	$C2/m(12)$	$C2/m(12)$	$C2/m(12)$	Insulator	
1	28	8	-216.750766	7.211021	99.95701	-212.251935	297.959334	$Cmmm(65)$	$Cmmm(65)$	$Cmmm(65)$	$Pm-3m(221)$	Metal	
1	26	2	-216.898529	7.47395	99.974467	-212.234847	315.047334	$P-6m2(187)$	$P-6m2(187)$	$P-6m2(187)$	$P-6m2(187)$	Metal	
8	8	1	-216.927297	7.506587	100.330951	-212.226548	323.346334	$P1(1)$	$P-1(2)$	$P-1(2)$	$P-1(2)$	Insulator	
8	13	3	-216.836488	7.443117	99.995503	-212.191069	358.825334	$P1(1)$	$P1(1)$	$P1(1)$	$P1(1)$	Insulator	
1	22	10	-216.714637	7.169591	102.498348	-212.127931	421.963334	$Cmmm(65)$	$Cmmm(65)$	$Cmmm(65)$	$Cmmm(650)$	Metal	
8	4	6	-216.787073	7.802667	99.98903	-211.917565	632.329334	$I4_1cd(110)$	$I4_1cd(110)$	$I4_1cd(110)$	$I4_1cd(110)$	Insulator	
4	9	2	-216.69271	7.70194	100.069398	-211.882201	667.693334	$I4/mmm(139)$	$I4/mmm(139)$	$I4/mmm(139)$	$I4/mmm(139)$	Insulator	
4	7	1	-216.591522	7.95564	100.108234	-211.620628	929.266334	$I4/m(87)$	$I4/m(87)$	$I4/m(87)$	$I4/m(87)$	Insulator	
1	27	9	-216.223456	7.946603	100.155112	-211.255883	1294.011334	$P4/mmm(123)$	$P4/mmm(123)$	$P4/mmm(123)$	$P4/mmm(123)$	Metal	
8	13	9	-216.406233	8.449061	99.987265	-211.133415	1416.479334	$I4cm(108)$	$I4cm(108)$	$I4cm(108)$	$I4cm(108)$	Insulator	
4	3	10	-216.291699	8.363081	99.973878	-211.073239	1476.655334	$P4_2/mnm(136)$	$P4_2/mnm(136)$	$P4_2/mnm(136)$	$P4_2/mnm(136)$	Metal	
8	4	2	-215.831893	7.762714	99.978389	-210.987834	1562.060334	$I4/mcm(140)$	$I4/mcm(140)$	$I4/mcm(140)$	$I4/mcm(140)$	Metal	
8	7	3	-215.799383	7.913373	99.984323	-210.861018	1688.876334	$Fmmm(69)$	$Fmmm(69)$	$Fmmm(69)$	$Fmmm(69)$	Metal	
4	1	10	-215.727692	7.872	100.051991	-210.811821	1738.073334	$P6/mmm(191)$	$P6/mmm(191)$	$P6/mmm(191)$	$P6/mmm(191)$	Metal	

Table 6.2: Crystal structure prediction of LiH system for three different formula units (1, 4, and 8) at target pressure of 100 GPa, repeated structures are filtered out: f.u. stands for formula unit, Gen. for generation, Con. for configuration, E is the total energy of the optimized structure, V is the volume of the structure, H is the minimum enthalpy, ΔH is the enthalpy difference with respect to H_{B1} static calculation, $SG-\#$ stands for space group tolerance parameter for space group recognition for each optimised calculation for four different tolerance values (0.05, 0.10, 0.20 and 0.30 Å), Density of State (DOS) classification (Metal/Insulator) and the H_{B1} is the enthalpy B1 phase from the static calculation in (eV).

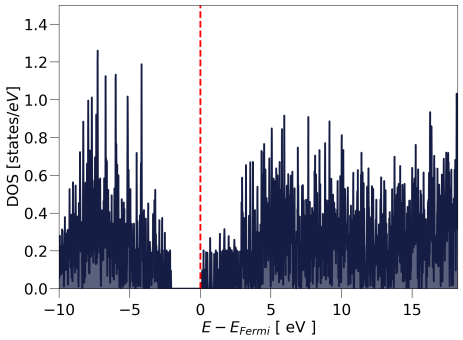

a DOS Fm-3m(225)

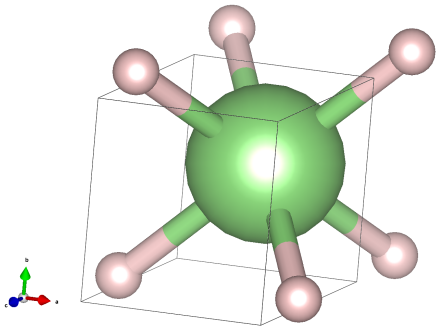

b Fm-3m(225)

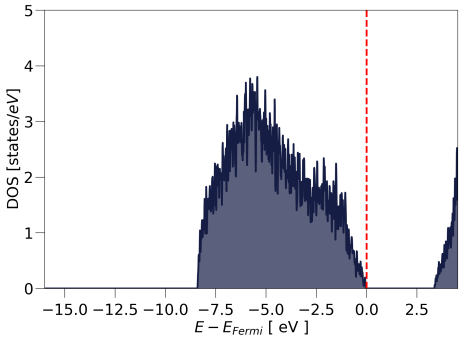

c DOS $P6_3/mmc(194)$

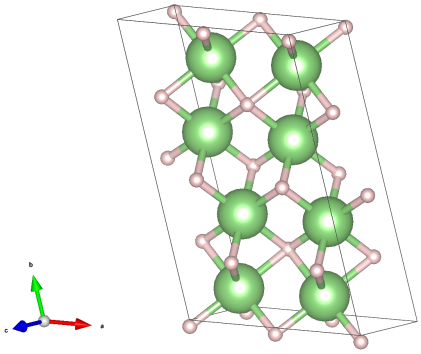

d $P6_3/mmc(194)$

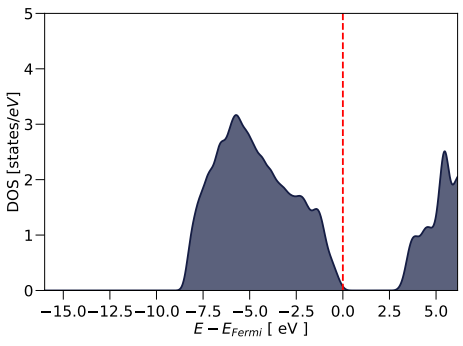

e DOS R-3m(166)

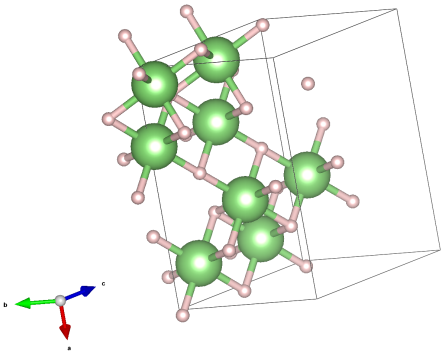

f R-3m(166)

Figure 6.7: The best optimised structures for LiH as ranked on Table 6.2: (left) DOS calculation for each structure and (right) the corresponding crystal structure file of each optimised structure at target pressure of $100\,\mathrm{GPa}$.

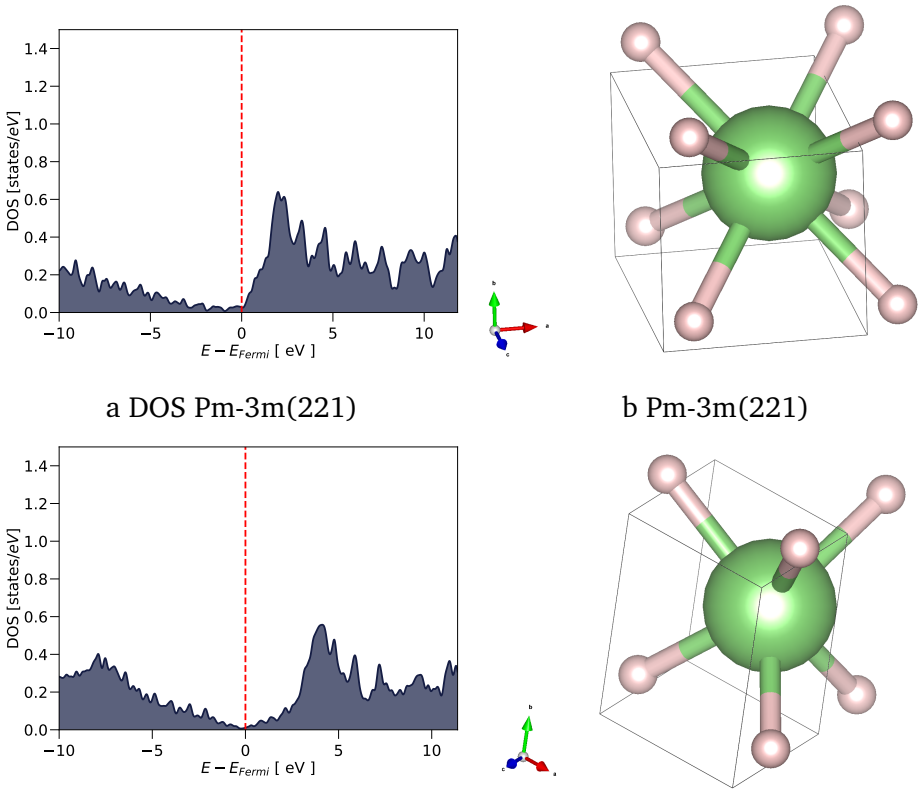

a DOS Pm-3m(221) b Pm-3m(221)

c DOS $\mathrm{P}-6\mathrm{m}2(187)$ d $\mathrm{P}-6\mathrm{m}2(187)$

Figure 6.8: Metallic phases of LiH one in the $\mathrm{Pm}-3\mathrm{m}$ phase and the second in the $\mathrm{P}-6\mathrm{m}2$ as shown in the ranking Table 6.2: (a) and (b) the dos and the crystal structure file for the $\mathrm{Pm}-3\mathrm{m}$ structure, and the (c) and (d) for the $\mathrm{P}-6\mathrm{m}2$ structure respectively at target pressure of $100\,\mathrm{GPa}$.

6.3.2 250 GPa all f.u. optimisations

Table 6.3 we summarize crystal structure prediction of LiH ranked with respect to the lowest enthalpy structure analysed with four different tolerance threshold for symmetry analyses of given structure. We have excluded structures labeled with the same space group, we keep always the one with the lowest enthalpy. In Table 6.3 we have combined the structures that are found at the same target pressure from higher formula units (8) system. One can observe the evolution of the structures that are found with the best being the insulating structure B1 with space group $\mathrm{Fm}-3\mathrm{m}(225)$ in all space group tolerance analysis which is in agreement with theoretical calculations. Although

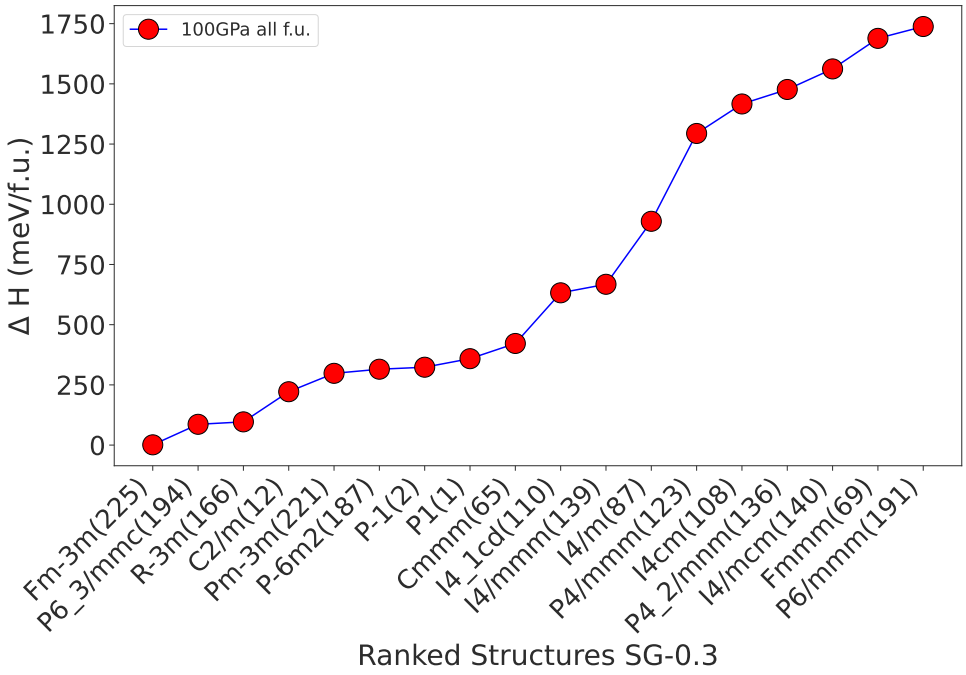

Figure 6.9: Ranked high pressure structures as function of the enthalpy difference analysed with the highest space group tolerance for symmetry analysis of given structures at $100\,\mathrm{GPa}$.

three more insulating structures are followed to have the same trend, with the latest insulating structure transitioning from $\mathrm{Fm}-3\mathrm{m}(225)$ with $\mathrm{SG}-0\,05$ to $\mathrm{Pm}-3\mathrm{m}(221)$ for higher tolerance analysis. Concluding in Figure 6.10 we present the six best ranked optimised structures with the lowest enthalpy difference and the type of the structure which is either metallic or insulating by looking at the DOS calculation and the crystal structure file of the predicted optimised structure. Figure 6.12 is presenting the trend of the structures at $250\,\mathrm{GPa}$ analysed with the highest space group tolerance for symmetry ranking of given structure. The reduced table after filtering resulted in 11 insulating structures and 11 metallic.

f.u.	Gen.	Con.	E (eV/f.u.)	V (Å^3/f.u.)	P (GPa)	H (eV/f.u.)	ΔH (meV/f.u.)	SG-0.05 (Å)	SG-0.10 (Å)	SG-0.20 (Å)	SG-0.30 (Å)	DOS	H_{B1} (eV/f.u.)
8	14	2	-215.072464	5.354326	249.566442	-206.732185	-7.2837	Fm − 3m(225)	Fm − 3m(225)	Fm − 3m(225)	Fm − 3m(225)	Insulator	-206.724901310862
8	7	8	-214.66313	5.146691	249.840646	-206.63747	87.4313	R − 3m(166)	Pm − 3m(221)	Pm − 3m(221)	Pm − 3m(221)	Metal	
8	12	1	-214.972345	5.33648	250.274802	-206.63627	88.6313	R − 3m(166	R − 3m(166)	R − 3m(166)	R − 3m(166)	Insulator	
8	13	4	-214.965723	5.347083	250.033011	-206.621154	103.7473	P3m1(156)	P3m1(156)	P3m1(156)	P3m1(156)	Insulator	
4	5	10	-214.810165	5.250083	249.975591	-206.618854	106.0473	$P2_1$/m(11	$P2_1$/m(11)	Cmcm(63)	Cmcm(63)	Insulator	
8	10	2	-214.665629	5.147594	251.205683	-206.594703	130.1983	Cmcm(63)	Cmcm(63)	Cmmm(65)	Cmmm(65)	Insulator	
8	9	9	-214.664851	5.223858	250.200122	-206.507137	217.7643	C2/c(15)	C2/c(15)	C2/c(15)	C2/c(15)	Insulator	
8	6	4	-214.81511	5.330416	250.084301	-206.494845	230.0563	6_3/mmc(1	$P6_3$/mmc(194)	$P6_3$/mmc(194)	$P6_3$/mmc(194)	Insulator	
8	4	9	-214.676761	5.287842	250.105435	-206.422253	302.6483	P1(1)	Cm(8)	Cm(8)	Cm(8)	Metal	
1	21	7	-214.717405	5.317114	249.987702	-206.421109	303.7923	P − 6m2(187	P − 6m2(187)	P − 6m2(187)	P − 6m2(187)	Insulator	
8	5	6	-214.565534	5.23164	250.023596	-206.401432	323.4693	Cc(9)	Cc(9)	Ama2(40)	Ama2(40)	Metal	
1	22	5	-214.552994	5.083858	258.583591	-206.347893	377.0083	P − 1(2)	C2/m(12)	C2/m(12)	C2/m(12)	Insulator	
8	10	3	-214.55536	5.272218	250.172074	-206.323049	401.8523	P1(1)	P1(1)	P1(1)	P1(1)	Insulator	
8	3	4	-214.723461	5.293595	255.223417	-206.290874	434.0273	$P2_1$/m(11)	$P2_1$/m(11)	$P2_1$/m(11)	$P2_1$/m(11)	Metal	
4	13	2	-213.953482	5.307703	249.960782	-205.672762	1052.1393	I − 42d(122)	I − 42d(122)	I − 42d(122)	I − 42d(122)	Metal	
8	10	8	-213.924136	5.316051	250.10009	-205.625769	1099.1323	Fddd(70)	Fddd(70)	Fddd(70)	Fddd(70)	Metal	
4	12	1	-214.29937	5.754343	250.118037	-205.316184	1408.7173	F − 43m(216)	F − 43m(216)	F − 43m(216)	F − 43m(216)	Insulator	
8	3	5	-213.573207	5.350468	249.97662	-205.22524	1499.6613	I4/mmm(139)	I4/mmm(139)	I4/mmm(139)	I4/mmm(139)	Metal	
1	16	4	-213.581648	5.41183	260.607119	-204.778865	1946.0363	P4/mmm(123)	P4/mmm(123)	P4/mmm(123)	P4/mmm(123)	Metal	
4	13	1	-213.17548	5.443719	250.170995	-204.675415	2049.4863	$P4_2$/mmc(131)	$P4_2$/mmc(131)	$P4_2$/mmc(131)	$P4_2$/mmc(131)	Metal	
1	17	4	-211.885549	5.680654	249.958526	-203.023056	3701.8453	P6/mmm(191)	P6/mmm(191)	P6/mmm(191)	P6/mmm(191)	Metal	
8	3	1	-211.10311	6.188128	250.179086	-201.440378	5284.5233	$P4_132$(214)	$I4_132$(214)	$I4_132$(214)	$I4_132$(214)	Insulator	

Table 6.3: Crystal structure prediction of LiH system for three different formula units (1, 4, and 8) at target pressure of $250\,\mathrm{GPa}$, repeated structures are filtered out: f.u. stands for formula unit, Gen. for generation, Con. for configuration, E is the total energy of the optimized structure, V is the volume of the structure, H is the minimum enthalpy, ΔH is the enthalpy difference with respect to $\mathrm{H_{B1}}$ static calculation, SG-Num. stands for space group tolerance parameter for space group recognition for each optimised calculation for four different tolerance values (0.05, 0.10, 0.20 and 0.30 Å), Density of State (DOS) classification (Metal/Insulator) and the $\mathrm{H_{B1}}$ is the enthalpy B1 phase from the static calculation in (eV).

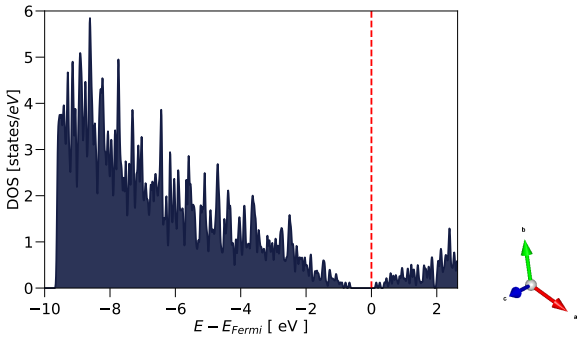

a DOS Fm-3m(225)

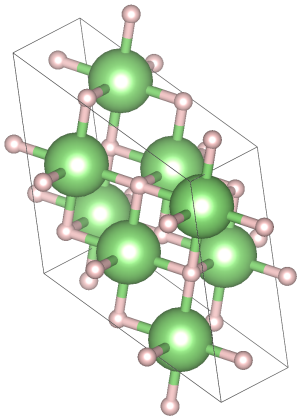

b Fm-3m(225)

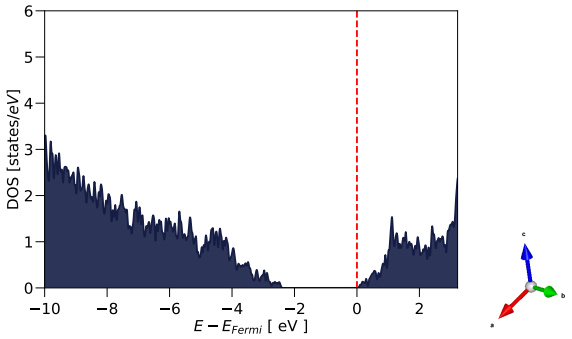

c DOS R-3m(166)

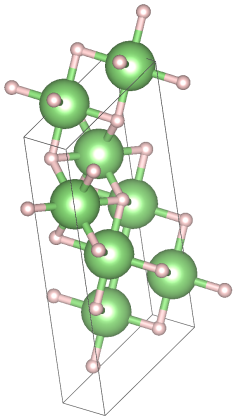

d R-3m(166)

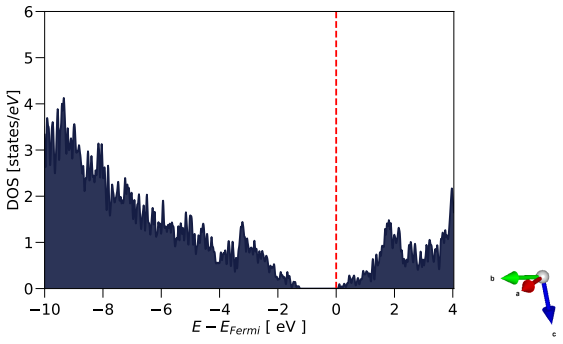

e DOS P3m1(156)

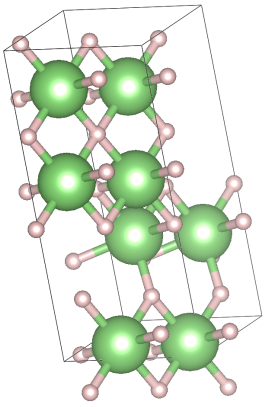

f P3m1(156)

Figure 6.10: The best optimised structures for the as ranked on Table 6.3: (left) DOS calculation for each structure and (right) the corresponding crystal structure file of each optimised structure at target pressure of $250\,\mathrm{GPa}$.

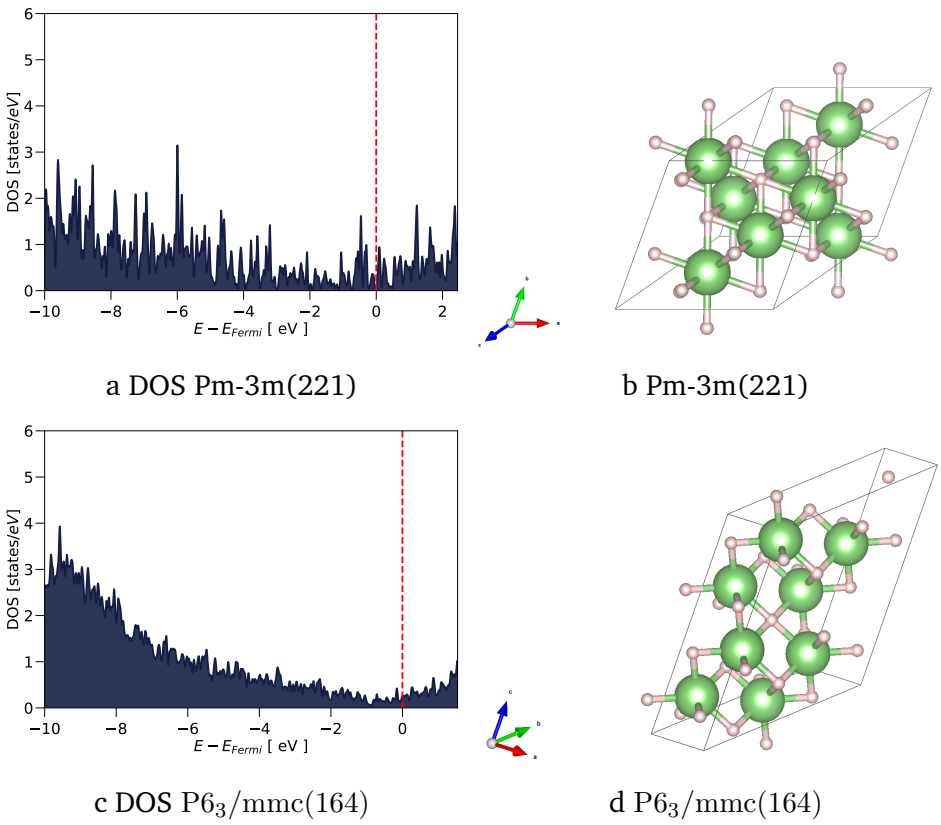

a DOS Pm-3m(221) b Pm-3m(221)

c DOS $P6_3/mmc(164)$ d $P6_3/mmc(164)$

Figure 6.11: Metallic structures of LiH one in the $Pm-3m$ phase and the second in the P_63/mmc as shown in the ranking Table 6.3: (a), (b) the dos and the crystal structure file for the $Pm-3m$ structure, and the (c) and (d) for the P_63/mmc structure respectively at target pressure of $250\,GPa$.

6.3.3 300 GPa all f.u. optimisations

Table 6.4 we summarize crystal structure prediction of LiH ranked with respect to the lowest enthalpy structure analysed with four different tolerance threshold for symmetry analyses of given structure. We have excluded structures labeled with the same space group, we keep always the one with the lowest enthalpy. At this target pressure the $8\,f\,u$ system is dominating. In Table 6.4 we have combined the structures that are found at the same target pressure from higher formula units (4 and 8) system. At this we can see that the evolution of the structures that are found with the best being the insulating structure B1 with space group $Pm-3m(221)$ in all space group tolerance analysis which close to our predicted transition pressure. Although three more insulating structures are

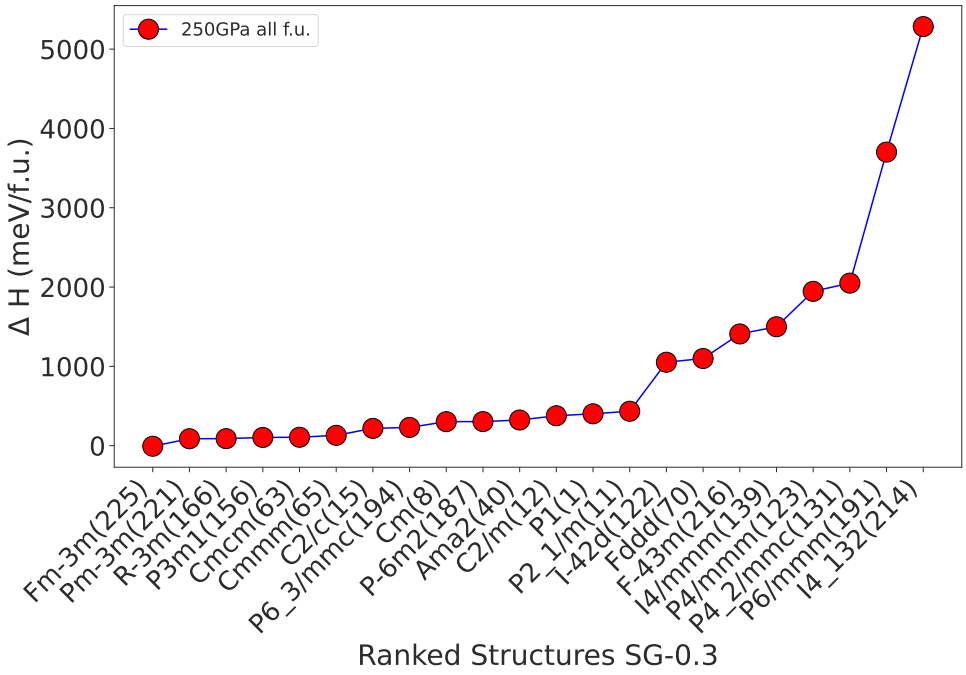

Figure 6.12: Ranked high pressure structures as function of the enthalpy difference analysed with the highest space group tolerance for symmetry analysis of given structures at $250\,\mathrm{GPa}$.

followed to have the same trend, with the latest insulating structure transitioning from $\mathrm{Fm-3m(225)}$ with $\mathrm{SG-0\,05}$ to $\mathrm{C2/c(15)}$ for higher tolerance analysis. Concluding in Figure 6.13 we present the six best ranked optimised structures with the lowest enthalpy difference and the type of the structure which is either metallic or insulating by looking at the DOS calculation and the crystal structure file of the optimised structure. Figure 6.15 is presenting the trend of the structures at $300\,\mathrm{GPa}$ analysed with the highest space group tolerance for symmetry ranking of given structure. The reduced table after filtering resulted in 11 insulating structures and 12 metallic.

f.u.	Gen.	Con.	E (eV/f.u.)	V (Å^3/f.u.)	P (GPa)	H (eV/f.u.)	ΔH (meV/f.u.)	SG-0.05 (Å)	SG-0.10 (Å)	SG-0.20 (Å)	SG-0.30 (Å)	DOS	H_{B1} (eV/f.u.)
1	11	9	-214.058916	4.794894	299.103289	-205.107539	2.36653716189039	Pm − 3m(221)	Pm − 3m(221)	Pm − 3m(221)	Pm − 3m(221)	Metal	-205.109905537162
8	12	2	-214.436589	4.984216	299.991215	-205.104153	5.7525371618965	Fm − 3m(225)	Fm − 3m(225)	Fm − 3m(225)	Fm − 3m(225)	Insulator	
8	6	8	-214.17882	4.882657	299.981898	-205.036827	73.0785371619049	Cmcm(63)	Cmcm(63)	Cmcm(63)	Cmcm(63)	Insulator	
4	2	10	-214.334592	4.966222	300.57277	-205.017822	92.0835371618978	R − 3m(166)	R − 3m(166)	R − 3m(166)	R − 3m(166)	Insulator	
8	3	4	-214.261731	4.948767	300.046576	-204.99396	115.945537161906	$P6_3/mmc(194)$	$P6_3/mmc(194)$	$P6_3/mmc(194)$	$P6_3/mmc(194)$	Insulator	
8	10	6	-214.037138	4.85895	300.189611	-204.933233	176.672537161892	C2/c(15)	C2/c(15)	C2/c(15)	C2/c(15)	Insulator	
4	3	7	-213.989422	4.761766	304.945125	-204.926268	183.6375371619	Cmmm(65)	Cmmm(65)	Cmmm(65)	Cmmm(65)	Metal	
8	13	10	-214.081903	4.909998	300.040103	-204.886935	222.970537161899	C2/m(12)	C2/m(12)	C2/m(12)	C2/m(12)	Insulator	
8	9	5	-214.080515	4.939411	300.111302	-204.828271	281.634537161892	R − 3(148)	R − 3(148)	R − 3(148)	R − 3(148)	Metal	
8	7	3	-214.051116	4.92884	300.023774	-204.821365	288.540537161907	P1(1)	P1(1)	P1(1)	P1(1)	Insulator	
8	9	10	-214.072834	4.942207	300.209666	-204.812318	297.587537161888	P − 6m2(187)	P − 6m2(187)	P − 6m2(187)	P − 6m2(187)	Insulator	
1	8	2	-214.212589	4.91415	306.66905	-204.806524	303.381537161897	C2/m(12)	C2/m(12)	Immm(71)	Immm(71)	Metal	
8	13	3	-213.872511	4.902985	300.101838	-204.688786	421.1195371619	Cm(8)	Cm(8)	Cm(8)	Cm(8)	Insulator	
8	1	3	-213.788934	4.861914	300.082862	-204.682715	427.190537161891	Pbcm(57)	Pbcm(57)	Pbcm(57)	Pbcm(57)	Insulator	
4	2	2	-213.780156	4.877678	300.1241	-204.643156	466.749537161888	$I4_1/amd(141)$	$I4_1/amd(141)$	$I4_1/amd(141)$	$I4_1/amd(141)$	Metal	
8	12	9	-213.788807	4.883053	300.208783	-204.639158	470.747537161884	Cccm(66)	Cccm(66)	Cccm(66)	Cccm(66)	Metal	
8	11	8	-213.810698	4.955656	300.004602	-204.531324	578.581537161881	$P2_1/m(11)$	$P2_1/m(11)$	$P2_1/m(11)$	$P2_1/m(11)$	Metal	
8	10	1	-213.77728	5.156892	300.246099	-204.113323	996.582537161885	Pa − 3(205)	Pa − 3(205)	Pa − 3(205)	Pa − 3(205)	Insulator	
4	2	7	-213.294452	4.924547	300.184805	-204.06779	1042.11553716189	I − 42d(122)	I − 42d(122)	I − 42d(122)	I − 42d(122)	Metal	
4	10	5	-213.375974	5.002282	301.827724	-203.952373	1157.5325371619	P − 1(2)	P − 1(2)	P − 1(2)	P − 1(2)	Metal	
8	1	1	-213.00397	4.964222	300.108654	-203.705332	1404.57353716189	P4/mnc(128)	P4/mnc(128)	P4/mnc(128)	P4/mnc(128)	Metal	
4	2	4	-212.46191	5.267944	300.280277	-202.588719	2521.1865371619	P4/mmm(123)	P4/mmm(123)	P4/mmm(123)	P4/mmm(123)	Metal	
1	6	6	-211.102857	5.225829	300.314601	-201.307477	3802.42853716189	P6/mmm(191)	P6/mmm(191)	P6/mmm(191)	P6/mmm(191)	Metal	

Table 6.4: Crystal structure prediction of LiH system for three different formula units (1, 4, and 8) at target pressure of $300\,\mathrm{GPa}$, repeated structures are filtered out: f.u. stands for formula unit, Gen. for generation, Con. for configuration, E is the total energy of the optimized structure, V is the volume of the structure, H is the minimum enthalpy, ΔH is the enthalpy difference with respect to $\mathrm{H_{B1}}$ static calculation, SG-Num. stands for space group tolerance parameter for space group recognition for each optimised calculation for four different tolerance values (0.05, 0.10, 0.20 and 0.30 Å), Density of State (DOS) classification (Metal/Insulator) and the $\mathrm{H_{B1}}$ is the enthalpy B1 phase from the static calculation in (eV).

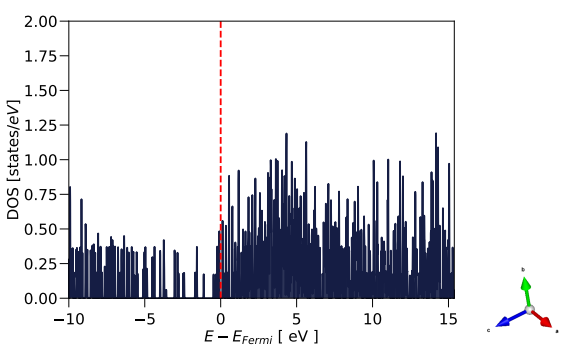

a DOS Fm-3m (225)

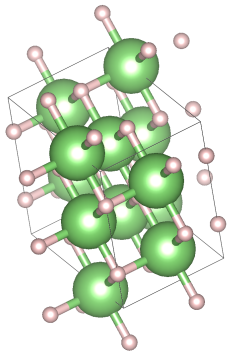

b Fm-3m(225)

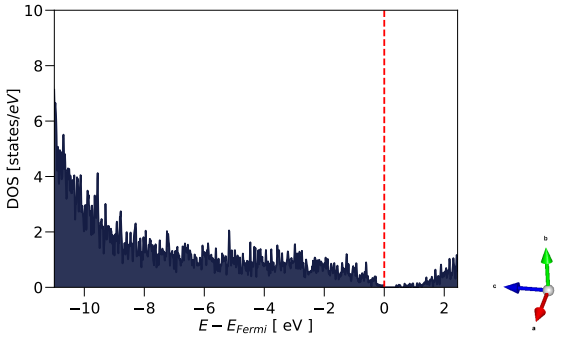

c DOS Cmcm(63)

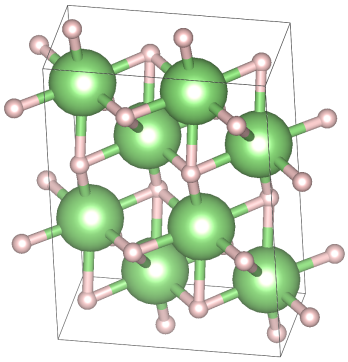

d Cmcm(63)

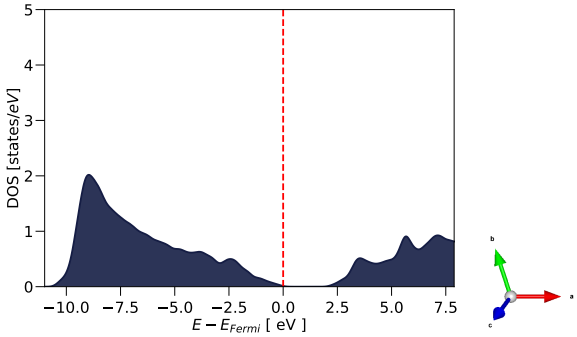

e DOS R-3m(166)

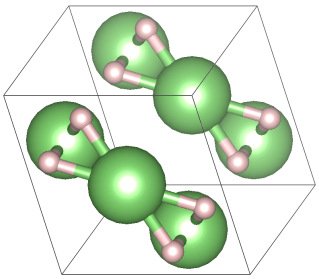

f R-3m(163)

Figure 6.13: The best optimised structures for the as ranked on Table 6.4: (left) DOS calculation for each structure and (right) the corresponding crystal structure file of each optimised structure at target pressure of $300\,\mathrm{GPa}$.

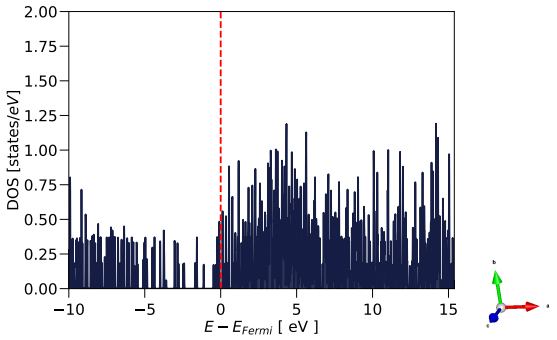

a DOS Pm-3m(221)

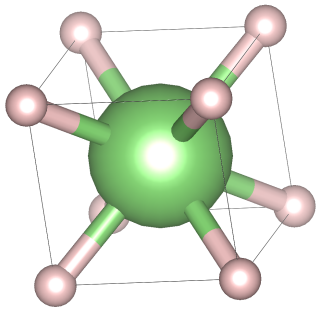

b Pm-3m(221)

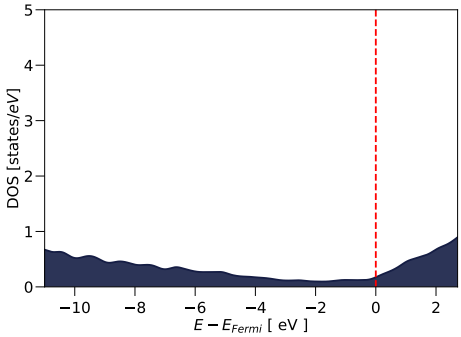

c DOS Cmmm(65)

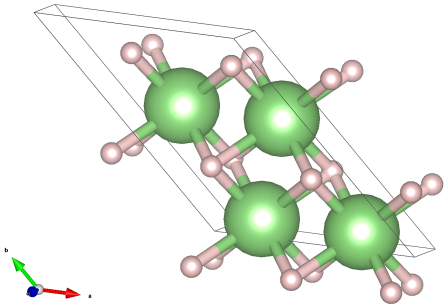

d Cmmm(65)

Figure 6.14: Metallic phases of LiH one in the $\mathrm{Pm}-3\mathrm{m}(221)$ phase and the second in the $\mathrm{Cmmm}(65)$ as shown in the ranking Table 6.4: (a) and (b) the dos and the crystal structure file for the $\mathrm{Pm}-3\mathrm{m}(221)$ structure, and the (c) and (d) for the $\mathrm{Cmmm}(65)$ structure respectively at $300\,\mathrm{GPa}$

6.3.4 350 GPa all f.u. optimisations

Finally in Table 6.5 we summarize crystal structure prediction of LiH ranked with respect to the lowest enthalpy structure analysed with four different tolerance threshold for symmetry analyses of given structure. We have excluded structures labeled with the same space group, we keep always the one with the lowest enthalpy. In Table 6.5 we have combined the structures that are found at the same target pressure from higher formula units (4 and 8) system. At this we can see that the evolution of the structures that are found with the best being the insulating structure B1 with space group $\mathrm{Pm}-3\mathrm{m}(221)$ in all space group tolerance analysis which close to our predicted tran-

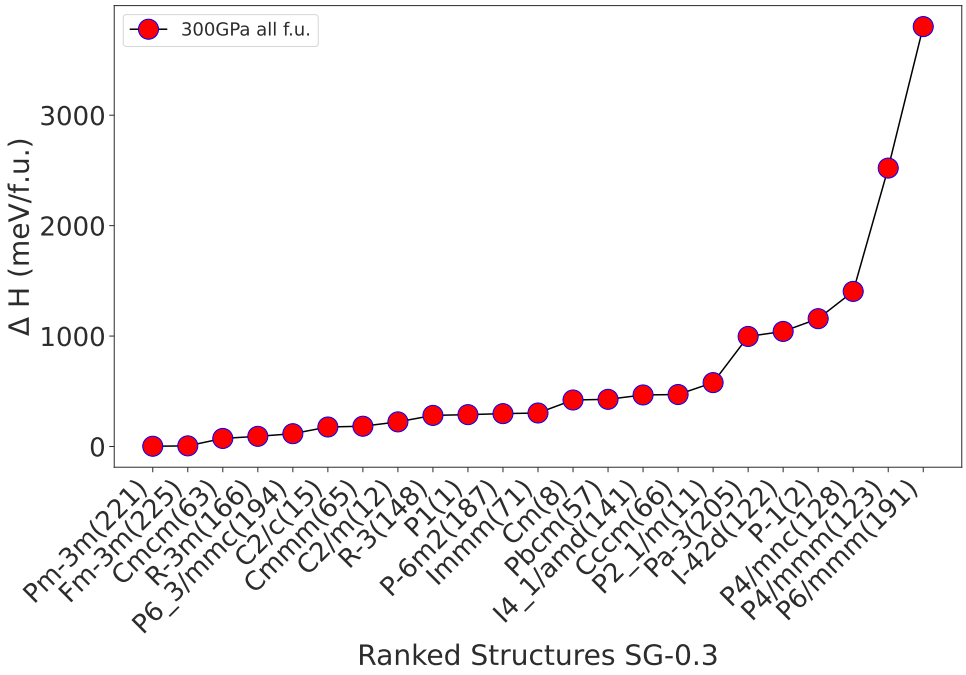

Figure 6.15: Ranked high pressure structures as function of the enthalpy difference analysed with the highest space group tolerance for symmetry analysis of given structures at $300\,\mathrm{GPa}$.

sition pressure. Although three more insulating structures are followed to have the same trend, with the latest insulating structure transitioning from $\mathrm{Fm}-3\mathrm{m}(225)$ with $\mathrm{SG}-0\,05$ to $\mathrm{Cmcm}(63)$ for higher tolerance analysis. Concluding in Figure 6.16 we present the six best ranked optimised structures with the lowest enthalpy difference and the type of the structure in insulating phase by looking at the DOS calculation and the crystal structure file of the optimised structure and Figure 6.17 the two metallic ranked with lowest enthalpy of formation. Figure 6.18 is presenting the trend of the structures at $350\,\mathrm{GPa}$ analysed with the highest space group tolerance for symmetry ranking of given structure. The reduced table after filtering resulted in 7 insulating structures and 10 metallic.

f.u.	Gen.	Con.	E (eV/f.u.)	V (Å^3/f.u.)	P (GPa)	H (eV/f.u.)	ΔH (meV/f.u.)	SG-0.05 (Å)	SG-0.10 (Å)	SG-0.20 (Å)	SG-0.30 (Å)	DOS	H_{B1} (eV/f.u.)
8	6	2	-213.461691	4.500224	349.988108	-203.631158	-28.3959071521735	R − 3m(166)	Pm − 3m(221)	Pm − 3m(221)	Pm − 3m(221)	Metal	-203.602762092848
4	5	4	-213.838566	4.690313	349.707726	-203.601002	1.76009284783163	Fm − 3m(225)	Fm − 3m(225)	Fm − 3m(225)	Fm − 3m(225)	Insulator	
4	5	10	-213.581626	4.588958	349.974182	-203.557658	45.1040928478221	Cmcm(63)	Cmcm(63)	Cmcm(63)	Cmcm(63)	Insulator	
8	11	5	-213.568727	4.593316	350.154239	-203.530076	72.6860928478175	P2/m(10)	P2/m(10)	P2/m(10)	Pmmm(47)	Metal	
4	9	2	-213.391274	4.4721	356.498537	-203.440453	162.309092847835	Cmmm(65)	Cmmm(65)	Cmmm(65)	Cmmm(65)	Insulator	
8	10	6	-213.442519	4.61324	350.063034	-203.362951	239.811092847816	P1(1)	P1(1)	P1(1)	P1(1)	Insulator	
8	11	6	-213.461129	4.632446	350.326646	-203.331976	270.786092847828	R − 3(148)	R − 3(148)	R − 3(148)	R − 3(148)	Metal	
1	24	9	-213.335734	4.451601	360.516124	-203.318898	283.864092847836	C2/m(12)	C2/m(12)	C2/m(12)	C2/m(12)	Metal	
1	20	2	-213.645633	4.623954	360.280805	-203.247765	354.997092847839	C2/m(12)	C2/m(12)	R − 3m(166)	R − 3m(166)	Insulator	
8	4	10	-213.188606	4.588022	349.988304	-203.166276	436.486092847815	Cccm(66)	Cccm(66)	Cccm(66)	Cccm(66)	Insulator	
8	11	9	-213.321054	4.606561	353.572765	-203.155169	447.593092847825	Fddd(70)	Fddd(70)	Fddd(70)	Fddd(70)	Insulator	
8	13	1	-212.996862	4.673847	350.23343	-202.779901	822.86109284783	$P4_3$(78)	$P4_3$(78)	$P4_3$(78)	$P4_3$(78)	Metal	
4	2	4	-212.924898	5.015648	350.179296	-201.962461	1640.30109284784	F − 43m(216)	F − 43m(216)	F − 43m(216)	F − 43m(216)	Insulator	
8	4	9	-211.743948	4.693043	349.976879	-201.492541	2110.22109284784	$P4_2$/mcm(132)	$P4_2$/mcm(132)	$P4_2$/mcm(132)	$P4_2$/mcm(132)	Metal	
4	11	8	-212.513833	5.217008	349.969034	-201.11814	2484.62209284781	I4/mcm(140)	I4/mcm(140)	I4/mcm(140)	I4/mcm(140)	Metal	
1	15	6	-210.323934	4.833693	350.242453	-199.757281	3845.48109284782	P4/mmm(123)	P4/mmm(123)	P4/mmm(123)	P4/mmm(123)	Metal	
1	13	6	-210.355736	4.859815	352.874555	-199.652141	3950.62109284783	P6/mmm(191)	P6/mmm(191)	P6/mmm(191)	P6/mmm(191)	Metal	

Table 6.5: Crystal structure prediction of LiH system for three different formula units (1, 4, and 8) at target pressure of $350\,\mathrm{GPa}$, repeated structures are filtered out: f.u. stands for formula unit, Gen. for generation, Con. for configuration, E is the total energy of the optimized structure, V is the volume of the structure, H is the minimum enthalpy, ΔH is the enthalpy difference with respect to H_{B1} static calculation, SG-Number. stands for space group tolerance parameter for space group recognition for each optimised calculation for four different tolerance values (0.05, 0.10, 0.20 and 0.30 Å), Density of State (DOS) classification (Metal/Insulator) and the H_{B1} is the enthalpy B1 phase from the static calculation in (eV).

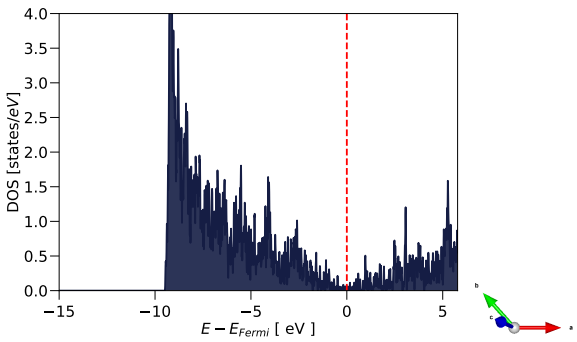

a DOS Fm-3m(225)

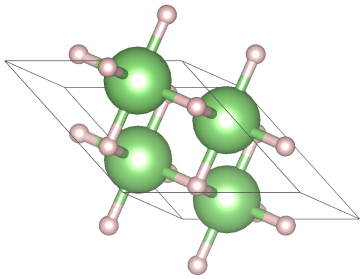

b Fm-3m(225)

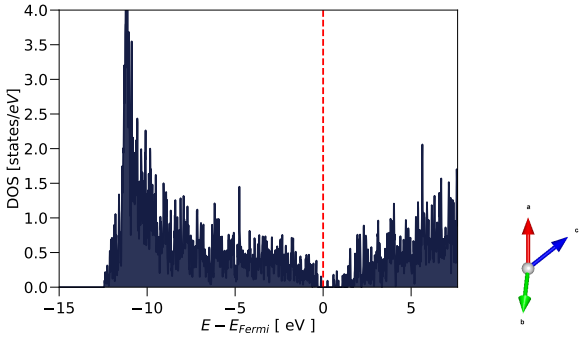

c DOS Cmcm(63)

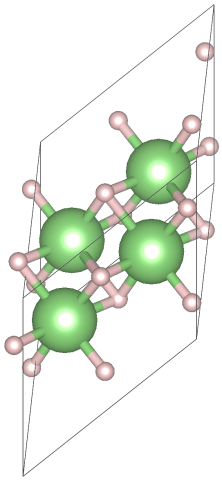

d Cmcm(63)

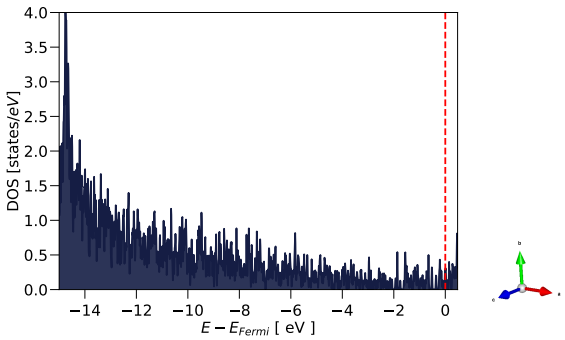

e DOS Cmmm(65)

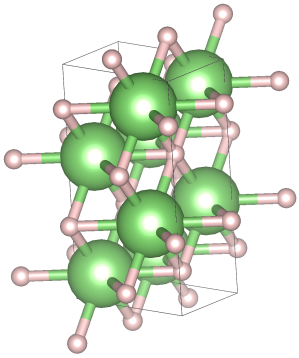

f Cmmm(65)

Figure 6.16: The best optimised structures for the as ranked on Table 6.5: (left) density of state calculation for each structure and (right) the corresponding crystal structure file of each optimised structure at target pressure of $350\,\mathrm{GPa}$.

In conclusion we compare the enthalpy difference of the crystal structure

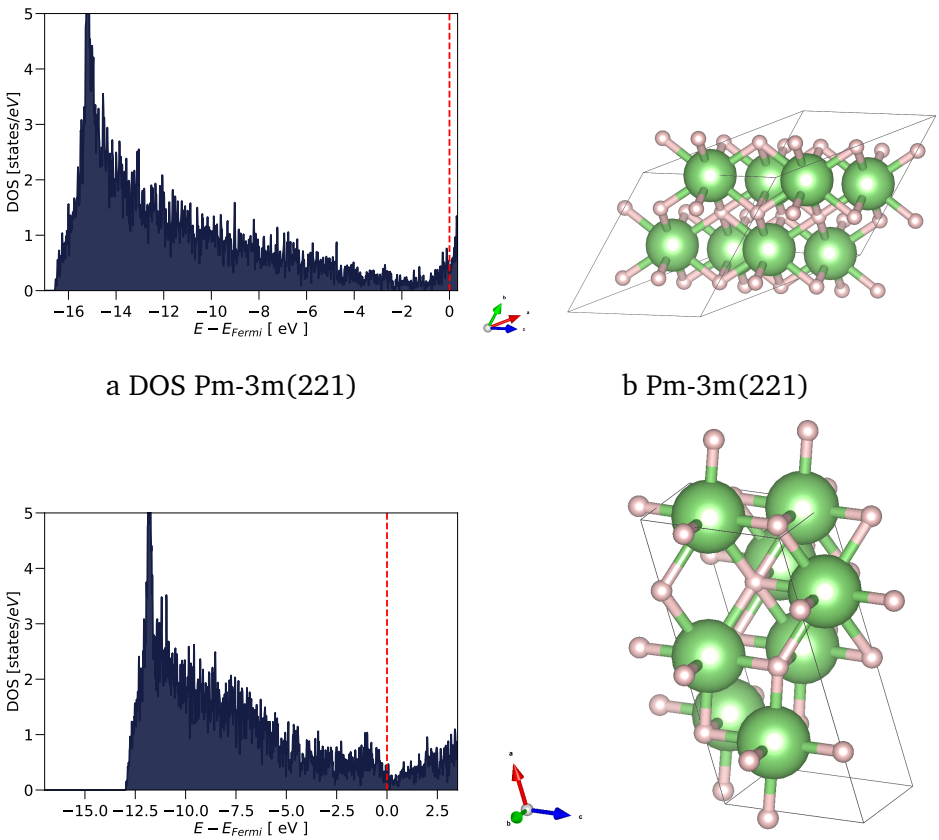

a DOS Pm-3m(221) b Pm-3m(221)

c DOS Pmmm(47) d Pmmm(47)

Figure 6.17: Metallic phases of LiH one in the $\mathrm{Pm}-3\mathrm{m}(221)$ phase and the second in the $\mathrm{Pmmm}(47)$ as shown in the ranking Tab. 6.5: (a) and (b) the dos and the crystal structure file for the $\mathrm{Pm}-3\mathrm{m}(221)$ structure, and the (c) and (d) for the $\mathrm{Pmmm}(47)$ structure respectively at target pressure of $350\,\mathrm{GPa}$.

prediction with the static calculation of the B1 and B2 phases as a function of pressure. Our calculations indicate a transition pressure of 319 GPa as shown in Figure 6.4, which is in good agreement with other first principle calculations [Stephens and Lilley, 1968, Gerlich and Smith, 1974, Yu et al., 2007, Zurek et al., 2009, Horner et al., 2009, Chen et al., 2016, Biswas et al., 2019]. Figure 6.19 shows all the predicted structures with respect to the B1 phase, by subtracting the enthalpy difference of the predicted high pressure phase from the B1 static calculation. On Figure 6.20 in zoomed region for better visibility. The Figure of merit that can be drawn from such results is that the best candidate is the B2 phase so far.

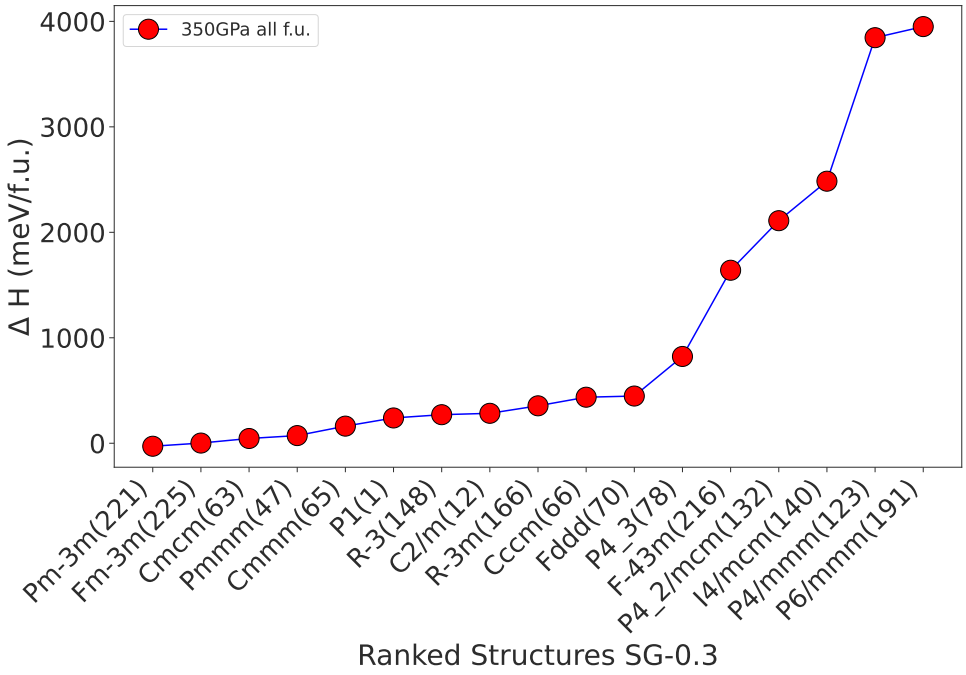

Figure 6.18: Ranked high pressure structures as function of the enthalpy difference analysed with the highest space group tolerance for symmetry analysis of given structures at pressure of $350\,\mathrm{GPa}$ for all formula unit system.

6.4 Conclusions and Perspectives

In this chapter, we reported on crystal structure optimization calculation combined with DFT techniques on LiH systems at three different formula units and target pressures. Ranking tables of the predicted structures are reported and compared with static calculation with respect to the B1 - B2 phases. Our results are in good agreement with previous theoretical works, however, these results are in contradiction with the experimental evidence reported by [Molodets et al., 2014]. The main conclusion that can be drown is that from the crystal structure predictions we found that there are not better candidates than the Pm-3m. Although there are other meta-stable insulating structures closer in energy. However their band gap is big approximately $3\,\mathrm{eV}$ similar to the gap of Fm-3m, so they aren't expected to be the candidates observed experimentally by Molodets et al. [Molodets et al., 2014], as they would behave electronically like the B1. The other possibility is that the metallic structure $\mathrm{P}-6\mathrm{m}2(187)$ that we found at

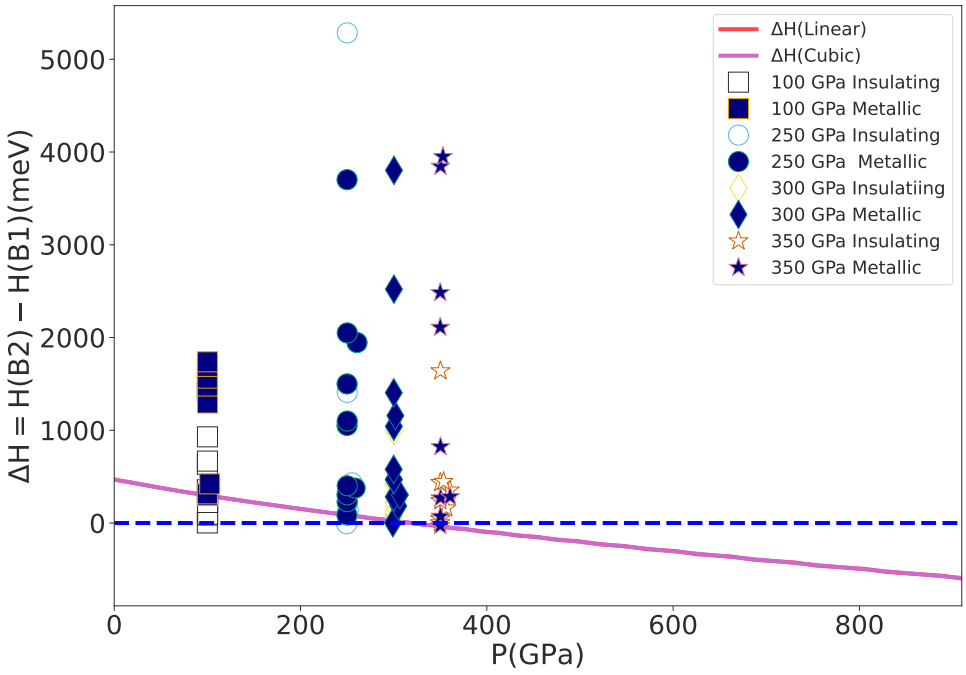

Figure 6.19: Relative enthalpy ΔH is plotted as a function of pressure, we also plot the enthalpy difference from crystal structure prediction at (1, 4 and 8) formula unit system optimized at target pressures of (100, 250, 300 and $350\,\mathrm{GPa}$). Blue filled symbols present the metallic phase ranked with respect to B1 phase for each formula unit and target pressure respectively.

pressure of $100\,\mathrm{GPa}$ is also close in energy with the B2 could be the one observed in Molodets et al. experiment. In this context following our crystal structure prediction results, we propose a dedicated experimental platform on pure LiH crystals in order to confirm or not our study and define the metal-insulator transition point. In the final Chapter 7 we present preliminary results held at the PALS laser facility which indicate that careful optimization for each particular diagnostic is necessary.

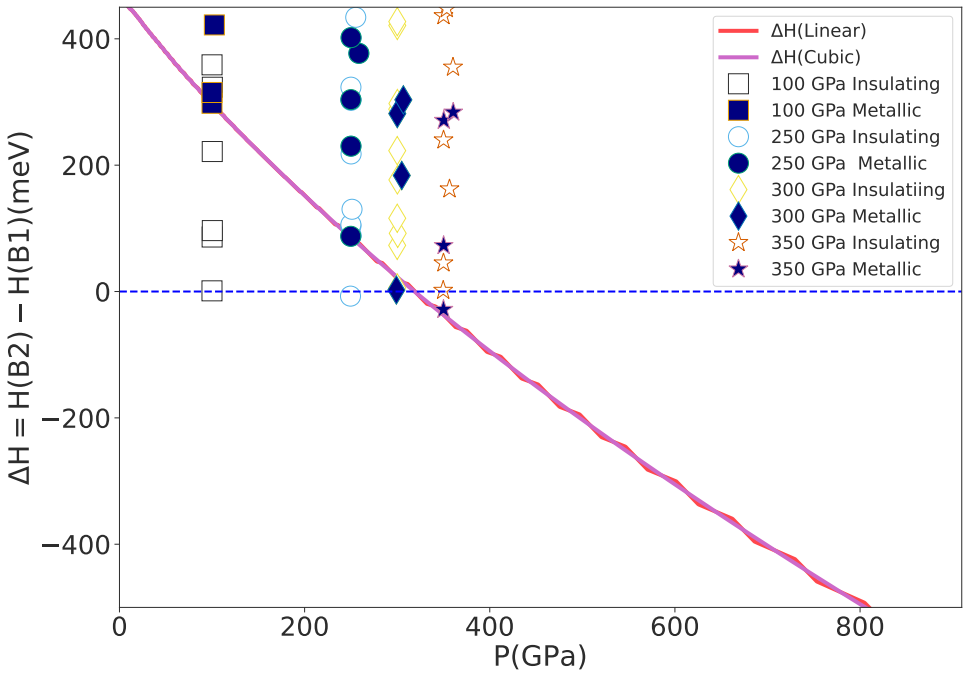

Figure 6.20: (*Zoomed*)Relative enthalpy ΔH is plotted as a function of pressure, we also plot the enthalpy difference from crystal structure prediction at (1, 4 and 8) formula unit system optimized at target pressures of (100, 250, 300 and $350\,\mathrm{GPa}$). Blue filled symbols present the metallic phase ranked with respect to B1 phase for each formula unit and target pressure respectively.

Chapter 7

High Repetition Rate Laser system

Contents

7.1 Frontiers in High-Repetition Rate Moderate Laser and EOS Study

Usually HED states of matter are produced by using high-energy laser pulse ($\sim kJ$ energy) focused on targets to generate a plasma. Unfortunately such high-energy laser

systems are affected by very low repetition rate (practically single shot operation) which severely limits the potential of HED studies and especially prevents obtaining data with a statistical meaning, i.e. evaluating error bars of experimental results by the measurement of their standard deviation.

This situation can however completely change in the next few years. New kJ-class lasers have been designed and built to provide both high-energy pulses and much higher repetition frequencies. The prototype of this technology is the new laser system L4n at ELI Beam-lines in Prague. Such systems will be operated either in the nanosecond or in the picosecond regime, allowing to obtain HED states respectively by shock wave compression or by isochoric heating of matter. Research is also going on in the USA (namely at the partner University of Rochester) for developing laser systems operating at high repetition rate (HRR) with unique large broadband, providing a possibility to explore new regimes of laser plasma interaction. By shooting kJ pulses at shot rate of less than 1 min, it will be possible to accumulate a huge amount of data. This means that it will be possible to do many more experiments, probe many more materials, and also statistically validate the results. This will have a deep impact on the above mentioned fields.

However, new systems pose new challenges requiring high quality and credible research and innovation actions. Challenges must be addressed so to take advantage of possibilities offered by the new technology:

- Target development: today's HED targets are usually quite complex (and expensive) and require long alignment procedures. We must develop targets which allow extracting the desired information but are much cheaper, and target holders which allows quick alignment and HRR.

- Diagnostics: future high-repetition rate (HRR) experiments require diagnostics providing results in real-time, avoiding long procedure related to developing and scanning films or imaging plates.

- Activation: energetic particles (protons, electrons) and hard X-rays are generated

by the interaction of the laser with the target. At high repetition rate (HRR), this means a large generated radioactive dose with the possibility of activating the materials of the target chamber.

- EMP: large electromagnetic pulses are generated during laser-target interaction with electric fields which in the picosecond pulse regime may exceed MV/m, representing a real risk for all diagnostics devices based on electronics.

- Simulations: HED experiments often require the support of sophisticated numerical simulations which may be very lengthy even on today's supercomputers. New methods for getting results on faster time scale need to be studied, including systems based on deep learning

- Data base: HRR experiments will create huge data base requiring a dedicated approach for data base development and the use of data mining techniques for extracting data from the data base

- System management: all above issues must be coordinated within a proper management of the system. Typical HRR rate experiment in vacuum require a high level of automatisation.

We propose a strong international program in HED physics that will transform HED science by transitioning from single-shot to multi-shot experiments thus producing statistically validated data. The level of novelty of the project is very high: it does not only concern development connected to the technological progress in laser facilities. It also addresses salient aspects of HED physics by developing theoretical models, innovative diagnostics and performing high profile experiments on HRR high-energy laser facilities, like L4 in Prague. The new results obtained on the L4 system will be compared to data obtained in similar conditions, but in single shots, at OMEGA laser facility in the USA. Our project will also explore the ultra-high pressure regimes obtained by converging implosions on the OMEGA facility capable of accessing multi-gigabar pressures that are typical of the interiors of stars and brown dwarfs.

7.1.1 $L4n$ on $P3$ platform at ELI-Beamlines

The P3 Platform dedicated to plasma physics at ELI-Beamlines is expected to be the first high-energy laser installation operating at a high-repetition rate [Weber et al., 2017]. Among the four beams that will be available on this platform, the nanosecond L4n beam ($1.2\ kJ$, 0.5-10 ns, $\lambda = 1053\ nm$) will be ideal for high-pressure physics experiments as shown in Figure 7.1.

Installation	Operation facility	$\lambda(nm)$	Maximum energy (long pulse)	Repetition rate
NIF	LLNL (Livermore, USA)	1053	$2.1MJ(3\omega, 3ns - 15ns)$	Every 8 h
LMJ	CEA (Le Barp, France)	1053	$1.4MJ(3\omega, 3ns - 15ns)$	Every 8 h
Omega EP	LLE (Rochester, USA)	1053	$30kJ(3\omega, 1ns3ns)$	Every 90 min
SG-II-UP	SIOM (Shanghai, China)	1053	$24kJ(3\omega, 3ns)$	Every 3 h
Gekko XII	ILE (Osaka, Japan)	1053	$10kJ(2\omega, 1ns)$	Every 30 min
Orion	AWE (Aldermaston, UK)	1053	$5kJ(3\omega, 1ns)$	Every 45 min
L4n	ELI-Beamlines (Prague, Czech Republic)	1053	$1.2kJ(2\omega, 1ns5ns)$	1shot/min
VULCAN	CLF, STFC (Oxford, UK)	1053	$1kJ(2\omega, 1ns - 10ns)$	2 shots /day
PALS	IoP (Prague, Czech Republic)	1053	$200J(3\omega, 250ps)$	Every 30 min
LULI2000	LULI, CEA (Paris, France)	1053	$750J(2\omega, 1.5ns)$	Every 90 min
MEC	SLAC (Menlo Park, USA)	1053	$60J(2\omega, 10ns)$	Every 7 min
PHELIX	GSI (Darmstad, Germany)	1053	$1kJ(2\omega, 1ns - 10ns)$	Every 45 min
HIBEF	Eu-XFEL (Schenefeld, Germany)	1053	$100J(1\omega, 10ns)$	10 Hz

Table 7.1: Overview of the current performance of major high-energy laser facilities in a long-pulse configuration listing the name of the installation, the operating entity, the laser wavelength in manometers, the maximum energy available per shot, and the operating repetition rate

High repetition rates will become extremely relevant in these experiments for example in EOS measurements where error bars can be important and complicate the interpretations. This high- pressure physics field also spans a broad range of applications that includes inertial confinement fusion or planetology. The first experiment using $L4n$ nanosecond beam, which is scheduled for 2020, will aim at measuring the EOS of MgO. Similar to silicon dioxide SiO2, MgO is of strong interest for the modelling of interior of Earth like planets. So far, experimental EOS data coming from different groups are still controversial and illustrate the strong need for repetitive shots to improve the statistics [Bolis et al., 2016]. Such an experiment conducted at ELI-Beamlines where we expect $10\ shots/hour$ could help to strengthen the data sets by reducing the error bars,

and therefore facilitate the interpretations. The success of this $L4n$ first experiment will mainly depend on our ability to collect data at a high-repetition rate. This is challenging because of the very high laser energy, which requires some time after shots to let all the optics and the laser system cool down. Moreover, the laser stability is a crucial point if we want to reach similar shock conditions to improve the data sets. Pulse shaping (e.g. for ramp compression, double shock or decaying shocks) is also of great importance in this field in order to reach off-Hugoniot states. Another main issue of high-repetition experiments at high-energy is the targetry and the need for fast samples deliveries in a very precise way ($\sim$ few μm precision). Target design and alignment techniques are then of primary importance. In current experiments, shots are fired every ~ 30 minutes at best. In these conditions, targets are manually pre-aligned on a separated setup, then placed in the vacuum chamber. This is not practical when dealing with high-repetition rate. A large number of targets need to be put in a cassette in such a way that each of them can be shot separately without damaging the neighbours as shown in Figure 7.3. Furthermore, interaction of the laser with the sample generates ablation of the target materials and ejection of high speed fragments. These debris which are emitted in every direction and have to be well characterised. The debris can cause serious damages to the optics and/or our inability to use the diagnostics so the protection setup needs to be designed. For all these reasons, an experiment prior to the first $L4n$ experiment is necessary to test prototype target setups, to define their alignment procedures and also to characterise the debris. We present in the remainder of this document the experimental setup and technical details.

7.2 Physics Program

The P3 will be a multi purpose research platform for laser plasma interaction experiments and fundamental science. It will also serve as a platform for secondary sources which will be used in combination with other beam-lines. Here we present a list of science topics suitable for the P3 platform.

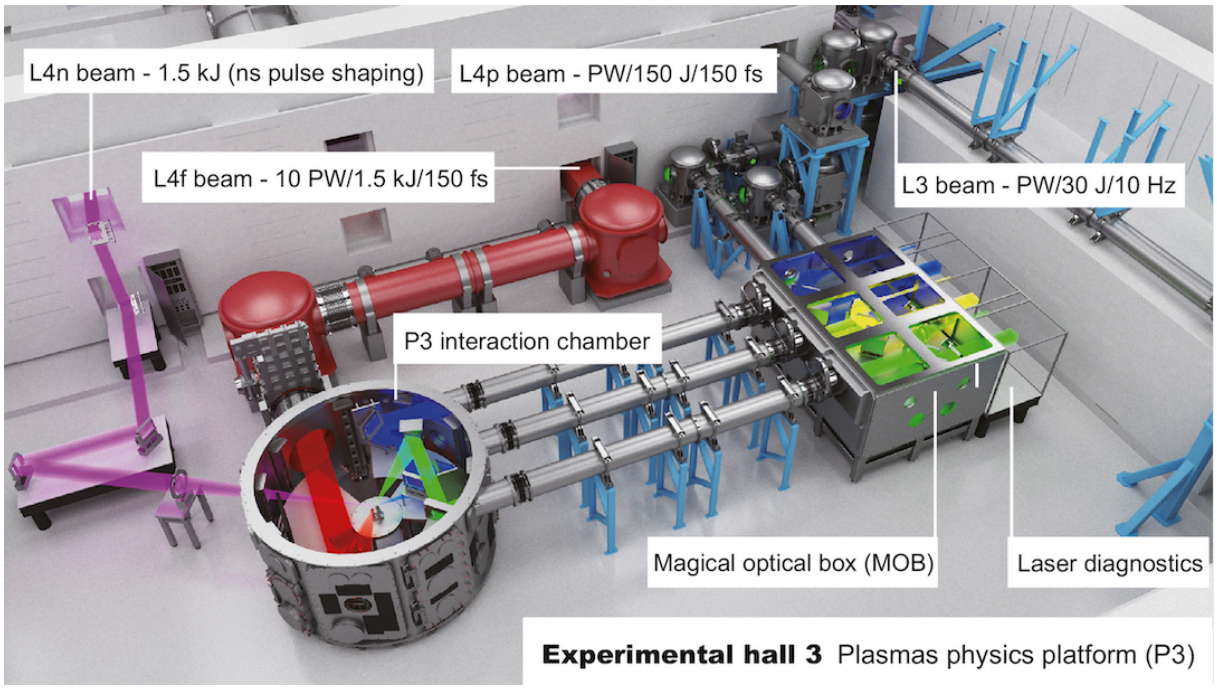

Figure 7.1: Design picture of the expected final layout of the experimental hall E3. The details of the beam transport will probably change due to constructional constraints. [Weber et al., 2017]

- Laboratory Astrophysics (collision-less shocks, cosmic ray physics, magnetic re connection, jet formation, radiation hydrodynamics)
- Ultra-High Intensity (radiation damping, electron–positron pair generation).
- Warm Dense Matter and High-Energy Density Physics (planetary cores, shock waves, thermonuclear fusion for energy, opacity's, equation of state etc.) [Koenig et al., 2005, Schönlein et al., 2016, Falk, 2018, Antonelli et al., 2019]
- Laser-Plasma Interaction (shock-ignition scheme of ICF, laser absorption)
- Plasma Optics (plasma amplification, plasma focusing)

7.3 Preliminary Campaign at PALS laser facility

7.3.1 Target design and optimisation

The experimental setup is drawn from countless previous laser-shock driven experiments and is represented in Figure 7.2. In this experimental scheme, the high-energy nanosecond beam is focused into a sample and generates a strong shock. At PALS, we used the beam in the frequency-tripled configuration ($\lambda = 438\ nm$) to get the highest absorption rate. Considering typical operation energy at $3\ \omega$ is $\sim 200\ J$and duration is $\sim 250\ ps$, focal spot on target will be around $500\ \mu m$ in order to reach intensities of 10^{14} W/cm^2. A phase plate will also be placed on the laser beam path for beam smoothing. This ensures a good shock planarity on the whole diameter spot. However this type of target design is not widely used in high energy laser facilities due to low repetition rate. In our experiment we tested two different target holders with orthogonal and circular aperture in order to check the effects of the laser shock and the unconverted laser beam as well. During first shots, it happened that the coating of all surrounding targets were gone after shooting. To overcome this effect of the unconverted laser beam we placed.

an iris (opened at $\sim$ 3-4 mm diameter) encircled by black paper was then placed few cm from the target to block the laser light .

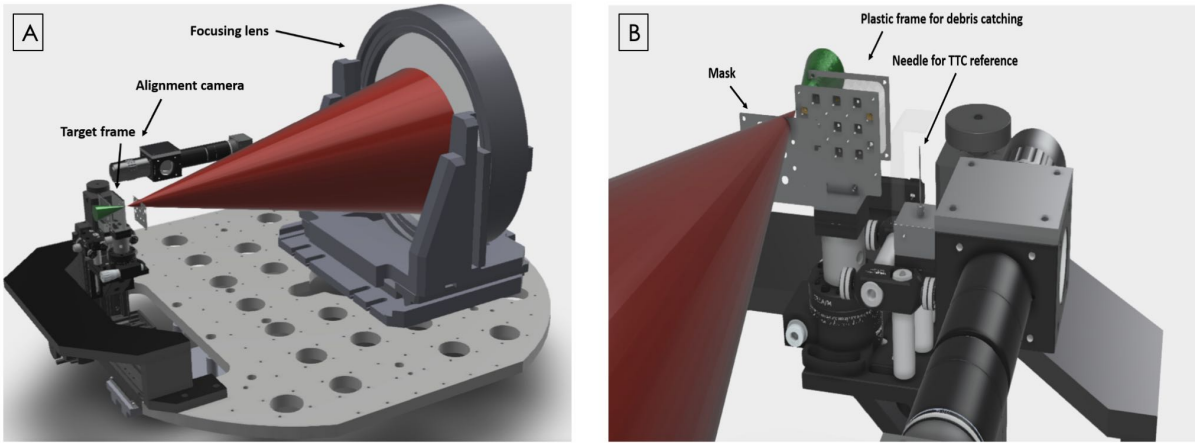

Figure 7.2: CAD design for PALS drive bean and the specially designed motorised target holder suitable for HRR experiment taking into account the real size of the beam and the chamber space. (A) Side view of the target frame and the focusing lens and (B) Front view of the target holder where we highlight the needle target for setting a reference point on the TCC, the mask in front of the target holder and the plastic frame placed to protect optics from derbies.

7.3.2 Optical diagnostics

As previously, VISAR and SOP were deployed as optical diagnostics in this experiment was used to characterise dynamics of the shock wave. They have been widely used in laser-shock experiments, and their combination can provide spatial and temporal evolution of hydrodynamic parameters encountered during the shock propagation in the target. However due to COVID-19 pandemic the VISAR was not optimised therefore we will show results from SOP only. The optical line for the SOP and VISAR is shown in

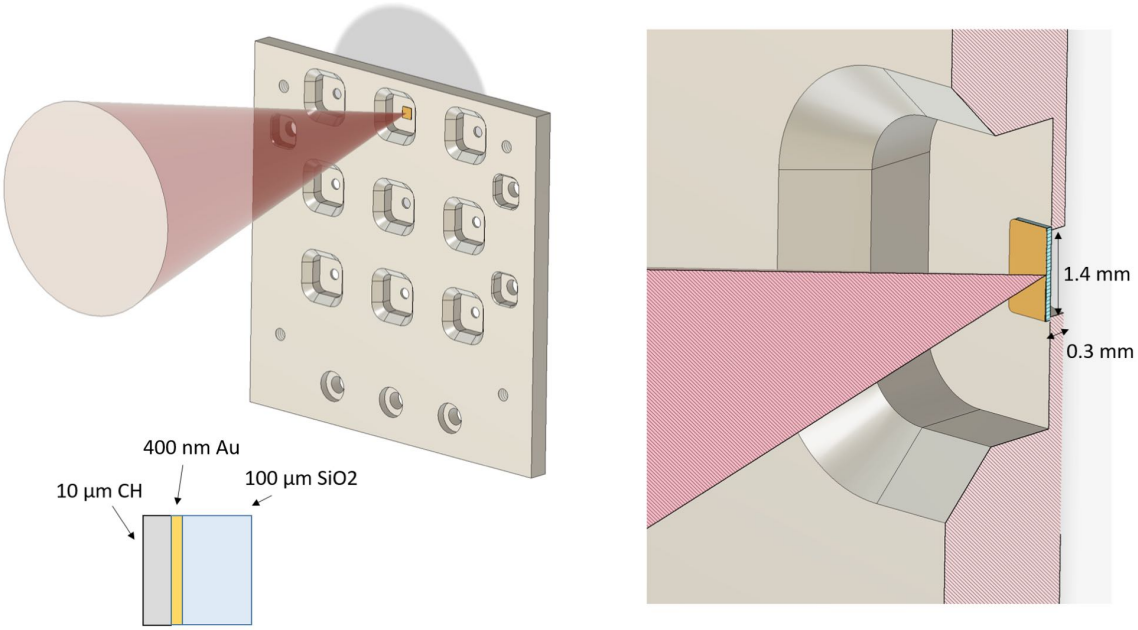

Figure 7.3: Conceptual CAD design of the target frame and the characteristics of the multilayered target with its associated thicknesses holder aperture and frame thickness.

Figure 7.6. Once the optical line is set we then place a grid target on the TCC and shine with the alignment HeNe laser such optimisation result can me shown in Figure 7.7 (A) and a line out taken from raw data resulting in an active area of the observed object of the order of $\sim 750\,\mu\mathrm{m}$ as showed in Figure 7.7 (B).

After improving the imaging SOP setup, we observed typical shock emission signal. However the halo of light was still observed at first instants same time as laser. The drive parameters for shot 55029 were $E_{3\omega}$ $113\,\mathrm{J}$ at an intensity on target ($3.6x10^{14}$ W/cm^2). The sweep window on the streak was set at $20\,\mathrm{ns}$ and the slit width of the order of $150\,\mu\mathrm{m}$. After improving the optical setup of the SOP and by gluing an additional layer in the front side of the target in order to avoid shine-through effect of the laser and suppress the Halo effect as shown in shot 55029 and the improved result 55051.

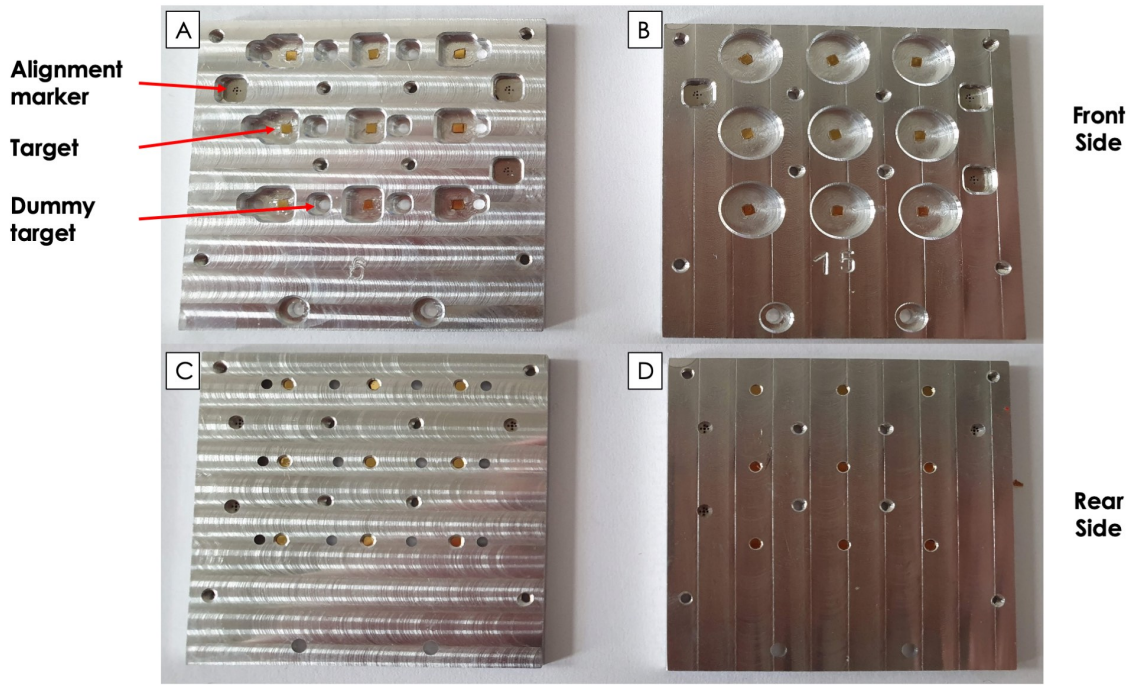

Figure 7.4: Images of the HRR target frames with two different designs: (A) With squared aperture and machined alignment markers and dummy targets for optimisation process front side, (B) framed with circular aperture respectively, (C) Rear side of frame (A) and (D) rear side of frame (B).

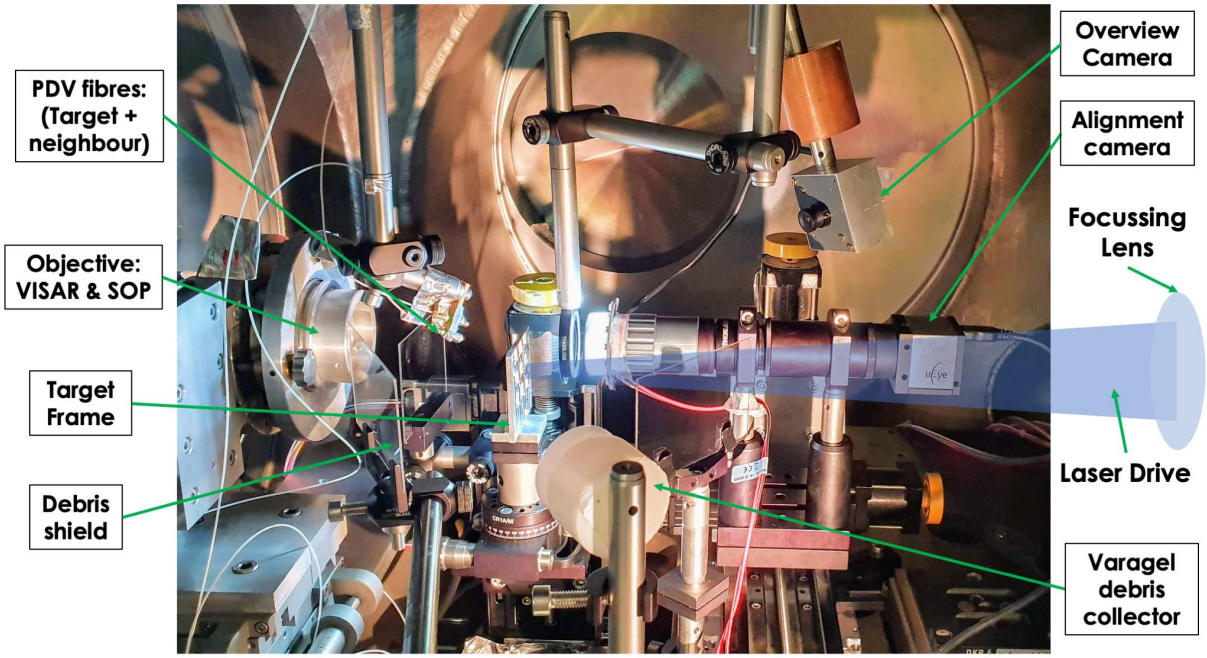

Figure 7.5: Image of the interaction chamber filled with the main diagnostics used in the experiment.

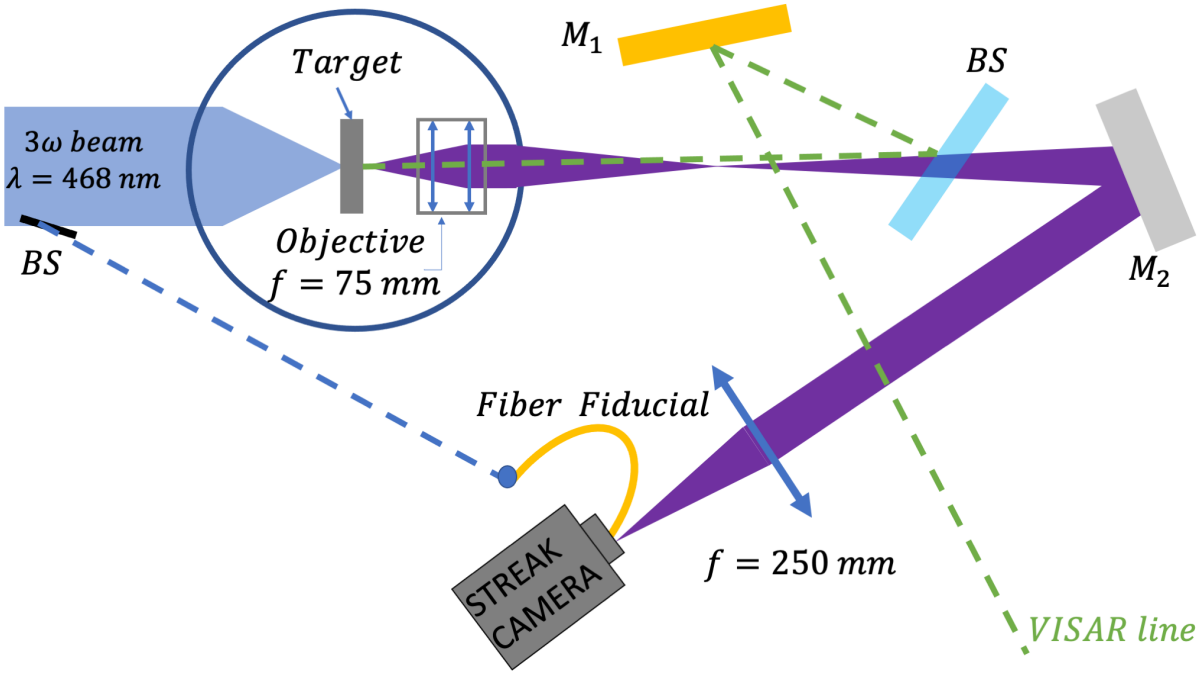

Figure 7.6: Optical line of the SOP and VISAR set for the P3 experimental campaign

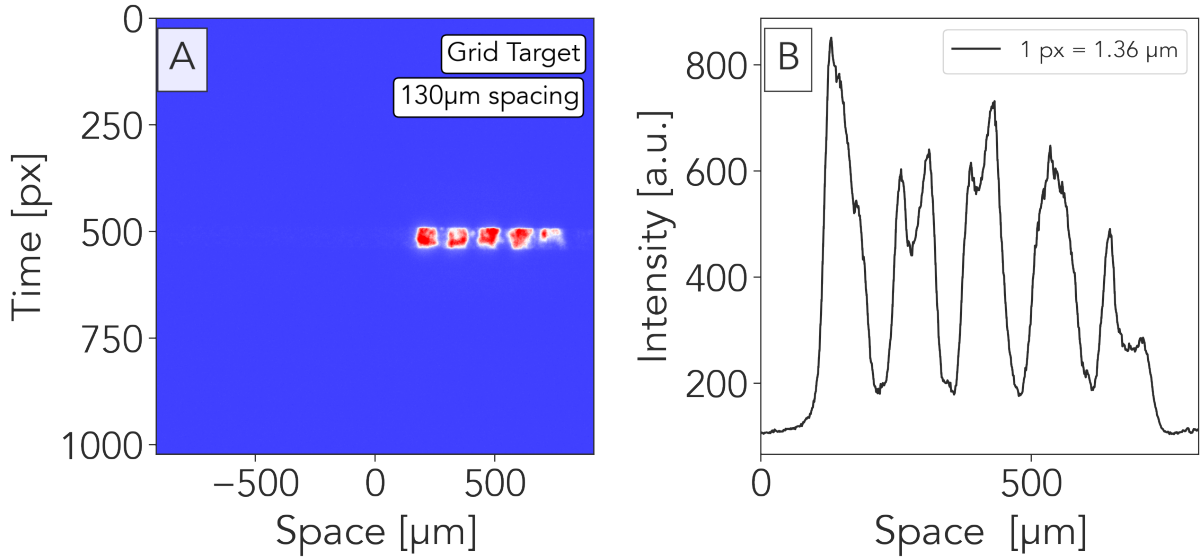

Figure 7.7: Grid target was used to test and optimise the optical path of the SOP. (A) typical raw data on streak camera in continuous mode. (B) Line out streaked grig sample, the spacing of the grid was $130\,\mu\mathrm{m}$ resulting in active field of view of $\approx 750\,\mu\mathrm{m}$

7.3.3 Hydro Simulation

To interpret our experimental results, we performed 1D radiative hydrodynamic simulations with the code ESTHER [Colombier et al., 2005] . The laser pulse was flat top in time with a plateau duration of 127 ns at FWHM at 3ω. In the simulation we utilised the SESAME tables of the following materials which consist our target SESAME table 7770 for parylene , SESAME table 2700 for gold , SESAME 7385 for quartz. The target composition consist of $8\,\mu\mathrm{m}$ Al/ $10\,\mu\mathrm{m}$ CH / $0.4\,\mu\mathrm{m}$ Au/ $100\,\mu\mathrm{m}$100 $\mathrm{SiO_2}$ indicates a shock breakout in gold layer at ∼0.65-0.7 ns. This is compatible with the breakout time observed on SOP signal. We do not observe any change in signal that could be representative of shock breakout in SiO2 (even on shots with 20 ns sweep window). It might have been easier to see it with VISAR diagnostics. Figure 7.9 shows the density map reproducing the shot SID : 5505 in this case the chock in SiO2 is expected to breakout at $\sim 9\,\mathrm{ns}$, which on the other hand indicates a shock velocity of the order of. $12.5\,\mathrm{km/s}$.

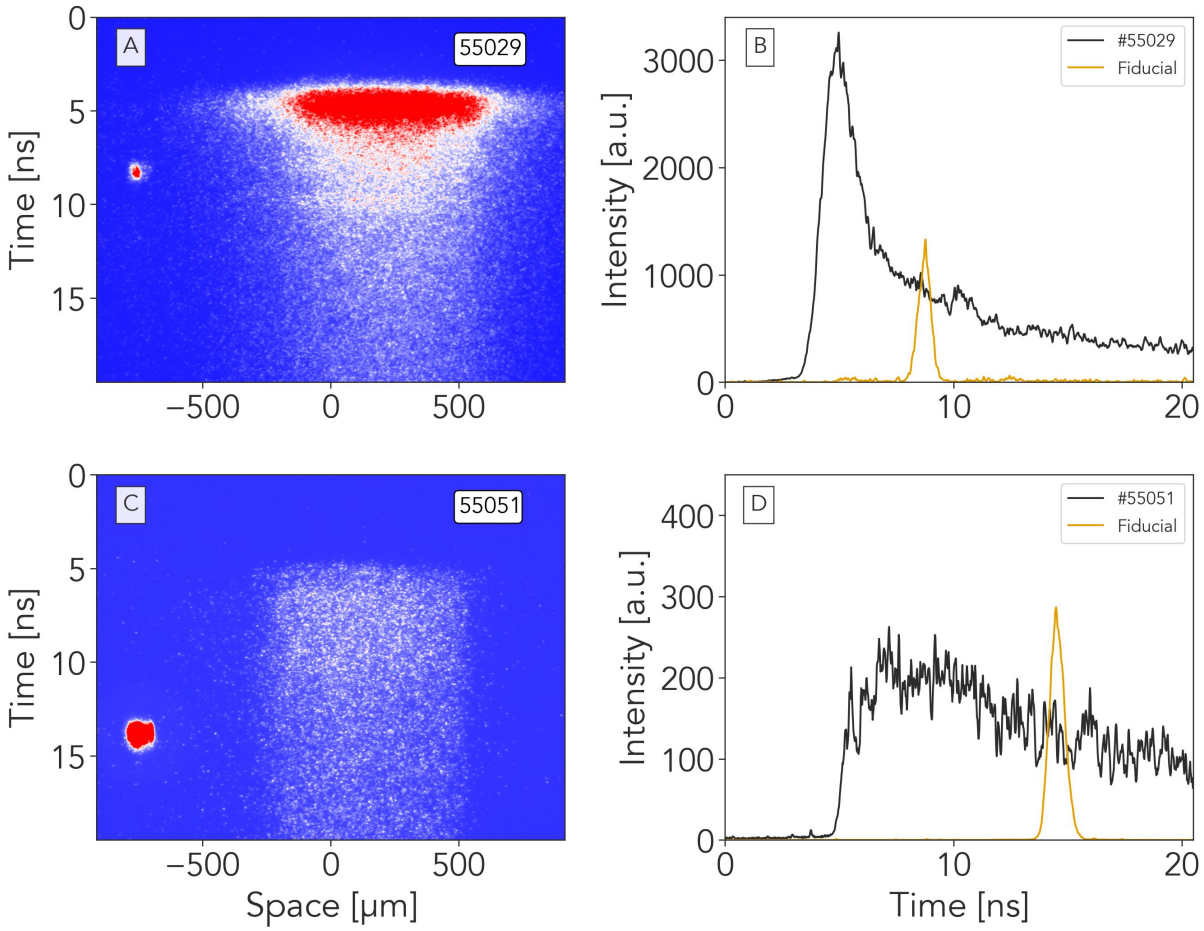

Figure 7.8: SOP streaked imaged obtained at PALS: (A) shot 55029 at laser energy of 113 J and sweep time of 20 ns however the halo of light was still observed at first instants ($\sim$ same time as laser, the delay between laser and fiducial was $5.3\,\mathrm{ns}$). (B) Result for shot 55051 with laser energy 33 J Halo of light was suppressed by adding an Al layer (8 μm). This thin metallic layer allowed us to get rid of shine-through effect the delay between laser and fiducial was $4.83\,\mathrm{ns}$. (C) and (D) are line outs taken form experimental images 55029 and 55051 respectively.

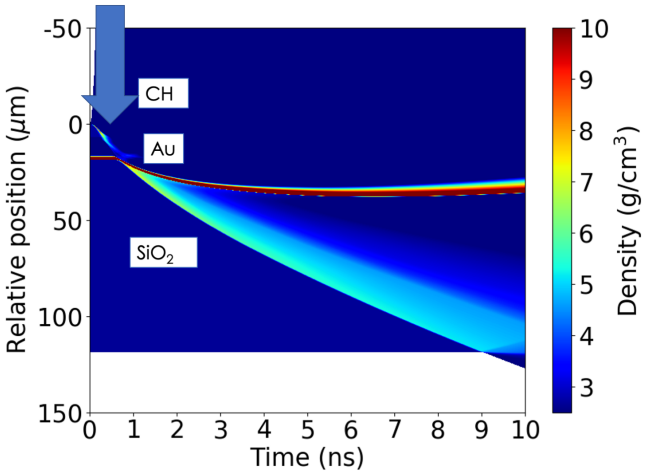

Figure 7.9: Density map from radiative hydrodynamic simulations using ESTHER code. Simulation indicate shock breakout in gold layer at $\sim$ 0.65-0.7 ns.The target and laser parameter where the same as the one stated in 7.3.3.

7.3.4 Derbis Characterisation

It is possible to collect the targets ejected fragments for example using gel or aerogel placed in a collector located few centimetres away from the target [E. Lescoute et al. 2012]. This is the strategy we will adopt in order to characterise the debris emission. Several collectors at different locations were setup to provide a more complete debris study. Additionally, one can use a fast camera for visualisation of the debris in flight. However the analysis of such detectors is not trivial since it requires to do a tomographic scans of the detector and then deduce the number of particles and projectile velocity. As a secondary diagnostic we implemented to replace the gel detectors, a Photonic Doppler Velocimetry (PDV) is a fibre-based diagnostic for the extreme conditions created by high-speed impact, explosive detonation, electrical pulsed power, and intense laser ablation. In this method, optical fibres are used to transport light (at frequency f_0) to a probe containing a lens that focuses the light onto the moving target. This same probe then collects a fraction of the light scattered or reflected from the moving surface and sends the Doppler-shifted light (frequency f_d) to the detector. A similar

amount of non-Doppler-shifted light (frequency f_0) is sent directly from the laser to the detector. The general setup of such device is shown in Figure 7.10 below. A beat signal is then generated at the detector by mixing the two signals at frequencies f_0 and f_d. After analysing the data using Fourier transform, it is possible to trace particles velocities. Several velocities can be measured at the same time with this technique (e.g. 4 particles with 4 different velocities will give 4 measured components). PDV technique can generally provide surface velocity measurements with only few $\%$ uncertainties. For particle velocity measurements, uncertainties are of the order of 5 -10%. PDV system is supported in a rack of dimensions $\sim 80x60x80\ cm^3$. It also requires an oscilloscope and an optical fibre. We used an oscilloscope of $6\,\mathrm{GHz}$ bandwidth and 4 channels. Typical results are shown in Figure 7.11. Using Fourier analysis procedure on the obtained spectrograph we get PDV velocity of the derbies ejected from the shocked sample, such results is shown in Figure 7.12. From this result we get information of the fast particles population from two probes placed the 0 and 20 degrees. Fast particles (from front or rear side). These fast particles quickly leave the field of observation. Very fast particles are detected $1\,\mu\mathrm{s}$ after slower ones (500 m/s).

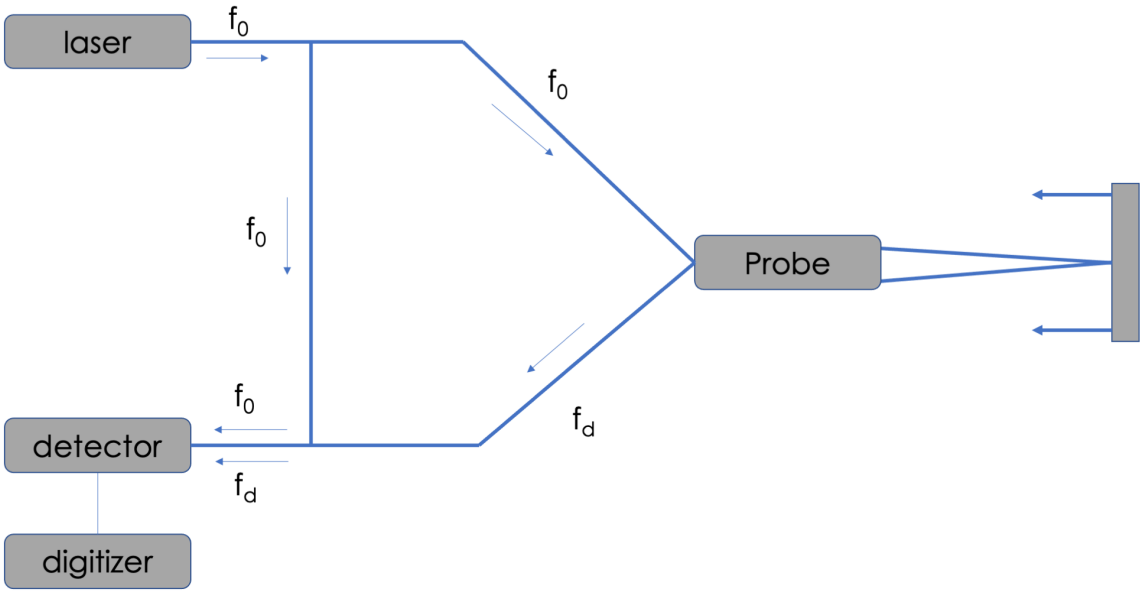

Figure 7.10: PDV velocimeter working principle

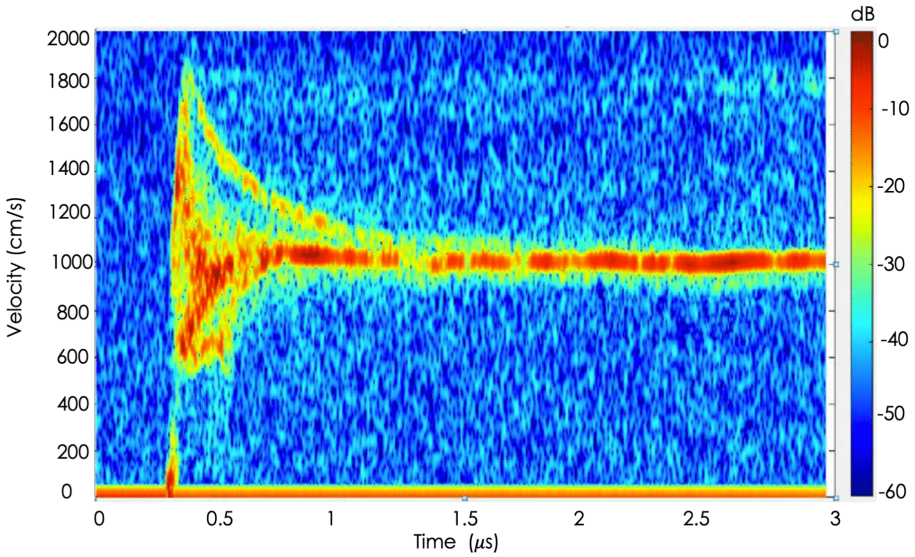

Figure 7.11: Typical PDV spectrogram obtained in our experiment.

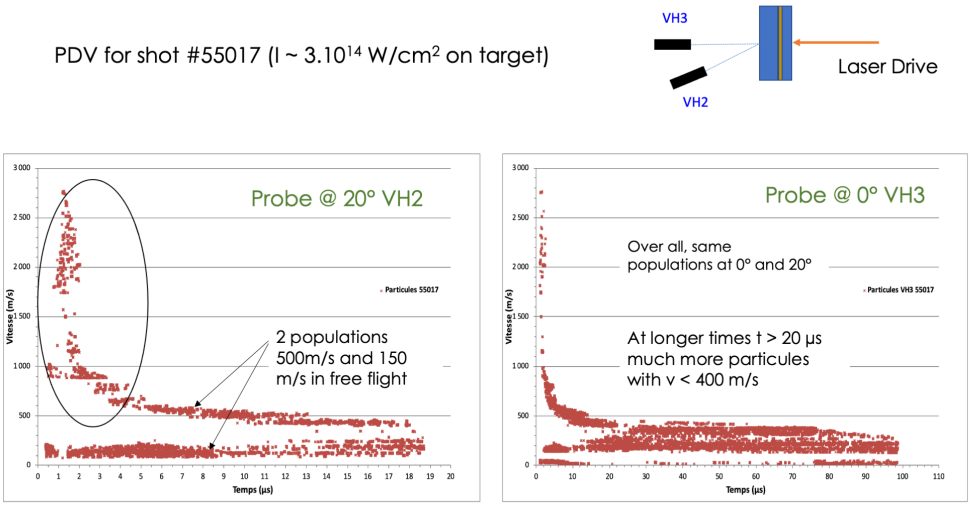

Figure 7.12: Results from PDV for shot #55017 the laser intensity was $\approx 3x10^{14}\ W/cm^2$ on target with the fibres placed to look at two different angles 0 and 20 degrees respectively.

7.4 Conclusions and Perspectives

In this final chapter we have reported on the capabilities (e.g. chances to collect data with small uncertainties), challenges (e.g. HRR targetry, URR diagnostics etc.) on new upcoming high-power and high repetition rate laser facility. Which will be part of ELI pillar in Europe and a unique facility if its kind. For this particular case we designed a preliminary experimental campaign at PALS laser facility to test the feasibility of such experimental study and the challenges we will face. Here we point out some of the main issues such as: high repetition rate target design and alignment process and optimisation, optical diagnostics (VISAR - SOP - SSOP etc.), debris characterisation which have to be taken in consideration in order to avoid optics damage and laser parameter optimisation (beam transport, pulse shaping, energy monitoring etc.). Such experimental platform will allow research groups to study physics problem in many interdisciplinary areas. Finally we present preliminary held at PALS laser facility which indicate that careful optimisation for each particular diagnostic is necessary.

Conclusion and perspectives

Contents

I . Conclusion

This objective of this thesis is to give an overview of the description appropriate equation of state (EOS) data is of high interest in the growing field of high energy density physics, warm dense matter, material science and especially essential for hydrodynamic simulation codes. Accurate EOS models, relating the thermodynamic state variables of a material, are essential to materials science, plasma and high energy density physics and warm dense matter studies since they are required to enforce the conservation laws in multi-physics simulations. In high energy density physics applications, the EOS must describe the material response over huge ranges of conditions covering the full variety of phases from crystalline or amorphous solid to ionized plasma. The large range of conditions and their extreme nature make it impossible to completely explore the EOS experimentally and so researchers must rely on theoretical calculations, bench-marked against experiments at a few temperature and density points.Where data do not exist, confidence in EOS models can be built by comparing calculations from fundamentally different approaches (ab-initio DFT, TF models of electron gas). This process is essential to the development of reliable EOS models.

In ***Chapter 1*** we described the main motivation that drive the study of the equation of state and the key factors that are keeping this domain ongoing for decades. Then we pinpoint the importance of the EOS and the warn dense matter which can be created in laboratory conditions. The key role of EOS in ICF and WDM research. Then we do a brief introduction to Laser matter interaction mechanism followed by ablation when laser beam is focused onto a solid multilayered target in planar geometry. Finally we described the basic scaling laws with respect to laser intensity, from which we can have an estimate of the ablation pressure and the mas ablation rate of the laser drive. A good understanding of the hydrodynamic of the shocks in the context of dynamic compression of layered targets is also necessary.

In ***Chapter 2***, the basic shock physics and the hydrodynamics are presented and the Impedance mismatch method was addressed. In this context the coupled python with FORTRAN routines responsible for handling tabulated data form the SESAME EOS database for different simple material and mixtures has been developed. This tool allows to calculate the shock polar curves (Hugoniot curves) also able to extract iso-S-expansion (RELAXATION) curves and iso-S-compression curves and many other options 11 in total. It has been used to obtain all the possible shock state from the standard material using the relaxation curves.

In the ***Chapter 3***, time resolved diagnostics such as velocity interferometry system for any reflector (VISAR) and streaked optical pyrometry (SOP) have been implemented as the main diagnostic platform to measure the equation of state of the shocked samples. One dimensional radiative hydrodynamic code MULTI and density functional theory (DFT) simulation tools are addressed. (VISAR) measures the velocity of a moving surface by recording its Doppler wavelength shift. SOP is responsible for the measurement of the self emission of the shocked target. On the other hand the Hydrodynamic simulations are necessary in order to design an experimental campaign on EOS study in planar geometry and compare the numerical results with the experiment. Furthermore due to good shock planarity in our experiment the 1D Hydro was sufficient to reproduce well the experimental results no need for 2D which are computationally expensive

studies.

In the ***Chapter 4*** Experiment have been designed and realised at PHELIX GSI laser facility using layered targets in planar geometry. In this experiment multilayered targets of different diamond thicknesses ranging from (250 -μm to $270\,\mu$m) have ben irradiated with long pulse 1.3 ns, of wavelength of $527\,\mu$m resulting in peak intensity of the order of $8\times10^{13}\,\mathrm{W/cm^2}$ to $9\times10^{13}\,\mathrm{W/cm^2}$. Diamond is a leading candidate as ablator to be used in implosion experiments related to inertial confinement fusion. The behaviour of Diamond at very large pressures is of interest for astrophysics and planetology. On the rear surface of the diamond $25\,\mu$m Ni step was placed. This type of target design allows to measure both the shock transit time in diamond and Ni using both VISAR and SOP and the free surface velocity of diamond and nickel surfaces after the shock breakout. Our measurements show that for the pressures obtained in diamond (between 3 and $9\,\mathrm{Mbar}$), the propagation of the shock induces a reflecting state of the material. Radiative hydrodynamic simulations using MULTI 1D code have been used for the interpretation of experimental data and in the initial design of the experiment proposed at PHELIX GSI in planar geometry.

In ***Chapter 5***, we presented equation of state study of water samples at two different high power laser facilities (*GEKKO XII* in Japan and *PHELIX* at GSI in Germany) with interest in planetary astrophysics. Both experimental campaigns were designed using MULTI 1D radiative hydrodynamic code in plane geometry. The water cells had a standard material which allowed us to use the Impedance Mismatch method in order to obtain the state of the compressed water. VISAR and SOP were the primary optical diagnostics. The velocity and temperature profiles were analysed using NEUTRINO tool and we compare our results with tabulated SESAME data and experimental results form other related works. We observed good agreement with certain EOS models.

In the ***Chapter 6***, we present ab-initio calculations on LiH system based on DFT and crystal structure optimisation techniques. LiH is interesting material for hydrogen storage technologies particularly in the aviation field and because of their use in nuclear industry. In addition, LiH offers a perfect system to study the crossover between quan-

tum and classical effects using available Density Functional Theory (DFT) codes and variational Monte Carlo simulations. We compare ab-initio calculation off the B1−B2 phase with random crystal structure prediction results were we utilised CALYPSO code coupled with Quantum Espresso DFT code. An extensive study have been done with different formula unit systems (1, 4 and 8) at four different target pressures 100, 200, 300 and 350 GPa respectively. The structures are then compared to the static B1−B2 phase in terms of enthalpy difference with respect to B1 phase. Concluding a dedicated experimental campaign to study the equation of state of LiH at different thermodynamic conditions must be carried out with the possibility to detect or not the B1−B2 phase transformation, also check whether or not the metastable structure can be measured in the experiment.

Finally in ***Chapter 7***, we present a preliminary results on high repetition rate and high energy laser pulses of the order of kJ focused on targets to generate plasma. Up to now such high energy laser system are affected by very low repetition rate. Due to the advance-met of laser technology new classes of laser systems are emerging (such laser facility is on the the pillars of ELI beam-line network) in Prague. The preliminary experiment was held at PALS laser facility in Prague. Special automated target mount was design from the target lab at GSI in order to mimic the HRR experiment. Main issue from such targets is the accumulated debris that is ejected from the target and is scattered around the interaction chamber onto the diagnostics lines. We list several issues that must be taken into account in such experimental campaign (electromagnetic pulse (EMP), data base management, system management, diagnostics for HRR, activation and target development).

Bibliography

[Ancilotto et al., 1997] Ancilotto, F., Chiarotti, G. L., Scandolo, S., and Tosatti, E. (1997). Dissociation of methane into hydrocarbons at extreme (planetary) pressure and temperature. *Science*, 275(5304):1288–1290.

[Antonelli et al., 2019] Antonelli, L., Barbato, F., Mancelli, D., Trela, J., Zeraouli, G., Boutoux, G., Neumayer, P., Atzeni, S., Schiavi, A., Volpe, L., Bagnoud, V., Brabetz, C., Zielbauer, B., Bradford, P., Woolsey, N., Borm, B., and Batani, D. (2019). X-ray phase-contrast imaging for laser-induced shock waves. *EPL (Europhysics Letters)*, 125(3):35002.

[Atzeni and Meyer-ter Vehn, 2004] Atzeni, S. and Meyer-ter Vehn, J. (2004). *The Physics of Inertial Fusion: BeamPlasma Interaction, Hydrodynamics, Hot Dense Matter*. Oxford University Press, Oxford.

[Banger et al., 2018] Banger, S., Nayak, V., and Verma, U. P. (2018). Hydrogen storage in lithium hydride: A theoretical approach. *Journal of Physics and Chemistry of Solids*, 115:6–17.

[Barker and Hollenbach, 1972] Barker, L. M. and Hollenbach, R. E. (1972). Laser interferometer for measuring high velocities of any reflecting surface. *Journal of Applied Physics*, 43(11):4669–4675.

[Barker and Schuler, 1974] Barker, L. M. and Schuler, K. W. (1974). Correction to the velocity-per-fringe relationship for the visar interferometer. *Journal of Applied Physics*, 45(8):3692–3693.

[Basov et al., 1985] Basov, N. G., Gus'kov, S. Y., Danilova, G. V., Demchenko, N. N., Zmitrenko, N. V., Karpov, V. Y., Mishchenko, T. V., Rozanov, V. B., and Samarskiĭ, A. A. (1985). Thermonuclear yield of targets under the action of high-power short-wavelength ($\lambda \leq 1\mu$) lasers. *Soviet Journal of Quantum Electronics*, 15(6):852–855.

[Basov et al., 1992] Basov, N. G., Gus'kov, S. Y., and Feokistov, L. P. (1992). Thermonuclear gain of ICF targets with direct heating of ignitor. *Journal of Soviet Laser Research*, 13(5):396–399.

[Batani et al., 2001] Batani, D., Balducci, A., Nazarov, W., Löwer, T., Hall, T., Koenig, M., Faral, B., Benuzzi, A., and Temporal, M. (2001). Use of low-density foams as pressure amplifiers in equation-of-state experiments with laser-driven shock waves. *Phys. Rev. E*, 63:046410.

[Batani et al., 2015a] Batani, D., Jakubowska, K., Benuzzi-Mounaix, A., Cavazzoni, C., Danson, C., Hall, T., Kimpel, M., Neely, D., Pasley, J., Gloahec, M. R. L., and Telaro, B. (2015a). Refraction index of shock compressed water in the megabar pressure range. *EPL (Europhysics Letters)*, 112(3):36001.

[Batani et al., 2015b] Batani, D., Jakubowska, K., Benuzzi-Mounaix, A., Cavazzoni, C., Danson, C., Hall, T., Kimpel, M., Neely, D., Pasley, J., Gloahec, M. R. L., and Telaro, B. (2015b). Refraction index of shock compressed water in the megabar pressure range. *EPL (Europhysics Letters)*, 112(3):36001.

[Batani et al., 2004] Batani, D., Strati, F., Stabile, H., Tomasini, M., Lucchini, G., Ravasio, A., Koenig, M., Benuzzi-Mounaix, A., Nishimura, H., Ochi, Y., Ullschmied, J., Skala, J., Kralikova, B., Pfeifer, M., Kadlec, C., Mocek, T., Präg, A., Hall, T., Mi-

lani, P., Barborini, E., and Piseri, P. (2004). Hugoniot data for carbon at megabar pressures. *Phys. Rev. Lett.*, 92:065503.

[Behunin et al., 2014] Behunin, R., Dalvit, D., Decca, R., Genet, C., Jung, I., Lambrecht, A., Liscio, A., López, D., Reynaud, S., Schnoering, G., Voisin, G., Zeng, Y., Holst, B., Recoules, V., Mazevet, S., Torrent, M., Ng, A., Chen, Z., Kirkwood, S., Sametoglu, V., Reid, M., and Tsui, Y. (2014). Ab initio model of optical properties of two-temperature warm dense matter. *Physical Review B: Condensed Matter and Materials Physics (1998-2015)*, 90(3).

[Benedetti et al., 1999] Benedetti, L. R., Nguyen, J. H., Caldwell, W. A., Liu, H., Kruger, M., and Jeanloz, R. (1999). Dissociation of ch4 at high pressures and temperatures: Diamond formation in giant planet interiors? *Science*, 286(5437):100–102.

[Benuzzi et al., 1998] Benuzzi, A., Koenig, M., Faral, B., Krishnan, J., Pisani, F., Batani, D., Bossi, S., Beretta, D., Hall, T., Ellwi, S., Hüller, S., Honrubia, J., and Grandjouan, N. (1998). Preheating study by reflectivity measurements in laser-driven shocks. *Physics of Plasmas*, 5(6):2410–2420.

[Benuzzi-Mounaix et al., 2004] Benuzzi-Mounaix, A., Koenig, M., Huser, G., Faral, B., Grandjouan, N., Batani, D., Henry, E., Tomasini, M., Hall, T. A., and Guyot, F. (2004). Generation of a double shock driven by laser. *Phys. Rev. E*, 70:045401.

[Betti and Hurricane, 2016] Betti, R. and Hurricane, O. A. (2016). Inertial-confinement fusion with lasers. *Nature Physics*, 12(5):435–448.

[Birch, 1947] Birch, F. (1947). Finite elastic strain of cubic crystals. *Phys. Rev.*, 71:809–824.

[Biswas et al., 1984] Biswas, R., Martin, R. M., Needs, R. J., and Nielsen, O. H. (1984). Complex tetrahedral structures of silicon and carbon under pressure. *Phys. Rev. B*, 30:3210–3213.

[Biswas et al., 2019] Biswas, S., Errea, I., Calandra, M., Mauri, F., and Scandolo, S. (2019). Ab initio study of the lih phase diagram at extreme pressures and temperatures. *Phys. Rev. B*, 99:024108.

[Blöchl, 1994] Blöchl, P. E. (1994). Projector augmented-wave method. *Phys. Rev. B*, 50:17953–17979.

[Bloomquist and Sheffield, 1983] Bloomquist, D. D. and Sheffield, S. A. (1983). Optically recording interferometer for velocity measurements with subnanosecond resolution. *Journal of Applied Physics*, 54(4):1717–1722.

[Boehler, 2005] Boehler, R. (2005). Diamond cells and new materials. *Materials Today*, 8(11):34–42.

[Boehly et al., 2011] Boehly, T. R., Goncharov, V. N., Seka, W., Barrios, M. A., Celliers, P. M., Hicks, D. G., Collins, G. W., Hu, S. X., Marozas, J. A., and Meyerhofer, D. D. (2011). Velocity and timing of multiple spherically converging shock waves in liquid deuterium. *Phys. Rev. Lett.*, 106:195005.

[Boehly et al., 2009] Boehly, T. R., Munro, D., Celliers, P. M., Olson, R. E., Hicks, D. G., Goncharov, V. N., Collins, G. W., Robey, H. F., Hu, S. X., Morozas, J. A., Sangster, T. C., Landen, O. L., and Meyerhofer, D. D. (2009). Demonstration of the shock-timing technique for ignition targets on the national ignition facility. *Physics of Plasmas*, 16(5):056302.

[Bolis et al., 2016] Bolis, R. M., Morard, G., Vinci, T., Ravasio, A., Bambrink, E., Guarguaglini, M., Koenig, M., Musella, R., Remus, F., Bouchet, J., Ozaki, N., Miyanishi, K., Sekine, T., Sakawa, Y., Sano, T., Kodama, R., Guyot, F., and Benuzzi-Mounaix, A. (2016). Decaying shock studies of phase transitions in mgo-sio2 systems: Implications for the super-earths' interiors. *Geophysical Research Letters*, 43(18):9475–9483.

[Bolme and Ramos, 2013] Bolme, C. A. and Ramos, K. J. (2013). Line-imaging velocimetry for observing spatially heterogeneous mechanical and chemical re-

sponses in plastic bonded explosives during impact. *Review of Scientific Instruments*, 84(8):083903.

[Bonitz et al., 2020] Bonitz, M., Dornheim, T., Moldabekov, Z. A., Zhang, S., Hamann, P., Kählert, H., Filinov, A., Ramakrishna, K., and Vorberger, J. (2020). Ab initio simulation of warm dense matter. *Physics of Plasmas*, 27(4):042710.

[Born and Oppenheimer, 1927] Born, M. and Oppenheimer, R. (1927). Zur quantentheorie der molekeln. *Annalen der Physik*, 389(20):457–484. PDF of an english translation by S.M. Blinder is available.

[Boronat et al., 2004] Boronat, J., Cazorla, C., Colognesi, D., and Zoppi, M. (2004). Quantum hydrogen vibrational dynamics in lih: Neutron-scattering measurements and variational monte carlo simulations. *Phys. Rev. B*, 69:174302.

[Bossi et al., 1997] Bossi, S., Hall, T. A., Mahdieh, M., Batani, D., Koenig, M., Krishnan, J., Benuzzi, A., Boudenne, J. M., and Lower, T. (1997). Determination of the color temperature in laser-produced shocks. *Laser and Particle Beams*, 15(4):485–493.

[Bradley et al., 2004] Bradley, D., K., Eggert, J. H., Hicks, D. G., Celliers, P. M., Moon, S. J., Cauble, R. C., and Collins, G. W. (2004). Shock compressing diamond to a conducting fluid. *Phys. Rev. Lett.*, 93:195506.

[Brygoo et al., 2015] Brygoo, S., Millot, M., Loubeyre, P., Lazicki, A. E., Hamel, S., Qi, T., Celliers, P. M., Coppari, F., Eggert, J. H., Fratanduono, D. E., Hicks, D. G., Rygg, J. R., Smith, R. F., Swift, D. C., Collins, G. W., and Jeanloz, R. (2015). Analysis of laser shock experiments on precompressed samples using a quartz reference and application to warm dense hydrogen and helium. *Journal of Applied Physics*, 118(19):195901.

[Bundy, 1989] Bundy, F. (1989). Pressure-temperature phase diagram of elemental carbon. *Physica A: Statistical Mechanics and its Applications*, 156(1):169 – 178.

[Cavalleri et al., 2002] Cavalleri, A., Sokolowski-Tinten, K., von der Linde, D., Spagnolatti, I., Bernasconi, M., Benedek, G., Podestà, A., and Milani, P. (2002). Generation of the low-density liquid phase of carbon by non-thermal melting of fullerite. *Europhysics Letters (EPL)*, 57(2):281–287.

[Cavazzoni et al., 1999] Cavazzoni, C., Chiarotti, G. L., Scandolo, S., Tosatti, E., Bernasconi, M., and Parrinello, M. (1999). Superionic and metallic states of water and ammonia at giant planet conditions. *Science*, 283(5398):44–46.

[Celliers et al., 2004a] Celliers, P. M., Bradley, D. K., Collins, G. W., Hicks, D. G., Boehly, T. R., and Armstrong, W. J. (2004a). Line-imaging velocimeter for shock diagnostics at the omega laser facility. *Review of Scientific Instruments*, 75(11):4916–4929.

[Celliers et al., 2004b] Celliers, P. M., Collins, G. W., Hicks, D. G., Koenig, M., Henry, E., Benuzzi-Mounaix, A., Batani, D., Bradley, D. K., Da Silva, L. B., Wallace, R. J., Moon, S. J., Eggert, J. H., Lee, K. K. M., Benedetti, L. R., Jeanloz, R., Masclet, I., Dague, N., Marchet, B., Rabec Le Gloahec, M., Reverdin, C., Pasley, J., Willi, O., Neely, D., and Danson, C. (2004b). Electronic conduction in shock-compressed water. *Physics of Plasmas*, 11(8):L41–L44.

[Chen et al., 2020] Chen, P., Hu, R., Zhou, H., Tao, Z., Gao, G., He, K., Wang, T., Tian, J., Yi, T., Lv, M., and et al. (2020). Numerical investigation of radiation ablation and acceleration of high-density carbon foils. *Laser and Particle Beams*, 38(4):239–243.

[Chen et al., 2016] Chen, Y. M., Chen, X. R., Wu, Q., Geng, H. Y., Yan, X. Z., Wang, Y. X., and Wang, Z. W. (2016). Compression and phase diagram of lithium hydrides at elevated pressures and temperatures by first-principles calculation. *Journal of Physics D: Applied Physics*, 49(35):355305.

[Chen et al., 2021] Chen, Z., Na, X., Curry, C. B., Liang, S., French, M., Descamps, A., DePonte, D. P., Koralek, J. D., Kim, J. B., Lebovitz, S., Nakatsutsumi, M., Ofori-Okai, B. K., Redmer, R., Roedel, C., Schörner, M., Skruszewicz, S., Sperling, P., Toleikis,

S., Mo, M. Z., and Glenzer, S. H. (2021). Observation of a highly conductive warm dense state of water with ultrafast pump–probe free-electron-laser measurements. *Matter and Radiation at Extremes*, 6(5):054401.

[Clark et al., 2010] Clark, D. S., Haan, S. W., Hammel, B. A., Salmonson, J. D., Callahan, D. A., and Town, R. P. J. (2010). Plastic ablator ignition capsule design for the national ignition facility. *Physics of Plasmas*, 17(5):052703.

[Colombier et al., 2005] Colombier, J. P., Combis, P., Bonneau, F., Le Harzic, R., and Audouard, E. (2005). Hydrodynamic simulations of metal ablation by femtosecond laser irradiation. *Phys. Rev. B*, 71:165406.

[Connerney et al., 1992] Connerney, J., Acuña, M. H., and Ness, N. F. (1992). The magnetic field of neptune. *Advances in Space Research*, 12(8):239–248.

[Connerney et al., 1987] Connerney, J. E. P., Acuña, M. H., and Ness, N. F. (1987). The magnetic field of uranus. *Journal of Geophysical Research: Space Physics*, 92(A13):15329–15336.

[D. Saumon, 1995] D. Saumon, G. Chabrier, H. H. (1995). An equation of state for low-mass stars and giant planets. *APJS*, 99:713.

[Dahmani, 1993] Dahmani, F. (1993). Experimental scaling laws for mass-ablation rate, ablation pressure in planar laser-produced plasmas with laser intensity, laser wavelength, and target atomic number. *Journal of Applied Physics*, 74(1):622–634.

[Dalladay-Simpson P., 2016] Dalladay-Simpson P., Howie R. T., G. E. (2016). Evidence for a new phase of dense hydrogen above 325 gigapascals. *Nature*, 529:63.

[Dammak et al., 2012] Dammak, H., Antoshchenkova, E., Hayoun, M., and Finocchi, F. (2012). Isotope effects in lithium hydride and lithium deuteride crystals by molecular dynamics simulations. *J. Phys.: Condens. Matter*, 24(43):435402.

[Dias and Silvera, 2017] Dias, R. P. and Silvera, I. F. (2017). Observation of the wigner-huntington transition to metallic hydrogen. *Science*, 355(6326):715–718.

[Dolan et al., 2007] Dolan, D. H., Knudson, M. D., Hall, C. A., and Deeney, C. (2007). A metastable limit for compressed liquid water. *Nature Physics*, 3(5):339–342.

[Eberhart and Kennedy, 1995] Eberhart, R. and Kennedy, J. (1995). A new optimizer using particle swarm theory. In *MHS'95. Proceedings of the Sixth International Symposium on Micro Machine and Human Science*, pages 39–43.

[Edwards et al., 2013] Edwards, M. J., Patel, P. K., Lindl, J. D., Atherton, L. J., Glenzer, S. H., Haan, S. W., Kilkenny, J. D., Landen, O. L., Moses, E. I., Nikroo, A., Petrasso, R., Sangster, T. C., Springer, P. T., Batha, S., Benedetti, R., Bernstein, L., Betti, R., Bleuel, D. L., Boehly, T. R., Bradley, D. K., Caggiano, J. A., Callahan, D. A., Celliers, P. M., Cerjan, C. J., Chen, K. C., Clark, D. S., Collins, G. W., Dewald, E. L., Divol, L., Dixit, S., Doeppner, T., Edgell, D. H., Fair, J. E., Farrell, M., Fortner, R. J., Frenje, J., Gatu Johnson, M. G., Giraldez, E., Glebov, V. Y., Grim, G., Hammel, B. A., Hamza, A. V., Harding, D. R., Hatchett, S. P., Hein, N., Herrmann, H. W., Hicks, D., Hinkel, D. E., Hoppe, M., Hsing, W. W., Izumi, N., Jacoby, B., Jones, O. S., Kalantar, D., Kauffman, R., Kline, J. L., Knauer, J. P., Koch, J. A., Kozioziemski, B. J., Kyrala, G., LaFortune, K. N., Pape, S. L., Leeper, R. J., Lerche, R., Ma, T., MacGowan, B. J., MacKinnon, A. J., Macphee, A., Mapoles, E. R., Marinak, M. M., Mauldin, M., McKenty, P. W., Meezan, M., Michel, P. A., Milovich, J., Moody, J. D., Moran, M., Munro, D. H., Olson, C. L., Opachich, K., Pak, A. E., Parham, T., Park, H.-S., Ralph, J. E., Regan, S. P., Remington, B., Rinderknecht, H., Robey, H. F., Rosen, M., Ross, S., Salmonson, J. D., Sater, J., Schneider, D. H., Séguin, F. H., Sepke, S. M., Shaughnessy, D. A., Smalyuk, V. A., Spears, B. K., Stoeckl, C., Stoeffl, W., Suter, L., Thomas, C. A., Tommasini, R., Town, R. P., Weber, S. V., Wegner, P. J., Widman, K., Wilke, M., Wilson, D. C., Yeamans, C. B., and Zylstra, A. (2013). Progress towards ignition on the national ignition facility. *Physics of Plasmas*, 20(7):070501.

[Eggert et al., 2010a] Eggert, J. H., Hicks, D. G., Celliers, P. M., Bradley, D. K., McWilliams, R. S., Jeanloz, R., Miller, J. E., Boehly, T. R., and Collins, G. W. (2010a). Melting temperature of diamond at ultrahigh pressure. *Nature Physics*, 6(1):40–43.

[Eggert et al., 2010b] Eggert, J. H., Hicks, D. G., Celliers, P. M., Bradley, D. K., McWilliams, R. S., Jeanloz, R., Miller, J. E., Boehly, T. R., and Collins, G. W. (2010b). Melting temperature of diamond at ultrahigh pressure. *Nature Physics*, 6(1):40–43.

[Fahy and Louie, 1987] Fahy, S. and Louie, S. G. (1987). High-pressure structural and electronic properties of carbon. *Phys. Rev. B*, 36:3373–3385.

[Faik et al., 2018] Faik, S., Tauschwitz, A., and Iosilevskiy, I. (2018). The equation of state package feos for high energy density matter. *Computer Physics Communications*, 227:117–125.

[Falk, 2018] Falk, K. (2018). Experimental methods for warm dense matter research. *High Power Laser Science and Engineering*, 6:e59.

[Flacco A., 2011] Flacco A., V. T. (2011). Neutrino: A light, expandable and full featured image analysis tool for research. *https://github.com/NeutrinoToolkit/Neutrino*.

[Fox, 2007] Fox, M. (2007). Hot "ice" may cover recently discovered planet. *Science News (Scientific American.com)*.

[French et al., 2012] French, M., Becker, A., Lorenzen, W., Nettelmann, N., Bethkenhagen, M., Wicht, J., and Redmer, R. (2012). AB INITIO SIMULATIONS FOR MATERIAL PROPERTIES ALONG THE JUPITER ADIABAT. *The Astrophysical Journal Supplement Series*, 202(1):5.

[French et al., 2016] French, M., Desjarlais, M. P., and Redmer, R. (2016). Ab initio calculation of thermodynamic potentials and entropies for superionic water. *Phys. Rev. E*, 93:022140.

[French et al., 2009] French, M., Mattsson, T. R., Nettelmann, N., and Redmer, R. (2009). Equation of state and phase diagram of water at ultrahigh pressures as in planetary interiors. *Phys. Rev. B*, 79:054107.

[Fujioka et al., 2012] Fujioka, S., Zhang, Z., Yamamoto, N., Ohira, S., Fujii, Y., Ishihara, K., Johzaki, T., Sunahara, A., Arikawa, Y., Shigemori, K., Hironaka, Y., Sakawa, Y., Nakata, Y., Kawanaka, J., Nagatomo, H., Shiraga, H., Miyanaga, N., Norimatsu, T., Nishimura, H., and Azechi, H. (2012). High-energy-density plasmas generation on GEKKO-LFEX laser facility for fast-ignition laser fusion studies and laboratory astrophysics. *Plasma Physics and Controlled Fusion*, 54(12):124042.

[Gamboa et al., 2015] Gamboa, E. J., Fletcher, L. B., Lee, H. J., Zastrau, U., Galtier, E., MacDonald, M. J., Gauthier, M., Vorberger, J., Gericke, D. O., Granados, E., Hastings, J. B., and Glenzer, S. H. (2015). Single-shot measurements of plasmons in compressed diamond with an x-ray laser. *Physics of Plasmas*, 22(5):056319.

[Garban-Labaune et al., 1982] Garban-Labaune, C., Fabre, E., Max, C. E., Fabbro, R., Amiranoff, F., Virmont, J., Weinfeld, M., and Michard, A. (1982). Effect of laser wavelength and pulse duration on laser-light absorption and back reflection. *Phys. Rev. Lett.*, 48:1018–1021.

[George and Saxena, 2010] George, L. and Saxena, S. K. (2010). Structural stability of metal hydrides, alanates and borohydrides of alkali and alkali- earth elements: A review. *International Journal of Hydrogen Energy*, 35(11):5454–5470. 3rd Argentinean and 2nd Latin American Congress inHydrogen and Sustainable Energy Sources.

[Gerald I. Kerley, 2001] Gerald I. Kerley, L. C. (2001). Multicomponent-multiphase equation of state for carbon. *Sandia Report*, SAND2001-2619.

[Gerlich and Smith, 1974] Gerlich, D. and Smith, C. (1974). The pressure and temperature derivatives of the elastic moduli of lithium hydride. *Journal of Physics and Chemistry of Solids*, 35(12):1587–1592.

[Giannozzi et al., 2017] Giannozzi, P., Andreussi, O., Brumme, T., Bunau, O., Nardelli, M. B., Calandra, M., Car, R., Cavazzoni, C., Ceresoli, D., Cococcioni, M., Colonna, N., Carnimeo, I., Corso, A. D., de Gironcoli, S., Delugas, P., DiStasio, R. A., Ferretti, A., Floris, A., Fratesi, G., Fugallo, G., Gebauer, R., Gerstmann, U., Giustino, F., Gorni, T., Jia, J., Kawamura, M., Ko, H.-Y., Kokalj, A., Küçükbenli, E., Lazzeri, M., Marsili, M., Marzari, N., Mauri, F., Nguyen, N. L., Nguyen, H.-V., de-la Roza, A. O., Paulatto, L., Poncé, S., Rocca, D., Sabatini, R., Santra, B., Schlipf, M., Seitsonen, A. P., Smogunov, A., Timrov, I., Thonhauser, T., Umari, P., Vast, N., Wu, X., and Baroni, S. (2017). Advanced capabilities for materials modelling with quantum ESPRESSO. *Journal of Physics: Condensed Matter*, 29(46):465901.

[Giannozzi et al., 2009] Giannozzi, P., Baroni, S., Bonini, N., Calandra, M., Car, R., Cavazzoni, C., Ceresoli, D., Chiarotti, G. L., Cococcioni, M., Dabo, I., Corso, A. D., de Gironcoli, S., Fabris, S., Fratesi, G., Gebauer, R., Gerstmann, U., Gougoussis, C., Kokalj, A., Lazzeri, M., Martin-Samos, L., Marzari, N., Mauri, F., Mazzarello, R., Paolini, S., Pasquarello, A., Paulatto, L., Sbraccia, C., Scandolo, S., Sclauzero, G., Seitsonen, A. P., Smogunov, A., Umari, P., and Wentzcovitch, R. M. (2009). QUANTUM ESPRESSO: a modular and open-source software project for quantum simulations of materials. *Journal of Physics: Condensed Matter*, 21(39):395502.

[Giannozzi et al., 2020] Giannozzi, P., Baseggio, O., Bonfà, P., Brunato, D., Car, R., Carnimeo, I., Cavazzoni, C., de Gironcoli, S., Delugas, P., Ferrari Ruffino, F., Ferretti, A., Marzari, N., Timrov, I., Urru, A., and Baroni, S. (2020). Quantum espresso toward the exascale. *The Journal of Chemical Physics*, 152(15):154105.

[Glenzer et al., 2016] Glenzer, S. H., Fletcher, L. B., Lee, H. J., MacDonald, M. J., Zastrau, U., Gauthier, M., Gericke, D. O., Vorberger, J., Granados, E., Hastings, J. B., and Gamboa, E. J. (2016). Plasmon scattering probing of electronic states in diamond at extreme conditions. *SLAC-PUB-16770*, AC02-76SF00515(1270625).

[Goldman et al., 2009] Goldman, N., Reed, E. J., Kuo, I.-F. W., Fried, L. E., Mundy, C. J., and Curioni, A. (2009). Ab initio simulation of the equation of state and kinetics of shocked water. *The Journal of Chemical Physics*, 130(12):124517.

[Goncharov et al., 2006] Goncharov, V. N., Gotchev, O. V., Vianello, E., Boehly, T. R., Knauer, J. P., McKenty, P. W., Radha, P. B., Regan, S. P., Sangster, T. C., Skupsky, S., Smalyuk, V. A., Betti, R., McCrory, R. L., Meyerhofer, D. D., and Cherfils-Clérouin, C. (2006). Early stage of implosion in inertial confinement fusion: Shock timing and perturbation evolution. *Physics of Plasmas*, 13(1):012702.

[Gregor et al., 2016] Gregor, M. C., Boni, R., Sorce, A., Kendrick, J., McCoy, C. A., Polsin, D. N., Boehly, T. R., Celliers, P. M., Collins, G. W., Fratanduono, D. E., Eggert, J. H., and Millot, M. (2016). Absolute calibration of the omega streaked optical pyrometer for temperature measurements of compressed materials. *Review of Scientific Instruments*, 87(11):114903.

[Gregor et al., 2017] Gregor, M. C., Fratanduono, D. E., McCoy, C. A., Polsin, D. N., Sorce, A., Rygg, J. R., Collins, G. W., Braun, T., Celliers, P. M., Eggert, J. H., Meyerhofer, D. D., and Boehly, T. R. (2017). Hugoniot and release measurements in diamond shocked up to 26 mbar. *Phys. Rev. B*, 95:144114.

[Gregoryanz et al., 2020] Gregoryanz, E., Ji, C., Dalladay-Simpson, P., Li, B., Howie, R. T., and Mao, H.-K. (2020). Everything you always wanted to know about metallic hydrogen but were afraid to ask. *Matter and Radiation at Extremes*, 5(3):038101.

[Grover, 1979] Grover, R. (1979). Does diamond melt? *The Journal of Chemical Physics*, 71(9):3824–3829.

[Grumbach and Martin, 1996] Grumbach, M. P. and Martin, R. M. (1996). Phase diagram of carbon at high pressures and temperatures. *Phys. Rev. B*, 54:15730–15741.

[Grüneis, 2015] Grüneis, A. (2015). A coupled cluster and møller-plesset perturbation theory study of the pressure induced phase transition in the lih crystal. *The Journal of Chemical Physics*, 143(10):102817.

[Guarguaglini et al., 2019] Guarguaglini, M., Hernandez, J.-A., Okuchi, T., Barroso, P., Benuzzi-Mounaix, A., Bethkenhagen, M., Bolis, R., Brambrink, E., French, M., Fujimoto, Y., Kodama, R., Koenig, M., Lefevre, F., Miyanishi, K., Ozaki, N., Redmer, R., Sano, T., Umeda, Y., Vinci, T., and Ravasio, A. (2019). Laser-driven shock compression of "synthetic planetary mixtures" of water, ethanol, and ammonia. *Scientific Reports*, 9(1):10155.

[Guillot, 1999] Guillot, T. (1999). Interiors of giant planets inside and outside the solar system. *Science*, 286(5437):72–77.

[Hammel et al., 2010] Hammel, B., Haan, S., Clark, D., Edwards, M., Langer, S., Marinak, M., Patel, M., Salmonson, J., and Scott, H. (2010). High-mode rayleigh-taylor growth in nif ignition capsules. *High Energy Density Physics*, 6(2):171 – 178. ICHED 2009 - 2nd International Conference on High Energy Density Physics.

[He et al., 2019] He, Z., Jia, G., Zhang, F., Huang, X., Fang, Z., Dong, J., Shu, H., Ye, J., Xie, Z., Tu, Y., and et al. (2019). Calibration and verification of streaked optical pyrometer system used for laser-induced shock experiments. *High Power Laser Science and Engineering*, 7:e49.

[Hohenberg and Kohn, 1964] Hohenberg, P. and Kohn, W. (1964). Inhomogeneous electron gas. *Phys. Rev.*, 136:B864–B871.

[Horner et al., 2009] Horner, D. A., Lambert, F., Kress, J. D., and Collins, L. A. (2009). Transport properties of lithium hydride from quantum molecular dynamics and orbital-free molecular dynamics. *Phys. Rev. B*, 80:024305.

[Hu et al., 2018] Hu, S. X., Collins, L. A., Boehly, T. R., Ding, Y. H., Radha, P. B., Goncharov, V. N., Karasiev, V. V., Collins, G. W., Regan, S. P., and Campbell, E. M. (2018).

A review on ab initio studies of static, transport, and optical properties of polystyrene under extreme conditions for inertial confinement fusion applications. *Physics of Plasmas*, 25(5):056306.

[Hu et al., 2015] Hu, S. X., Goncharov, V. N., Boehly, T. R., McCrory, R. L., Skupsky, S., Collins, L. A., Kress, J. D., and Militzer, B. (2015). Impact of first-principles properties of deuterium–tritium on inertial confinement fusion target designs. *Physics of Plasmas*, 22(5):056304.

[Hu et al., 2008] Hu, S. X., Smalyuk, V. A., Goncharov, V. N., Knauer, J. P., Radha, P. B., Igumenshchev, I. V., Marozas, J. A., Stoeckl, C., Yaakobi, B., Shvarts, D., Sangster, T. C., McKenty, P. W., Meyerhofer, D. D., Skupsky, S., and McCrory, R. L. (2008). Studies of plastic-ablator compressibility for direct-drive inertial confinement fusion on omega. *Phys. Rev. Lett.*, 100:185003.

[Hurricane et al., 2014] Hurricane, O. A., Callahan, D. A., Casey, D. T., Dewald, E. L., Dittrich, T. R., Döppner, T., Barrios Garcia, M. A., Hinkel, D. E., Berzak Hopkins, L. F., Kervin, P., Kline, J. L., Pape, S. L., Ma, T., MacPhee, A. G., Milovich, J. L., Moody, J., Pak, A. E., Patel, P. K., Park, H.-S., Remington, B. A., Robey, H. F., Salmonson, J. D., Springer, P. T., Tommasini, R., Benedetti, L. R., Caggiano, J. A., Celliers, P., Cerjan, C., Dylla-Spears, R., Edgell, D., Edwards, M. J., Fittinghoff, D., Grim, G. P., Guler, N., Izumi, N., Frenje, J. A., Gatu Johnson, M., Haan, S., Hatarik, R., Herrmann, H., Khan, S., Knauer, J., Kozioziemski, B. J., Kritcher, A. L., Kyrala, G., Maclaren, S. A., Merrill, F. E., Michel, P., Ralph, J., Ross, J. S., Rygg, J. R., Schneider, M. B., Spears, B. K., Widmann, K., and Yeamans, C. B. (2014). The high-foot implosion campaign on the national ignition facility. *Physics of Plasmas*, 21(5):056314.

[Jakubowska et al., 2019] Jakubowska, K., Batani, D., Clerouin, J., and Siberchicot, B. (2019). Theoretical and experimental refraction index of shock compressed and pre-compressed water in the megabar pressure range. *EPL (Europhysics Letters)*, 126(5):56001.

[Jakubowska et al., 2021] Jakubowska, K., Mancelli, D., Benocci, R., Trela, J., Errea, I., Martynenko, A. S., Neumayer, P., Rosmej, O., Borm, B., Molineri, A., and et al. (2021). Reflecting laser-driven shocks in diamond in the megabar pressure range. *High Power Laser Science and Engineering*, 9:e3.

[Jaradat et al., 2017] Jaradat, R., Abu-Jafar, M., Abdelraziq, I., Khenata, R., Varshney, D., Omran, S. B., and Al-Qaisi, S. (2017). High-pressure structural phase transition and electronic properties of the alkali hydrides compounds xh (x = li, na). *Phase Transitions*, 90(9):914–927.

[Karsai et al., 2018] Karsai, F., Engel, M., Flage-Larsen, E., and Kresse, G. (2018). Electron–phonon coupling in semiconductors within the GW approximation. *New Journal of Physics*, 20(12):123008.

[Katagiri et al., 2020] Katagiri, K., Ozaki, N., Miyanishi, K., Kamimura, N., Umeda, Y., Sano, T., Sekine, T., and Kodama, R. (2020). Optical properties of shock-compressed diamond up to 550 gpa. *Phys. Rev. B*, 101:184106.

[Kemp and ter Vehn, 1998] Kemp, A. and ter Vehn, J. M. (1998). An equation of state code for hot dense matter, based on the qeos description. *Nuclear Instruments and Methods in Physics Research Section A: Accelerators, Spectrometers, Detectors and Associated Equipment*, 415(3):674–676.

[Kennedy and Eberhart, 1995] Kennedy, J. and Eberhart, R. (1995). Particle swarm optimization. In *Proceedings of ICNN'95 - International Conference on Neural Networks*, volume 4, pages 1942–1948 vol.4.

[Kimura et al., 2015] Kimura, T., Ozaki, N., Sano, T., Okuchi, T., Sano, T., Shimizu, K., Miyanishi, K., Terai, T., Kakeshita, T., Sakawa, Y., and Kodama, R. (2015). P-ρ-t measurements of h2o up to 260 gpa under laser-driven shock loading. *The Journal of Chemical Physics*, 142(16):164504.

[Knudson and Desjarlais, 2013] Knudson, M. D. and Desjarlais, M. P. (2013). Adiabatic release measurements in α-quartz between 300 and 1200 gpa: Characterization of α-quartz as a shock standard in the multimegabar regime. *Phys. Rev. B*, 88:184107.

[Knudson et al., 2012] Knudson, M. D., Desjarlais, M. P., Lemke, R. W., Mattsson, T. R., French, M., Nettelmann, N., and Redmer, R. (2012). Probing the interiors of the ice giants: Shock compression of water to 700 gpa and 3.8 $\mathrm{g/cm^3}$. *Phys. Rev. Lett.*, 108:091102.

[Koenig et al., 2005] Koenig, M., Benuzzi-Mounaix, A., Ravasio, A., Vinci, T., Ozaki, N., Lepape, S., Batani, D., Huser, G., Hall, T., Hicks, D., MacKinnon, A., Patel, P., Park, H. S., Boehly, T., Borghesi, M., Kar, S., and Romagnani, L. (2005). Progress in the study of warm dense matter. *Plasma Physics and Controlled Fusion*, 47(12B):B441–B449.

[Koenig et al., 1994] Koenig, M., Faral, B., Boudenne, J. M., Batani, D., Benuzzi, A., and Bossi, S. (1994). Optical smoothing techniques for shock wave generation in laser-produced plasmas. *Phys. Rev. E*, 50:R3314–R3317.

[Kondo and Asaumi, 1988] Kondo, Y. and Asaumi, K. (1988). Effect of pressure on the direct energy gap of lih. *Journal of the Physical Society of Japan*, 57(1):367–371.

[Kundrata et al., 2019] Kundrata, I., Fröhlich, K., Vančo, L., Mičušík, M., and Bachmann, J. (2019). Growth of lithium hydride thin films from solutions: Towards solution atomic layer deposition of lithiated films. *Beilstein Journal of Nanotechnology*, 10:1443–1451.

[Landen et al., 2020] Landen, O., Casey, D., DiNicola, J., Doeppner, T., Hartouni, E., Hinkel, D., Berzak Hopkins, L., Hohenberger, M., Kritcher, A., LePape, S., MacGowan, B., Maclaren, S., Meaney, K., Millot, M., Patel, P., Park, J., Pickworth, L., Robey, H., Ross, J., Yang, S., Zylstra, A., Baker, K., Callahan, D., Celliers, P., Edwards, M., Hurricane, O., Lindl, J., Moody, J., Ralph, J., Smalyuk, V., Thomas, C., Van Wonterghem,

B., and Weber, C. (2020). Yield and compression trends and reproducibility at nif*. *High Energy Density Physics*, 36:100755.

[LANL, 1992] LANL, T. G. (1992). Eos sesame tables developed at the los alamos laboratory (sesame report on the los alamos equation-of- state library, report no. lalp-83-4, 1983, and report la-ur-92-3407, 1992, t4 group lanl, los alamos). *Report LA-UR-92-3407*.

[Latimer et al., 2018] Latimer, K., Dwaraknath, S., Mathew, K., Winston, D., and Persson, K. A. (2018). Evaluation of thermodynamic equations of state across chemistry and structure in the materials project. *npj Computational Materials*, 4(1):40.

[Laudernet et al., 2004] Laudernet, Y., Clérouin, J., and Mazevet, S. (2004). Ab initio simulations of the electrical and optical properties of shock-compressed $\mathrm{sio_2}$. *Phys. Rev. B*, 70:165108.

[Lazicki et al., 2012] Lazicki, A., Loubeyre, P., Occelli, F., Hemley, R. J., and Mezouar, M. (2012). Static compression of lih to 250 gpa. *Phys. Rev. B*, 85:054103.

[Lei et al., 2021] Lei, H., Li, X., Lin, W., and Wang, K. (2021). Predicted metallization of hydrogen nanograins at low pressures. *Applied Physics Letters*, 119(12):121602.

[Li et al., 2017] Li, C.-C., Gong, M., Chen, X.-D., Li, S., Zhao, B.-W., Dong, Y., Guo, G.-C., and Sun, F.-W. (2017). Temperature dependent energy gap shifts of single color center in diamond based on modified varshni equation. *Diamond and Related Materials*, 74:119–124.

[Li et al., 2011] Li, H.-W., Yan, Y., Orimo, S.-i., Züttel, A., and Jensen, C. M. (2011). Recent progress in metal borohydrides for hydrogen storage. *Energies*, 4(1):185–214.

[Lindl, 1995] Lindl, J. (1995). Development of the indirect-drive approach to inertial confinement fusion and the target physics basis for ignition and gain. *Physics of Plasmas*, 2(11):3933–4024.

[Lindl and Moses, 2011] Lindl, J. D. and Moses, E. I. (2011). Special topic: Plans for the national ignition campaign (nic) on the national ignition facility (nif): On the threshold of initiating ignition experiments. *Physics of Plasmas*, 18(5):050901.

[Logothetidis et al., 1992] Logothetidis, S., Petalas, J., Polatoglou, H. M., and Fuchs, D. (1992). Origin and temperature dependence of the first direct gap of diamond. *Phys. Rev. B*, 46:4483–4494.

[Loubeyre et al., 1998] Loubeyre, P., Le Toullec, R., Hanfland, M., Ulivi, L., Datchi, F., and Hausermann, D. (1998). Equation of state of ^{7}LiH and ^{7}LiD from x-ray diffraction to 94 gpa. *Phys. Rev. B*, 57:10403–10406.

[Lu, 2002] Lu, H. (2002). Dynamic population strategy assisted particle swarm optimization in multiobjective evolutionary algorithm design. *IEEE Neural Network Society, IEEE NNS Student Research Grants*.

[Lyzenga et al., 1982] Lyzenga, G. A., Ahrens, T. J., Nellis, W. J., and Mitchell, A. C. (1982). The temperature of shock-compressed water. *The Journal of Chemical Physics*, 76(12):6282–6286.

[MacKinnon et al., 2014] MacKinnon, A. J., Meezan, N. B., Ross, J. S., Le Pape, S., Berzak Hopkins, L., Divol, L., Ho, D., Milovich, J., Pak, A., Ralph, J., Döppner, T., Patel, P. K., Thomas, C., Tommasini, R., Haan, S., MacPhee, A. G., McNaney, J., Caggiano, J., Hatarik, R., Bionta, R., Ma, T., Spears, B., Rygg, J. R., Benedetti, L. R., Town, R. P. J., Bradley, D. K., Dewald, E. L., Fittinghoff, D., Jones, O. S., Robey, H. R., Moody, J. D., Khan, S., Callahan, D. A., Hamza, A., Biener, J., Celliers, P. M., Braun, D. G., Erskine, D. J., Prisbrey, S. T., Wallace, R. J., Kozioziemski, B., Dylla-Spears, R., Sater, J., Collins, G., Storm, E., Hsing, W., Landen, O., Atherton, J. L., Lindl, J. D., Edwards, M. J., Frenje, J. A., Gatu-Johnson, M., Li, C. K., Petrasso, R., Rinderknecht, H., Rosenberg, M., Séguin, F. H., Zylstra, A., Knauer, J. P., Grim, G., Guler, N., Merrill, F., Olson, R., Kyrala, G. A., Kilkenny, J. D., Nikroo, A., Moreno, K., Hoover,

D. E., Wild, C., and Werner, E. (2014). High-density carbon ablator experiments on the national ignition facility. *Physics of Plasmas*, 21(5):056318.

[MAO, 1978] MAO, H. K. (1978). High-pressure physics: Sustained static generation of 1.36 to 1.72 megabars. *Science*, 200(4346):1145–1147.

[Mao and Hemley, 1994] Mao, H.-k. and Hemley, R. J. (1994). Ultrahigh-pressure transitions in solid hydrogen. *Rev. Mod. Phys.*, 66:671–692.

[Marshall et al., 2019] Marshall, M. C., Lazicki, A. E., Erskine, D., London, R. A., Fratanduono, D. E., Celliers, P. M., Eggert, J. H., Coppari, F., Swift, D. C., Sterne, P. A., Whitley, H. D., and Nilsen, J. (2019). Developing quartz and molybdenum as impedance-matching standards in the 100-mbar regime. *Phys. Rev. B*, 99:174101.

[Mattsson and Desjarlais, 2006] Mattsson, T. R. and Desjarlais, M. P. (2006). Phase diagram and electrical conductivity of high energy-density water from density functional theory. *Phys. Rev. Lett.*, 97:017801.

[Mazevet et al., 2019] Mazevet, S., Licari, A., Chabrier, G., and Potekhin, A. Y. (2019). Ab initio based equation of state of dense water for planetary and exoplanetary modeling. *A&A*, 621:A128.

[McMahon et al., 2012] McMahon, J. M., Morales, M. A., Pierleoni, C., and Ceperley, D. M. (2012). The properties of hydrogen and helium under extreme conditions. *Rev. Mod. Phys.*, 84:1607–1653.

[Methfessel and Paxton, 1989] Methfessel, M. and Paxton, A. T. (1989). High-precision sampling for brillouin-zone integration in metals. *Phys. Rev. B*, 40:3616–3621.

[Militzer et al., 2021] Militzer, B., González-Cataldo, F., Zhang, S., Driver, K. P., and Soubiran, F. m. c. (2021). First-principles equation of state database for warm dense matter computation. *Phys. Rev. E*, 103:013203.

[Militzer et al., 2020] Militzer, B., Gonzalez-Cataldo, F., Zhang, S., Whitley, H. D., Swift, D. C., and Millot, M. (2020). Nonideal mixing effects in warm dense matter studied with first-principles computer simulations.

[Miller et al., 2007] Miller, J. E., Boehly, T. R., Melchior, A., Meyerhofer, D. D., Celliers, P. M., Eggert, J. H., Hicks, D. G., Sorce, C. M., Oertel, J. A., and Emmel, P. M. (2007). Streaked optical pyrometer system for laser-driven shock-wave experiments on omega. *Review of Scientific Instruments*, 78(3):034903.

[Millot et al., 2018a] Millot, M., Celliers, P. M., Sterne, P. A., Benedict, L. X., Correa, A. A., Hamel, S., Ali, S. J., Baker, K. L., Berzak Hopkins, L. F., Biener, J., Collins, G. W., Coppari, F., Divol, L., Fernandez-Panella, A., Fratanduono, D. E., Haan, S. W., Le Pape, S., Meezan, N. B., Moore, A. S., Moody, J. D., Ralph, J. E., Ross, J. S., Rygg, J. R., Thomas, C., Turnbull, D. P., Wild, C., and Eggert, J. H. (2018a). Measuring the shock impedance mismatch between high-density carbon and deuterium at the national ignition facility. *Phys. Rev. B*, 97:144108.

[Millot et al., 2019] Millot, M., Coppari, F., Rygg, J. R., Correa Barrios, A., Hamel, S., Swift, D. C., and Eggert, J. H. (2019). Nanosecond X-ray diffraction of shock-compressed superionic water ice. *Nature*, 569(7755):251–255.

[Millot et al., 2018b] Millot, M., Hamel, S., Rygg, J. R., Celliers, P. M., Collins, G. W., Coppari, F., Fratanduono, D. E., Jeanloz, R., Swift, D. C., and Eggert, J. H. (2018b). Experimental evidence for superionic water ice using shock compression. *Nature Physics*, 14(3):297–302.

[Møller and Plesset, 1934] Møller, C. and Plesset, M. S. (1934). Note on an approximation treatment for many-electron systems. *Phys. Rev.*, 46:618–622.

[Molodets et al., 2014] Molodets, A. M., Shakhrai, D. V., and Fortov, V. E. (2014). Thermophysical properties of the polymorphic modifications of lithium hydride in

the megabar shock pressure range. *Journal of Experimental and Theoretical Physics*, 118(6):896–903.

[Monkhorst and Pack, 1976] Monkhorst, H. J. and Pack, J. D. (1976). Special points for brillouin-zone integrations. *Phys. Rev. B*, 13:5188–5192.

[Montgomery, 1973] Montgomery, C. D. (1973). Fabrication and properties of lithium hydride. *Nuclear Engineering and Design*, 25(2):309–314.

[Mora, 1982a] Mora, P. (1982a). Theoretical model of absorption of laser light by a plasma. *The Physics of Fluids*, 25(6):1051–1056.

[Mora, 1982b] Mora, P. (1982b). Theoretical model of absorption of laser light by a plasma. *The Physics of Fluids*, 25(6):1051–1056.

[More et al., 1988] More, R. M., Warren, K. H., Young, D. A., and Zimmerman, G. B. (1988). A new quotidian equation of state (qeos) for hot dense matter. *The Physics of Fluids*, 31(10):3059–3078.

[Murnaghan, 1944] Murnaghan, F. D. (1944). The compressibility of media under extreme pressures. *Proceedings of the National Academy of Sciences*, 30(9):244–247.

[Nagao et al., 2006] Nagao, H., Nakamura, K. G., Kondo, K., Ozaki, N., Takamatsu, K., Ono, T., Shiota, T., Ichinose, D., Tanaka, K. A., Wakabayashi, K., Okada, K., Yoshida, M., Nakai, M., Nagai, K., Shigemori, K., Sakaiya, T., and Otani, K. (2006). Hugoniot measurement of diamond under laser shock compression up to 2tpa. *Physics of Plasmas*, 13(5):052705.

[Nagayama et al., 2002] Nagayama, K., Mori, Y., Shimada, K., and Nakahara, M. (2002). Shock hugoniot compression curve for water up to 1 gpa by using a compressed gas gun. *Journal of Applied Physics*, 91(1):476–482.

[Napán and y Blancá, 2012] Napán, R. and y Blancá, E. L. P. (2012). First-principles studies of lithium hydride series for hydrogen storage. *International Journal of Hydrogen Energy*, 37:5784–5789.

[NELLIS et al., 1988] NELLIS, W. J., HAMILTON, D. C., HOLMES, N. C., RADOUSKY, H. B., REE, F. H., MITCHELL, A. C., and NICOL, M. (1988). The nature of the interior of uranus based on studies of planetary ices at high dynamic pressure. *Science*, 240(4853):779–781.

[Nellis et al., 1997] Nellis, W. J., Holmes, N. C., Mitchell, A. C., Hamilton, D. C., and Nicol, M. (1997). Equation of state and electrical conductivity of "synthetic uranus," a mixture of water, ammonia, and isopropanol, at shock pressure up to 200 gpa (2 mbar). *The Journal of Chemical Physics*, 107(21):9096–9100.

[NESS et al., 1986] NESS, N. F., ACUÑA, M. H., BEHANNON, K. W., BURLAGA, L. F., CONNERNEY, J. E. P., LEPPING, R. P., and NEUBAUER, F. M. (1986). Magnetic fields at uranus. *Science*, 233(4759):85–89.

[Ness et al., 1989] Ness, N. F., Acuna, M. H., Burlaga, L. F., Connerney, J. E. P., Lepping, R. P., and Neubauer, F. M. (1989). Magnetic fields at neptune. *Science*, 246(4936):1473–1478.

[NEUMAYER et al., 2005] NEUMAYER, P., BOCK, R., BORNEIS, S., BRAMBRINK, E., BRAND, H., CAIRD, J., CAMPBELL, E., GAUL, E., GOETTE, S., HAEFNER, C., and et al. (2005). Status of phelix laser and first experiments. *Laser and Particle Beams*, 23(3):385–389.

[NUCKOLLS et al., 1972] NUCKOLLS, J., WOOD, L., THIESSEN, A., and ZIMMERMAN, G. (1972). Laser compression of matter to super-high densities: Thermonuclear (ctr) applications. *Nature*, 239(5368):139–142.

[Oganov et al., 2019] Oganov, A. R., Pickard, C. J., Zhu, Q., and Needs, R. J. (2019). Structure prediction drives materials discovery. *Nature Reviews Materials*, 4(5):331–348.

[Ogitsu et al., 2003] Ogitsu, T., Schwegler, E., Gygi, F. m. c., and Galli, G. (2003). Melting of lithium hydride under pressure. *Phys. Rev. Lett.*, 91:175502.

[Paleari et al., 2013] Paleari, S., Batani, D., Vinci, T., Benocci, R., Shigemori, K., Hironaka, Y., Kadono, T., Shiroshita, A., Piseri, P., Bellucci, S., Mangione, A., and Aliverdiev, A. (2013). A new target design for laser shock-compression studies of carbon reflectivity in the megabar regime. *The European Physical Journal D*, 67(7):136.

[Pan et al., 2014] Pan, D., Wan, Q., and Galli, G. (2014). The refractive index and electronic gap of water and ice increase with increasing pressure. *Nature Communications*, 5(1):3919.

[Parr and Weitao, 1994] Parr, R. and Weitao, Y. (1994). *Density-Functional Theory of Atoms and Molecules*. International Series of Monographs on Chemistry. Oxford University Press.

[Parsopoulos and Vrahatis, 2002] Parsopoulos, K. E. and Vrahatis, M. N. (2002). Recent approaches to global optimization problems through particle swarm optimization. *Natural Computing*, 1(2):235–306.

[Perdew et al., 1996] Perdew, J. P., Burke, K., and Ernzerhof, M. (1996). Generalized gradient approximation made simple. *Phys. Rev. Lett.*, 77:3865–3868.

[Pierre-Henri Hugoniot, 1889] Pierre-Henri Hugoniot (1889). *Sur la propagation du mouvement dans les corps et spécialement dans les gaz parfaits*. Thesis, J. École Polytechnique, Paris.

[Ramis et al., 1988] Ramis, R., Schmalz, R., and Meyer-Ter-Vehn, J. (1988). Multi — a computer code for one-dimensional multigroup radiation hydrodynamics. *Computer Physics Communications*, 49(3):475 – 505.

[Reshak, 2013] Reshak, A. (2013). Mgh2 and lih metal hydrides crystals as novel hydrogen storage material: Electronic structure and optical properties. *International Journal of Hydrogen Energy*, 38(27):11946–11954.

[Robey et al., 2012] Robey, H. F., Boehly, T. R., Celliers, P. M., Eggert, J. H., Hicks, D., Smith, R. F., Collins, R., Bowers, M. W., Krauter, K. G., Datte, P. S., Munro, D. H., Milovich, J. L., Jones, O. S., Michel, P. A., Thomas, C. A., Olson, R. E., Pollaine, S., Town, R. P. J., Haan, S., Callahan, D., Clark, D., Edwards, J., Kline, J. L., Dixit, S., Schneider, M. B., Dewald, E. L., Widmann, K., Moody, J. D., Döppner, T., Radousky, H. B., Throop, A., Kalantar, D., DiNicola, P., Nikroo, A., Kroll, J. J., Hamza, A. V., Horner, J. B., Bhandarkar, S. D., Dzenitis, E., Alger, E., Giraldez, E., Castro, C., Moreno, K., Haynam, C., LaFortune, K. N., Widmayer, C., Shaw, M., Jancaitis, K., Parham, T., Holunga, D. M., Walters, C. F., Haid, B., Mapoles, E. R., Sater, J., Gibson, C. R., Malsbury, T., Fair, J., Trummer, D., Coffee, K. R., Burr, B., Berzins, L. V., Choate, C., Brereton, S. J., Azevedo, S., Chandrasekaran, H., Eder, D. C., Masters, N. D., Fisher, A. C., Sterne, P. A., Young, B. K., Landen, O. L., Van Wonterghem, B. M., MacGowan, B. J., Atherton, J., Lindl, J. D., Meyerhofer, D. D., and Moses, E. (2012). Shock timing experiments on the national ignition facility: Initial results and comparison with simulation. *Physics of Plasmas*, 19(4):042706.

[Robey et al., 2016] Robey, H. F., Celliers, P. M., Moody, J. D., Sater, J., Parham, T., Kozioziemski, B., Dylla-Spears, R., Ross, J. S., LePape, S., Ralph, J. E., Hohenberger, M., Dewald, E. L., Hopkins, L. B., Kroll, J. J., Yoxall, B. E., Hamza, A. V., Boehly, T. R., Nikroo, A., Landen, O. L., and Edwards, M. J. (2016). Advances in shock timing experiments on the national ignition facility. *Journal of Physics: Conference Series*, 688:012092.

[Roma et al., 1996] Roma, G., Bertoni, C. M., and Baroni, S. (1996). The phonon spectra of lih and lid from density-functional perturbation theory. *Solid State Communications*, 98(3):203–207.

[Romero and Mattson, 2007] Romero, N. A. and Mattson, W. D. (2007). Density-functional calculation of the shock hugoniot for diamond. *Phys. Rev. B*, 76:214113.

[Ross, 1981] Ross, M. (1981). The ice layer in uranus and neptune-diamonds in the sky? *Nature*, 292(5822):435–436.

[Ruoff and Luo, 1991] Ruoff, A. L. and Luo, H. (1991). Pressure strengthening: A possible route to obtaining 9 mbar and metallic diamonds. *Journal of Applied Physics*, 70(4):2066–2070.

[Sano et al., 2011] Sano, T., Ozaki, N., Sakaiya, T., Shigemori, K., Ikoma, M., Kimura, T., Miyanishi, K., Endo, T., Shiroshita, A., Takahashi, H., Jitsui, T., Hori, Y., Hironaka, Y., Iwamoto, A., Kadono, T., Nakai, M., Okuchi, T., Otani, K., Shimizu, K., Kondo, T., Kodama, R., and Mima, K. (2011). Laser-shock compression and hugoniot measurements of liquid hydrogen to 55 gpa. *Phys. Rev. B*, 83:054117.

[Scandolo et al., 1996] Scandolo, S., Chiarotti, G. L., and Tosatti, E. (1996). Sc4: A metallic phase of carbon at terapascal pressures. *Phys. Rev. B*, 53:5051–5054.

[Schönlein et al., 2016] Schönlein, A., Boutoux, G., Pikuz, S., Antonelli, L., Batani, D., Debayle, A., Franz, A., Giuffrida, L., Honrubia, J. J., Jacoby, J., Khaghani, D., Neumayer, P., Rosmej, O. N., Sakaki, T., Santos, J. J., and Sauteray, A. (2016). Generation and characterization of warm dense matter isochorically heated by laser-induced relativistic electrons in a wire target. *EPL (Europhysics Letters)*, 114(4):45002.

[Sekine, 1999] Sekine, T. (1999). Sixfold-coordinated carbon as a postdiamond phase. *Applied Physics Letters*, 74(3):350–352.

[Shaner et al., 1984] Shaner, J. W., Brown, J. M., Swenson, C. A., and McQueen, R. G. (1984). Sound velocity of carbon at high pressures. *J. Phys. Colloques*, 45(C8):C8–235–C8–237.

[Shi et al., 2001] Shi, Y. et al. (2001). Particle swarm optimization: developments, applications and resources. In *Proceedings of the 2001 congress on evolutionary computation (IEEE Cat. No. 01TH8546)*, volume 1, pages 81–86. IEEE.

[Stephens and Lilley, 1968] Stephens, D. R. and Lilley, E. M. (1968). Compressions of isotopic lithium hydrides. *Journal of Applied Physics*, 39(1):177–180.

[Strickland and Mourou, 1985] Strickland, D. and Mourou, G. (1985). Compression of amplified chirped optical pulses. *Optics Communications*, 56(3):219–221.

[Sun et al., 2012] Sun, X.-W., Cai, L.-C., Chen, Q.-F., Chen, X.-R., and Jing, F.-Q. (2012). Structural, thermodynamic, electronic, and optical properties of nah from first-principles calculations. *Materials Chemistry and Physics*, 133(1):346–355.

[Takeda et al., 1982] Takeda, M., Ina, H., and Kobayashi, S. (1982). Fourier-transform method of fringe-pattern analysis for computer-based topography and interferometry. *J. Opt. Soc. Am.*, 72(1):156–160.

[van Setten et al., 2007] van Setten, M. J., Popa, V. A., de Wijs, G. A., and Brocks, G. (2007). Electronic structure and optical properties of lightweight metal hydrides. *Phys. Rev. B*, 75:035204.

[van Thiel and Ree, 1995] van Thiel, M. and Ree, F. H. (1995). Entropy of melting: Its effect on the liquid-liquid phase change of carbon. *Journal of Applied Physics*, 77(9):4804–4806.

[Van Vechten, 1973] Van Vechten, J. A. (1973). Quantum dielectric theory of electronegativity in covalent systems. iii. pressure-temperature phase diagrams, heats of mixing, and distribution coefficients. *Phys. Rev. B*, 7:1479–1507.

[Varshni, 1967] Varshni, Y. (1967). Temperature dependence of the energy gap in semiconductors. *Physica*, 34(1):149–154.

[Vidal and Vidal-Valat, 1986] Vidal, J. P. and Vidal-Valat, G. (1986). Accurate Debye–Waller factors of ^{7}LiH and ^{7}LiD by neutron diffraction at three temperatures. *Acta Crystallographica Section B*, 42(2):131–137.

[Vinet et al., 1987] Vinet, P., Ferrante, J., Rose, J. H., and Smith, J. R. (1987). Compressibility of solids. *Journal of Geophysical Research: Solid Earth*, 92(B9):9319–9325.

[Wang et al., 2021] Wang, P., Zhang, C., Jiang, S., Duan, X., Zhang, H., Li, L., Yang, W., Liu, Y., Li, Y., Sun, L., Liu, H., and Wang, Z. (2021). Density-dependent shock hugoniot of polycrystalline diamond at pressures relevant to icf. *Matter and Radiation at Extremes*, 6(3):035902.

[Wang et al., 2010] Wang, Y., Lv, J., Zhu, L., and Ma, Y. (2010). Crystal structure prediction via particle-swarm optimization. *Phys. Rev. B*, 82:094116.

[Wang et al., 2012] Wang, Y., Lv, J., Zhu, L., and Ma, Y. (2012). Calypso: A method for crystal structure prediction. *Computer Physics Communications*, 183(10):2063–2070.

[Weber et al., 2017] Weber, S., Bechet, S., Borneis, S., Brabec, L., Bučka, M., Chacon-Golcher, E., Ciappina, M., DeMarco, M., Fajstavr, A., Falk, K., Garcia, E.-R., Grosz, J., Gu, Y.-J., Hernandez, J.-C., Holec, M., Janečka, P., Jantač, M., Jirka, M., Kadlecova, H., Khikhlukha, D., Klimo, O., Korn, G., Kramer, D., Kumar, D., Lastovička, T., Lutoslawski, P., Morejon, L., Olšovcová, V., Rajdl, M., Renner, O., Rus, B., Singh, S., Šmid, M., Sokol, M., Versaci, R., Vrána, R., Vranic, M., Vyskočil, J., Wolf, A., and Yu, Q. (2017). P3: An installation for high-energy density plasma physics and ultra-high intensity laser–matter interaction at eli-beamlines. *Matter and Radiation at Extremes*, 2(4):149–176.

[Wigner and Huntington, 1935] Wigner, E. and Huntington, H. B. (1935). On the possibility of a metallic modification of hydrogen. *The Journal of Chemical Physics*, 3(12):764–770.

[Yan et al., 2021] Yan, Z., Liu, H., Zhang, X., Ren, G., Liu, J., Kang, W., Zhang, W., and He, X. (2021). Dynamics of particles near the surface of a medium under ultra-strong shocks. *Matter and Radiation at Extremes*, 6(2):026903.

[Yin and Cohen, 1983] Yin, M. T. and Cohen, M. L. (1983). Will diamond transform under megabar pressures? *Phys. Rev. Lett.*, 50:2006–2009.

[Yu et al., 2007] Yu, W., Jin, C., and Kohlmeyer, A. (2007). First principles calculation of phonon dispersion, thermodynamic properties andB1-to-b2 phase transition of lighter alkali hydrides. *J. Phys.: Condens. Matter*, 19(8):086209.

[Zel'dovich and Raizer, 2002] Zel'dovich, I. and Raizer, Y. (2002). *Physics of Shock Waves and High-Temperature Hydrodynamic Phenomena*. Dover Books on Physics. Dover Publications.

[Zhang et al., 2007] Zhang, J., Zhang, L., Cui, T., Li, Y., He, Z., Ma, Y., and Zou, G. (2007). Phonon and elastic instabilities in rocksalt alkali hydrides under pressure: First-principles study. *Phys. Rev. B*, 75:104115.

[Zurek et al., 2009] Zurek, E., Hoffmann, R., Ashcroft, N. W., Oganov, A. R., and Lyakhov, A. O. (2009). A little bit of lithium does a lot for hydrogen. *Proceedings of the National Academy of Sciences*, 106(42):17640–17643.

Annexes

Contents

A . List of publications

1. Measurements of parametric instabilities at laser intensities relevant to strong shock generation. G Cristoforetti, L Antonelli, S Atzeni, F Baffigi, F Barbato, D Batani, G Boutoux, A Colaitis, J Dostal, R Dudzak, L Juha, P Koester, A Marocchino, **D Mancelli**, Ph Nicolai, O Renner, JJ Santos, A Schiavi, MM Skoric, M Smid, P Straka, LA Gizzi: Physics of Plasmas 25, 012702 (2018); https://doi.org/10.1063/1.5006021

2. Wavelength dependence of laser plasma interaction related to shock ignition approach. T Pisarczyk, SYu Gus'kov, R Dudzak, O Renner, D Batani, T Chodukowski, Z Rusiniak, J Dostal, NN Demchenko, M Rosinski, P Parys, M Smid, Ph Korneev, E Krousky, S Borodziuk, J Badziak, L Antonelli, L Gizzi, G Cristoforetti, P Koester,

Y Maheut, L Volpe, F Baffigi, T Levato, J Skala, A Zaras-Szydlowska, J Trela, **D Mancelli**, J Ullschmied, M Pfeifer, L Juha, M Krus, J Hrebicek, T Medrik, K Jungwirth, M Krupka, P Pisarczyk: Laser and Particle Beams, 36(3), 405-426. https://doi.org/10.1017/S0263034618000447

3. Progress in understunding the role of hot electrons for the shock ignition approach to inertial confinement fusion. D Batani, L Antonelli, F Barbato, G Boutoux, A Colaïtis, J-L Feugeas, G Folpini, **D Mancelli**, Ph Nicolai, J Santos, J Trela, V Tikhonchuk, J Badziak, T Chodukowski, K Jakubowska, Z Kalinowska, T Pisarczyk, M Rosinski, M Sawicka, F Baffigi, G Cristoforetti, F D'Amato, P Koester, LA Gizzi, S Viciani, S Atzeni, A Schiavi, M Skoric, S Gus'kov, J Honrubia, J Limpouch, O Klimo, J Skala, YJ Gu, E Krousky, O Renner, M Smid, S Weber, R Dudzak, M Krus, J Ullschmied: Nuclear Fusion:https://doi.org/10.1088/1741-4326/aaf0ed

4. Time evolution of stimulated Raman scattering and two-plasmon decay at laser intensities relevant for shock ignition in a hot plasma. G Cristoforetti, L Antonelli, **D Mancelli**, S Atzeni, F Baffigi, F Barbato, D Batani, G Boutoux, F D'Amato, J Dostal, R Dudzak, E Filippov, Y J Gu, L Juha, O Klimo, M Krus, S Malko, A S Martynenko, Ph Nicolai, V Ospina, S Pikuz, O Renner, J Santos, V T Tikhonchuk, J Trela, S Viciani, L Volpe, S Weber, L A Gizzi: High Power Laser Science and Engineering, V7, 2019: https://doi.org/10.1017/hpl.2019.37

5. X-ray phase-contrast imaging for laser-induced shock waves. L Antonelli, F Barbato, **D Mancelli**, J Trela, G Zeraouli, G Boutoux, P Neumayer, S Atzeni, A Schiavi, L Volpe, V Bagnoud, C Brabetz, B Zielbauer, P Bradford, N Woolsey, B Borm, D Batani: EPL 125 35002; https://doi.org/10.1209/0295-5075/125/35002

6. Propagation-based imaging phase-contrast enhanced imaging setup for single shot acquisition using laser-generated X-ray sources. F Barbato, D Batani, **D Mancelli**, J Trela, G Zeraouli, G Boutoux, P Neumayer, S Atzeni, A Schiavi, L Volpe, V Bagnoud, C Brabetz, B Zielbauer, P Bradford, N Woolsey, B Borm, L Antonelli: 2019

JINST 14 C03005, https://doi.org/10.1088/1748-0221/14/03/C03005

7. Optical Time-Resolved Diagnostics of Laser-Produced Plasmas. D Batani, J Santos, P Forestier-Colleoni, **D Mancelli**, M Ehret, J Trela, A Morace, K Jakubowska, L Antonelli, D del Sorbo, M Manclossi, M Veltcheva: J Fusion Energ 38, 299–314 (2019). https://doi.org/10.1007/s10894-019-00218-4

8. Laser-driven strong shocks with infrared lasers at intensity of $10^{16}\ W/cm^2$. L Antonelli, J Trela, F Barbato, G Boutoux, Ph Nicolaï, D Batani, V Tikhonchuk, **D Mancelli**, A Tentori, S Atzeni, A Schiavi, F Baffigi, G Cristoforetti, S Viciani, LA Gizzi, M Smid, O Renner, J Dostal, R Dudzak, L Juha, M Krus: Physics of Plasmas 26, 112708 (2019); https://doi.org/10.1063/1.5119697

9. Quantitative phase contrast imaging of a shock-wave with a laser-plasma based X-ray source. F Barbato, S Atzeni, D Batani, D Bleiner, G Boutoux, C Brabetz, P Bradford, D Mancelli, P Neumayer, A Schiavi, J Trela, L Volpe, G Zeraouli, N Woolsey, L Antonelli: Sci Rep 9, 18805 (2019). https://doi.org/10.1038/s41598-019-55074-1

10. X-ray time-resolved diagnostics of hot electron generation in shock ignition relevant experiments. ED Filippov, AS Martynenko, M Cervenak, L Antonelli, F Baffigi, G Cristoferetti, LA Gizzi, T Pisarczyk, **D Mancelli**, V Ospina, M Krus, R Dudzak, SA Pikuz, D Batani, O Renner: International Conference Laser Optics (ICLO), Saint Petersburg, 2020, pp. 1-1, https://doi.org/10.1109/ICLO48556.2020.9285718

11. Reflecting laser-driven shocks in diamond in the megabar pressure range. K Jakubowska, **D Mancelli**, R Benocci, J Trela, I Errea, AS Martynenko, P Neumayer, O Rosmej, B Borm, A Molineri, C Verona, D Cannatà, A Aliverdiev, HE Roman, D Batani: High Power Laser Science and Engineering, 9, E3. https://doi.org/10.1017/hpl.2020.38

12. Observation and modelling of Stimulated Raman Scattering driven by an optically

smoothed laser beam in experimental conditions relevant for Shock Ignition. G. Cristoforetti, S. Atzeni, F. Baffigi, D. Batani, C. Baird, N. Booth, M. Galimberti, K. Glize, A. Heron, S. Hüller, M. Khan, P. Koester, P. Loiseau, **D. Mancelli**, M. Notley, P. Oliveira, O. Renner, M. Smid, A. Schiavi, G. Tran, N.C. Woolsey, L.A. Gizzi: High Power Laser Science and Engineering. https://dx.doi.org/10.1017/hpl.2021.48

13. Shock Hugoniot data for Water up to 5 Mbar obtained with quartz standard at high-energy laser facilities. **D. Mancelli**, I. Errea, A. Tentori, O. Turianska, H. Larreur, D. Batani, K. Katagiri, N. Ozaki, N. Kamimura,D. Kamibayashi, K. Ishida, H. Ogura, K. Kawasaki, Y. Maeda, Y. Hironaka, K. Shigemori, K. Batani, G. Schaumann, O. Rosmej, P. Neumayer, B. Zielbauer, A.S. Martynenko, E.D. Filippov, S. Pikuz: Laser and Particle Beams. https://doi.org/10.1155/2021/4141522

B . Conducted experimental campaigns

- **2016**
  - 01/02/2016 – 30/09/2016 “Data analysis of the GSI campaign on Diamond study” (Study the behavior of diamond compressed to Mbar pressures by laser-driven shocks using a VISAR diagnostics)
- **2017**
  - 27/02/17 - 24/03/17, "Understanding the effects of hot electron preheating on shock break-out times and pressure measurements" at the Prague Asterix Laser System (PALS)
  - 28/05/2017 - 24/06/17 "X-ray phase contrast imaging of laser-produced shock wave propagating in low-density material" a proof of principle experiment conducted on PHELIX facility in Darmstadt in Germany
- **2018**
  - 2/04/18 - 21/04/18, "Experimental platform to characterize temperature and density of a Titanium wire isochoric heated by laser-accelerated electrons" - test of a novel approach to study EOS in the WDM regime, (P-166) experiment conducted on PHELIX facility in Darmstadt in Germany
  - 16/09/18 - 29/09/18, "Understanding the effects of hot electron preheating on shock break-out times and pressure measurements" at the Prague Asterix Laser System (PALS)
  - 29/10/18 - 23/11/18, "Generation of transient very strong shocks by fs-Lasers" VEGA II CLPU Salamanca Spain
  - 5/11/18 - 11/12/18, "Role of Laser Plasma Interactions in the Shock Ignition Regime (18110033)" VULCAN RAL-CLF Didcot United Kingdom

- **2019**
  - 02/09/2019 – 06/09/2019 ”Behavior and optical properties of materials of planetological interest (water and LiH) at Megabar pressures” GEKKO XII, Osaka, Japan
  - 08/09/2019 – 13/09/2019 ”Investigation of Laser-Plasma interaction and the hot electron generation in Shock ignition regime” GEKKO XII, Osaka, Japan
  - 16/09/2019 – 20/09/2019 ”Numerical investigation on non-thermal electron effects measured in a Gekko experiment at intensities relevant to shock ignition” GEKKO XII, Osaka, Japan
- **2020**
  - 02/02/2020 – 27/02/2020 ”PALS proposal for L4n preliminary experiment” PALS, Prague
  - 08/04/2020 – 03/04/2020 ”Investigation of Laser-Plasma interaction and the hot electron generation in Shock ignition regime” PALS, Prague
- **2021**
  - 30/11/2020 – 18/12/2020 ”Study of matter at extreme conditions” GSI-PHELIX, Germany
  - 06/07/2021– 16/07/2021 ”Study of Water and Diamond samples at extreme conditions at GEKKO XII laser facility”, ILE-GEKKO XII, Japan

C . International conferences and schools

- **2017**
  - 2nd European Conference on Plasma Diagnostics (ECPD), 18-21 April 2017 Bordeaux (France)
  - 8th Summer School: Atoms and Plasmas in Super-Intense Laser Fields, held at Erice, Sicily, Italy on July 7-17 (2017)
  - 10th International Fusion Science and Application Conference (September 11-15, 2017 in St-Malo)
- **2018**
  - PowerLaPs ”Innovative Education & Training in High Power Laser Plasmas” Erasmus + (July 2-13, 2018 Rethimo Crete, Greece)
  - 56th European High-Pressure Research Group Meeting Aveiro (EHPRG 2018) - Portugal, 2 - 7 September 2018
- **2019**
  - 15th Direct-Drive and Fast-Ignition Workshop, Rome, Italy 8-20 April, 2019
  - 3rd European Conference on Plasma Diagnostics (ECPD) Lisbon, Portugal 6-9 May 2019 (Chairman session and Poster Presentation)
  - PowerLaPs ”Innovative Education & Training in High Power Laser Plasmas” Erasmus + (July 1-13, 2019 Rethimo Crete, Greece)
  - 11th International Fusion Science and Application Conference (September 22-27, 2019 in Osaka, Japan, Poster Presentation)

- **2021**
  - 41st International Workshop on High Energy Density Physics with Intense Ion and Laser Beams 01-05 February, 2021 Online (ORAL Talk)
  - 4th European Conference on Plasma Diagnostics 2021, 7th - 11th June 2021 Online (two Poster Presentations)
  - 47th Conference on Plasma Physics - Satellite Meeting 28th - 29th June 2021, Online (Poster Presentation)

D . Laser System - Energy and Intensity Calculation

The total energy of the laser pulse is estimated with a calibrated pyrometer. The light intensity on target can. be calculated as follows the energy of the pulse is given by the integral of the. intensity over the target face and time:

$$E = \int_0^\infty dt \int_{R^2} dxdyI(x, y; t) \tag{9.1}$$

We approximate the laser focal spot as circular with flat top and fast raising and falling edge

$$I(x, y; t) = I_0\xi(t)I(x^2 + y^2 < R) \tag{9.2}$$

the maximum intensity in the spot can be given by

$$I_0 = \frac{E}{\pi R^2 \int_0^\infty dt\xi(t)} \tag{9.3}$$

E . Multi 1D Run File

```
&RBOUND
   TEMRAD = 0.0 , IEXT   = 0 , LTR   = 0 , XTR   = 0. ,
   ALPHAL = 0. , ALPHAR = 0. , BETAL = 0. , BETAR = 0. ,
   GAB    = 1. , GBA    = 1. , GOB   = 0. , GOA   = 0. ,
&END
## Simulation time & File Data writing
&INPUT
   IGEO     = 1 , NSPLIT = 1 , NDIV = 1 , VARNOM = 0.2,
   TEXIT    = 20.0e-09 , DTN  = 100.0E-12 , NEXIT  = 3000000, DT0=1e-18,
   TOUT     = 0.0E-12,  20.0e-09
&END
&FILM
   dtdisk =  10.e-12
&END
## Hydro Controls (Radiative or Non-Radiative)
```

```
&NGMK
   NLHYD = T,  NLRAD  =T , NL2TMP = F, NLZMOR = F , NLPICH = F ,
   NLMAC = T,  NLFUS = F,  ncolli = 2 ,
&END
## Target layers
&LAYER
  NC    =100 , THICK  = 10.0e-4  , ZONPAR = -1.06,
  R0    = 1.11 , TE0    = 0.025692 , TI0    = 0.025692 , v0   = 0.0 ,
  ATWGT = 6.51 , ATNUM0 = 3.51 , ZION   = 3.51 , zmin = 0.1 ,
  FIM = '~/Tables/Parylene/7770.ieos.gz'
  FIP = '~/Tables/Parylene/Parylene_planck_mult_gr.cens.gz'
  FIR = '~/Tables/Parylene/Parylene_rossla_mult_gr.cens.gz'
  FIZ = '~/Tables/Parylene/Parylene_zeff.cens.gz'
&END
&LAYER
  NC  = 100 , THICK  = 0.2e-4 ,  ZONPAR = 1.012,
  R0  = 19.3  , TE0    = 0.025692 , TI0    = 0.025692 , v0  = 0.0 ,
   ATWGT = 196.96654 , ATNUM0 =  79.0 , ZION   =  79.0    , zmin = 0.1 ,
   FIM = '~/Tables/Gold/ses_2700_multi_dm_feos.gz'
   FIE = '~/Tables/Gold/Au__NG.eps.gz'
   FIP = '~/Tables/Gold/Au__NG.opp.gz'
   FIR = '~/Tables/Gold/Au__NG.opr.gz'
   FIZ = '~/Tables/Gold/Au__NG.opz.gz'
&END
&LAYER
   NC    =  200  , THICK  = 100.0e-4 , ZONPAR = 1.023,
   R0    = 2.65  , TE0  = 0.025692 , TI0    =  0.025692 , v0   = 0.0  ,
   ATWGT =20.0  , ATNUM0 =  10.0  , ZION   =  10.0  , zmin = 0.01 ,
  FIM = '~/Tables/Quartz/SiO2_7386_feos_dm_multi.gz'
  FIZ = '~/Tables/Quartz/73822001.opz.gz'
  FIP = '~/Tables/Quartz/73823001.opp.gz'
  FIR = '~/Tables/Quartz/73824001.opr.gz'
  FIE = '~/Tables/Quartz/73825001.eps.gz'
&END
```

```
&LAYER
   NC     = 200   , THICK   = 200.0e-4 , ZONPAR = 0.97000,
   R0     =0.98   , TE0     = 0.025692 , TI0    = 0.025692 , v0    = 0.0   ,
   ATWGT =6   , ATNUM0 = 3.33   , ZION    =  3.33     , zmin = 0.01 ,
  FIM = '~/Tables/Water/7154.ieos.multi.gz'
  FIE = '~/Tables/Water/Water.ope.gz'
  FIP = '~/Tables/Water/Water.opp.gz'
  FIR = '~/Tables/Water/Water.opr.gz'
  FIZ = '~/Tables/Water/Water.opz.gz'
&END
## Laser Pulse
&PULSE
   INTER=0
   WL = 0.351E-4   ,
   DELTA   = 0.0 , ITYPE    = 9   , IDEP = 0,
   TMONTE = 0.1E-9, TDESCE = 0.1E-9,
   PIMAX   =1.6E+21, PINACH= 1.6E+21,
   PITIME   = 2.3E-9, TMAX   = 0.1E-9,
&END
## Spitzer Flux limiter
&THERM
   FFACTOR =0.06   ,
&END
```

Listing 9.1: Multi 1D Run File example